

**Sub synchronous oscillations in modern transmission grids
Design and validation of novel concepts for mitigating adverse dfig-ssr interactions**

Sewdien, V.N.

DOI

[10.4233/uuid:8b23ce5e-fd8c-4475-972d-bc50d7a2df1a](https://doi.org/10.4233/uuid:8b23ce5e-fd8c-4475-972d-bc50d7a2df1a)

Publication date

2021

Document Version

Final published version

Citation (APA)

Sewdien, V. N. (2021). *Sub synchronous oscillations in modern transmission grids: Design and validation of novel concepts for mitigating adverse dfig-ssr interactions*. [Dissertation (TU Delft), Delft University of Technology]. <https://doi.org/10.4233/uuid:8b23ce5e-fd8c-4475-972d-bc50d7a2df1a>

Important note

To cite this publication, please use the final published version (if applicable).
Please check the document version above.

Copyright

Other than for strictly personal use, it is not permitted to download, forward or distribute the text or part of it, without the consent of the author(s) and/or copyright holder(s), unless the work is under an open content license such as Creative Commons.

Takedown policy

Please contact us and provide details if you believe this document breaches copyrights.
We will remove access to the work immediately and investigate your claim.

SUB SYNCHRONOUS OSCILLATIONS IN MODERN TRANSMISSION GRIDS

DESIGN AND VALIDATION OF NOVEL CONCEPTS FOR MITIGATING
ADVERSE DFIG-SSR INTERACTIONS



VINAY SEWDIEN

SUB SYNCHRONOUS OSCILLATIONS IN MODERN TRANSMISSION GRIDS

DESIGN AND VALIDATION OF NOVEL CONCEPTS FOR MITIGATING
ADVERSE DFIG-SSR INTERACTIONS

SUB SYNCHRONOUS OSCILLATIONS IN MODERN TRANSMISSION GRIDS

DESIGN AND VALIDATION OF NOVEL CONCEPTS FOR MITIGATING
ADVERSE DFIG-SSR INTERACTIONS

Proefschrift

ter verkrijging van de graad van doctor
aan de Technische Universiteit Delft,
op gezag van de Rector Magnificus Prof.dr.ir. T.H.J.J. van der Hagen
voorzitter van het College voor Promoties,
in het openbaar te verdedigen op
donderdag 24 juni 2021 om 15.00 uur

door

Vinay Naraindatt SEWDIEN
burgelijk ingenieur, KU Leuven, België
geboren te Paramaribo, Suriname

Dit proefschrift is goedgekeurd door de promotoren.

Samenstelling promotiecommissie:

Rector Magnificus,	voorzitter
Prof.ir. M.A.M.M. van der Meijden	Technische Universiteit Delft, promotor
Dr.ir. J.L. Rueda Torres	Technische Universiteit Delft, promotor

Onafhankelijke leden:

Prof.dr.ir. U. Annakkage	University of Manitoba
Prof.dr.ir. V. Terzija	Skolkovo Institute of Science and Technology
Prof.Dr.-Ing. habil. L. Hofmann	Leibniz Universität Hannover
Prof.dr. P. Palensky	Technische Universiteit Delft
Ir. C.P.J. Jansen	TenneT TSO BV
Dr.ir. M. Popov	Technische Universiteit Delft, <i>reservelid</i>

Dit onderzoek is gefinancierd door TenneT TSO BV binnen de kaders van het Horizon 2020 project MIGRATE.



This research was carried out as part of the MIGRATE project. This project has received funding from the European Union's Horizon 2020 research and innovation programme under grant agreement No 691800. This dissertation reflects only the authors' views and the European Commission is not responsible for any use that may be made of the information it contains.

Copyright © 2021 by V.N. Sewdien

ISBN 978-94-6384-215-0

Omslagontwerp: Bart Velmans

Omslagfoto: Anholt Wind Farm (Denmark). Courtesy of Ørsted

Dit proefschrift is in elektronische vorm beschikbaar op <https://repository.tudelft.nl/>

*Dedicated to
my Mom, for the unconditional love, support and motivation,
my brother Ajay and sister-in-law Vanya, for showing that family is everything,
my brother Jayant, for showing that with patience and perseverance a lot is possible,
my sister Varsha, who is the avatar of disciple, fun and balance.*

SUMMARY

The ongoing energy transition results on the one hand in a proliferation of power electronics interfaced devices and on the other hand in a decreasing availability of conventional synchronous generation. These developments pose important challenges for transmission system operators to operate a low inertia power system. As part of my research I have created a list of 28 related challenges, validated by industry, that are grouped into three categories: (i) Reduced Voltage and Frequency Support, (ii) New Operation of the Power System and (iii) New Behaviour of the Power System. The focus of this research is on category (iii) and addresses the sub synchronous resonance (SSR) phenomenon between a doubly fed induction generator (DFIG) and a series compensated transmission line. This phenomenon is denoted as DFIG-SSR in this thesis. Failing to adequately address resonances results in among others degradation of the power quality, protection tripping, physical damage to power system equipment and ultimately instability in the power system.

The main objective of this research is to investigate and validate the degree of effectiveness of the existing phase imbalance compensation concept, as well as to design and validate a new prediction gain scheduling control concept for mitigating DFIG-SSR. For these investigation, design and validation activities, electromagnetic transient (EMT) simulation models of the DFIG wind turbine are developed using Power System Computer Aided Design (PSCAD). In line with common practice, the topology of the IEEE First Benchmark Model is used as a small-size study model, whereas the larger IEEE 39-Bus Model is used for validation of the obtained results. The impedance based stability method is used to quantify the impact of potential mitigation solutions on DFIG-SSR.

This dissertation has three main contributions.

First, recommendations are developed to obtain the frequency-dependent impedance of power electronics interfaced devices through numerical EMT simulations of black box, non-linear simulation models. These recommendations are crucial to perform interaction studies. The influence of the impedance calculation time, model granularity and composition of the perturbation signal on the obtained impedance is presented and guidelines are given on how to select the correct model and parameters for the numerical simulations.

Second, a methodology is developed that enables the systematic assessment and design of the phase imbalance compensation concept for mitigating DFIG-SSR. The phase imbalance compensation concept is an alternative way of fixed series compensation, where the imbalance is implemented as a series or as a parallel resonance scheme in either one or two phases of the transmission line. The influence of the series and parallel schemes as well as the influence of their different degrees of asymmetry on the stability of the system are rigorously investigated. The series scheme introduces one series resonance in the power system, where the resonance frequency increases as a function of the degree of asymmetry. The increase is more pronounced

when the series scheme is implemented in two phases. The parallel scheme on the other hand decreases the series resonance frequency and this decrease is more pronounced when the scheme is implemented in two phases. However, the parallel scheme introduces an additional parallel resonance with a frequency between 20 and 30 Hz, the stability of which depends on the degree of asymmetry.

Third, a predictive gain scheduling control is developed, which addresses three main drawbacks of existing adaptive control solutions, i.e. (i) *a priori* knowledge of operating conditions, (ii) the need for a wide area measurement system and (iii) the validation of the developed control against fault ride through and small-signal stability requirements. The developed solution utilises the forecasted wind speed to schedule two parameters in the rectifier's double loop control. For these two parameters, which are identified through monothetic sensitivity analysis, a control rule is developed to determine their optimum values. Furthermore, a forecasting algorithm is developed to predict the wind speed. Using actual wind speeds and transmission line failure data, it is found that the developed predictive gain scheduling control reduces the DFIG-SSR risk with a factor up to 16.95, compared to classical compensation. Detailed analysis also shows that the developed control is able to successfully mitigate DFIG-SSR in a multi-DFIG representation of a wind power plant, while accounting for non-identical operating conditions of the individual DFIGs. To achieve this, a decentralised control deployed in each DFIG is required.

The main conclusion of this dissertation is that DFIG-SSR can be mitigated using a hardware solution such as phase imbalance compensation, or through system level coordination such as the developed prediction gain scheduling control. In this context, grid forming control concepts are increasingly being investigated in academia and industry as a potential solution for some of the 28 challenges identified in this thesis. A recommendation for future research is to investigate the impact of the various grid forming control concepts on DFIG-SSR and their capability to mitigate it.

SAMENVATTING

Als gevolg van de huidige energietransitie ervaren hoogspanningsnetbeheerders enerzijds een grote toename van aan vermogenselektronica gekoppelde productie-eenheden en interconnectoren, en anderzijds een afnemende beschikbaarheid van conventionele synchrone productie-eenheden. Deze ontwikkelingen brengen belangrijke technische uitdagingen voor de bedrijfsvoering van het hoogspanningsnet met zich mee. Deze uitdagingen zijn als onderdeel van dit onderzoek geïnventariseerd. Er is een overzicht van 28 gerelateerde en door de industrie gevalideerde uitdagingen opgesteld, waarbij de uitdagingen worden gegroepeerd in de categorieën (i) onvoldoende ondersteuning van de spanning en frequentie, (ii) noodzaak voor nieuwe bedrijfsvoering concepten en (iii) het nieuwe gedrag van het elektriciteitssysteem. Dit proefschrift betreft categorie (iii) en onderzoekt de sub-synchrone resonantie (SSR) tussen een dubbel gevoede inductiegenerator (*DFIG*) en een serie gecompenseerde transmissielijn. Dit fenomeen wordt in dit proefschrift aangeduid als *DFIG-SSR*. Indien resonanties niet adequaat worden aangepakt, leidt dit onder andere tot een verslechtering van de spanningskwaliteit, uitschakeling door de beveiliging, fysieke schade aan componenten in het elektriciteitssysteem en uiteindelijk instabiliteit in het hoogspanningsnet.

Het hoofddoel van dit proefschrift is het onderzoeken en valideren van de mate van effectiviteit van het bestaande fase-onbalansconcept, en het ontwerpen en valideren van een adaptief regelalgoritme voor het elimineren van *DFIG-SSR*. Voor deze onderzoeken, ontwerpen en validaties zijn elektromagnetische transiënte (EMT) simulatiemodellen van de *DFIG*-windturbine ontwikkeld met *Power System Computer Aided Design* (PSCAD). In overeenstemming met de gangbare praktijk wordt de topologie van het *IEEE First Benchmark Model* gebruikt als studiemodel. Het grotere *IEEE 39-Bus Model* wordt gebruikt voor validatie van de verkregen resultaten. De *impedance based stability*-methode wordt gebruikt voor het kwantificeren van de invloed van de oplossingen ter eliminatie van *DFIG-SSR*.

De bijdrage van dit proefschrift is driedelig.

Ten eerste worden aanbevelingen ontwikkeld om de frequentie-afhankelijke impedantie van aan vermogenselektronica gekoppelde componenten te verkrijgen via EMT-simulaties van black box en niet-lineaire simulatiemodellen. Deze aanbevelingen zijn cruciaal om interactiestudies uit te voeren. Daarbij worden er richtlijnen gegeven voor het selecteren van de juiste modellen en parameters voor deze simulaties.

Ten tweede is er een methodologie ontwikkeld die voorziet in de systematische analyse en ontwerp van het fase-onbalansconcept ten einde *DFIG-SSR* te elimineren. Hierbij worden enkele fundamentele openstaande vragen beantwoord en wordt er aangetoond dat de effectiviteit van het fase-onbalansconcept mede wordt bepaald door de vereiste compensatiegraad. Het concept van fase-onbalanscompensatie is een alternatieve manier voor serierecompensatie, waarbij de onbalans wordt geïmplementeerd als een serie- of

parallelresonantiecircuit in één of twee fasen van de gecompenseerde transmissielijn. De invloeden van de serie- en parallelcircuits en de verschillende mate van asymmetrie op de stabiliteit van het systeem worden uitvoerig onderzocht. Het seriecircuit introduceert één serie-resonantie in het elektriciteitsnet, waarbij de resonantiefrequentie toeneemt afhankelijk van de mate van asymmetrie. De toename in de resonantiefrequentie is groter wanneer het seriecircuit in twee fasen wordt geïmplementeerd. Het parallel circuit daarentegen verlaagt de serieresonantiefrequentie. Daarbij is deze afname groter wanneer het circuit in twee fasen wordt geïmplementeerd. Het parallelcircuit introduceert echter een additionele resonantie met een frequentie tussen 20 en 30 Hz, waarbij de demping van deze resonantie afhankelijk is van de mate van asymmetrie.

Ten derde is een adaptief regelalgoritme ontwikkeld, die drie cruciale tekortkomingen in bestaande, soortgelijke algoritmes oplost. De ontwikkelde oplossing maakt gebruik van de voorspelde windsnelheden om twee parameters in de regeling van de gelijkrichter op een dynamische manier aan te passen. Voor deze twee parameters, die geïdentificeerd worden door middel van een gevoeligheidsanalyse, is een formule ontwikkeld die hun optimale waarden bepaalt. De voorspelde windsnelheden worden verkregen met behulp van een eigen ontwikkeld algoritme. Met actuele windsnelheden en storingsgegevens is vastgesteld dat het ontwikkelde adaptieve regelalgoritme het risico op DFIG-SSR met een factor 16.95 verkleint. Nadere analyses tonen aan dat het ontwikkelde algoritme ook in staat is om DFIG-SSR met succes te elimineren wanneer een DFIG-windpark niet alleen als een geaggregeerde DFIG-turbine, maar ook met behulp van individuele DFIG-turbines wordt gesimuleerd. Hierbij wordt rekening gehouden met de niet-identieke werkpunten van individuele DFIGs. Om dit te bereiken, moet het adaptieve regelalgoritme in elke DFIG worden geïmplementeerd.

De belangrijkste conclusie van dit proefschrift is dat DFIG-SSR kan worden geëlimineerd door middel van een hardware-oplossing zoals het fase-onbalansconcept of op basis van systeemcoördinatie, zoals het ontworpen adaptieve regelalgoritme. Voor enkele van de 28 technische uitdagingen is het *grid forming* regelalgoritme in dit proefschrift als een van de mogelijke oplossingen geïdentificeerd. Het wordt dan ook aanbevolen om de invloed van *grid forming* op DFIG-SSR alsmede het vermogen van *grid forming* om DFIG-SSR te elimineren nader te onderzoeken.

TABLE OF CONTENTS

SUMMARY.....	vii
SAMENVATTING	ix
1. INTRODUCTION	1
1.1. System Operational Challenges	1
1.2. Problem Definition	5
1.3. Research Objective and Questions	6
1.4. Research Approach	8
1.5. Thesis Outline	9
1.6. Research Framework: H2020 Project MIGRATE.....	10
References.....	12
2. RECLASSIFICATION OF SUB SYNCHRONOUS OSCILLATIONS.....	15
2.1. Introduction.....	15
2.1.1. Sub Synchronous Resonance (SSR)	16
2.1.2. Device Dependent Sub Synchronous Oscillations (DDSSO).....	17
2.1.3. Emerging Sub Synchronous Oscillations	17
2.2. Fixed Series Compensation	18
2.2.1. Concept Description	18
2.2.2. Practical FSC Applications.....	21
2.3. DFIG-Series Capacitor Interaction	24
2.3.1. Description of Phenomenon	24
2.3.2. Practical Case: Texas, USA.....	26
2.4. Converter-Grid Interaction	27
2.4.1. Description of Phenomenon	27
2.4.2. Practical Case: Yorkshire, UK.....	30
2.5. Converter-Converter Interaction.....	31
2.5.1. Description of Phenomenon	31
2.5.2. Practical Case: Australia.....	32
2.6. Proposed Reclassification of SSO	33
2.7. Conclusions	35
References.....	36
3. REVIEW OF MITIGATION SOLUTIONS FOR EMERGING SSO PHENOMENA.....	41
3.1. Introduction.....	41
3.2. Control Solutions	43
3.2.1. Tuning of Converter Controller Parameters	43
3.2.2. Feedback Linearisation Control.....	45

3.2.3. Virtual Synchronous Machine	46
3.2.4. Digital Filters	46
3.2.5. Supplementary Damping Controller.....	47
3.3. Hardware Solutions	48
3.3.1. FACTS.....	49
3.3.2. Other VSC-based solutions.....	51
3.4. System Level Coordination	52
3.4.1. Adaptive Control	52
3.4.2. Protection.....	54
3.5. Conclusions	54
References.....	57
4. MODELS AND METHODOLOGIES	61
4.1. Introduction.....	61
4.2. Wind Turbine Generator Model	61
4.3. Screening: Impedance Based Stability Analysis	63
4.3.1. Methodology.....	64
4.3.2. Limitations and Assumptions	65
4.3.3. Modelling Requirements	65
4.3.4. Evaluation criteria.....	65
4.4. Impedance Calculation: Numerical Simulations	67
4.4.1. Impedance Calculation Time.....	69
4.4.2. Perturbation Signal	71
4.4.3. Simulation Model	72
4.4.4. Cross Coupling	73
4.5. Detailed Analysis.....	74
4.5.1. Eigenvalue Analysis	74
4.5.2. EMT Analysis.....	75
4.6. Grid Models	76
4.6.1. Single Machine Infinite Bus Model.....	76
4.6.2. IEEE 39-Bus system.....	77
4.7. Conclusions	77
References.....	79
5. PHASE IMBALANCE COMPENSATION CONCEPT.....	81
5.1. Introduction.....	81
5.2. Series Phase Imbalance Compensation	83
5.2.1. Concept Description	83
5.2.2. Series PIC Evaluation for DFIG-SSR Mitigation.....	87
5.3. Parallel Phase Imbalance Compensation	93
5.3.1. Concept Description	93
5.3.2. Parallel PIC Evaluation for DFIG-SSR Mitigation	95
5.4. System Strength Assessment	107
5.5. Average versus Detail DFIG EMT Model.....	108

5.6. Methodology for PIC evaluation	110
5.6.1. Description of Methodology	110
5.6.2. DFIG-SSR Mitigation in IEEE 39 Bus System.....	111
5.7. Mitigating Torsional SSR with PIC.....	113
5.8. Conclusions	114
References.....	116
6. SYSTEM LEVEL COORDINATION	117
6.1. Introduction.....	117
6.1.1. TenneT's Control Room of the Future Program.....	117
6.1.2. Examples of Adaptive Control	118
6.2. Proposed System Level Solution	120
6.2.1. Module 1: Gain Identification and Scheduling.....	120
6.2.2. Module 2: Prediction Algorithm.....	121
6.2.3. Module 3: Real-time Operation	123
6.3. Gain Identification	124
6.4. Development of Lookup Table	128
6.4.1. Optimisation	128
6.4.2. Lookup Table.....	129
6.4.3. Validation	131
6.5. Conclusions	133
References.....	135
7. FORECASTING MODULE DEVELOPMENT	137
7.1. Introduction.....	137
7.2. Forecasting in the Operational Planning Process	138
7.3. Artificial Neural Networks	139
7.4. Data.....	142
7.5. Tuning of ANN Structure and Algorithm.....	143
7.5.1. State of the art.....	144
7.5.2. Simulation Results	144
7.6. Tuning of FFBP Algorithm	147
7.6.1. Forecast Evaluation Metrics	147
7.6.2. Optimisers.....	148
7.6.3. Loss Functions	148
7.6.4. Simulation Results	149
7.7. Optimised Forecasting Algorithm	153
7.8. Conclusions	155
References.....	157
8. REAL-TIME OPERATIONS.....	161
8.1. Introduction.....	161
8.2. Real-time Operations Module.....	161
8.3. Performance of Predictive Gain Scheduling Control	163

8.4. Statistical Analysis of DFIG-SSR	163
8.5. Multi-DFIG System	166
8.5.1. Impact of Non Identical Controller Parameters.....	166
8.5.2. Impact of Wake Effect.....	169
8.5.3. IEEE 39-Bus System	176
8.6. Conclusions	177
References.....	179
9. CONCLUSIONS	181
9.1. Research Synthesis	181
9.1.1. Reclassification of SSO	182
9.1.2. Mitigation of DFIG-SSR	183
9.1.3. Hardware Solution: Phase Imbalance Compensation.....	183
9.1.4. System Level Coordination: Predictive Gain Scheduling Control.....	184
9.2. Scientific Contributions	186
9.3. Recommendations for Future Work	187
9.3.1. Impedance Based Stability Analysis	187
9.3.2. Grid Forming Control.....	187
9.3.3. Forecasting.....	187
APPENDIX A. DFIG EMT PARAMETERS	189
APPENDIX B. BEST PERFORMING ANN	193
APPENDIX C. OPTIMISERS AND LOSS FUNCTIONS.....	195
GLOSSARY.....	199
LIST OF FIGURES.....	205
LIST OF PUBLICATIONS.....	209
ACKNOWLEDGEMENT.....	213
CURRICULUM VITAE.....	215

1. INTRODUCTION

1.1. SYSTEM OPERATIONAL CHALLENGES

The worldwide energy landscape is undergoing a transition towards a more sustainable energy provision, characterised among others by a proliferation of power electronics interfaced devices (PEID) such as high voltage direct current (HVDC) transmission lines and wind and solar generation. From system operation perspective, the main contributing factors identified with regards to this ongoing energy transition are threefold.

Firstly, the transmission system connected conventional synchronous generator is rapidly being replaced by transmission and distribution connected variable renewable energy sources (RES) such as wind and solar generation. These are predominantly connected to the grid through power electronics (PE) converters. Depending on the defined scenarios, the International Energy Agency expects the global installed capacity of solar photovoltaic (PV) to increase from around 750 GW in 2020 to anywhere between 2,000 and 4,000 GW in 2030 [1]. On the other hand, the ambition in Europe for 2050 is to have around 450 GW of offshore wind, which will mostly be connected to the onshore transmission system through HVDC converters [2]. Figure 1.1 [3] illustrates the evolution of the annual electrical energy production from coal, wind and solar PV for Ireland, United Kingdom (UK), Denmark and Australia. Due to restricted access to the database, other generation sources could not be included in the graphs. In this figure, 100% indicates the sum of the electrical energy generation from coal, wind and solar PV. It illustrates the *relative* development of the annual electrical energy generation from these sources across different jurisdictions. It is observed that the combined annual electrical energy production from wind and solar PV already surpassed that of coal in Ireland, UK and Denmark.

Parts of this Chapter are published in V. N. Sewdien, R. Chatterjee, M. Val Escudero, and J. van Putten, "System Operational Challenges from the Energy Transition," *CIGRE Sci. Eng.*, vol. 17, pp. 5–20, 2020.

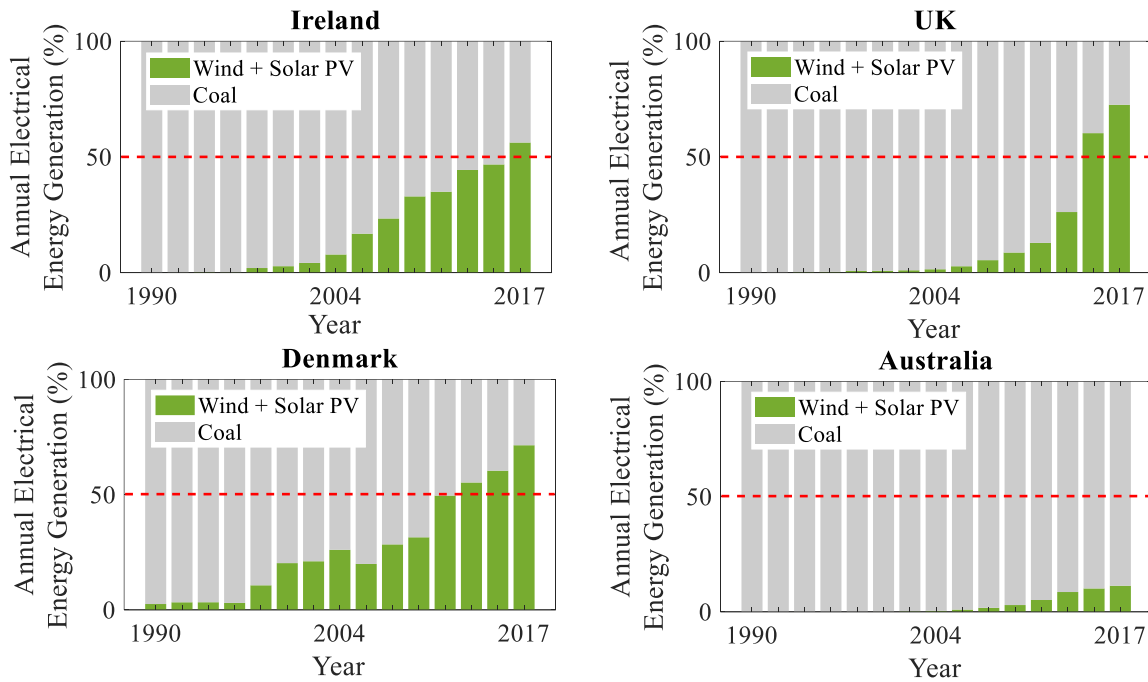


Figure 1.1 Annual electrical energy production from coal, wind and solar PV. Values are normalized using the sum of these three sources. Other fossil fuel and renewable energy sources are not considered in the figure (data retrieved from [3]).

Due to their intermittent nature and priority dispatch, these RES introduce a variability (additional to the load variability and stochastic outages) in the generation mix, resulting in a wide variety of operating conditions. These conditions range from almost no conventional synchronous generation due to high RES production, to conditions with low or no RES generation. High instantaneous levels of wind and solar generation relative to the demand are already being observed in Denmark (157%), South Australia (142%), Tasmania (70%) and UK (67%) [4], showing that the day-to-day observed share of RES can be significantly larger than their share in the annual electrical energy generation. Additionally, electricity markets with large penetration of RES tend to have more volatile day ahead electricity prices and fewer periods in which conventional power plants can compete (and, consequently, fewer running hours). This decreases the competitiveness of such conventional power plants in wholesale electricity markets. In the absence of other markets such as balancing and capacity markets, the decreased competitiveness can lead to decommissioning of the conventional power plants. The volatility in prices is also reflected as a result of system strength constraints (e.g. 15,000 AUD/MWh in Australia) or a major surplus of priority dispatch RES generation. The latter can lead to negative electricity prices, which is increasingly being observed by several system operators throughout the world. For example, Germany observed negative day ahead prices up to $-/-$ 54.97 EUR/MWh for seven consecutive hours on 4 October 2020, while negative day ahead prices ($< -/-$ 11 EUR/MWh) were observed for more than three consecutive hours in whole Central Western Europe on 2 November 2020 [5].

Secondly, the regulatory framework influences the design, planning and operation of the power system. Network codes and other regulatory requirements need to continuously provide an adequate and up-to-date framework to facilitate the ongoing energy transition. A harmonised regulatory framework is imperative not only on transmission, but also on distribution level. The

development of such regulatory frameworks evolves at a slower pace than the evolution of the generation. An example in Europe is the requirements and degrees of freedom from the System Operation Guideline [6] and Requirement for Generators [7] network codes.

Lastly, taking into account the stakeholder involvement which takes time in the process, the commissioning of new transmission assets lags behind the expansion of generation assets. Increasing public opposition for new overhead lines and challenges associated with long underground cables add delays in realising new transmission assets. Such cables introduce new technical challenges for the design and operation of the circuits, such as harmonic resonances, temporary overvoltages and amplification of harmonic distortion, which cannot be solely solved by expansion of transmission capacity. These challenges require expensive and complex mitigation solutions that affect the reliability of the circuit [8]. The very long times required to build additional transmission capacity increase the instances at which the power system is operated closer to its security limits and with congestion management schemes. In [9] it is shown that the congestion management costs in Germany are proportional to the wind penetration levels. This proportionality is also valid for the curtailment rate of wind generation in Britain and Germany[†], as is illustrated in Figure 1.2 [9].

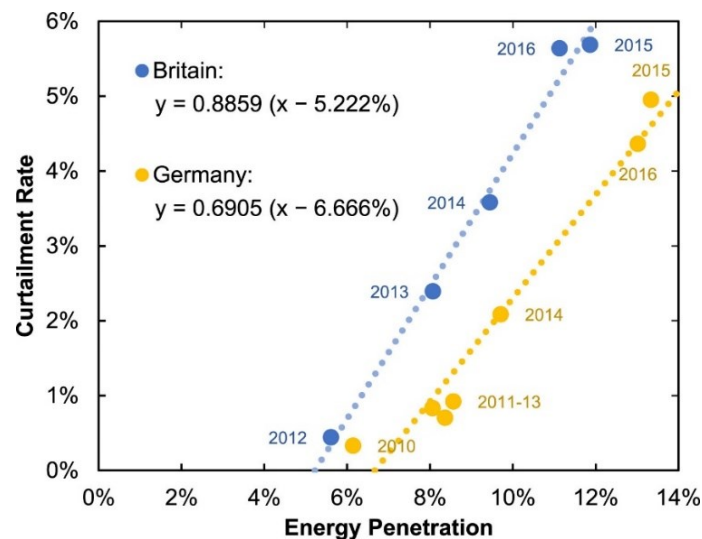


Figure 1.2 Curtailment rates against wind generation penetration levels in Britain and Germany [9].

Taking these observations into account, the energy transition poses important operational challenges for system operators, where the holistic question to be answered is:

Given today's level of operational reliability and affordability of the electricity supply, how should the future, power electronics dominated power system be operated?

One of the fundamental issues that first need to be addressed, is gaining insights in the operational challenges associated with the future power system. Based on extensive literature review, complemented by surveys and discussions with system operators, an overview of actual

[†] The reason for the reduced curtailment rate in 2016 for Germany is the implementation of a new concept of cost-optimised dispatch of power plants by the German TSOs.

and expected operational challenges was created and is shown in Figure 1.3 [10]. In total, 28 unique operational challenges were identified and validated by the industry. A detailed description of each phenomenon is provided in [10]–[13]. These challenges are grouped into the following three main categories.

Category 1: Reduced Voltage and Frequency Support

Small-signal as well as large disturbance stability will remain crucial, i.e. frequency, synchronising torque and voltage support requirements of the system will need to be maintained. The time constants associated with the phenomena in this category range from seconds (e.g. large disturbance frequency stability) up to hours (e.g. ramps management). This category deals with issues that result from insufficient availability or inability to meet the ancillary services demand, in terms of both type and volume. Practical examples of challenges in this category include the increasing rate of change of frequency (RoCoF) in Ireland [14], excessive frequency deviations in Continental Europe [15], static reactive power balance in Britain [16] and management of ramps in California [17].

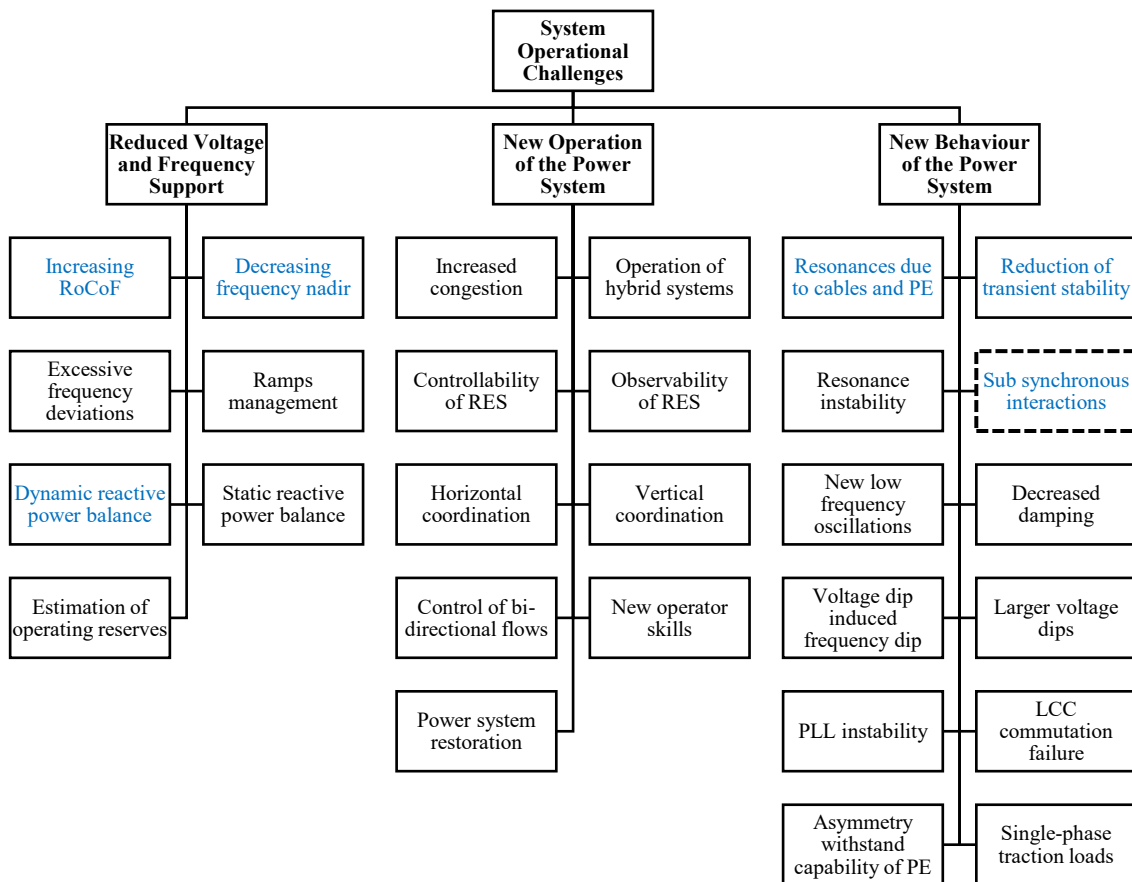


Figure 1.3 Overview of system operational challenges due to the energy transition [10]. The challenges in blue were addressed in the MIGRATE project. The dashed box is the focus of this thesis.

Category 2: New Operation of the Power System

The second category of issues identifies those areas where how we operate the power system needs to change. This includes the people, processes and tools in system operation that observe the bulk electric system and take necessary actions to maintain operational reliability.

A practical example is the increased congestion in Britain and Germany as reported in [9]. Other phenomena are expected to be too fast for a manual operational response. Therefore, the new operation of the power system will require increased automatic control actions in order to cope with the expected faster and more frequent dynamic behaviour of the power system.

Category 3: New Behaviour of the Power System

With increasing penetration of PEID, the power system's behaviour and response are bound to change. This category of identified issues focuses on the power system's new behaviour, which results from e.g. reduced damping, altered impedance response of the grid and reduced system strength. Practical examples include resonance instability in the TenneT transmission system [18], sub synchronous oscillations (SSO) in the Electricity Reliability Council of Texas (ERCOT) [19] and voltage dip induced frequency dip in the Irish power system [12].

It should be mentioned that although the identified issues are observed in operational time frames, their mitigation spans across a much wider time frame and ranges from long term planning to intraday operations. A summary of the capabilities of existing PEID in mitigating some of the identified challenges is given in [20].

1.2. PROBLEM DEFINITION

In the Horizon 2020 project MIGRATE (Massive InteGRATion of power Electronic devices, see Section 1.6), European transmission system operators (TSO) ranked the identified power system stability related operational challenges of Figure 1.3 based on their severity, probability and expected time to materialise in practice [21]. The challenges in blue topped this ranking and were further investigated in the project. From the top ranked challenges the increasing RoCoF, decreasing frequency nadir, dynamic reactive power balance and the reduction in transient stability margin challenges including their developed mitigation solutions are described in [22]. This thesis addresses the last challenge of the top ranking and relates to sub synchronous resonance (SSR), more specifically the adverse interaction between a doubly-fed induction generator (DFIG) and a series capacitor compensated transmission line. This interaction phenomenon is electromagnetic in nature and is defined in this thesis as DFIG-SSR. Besides DFIG-SSR, there are two other emerging electromagnetic sub synchronous interaction phenomena, which occur as interactions either between a PEID and a grid or among PEIDs.

As was mentioned earlier, the energy transition goes hand in hand with the proliferation of RES, often interfaced with PE. From these RES, wind generation has been showing the largest increase over time [3] and many new near- and offshore wind power plants are planned. The geographical location of these wind power plants require long distance transmission of the generated electrical energy. Combined with the increasing public opposition for new overhead lines on the one hand and technical challenges for utilising long distance underground cables on the other hand, system operators and transmission owners have to make the best use of existing transmission infrastructure. As such, series compensation is an effective way to increase the available transfer capability of existing transmission lines.

One of the major challenges of using series compensation in combination with DFIG wind power plants is the potential for DFIG-SSR. In a system with a series capacitor, a grid disturbance produces sub synchronous currents and voltages. At the sub synchronous frequency, the slip and consequently the damping of the DFIG become negative. When the net damping, which is the sum of the DFIG damping and the damping provided by the transmission system, is negative, the power system will experience rapidly growing oscillations. The first DFIG-SSR in a real power system was observed on 22 October 2009 in the power system of ERCOT [23], which resulted in rapidly growing current oscillations up to 3 per unit. The wind power plant suffered major damage resulting from this phenomenon. Between August and October 2017, three new DFIG-SSR events occurred in Texas [24], whereas between December 2012 and December 2013 58 events occurred in the Guyuan power system (China), sometimes tripping more than 1,000 wind turbine generators (WTG) at a time. Considering the uptake in wind generation, combined with the difficulties in building new transmission corridors, existing transmission lines may be upgraded more frequently using series compensation. Consequently, the likelihood of DFIG-SSR will increase. Failing to adequately address such undamped oscillations can lead to physical damage of power system equipment and potentially jeopardise system security, whereas sustained oscillations could lead to degradation of power quality and protection tripping.

1.3. RESEARCH OBJECTIVE AND QUESTIONS

The main objective of this research relates to addressing the challenge of DFIG-SSR and is formulated as:

Investigation and simulation validation of the degree of effectiveness of existing methods and the design and simulation validation of new principles to mitigate DFIG-SSR.

Solutions for mitigating DFIG-SSR can generally be categorised in (i) hardware solutions, (ii) principles based on system level coordination and (iii) control solutions [25]. Hardware concepts for addressing DFIG-SSR include flexible AC transmission system (FACTS) controllers and non-FACTS devices. Solutions that fall in this category mitigate DFIG-SSR by the commissioning of additional hardware (e.g. a thyristor controlled series capacitor, TCSC) in the power system or by modifying the control loops of new or existing hardware (e.g. adding a damping controller in a static compensator, STATCOM). The phase imbalance compensation concept is another way to achieve fixed series compensation and was initially designed to mitigate classical SSR problems [26], [27]. However, its applicability in mitigating DFIG-SSR as a potential hardware solution is rarely investigated and is thoroughly assessed in this thesis.

System level coordination can help to mitigate SSO in a rather unconventional way. In this concept, control actions are adjusted based on system parameters. Examples of such solutions are gain scheduling and protection. However, from the system operation perspective, protection solutions are the most intrusive, as they abruptly disconnect generation and transform a small-signal stability problem to a more severe large disturbance. In this thesis, a gain scheduling solution based on system level coordination is designed.

Finally, control solutions encompass those control/software solutions that are implemented within the control structure of the DFIG. It includes tuning of controller parameters, deploying new control concepts such as the feedback linearising control, and modifying existing control structures e.g. by adding digital filters and damping controllers.

To achieve the research objective, four research questions are defined and are introduced next. The first research question relates to the positioning of DFIG-SSR and other emerging electromagnetic SSO phenomena within the wider scope of SSO. The current SSO definition explicitly only considers electromechanical oscillations, thereby excluding DFIG-SSR. There is also a lack of consensus in academia and industry regarding the terminology of the emerging phenomena (i.e. controller interactions, controller instability and sub synchronous resonance), leading to addressing fundamentally different phenomena with the same terminology. These reasons underline the need for, on the one hand, a new definition of SSO, and on the other hand, a reclassification of SSO to include the new phenomena. The first research question addresses this scientific gap and is defined as:

RQ 1. How can emerging SSO phenomena be positioned in the existing classification of sub synchronous oscillations?

After the introduction of the new SSO classification, existing measures to mitigate the emerging SSO phenomena, with a focus on DFIG-SSR, should be reviewed. The second research question aims at evaluating these solutions (categorised in hardware solutions, solutions based on system level coordination and control solutions) and is formulated as:

RQ 2. What are the limitations and recognised application boundaries of existing approaches for mitigating DFIG-SSR?

The final two research questions aim to address outstanding gaps in scientific literature and to design a new DFIG-SSR mitigation measure. The phase imbalance compensation concept was originally designed in the 1990s to mitigate classical SSR. Research that methodically investigates the influence of this concept on the impedance behaviour of the grid as well its capability to address DFIG-SSR is lacking. The goal of the third research question is to systematically and thoroughly investigate to which extent phase imbalance compensation is able to mitigate DFIG-SSR. It is defined as:

RQ 3. To what extent is the phase imbalance compensation concept as a potential hardware solution able to mitigate DFIG-SSR?

Automated system level coordination is a novel concept for addressing adverse interactions. The main drawbacks of existing system level coordination based solutions include (i) the necessity to have in advance knowledge of the wind speed and grid damping for correct operation of adaptive controllers, (ii) the need for a wide area measurement system and (iii) lacking validation that the adaptive characteristic of adaptive controllers does not result in small-signal instability. The final research question aims at developing a system level coordination based measure that addresses these drawbacks and is formulated as:

RQ 4. How can gain scheduling control based on system level coordination be used to mitigate DFIG-SSR?

The first and second research question address the need for a reclassification of SSO phenomena and identify the limitations in existing mitigation solutions. The third research question investigates the degree of effectiveness of the phase imbalance compensation concept in mitigating DFIG-SSR. A methodology to assess and design the phase imbalance concept is proposed. This research question contributes to the first part of the overall research objective. For the final research question, a new mitigation solution is developed and validated using offline simulations. This question contributes to the second part of the overall research objective.

1.4. RESEARCH APPROACH

For the performance analysis, detail and average electromagnetic transient (EMT) simulation models of the DFIG wind turbine based on IEC Standard 61400-27-1 [28] are developed using Power System Computer Aided Design (PSCAD) version 4.6 in the framework of the MIGRATE project. The dynamic response of the models is further enhanced (e.g. based on [29] additional feedback loops are introduced in the pitch controller) and both models are used to provide a comparison of their performance and accuracy with regards to the DFIG-SSR phenomenon. The performance of the models was validated by a reference group consisting of wind turbine vendors.

In line with common practice for DFIG-SSR interaction studies, the network topology of the IEEE First Benchmark Model is adopted. To account for different grid operating conditions, the short circuit levels and electrical damping are varied to represent different underdamped scenarios. The larger IEEE 39-Bus Model is used for validation of the obtained results. These models are used in the subsequent analysis.

For the investigation of the phase imbalance compensation concept, first an analytical (mathematical) model that describes the relation between the degree of asymmetry and the resulting shift in resonance frequency is developed. This model is developed with the aim to understand the underlying reasons for why the phase imbalance compensation impacts DFIG-SSR in the way it does. Time domain EMT simulations are performed to validate the developed analytical model under different degrees of asymmetry.

The impedance based stability method [30] is used in this work to evaluate and quantify the impact of potential mitigation solutions on the occurrence of adverse interactions. This method is among the most widely recognised and accepted methods to screen for SSO [31]. The impedance based stability method and monothetic sensitivity analysis are used to identify the influence of the DFIG's rectifier and inverter control parameters on the phase margin. Parameters that show a sensitivity are selected for the gain scheduling based solution. As such, both time domain and frequency domain analysis are adopted in this thesis.

Finally, a short-term wind speed forecast model based on artificial neural networks is developed for forecast horizons of 5, 15, 30 and 60 minutes. As part of the development, the

influence of various variables on the forecast accuracy is assessed. Wind speed data is obtained from the National Renewable Energy Laboratory (NREL) open source Wind Prospector tool [32]. The wind speed forecast model is built in Python within the Keras framework of Google's TensorFlow platform. The gain scheduling based solution is also developed in Python.

1.5. THESIS OUTLINE

The outline of this thesis is graphically depicted in Figure 1.4. *Chapter 2* first gives a fundamental description of three emerging electromagnetic SSO phenomena. Then, the existing definition and classification of the SSO phenomena are reviewed. Based on the findings a new definition of SSO and a reclassification of SSO phenomena are proposed.

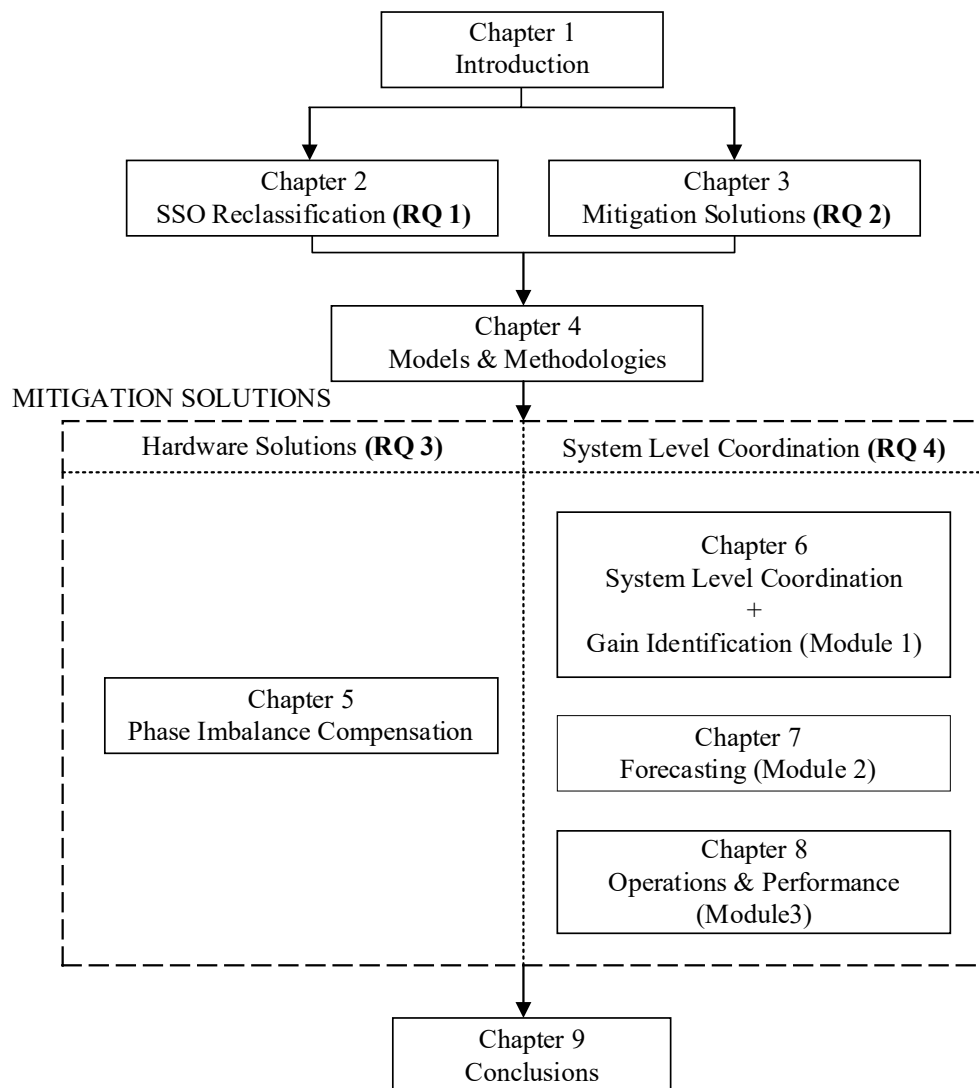


Figure 1.4 Thesis Outline.

Chapter 3 reviews the existing solutions for mitigating the previously introduced SSO phenomena. The mitigation solutions are categorised in hardware solutions, solutions based on system level coordination and control solutions.

Chapter 4 discusses the models and methodologies used for the subsequent analysis. First, the detail and average EMT models of the DFIG wind turbine generator that were developed in the context of the MIGRATE project are highlighted. Then, the impedance based stability method as a screening tool for potential SSO risks is reviewed. Finally, the perturbation method is introduced as a tool to determine the impedance of the DFIG. Guidelines to determine the impedance using the perturbation method are developed.

Chapter 5 moves on to evaluate the capability of the phase imbalance compensation concept as a potential hardware solution for mitigating DFIG-SSR. An analytical model of the phase imbalance compensation scheme is developed for this purpose. Comparisons between the performance of the classical compensation concept and the series and parallel schemes of the phase imbalance compensation concept are provided. A methodology to design the phase imbalance compensation concept is developed and applied on the IEEE 39-bus system.

The following three chapters discuss the development of a gain scheduling based mitigation solution (system level coordination). *Chapter 6* first reviews system level coordination based measures such as wide area control. It continues by giving a high level description of the proposed concept, which consists of the gain identification and scheduling module, the forecasting module and the real-time operation module. Monothetic sensitivity analysis is used to identify those controller parameters of the DFIG's converters that influence the electrical damping. Next, for wind speed dependent operating conditions parameter values are identified that can mitigate DFIG-SSR. The forecasting algorithm is developed in *Chapter 7* and is a short-term wind speed forecasting based on artificial neural networks. Critical parameters of the algorithm are identified and optimised to yield the most accurate forecast results. Finally, *Chapter 8* discusses the performance of the gain scheduling solution and quantifies the benefit of the developed solution. The suitability of the solution is also demonstrated using a wind power plant with a multi-DFIG representation, where the individual DFIGs have non-identical operating conditions.

Finally, *Chapter 9* discusses the scientific relevance of the work, provides the final conclusions and makes recommendations on the further improvement and extension of this research.

1.6. RESEARCH FRAMEWORK: H2020 PROJECT MIGRATE

The research in this thesis was performed under the framework of the Horizon 2020 MIGRATE project. MIGRATE was a four year research project that started in 2016 and aimed at finding solutions for the technological challenges that the transmission system will be facing in the future as a result of the ongoing proliferation of PEID. MIGRATE had five overall objectives. The first objective focused on the identification of power system stability issues and capabilities of existing PEIDs to mitigate these. The second objective dealt with the development of new forecasting and real-time monitoring solutions using phasor measurement units. Objective three covered the assessment of existing protection devices to operate correctly under high PEID penetration scenarios and development of new protection algorithms. The development of appropriate models and methodologies to evaluate the influence of PEIDs on power quality in future power systems was captured by the fourth objective. Finally, objective

five focused on the development of concepts to operate a transmission system with no synchronous generation.

This thesis contributed mainly to the project's first objective. The first contribution of this thesis is the identification and ranking of power system stability issues resulting from the proliferation of PEIDs (documented in [13], [21]). The list with issues was later expanded to also include non-stability related challenges [10]. Top ranked stability issues were further investigated by the consortium partners.

Next, the capability of existing PEIDs in mitigating sub synchronous interactions was analysed in [25]. Mitigation solutions were categorised in hardware solutions, solutions based on system level coordination and control solutions. The phase imbalance compensation concept is a potential hardware solution and its evaluation for mitigating DFIG-SSR is published in [33], [34]. The capabilities of existing PEIDs to mitigate other challenges are investigated in [20], whereas TSOs' experience with FACTS controllers to enhance stability and mitigate sub synchronous oscillations is described in [35]. The final contribution of this thesis to the MIGRATE project is the development of a gain scheduling based solution for mitigating DFIG-SSR and is partly documented in [36], [37].

All the activities ultimately contributed to five technical deliverables. In the first deliverable [21] a description of the expected systemic stability issues is provided. The second deliverable [38] evaluated existing power system analysis concepts' capability in accurately capturing the identified stability issues. The next deliverable [39] developed tools for forecasting and monitoring the penetration of PEID. New solutions to address the identified stability issues are reported in [22]. Finally, the last deliverable provided clarification on unclear grid code requirements and demonstrated some of the developed mitigation solutions using control hardware in the the loop simulations [40].

REFERENCES

- [1] IEA, “Global solar PV and coal-fired installed capacity by scenario, 2010-2030,” 2020. [Online]. Available: <https://www.iea.org/data-and-statistics/charts/global-solar-pv-and-coal-fired-installed-capacity-by-scenario-2010-2030>.
- [2] G. Kaendler, “ENTSO-E’s View on System Integration,” in *Vision for the future of the power system*, 2020.
- [3] International Energy Agency, “IEA Data & Statistics,” 2019. [Online]. Available: <https://www.iea.org/data-and-statistics/data-tables>. [Accessed: 10-Dec-2019].
- [4] AEMO, “Maintaining Power System Security with High Penetrations of Wind and Solar Generation,” 2019.
- [5] Nord Pool, “Nord Pool Market Data.” [Online]. Available: <https://www.nordpoolgroup.com/Market-data1/#/nordic/map>. [Accessed: 03-Nov-2020].
- [6] European Commission, “Commission Regulation (EU) 2017/1485 of 2 August 2017. Establishing a guideline on electricity transmission system operation,” *Off. J. Eur. Union*, no. L 220, pp. 1–120, 2017.
- [7] European Commission, “COMMISSION REGULATION (EU) 2016/1447 of 26 August 2016. Establishing a network code on requirements for grid connection of high voltage direct current systems and direct current-connected power park modules,” *Off. J. Eur. Union*, vol. 59, no. L 241, pp. 1–65, 2016.
- [8] M. Val Escudero, A. Martin, L. Fisher, and I. Dudurych, “Technical challenges associated with the integration of long HVAC cables and interver based renewable generation in weak transmission networks: the Irish experience,” in *Proceedings of the 2018 CIGRE Session*, 2018.
- [9] M. Joos and I. Staffell, “Short-term integration costs of variable renewable energy: Wind curtailment and balancing in Britain and Germany,” *Renewable and Sustainable Energy Reviews*, vol. 86. Elsevier Ltd, pp. 45–65, 01-Apr-2018.
- [10] V. N. Sewdien, R. Chatterjee, M. Val Escudero, and J. van Putten, “System Operational Challenges from the Energy Transition,” *CIGRE Sci. Eng.*, vol. 17, pp. 5–20, 2020.
- [11] CIGRE JWG C2/B4.38, “Capabilities and requirements definition for power electronics based technology for secure and efficient system operation and control,” Paris, 2020.
- [12] V. N. Sewdien *et al.*, “Effects of Increasing Power Electronics based Technology on Power System Stability: Performance and Operations,” *CIGRE Sci. Eng. J.*, vol. 11, pp. 5–17, 2018.
- [13] V. N. Sewdien *et al.*, “Effects of Increasing Power Electronics on System Stability: Results from MIGRATE Questionnaire,” in *2018 IEEE PES International Conference on Green Energy for Sustainable Development*, 2018, pp. 1–9.
- [14] EirGrid, “DS3 Programme.” [Online]. Available: <http://www.eirgridgroup.com/how-the-grid-works/ds3-programme/>. [Accessed: 16-Dec-2019].
- [15] ENTSO-E, “Report on Deterministic Frequency Deviations,” Brussels, 2020.
- [16] National Grid, “System Operability Framework,” Warwick, 2016.

-
- [17] Californian ISO, "What the duck curve tells us about managing a green grid," California, 2016.
- [18] C. Buchhagen, C. Rauscher, A. Menze, and J. Jung, "BorWin1 - First experiences with harmonic interactions in converter dominated grids," in *International ETG Congress 2015; Die Energiewende - Blueprints for the New Energy Age*, 2015, pp. 27–33.
- [19] J. Adams, C. Carter, and S. H. Huang, "ERCOT experience with Sub-synchronous Control Interaction and proposed remediation," in *Proceedings of the IEEE Power Engineering Society Transmission and Distribution Conference*, 2012, pp. 1–5.
- [20] P. Maibach, A. Hernandez, J. Peiro, C. Smith, V. Sewdien, and J. van Putten, "Capabilities of Power Electronic Devices in Enabling the Energy Transition and Mitigating System Operational Challenges (accepted for publication)," *CIGRE Sci. Eng. J.*, vol. 19, 2020.
- [21] T. Breithaupt *et al.*, "MIGRATE Deliverable D1.1 Report on Systemic Issues," 2016.
- [22] A. Kosenko *et al.*, "MIGRATE Deliverable D1.5 Power System Risk Analysis and Mitigation Measures," 2019.
- [23] J. Adams, V. A. Pappu, and A. Dixit, "Ercot experience screening for Sub-Synchronous Control Interaction in the vicinity of series capacitor banks," *IEEE Power Energy Soc. Gen. Meet.*, pp. 1–5, 2012.
- [24] Y. Li, L. Fan, and Z. Miao, "Replicating Real-World Wind Farm SSR Events," *IEEE Trans. Power Deliv. (early access)*, 2019.
- [25] V. N. Sewdien, X. Wang, J. L. Rueda Torres, and M. A. M. M. van der Meijden, "Critical Review of Mitigation Solutions for SSO in Modern Transmission Grids," *Energies*, vol. 13, no. 13, p. 3449, 2020.
- [26] A. A. Edris, "Subsynchronous resonance countermeasure using phase imbalance," *IEEE Trans. Power Syst.*, vol. 8, no. 4, pp. 1438–1447, 1993.
- [27] A.-A. Edris, "Series compensation schemes reducing the potential of subsynchronous resonance," *IEEE Trans. Power Syst.*, vol. 5, no. 1, pp. 219–226, 1990.
- [28] IEC, "International Standard 61400-27-1: Wind Turbines - Part 27-1: Electrical Simulation Models - Wind Turbines," Geneva, 2015.
- [29] D.H.R. Suriyaarachchi, "Sub-synchronous Interactions in a Wind Integrated Power System," University of Manitoba, 2014.
- [30] J. Sun, "Impedance-based stability criterion for grid-connected inverters," *IEEE Trans. Power Electron.*, vol. 26, no. 11, pp. 3075–3078, 2011.
- [31] W. Du, B. Ren, H. Wang, and Y. Wang, "Comparison of Methods to Examine Sub-synchronous Oscillations Caused by Grid-connected Wind Turbine Generators," *IEEE Trans. Power Syst.*, vol. 8950, no. c, pp. 1–1, 2019.
- [32] C. Draxl and A. Clifton, "A Guide to Using the WIND Toolkit Validation Code," 2014.
- [33] V. N. Sewdien and J. L. Rueda Torres, "Evaluation of Phase Imbalance Compensation for Mitigating DFIG-Series Capacitor Interaction," in *29th IEEE International Symposium on Industrial Electronics*, 2020.
- [34] V. N. Sewdien, J. L. Rueda Torres, and M. A. M. M. van der Meijden, "Evaluation of Phase

- Imbalance Compensation for Mitigating DFIG-Series Capacitor Interaction,” *Energies*, vol. 13, no. 17, p. 4512, 2020.
- [35] V. N. Sewdien, “Operation of FACTS Controllers,” in *Flexible AC Transmission Systems*, S. Nilsson and B. Andersen, Eds. Cham: Springer Nature, 2020, pp. 1063–1070.
- [36] V. N. Sewdien, R. Preece, J. L. Rueda Torres, E. Rakhshani, and M. A. M. M. van der Meijden, “Assessment of Critical Parameters for Artificial Neural Networks based Short-Term Wind Generation Forecasting,” *Renew. Energy*, vol. 161, pp. 878–892, 2020.
- [37] V. N. Sewdien, R. Preece, J. L. Rueda Torres, and M. A. M. M. van der Meijden, “Parametric Evaluation of Different ANN Architectures: Forecasting Wind Power Across Different Time Horizons,” in *2018 IEEE PES Transmission & Distribution Conference and Exhibition - Latin America (T&D-LA)*, 2018, pp. 1–5.
- [38] T. Breithaupt *et al.*, “MIGRATE Deliverable D1.2 Power System Analysis and KPIs,” 2018.
- [39] S. Asvapoositkul *et al.*, “MIGRATE Deliverable D1.4 Tools for Monitoring and Forecasting PE Penetration,” 2018.
- [40] T. Breithaupt *et al.*, “MIGRATE Deliverable D1.6 Demonstration of Mitigation Measures and Clarification of Unclear Grid Code Requirements,” 2019.

2. RECLASSIFICATION OF SUB SYNCHRONOUS OSCILLATIONS

2.1. INTRODUCTION

In recent years, the power industry has been experiencing new types of electromagnetic sub synchronous oscillations (SSO), which cannot be categorised under the existing SSO framework. These three new oscillation phenomena are fundamentally different from each other and occur under different circumstances. The first occurs in the presence of a DFIG based wind power plant and a series capacitor. The second phenomenon occurs following the operation of an inverter in weak grid conditions, whereas the last one occurs between electrically close PEIDs.

The current SSO definition explicitly only considers electromechanical oscillations, thereby excluding the above phenomena. Furthermore, there is a lack of consensus in academia and industry with regards to the terminology for the emerging phenomena, leading to addressing fundamentally different phenomena with the same terminology. These reasons underline the need for, on the one hand, a new definition of SSO, and on the other hand, a reclassification of SSO to include the new phenomena. This Chapter addresses this research gap and first gives a fundamental description of the emerging SSO phenomena. Each description is accompanied by a practical example. Then, taking into account the classical and emerging SSO phenomena, a new definition and classification for SSO are proposed.

Industry and academic interest in SSO was triggered by the Mohave SSR events in 1970 and 1971. According to [1], SSO is defined as an “*electromechanical interaction, either between a turbine-generator and passive system elements such as series capacitors, or between a turbine-generator and active system elements such as HVDC transmission equipment controls, and static VAR system controls*”. In [2], SSO is divided into two main categories: sub synchronous resonance (SSR) and device dependent sub synchronous oscillation (DDSSO).

Parts of this Chapter are published in V. N. Sewdien, X. Wang, J. L. Rueda Torres, and M. A. M. M. van der Meijden, “Critical Review of Mitigation Solutions for SSO in Modern Transmission Grids,” *Energies*, vol. 13, no. 13, p. 3449, 2020

SSO phenomena are currently categorised as shown in Figure 2.1. In this classification solid boxes represent electromechanical phenomena and the dashed box represents an electromagnetic phenomenon.

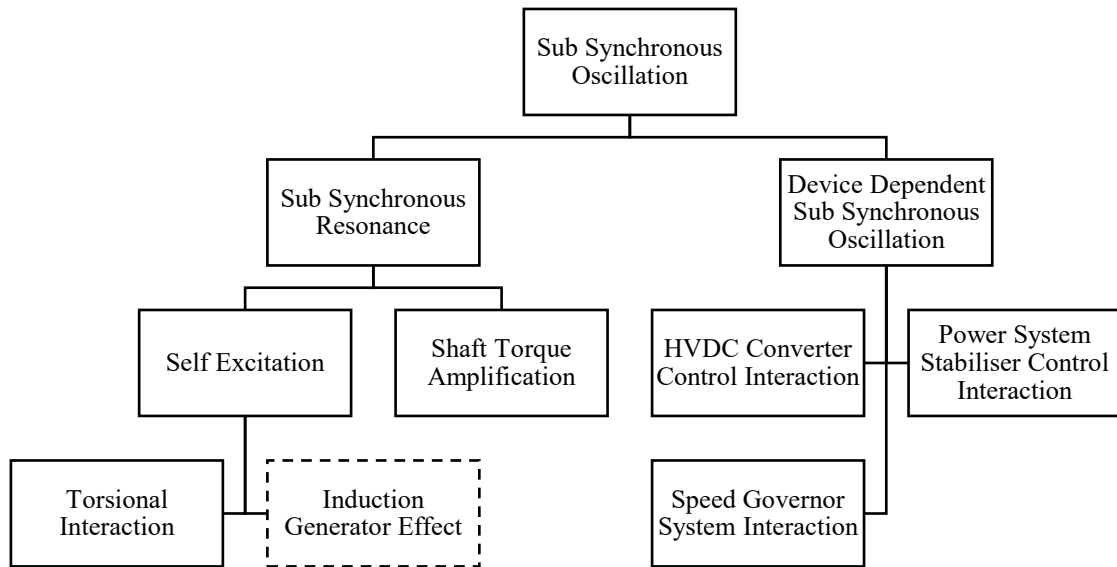


Figure 2.1 Existing classification of sub synchronous oscillations based on [1], [2]. Solid boxes represent SSO phenomena that are electromechanical in nature. The dashed box represents an electromagnetic phenomenon.

2.1.1. SUB SYNCHRONOUS RESONANCE (SSR)

SSR is defined in [3] as “an electric power system condition where the electric network exchanges energy with a turbine-generator at one or more of the natural frequencies of the combined system below the synchronous frequency of the system.”

For SSR to occur, a series capacitor is required. It can occur in the form of torsional interaction, induction generator effect and torque amplification. In all of these cases the SSR is the result of the interaction between the series capacitor and a turbine-generator. Assume the simple series compensated system given in Figure 2.2.

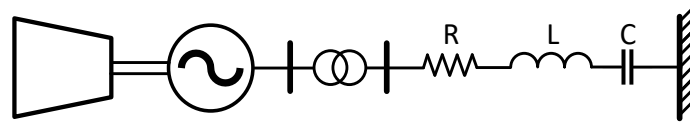


Figure 2.2 Turbine-Generator and series compensation single line diagram.

With fundamental frequency f_0 and reactance X_G , X_T , X_L and X_C of respectively the equivalent grid, transformer, transmission line and series capacitor, the electrical natural frequency f_r is defined as (2.1).

$$f_r = f_0 \sqrt{\frac{X_C}{X_G + X_T + X_L}} \quad (2.1)$$

Small-signal disturbances in the grid will cause sub synchronous currents with frequency f_r to flow and create a rotating magnetic field in the armature. As seen from the armature, the rotor resistance for this sub synchronous current is negative. When the negative resistance is larger than the positive damping provided by the grid at f_r , the electrical system is self-excited and leads to sustained sub synchronous currents. This phenomenon is known as the induction generator effect (IGE).

The turbine-generator system has a mechanical natural frequency f_m . Practical machines have multiple natural frequencies. When f_m is close to $f_0 - f_r$, an interaction is established between the turbine-generator system and the electrical system. Generator rotor oscillations with frequency f_m will result in a voltage component with sub synchronous frequency $f_0 - f_m$. When the sub synchronous frequency of the voltage component is close to f_r , a positive feedback loop is established and the generator rotor oscillations are sustained. This is known as torsional interaction.

2.1.2. DEVICE DEPENDENT SUB SYNCHRONOUS OSCILLATIONS (DDSSO)

In contrast to SSR, the series capacitor plays no role in the DDSSO phenomenon. DDSSO is defined as the interaction between turbine-generator torsional systems and active power system components such as HVDC converter controls, power system stabilisers and high speed governor controls [1], [2]. For DDSSO to occur, the torsional mass of a turbine-generator system is always required.

The most common case of DDSSO is the torsional interaction between synchronous machines and HVDC converters, and is defined as sub synchronous torsional interactions (SSTI). HVDC converters generate currents in a wide band of frequencies. When a synchronous machine is electrically close to an HVDC system, the electrical damping of the electrical system as seen from the generator can become negative. The power and current control of an HVDC rectifier station play a major role in this regard. When the mechanical natural frequencies of the turbine-generator fall within the rectifier's negative resistance region, torsional modes can get destabilised and lead to sustained or growing oscillations.

The first reported case of SSTI occurred in the Square Butte project [4], where a switching event triggered one of the torsional modes of a nearby turbine-generator and the HVDC converter amplified the resulting oscillations. Other examples of SSTI analysis in practical power systems are reported in [5] for hydro generators and in [6] for steam turbine-generators.

2.1.3. EMERGING SUB SYNCHRONOUS OSCILLATIONS

Since 2009, the power industry has experienced three new types of SSO, which are all electromagnetic in nature. The first type is the interaction that occurs when a DFIG wind power plant gets radially connected to a series capacitor compensated transmission line. This phenomenon is currently known as sub synchronous controller interaction and sub synchronous control instability (SSCI). However, in this thesis, this phenomenon will be referred to as *DFIG-SSR* for reasons that will be given in Section 2.3.1. The first reported case of DFIG-SSR occurred in the power system of ERCOT, Texas and is discussed in [7]. Other events are reported in [8]–[12].

The second type is the interaction of a power electronic converter with a weak grid. When a converter is connected to a weak grid, characterised by a low short circuit ratio (SCR), the converter can get unstable, which in turn could result in sub synchronous oscillations. In this thesis, this phenomenon will be referred to as *SSCI-CGI*, where ‘CGI’ is added to emphasise the converter-grid interaction. *SSCI-CGI* is explained in Section 2.4.1. A real example of this interaction occurred in 2015 in the Xinjiang power system and is described in [13]. Other events are reported in [14], [15].

Finally, the last new SSO phenomenon is another form of *SSCI* and manifests itself as an interaction between electrically close inverters. In this thesis, this phenomenon will be referred to as *SSCI-CCI*, where ‘CCI’ is added to emphasise the converter-converter interaction. It is described in Section 2.5.1 and a practical example is detailed in [16].

An overview of recent DFIG-SSR, *SSCI-CGI* and *SSCI-CCI* events is shown in Figure 2.3.

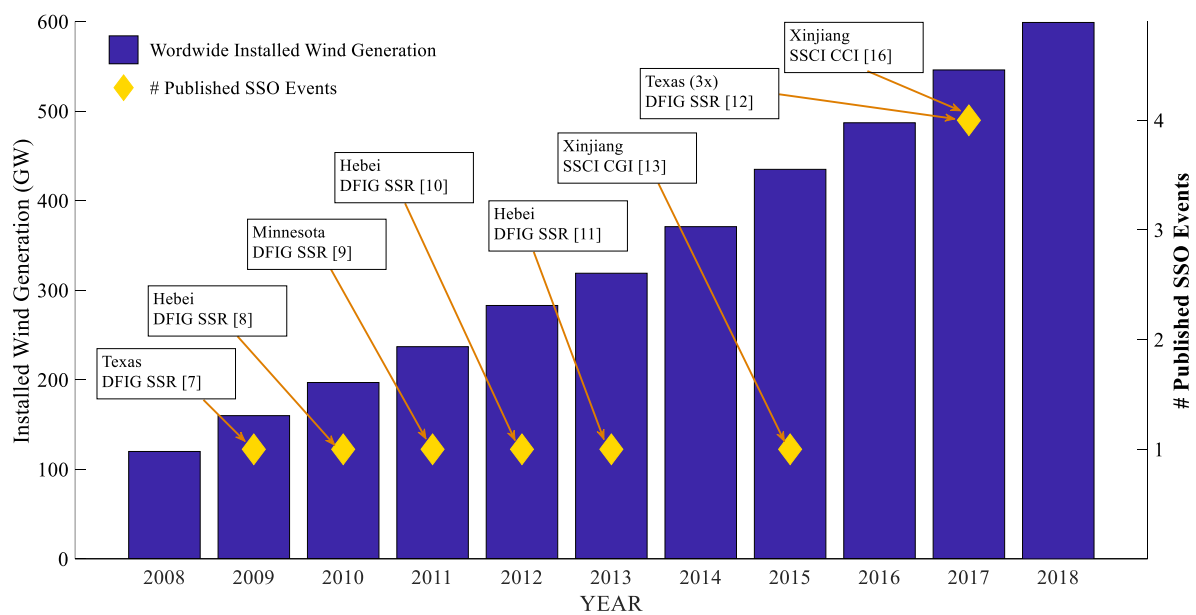


Figure 2.3 Overview of worldwide installed wind generation and the number of published SSO event. It should be remembered that not all events are published and for those that are published, there is a time lag between the actual occurrence of the event and its publication through scientific channels.

The three emerging phenomena are described next in more detail. As the DFIG-series capacitor interaction is the focus in this thesis, a review of fixed series compensation is given first. Methodologies for the assessment of DFIG-SSR are discussed in Chapter 4.

2.2. FIXED SERIES COMPENSATION

2.2.1. CONCEPT DESCRIPTION

Classical series compensation is mainly achieved through fixed series capacitors (FSC). In the classical compensation scheme, the transmission line with series inductance L is compensated symmetrically, i.e. the capacitance C of the series capacitor is the same across all three phases (see Figure 2.4).

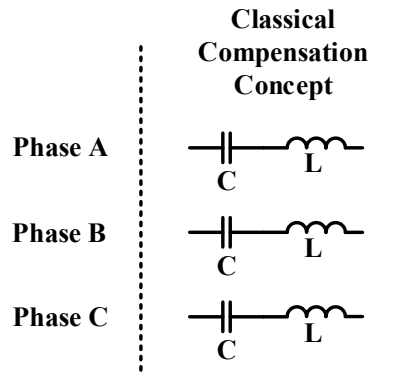


Figure 2.4 Overview of the classical compensation scheme.

Figure 2.5 illustrates the impact on the phase impedances of adding a series capacitor using the classical series compensation concept to an uncompensated transmission line.

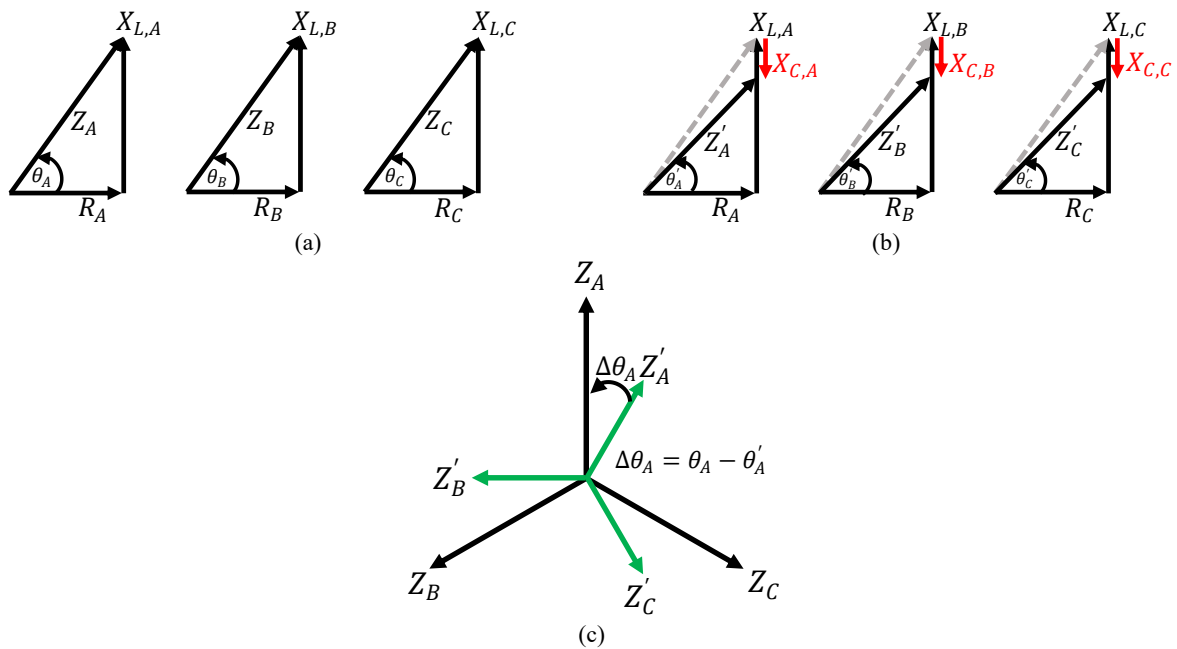


Figure 2.5 Vector diagram of the phase impedances at fundamental frequency. (a) without series compensation; (b) with series compensation; (c) phase diagram of the impedance.

Due to the symmetrical compensation of the three phases, a uniform reduction in the phase reactance is achieved (Figure 2.5b) and as a result a balanced equivalent impedance across the three phases is obtained (Figure 2.5c). The resulting rotating magnetomotive force (MMF) at sub synchronous frequencies will be symmetrical. As will be shown in Chapter 5, this is different for the phase imbalance compensation concept, where unbalanced phase impedances create an asymmetrically rotating MMF.

With balanced compensation, the resonance frequency ω_r is the same across all three phases and is defined as given in (2.2).

$$\omega_r = \sqrt{\frac{1}{LC}} \quad (2.2)$$

ω_r : resonance frequency (rad/s)
 L : transmission line inductance (H)
 C : capacitance of series capacitor (F)

The compensation degree k quantifies the ratio of the capacitive and inductive reactances and is defined as given in (2.3).

$$k = \frac{X_C}{X_L} \times 100\% \quad (2.3)$$

k : compensation degree
 X_C : capacitive reactance at f_0
 X_L : inductive reactance at f_0

The change in active power transfer as a function of k is defined by (2.4).

$$\Delta P = \frac{1}{1-k} - 1 \quad (2.4)$$

ΔP : change in active power transfer
 k : compensation degree

At the fundamental frequency ω_0 , $X_L = \omega_0 L$ and $X_C = 1/\omega_0 C$ and (2.3) can be rewritten as (2.5).

$$k\omega_0^2 = \frac{1}{LC} \quad (2.5)$$

The relation between ω_r and k can be derived by substituting (2.5) in (2.2), which results in (2.6).

$$\omega_r = \sqrt{k\omega_0^2} \quad (2.6)$$

Figure 2.6 graphically illustrates the relation between the compensation degree, the resonance frequency and the active power transfer. In practical series compensation applications k lies mostly between 20% and 80% [17]. In exceptional cases, k can be lower (e.g. the classical series compensation application in Hebei, China [10], has a k -value of 6.67%). This k range enables active power transfers between 1.25-5 per unit. With 50 Hz fundamental frequency f_0 , the corresponding resonance frequencies as seen from the point of common coupling (PCC) to the transmission network are between approx. 22 and 45 Hz. The actual resonance frequency could be different depending on the reactance of the generator. It should be recalled from (2.3) that k is always calculated at f_0 .

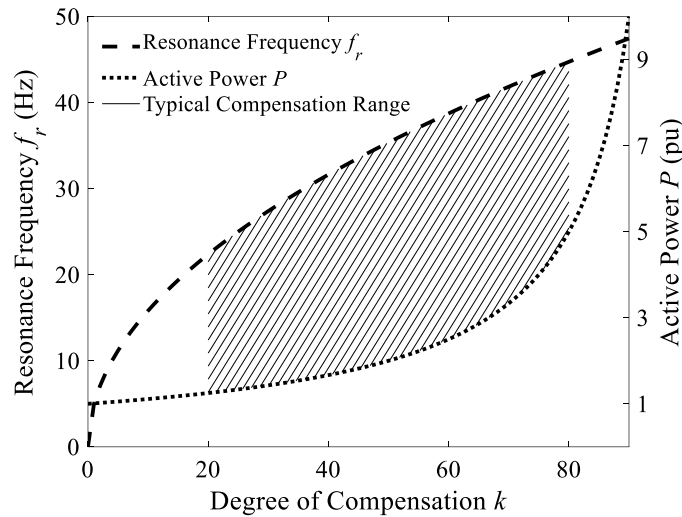


Figure 2.6 Influence of the compensation degree k on the resonance frequency f_r ($\omega_0 = 2\pi f_0 = 2\pi 50$) and active power transfer P .

2.2.2. PRACTICAL FSC APPLICATIONS

Below some practical applications of FSC in Argentina, Bangladesh, Canada, Finland, India, South Africa and Vietnam are given. Where available, the degree of compensation is mentioned as well. In these application examples, only the Canadian power system is operated at 60 Hz frequency. The other countries have 50 Hz based power systems.

Argentina

Ten series capacitors are installed in the four parallel lines of the 500 kV corridor in Argentina from Comahue to Buenos Aires, which stretch for over more than 1,000 km [18]. The compensation degree differs between 30% and 40%. The series capacitors are used to increase the transfer capacity by raising the transient stability limit of the lines, improving reactive power balance and voltage regulation and improving the active power sharing between the parallel lines. The ten series capacitors were installed in different steps. With the construction of the first two parallel lines, four series capacitors were installed, resulting in a transfer capacity of 1,650 MW. With the commissioning of the third line, four additional capacitors were installed, increasing the total transfer capacity to 2,900 MW. In the next stage, the first four capacitors were replaced by two larger units, leading to an additional 400 MW of transmission capacity. Finally, the commissioning of the fourth line included the installation of another four series capacitor, which ultimately lead to a transfer capacity of 4,600 MW across the corridor. All the series capacitors are operated at 500 kV and are rated 2,500 MVar in total.

Bangladesh

With the commissioning of a new generation facility of approx. 600 MW in Sylhet, reinforcement of the 132 kV double circuit transmission line between Sylhet and Ashuganj was necessary. This grid reinforcement was achieved through the use of series capacitors, where a 70% compensation degree was achieved.

Canada

In the Ontario province, Hydro One is operating two series capacitors in its 500 kV transmission grid [19]. Each series capacitor is rated at 750 MVar. The series capacitors are used to compensate two single line circuits of approx. 280 km each, connecting the north eastern part to the south. The degree of compensation is 50%. The main goal of the series compensation is to facilitate an increased active power transfer.

A 108 MVar series capacitor is installed in the 230 kV transmission system of Hydro-Quebec [20]. The main goal of the series compensation is to increase the transmission capacity of an existing transmission corridor, which facilitates power transfer of several remote hydro power plants to load areas. The single line diagram is shown in Figure 2.7. The corridor is 145 km long and consists of a single 230 kV circuit. The initial transmission capacity was exceeded as new hydro generation was coming online. Based on the analysis of the utility, series compensating the existing transmission line was more attractive than either building a new parallel 220 kV line or upgrading the existing line to a higher voltage. Compensation was achieved for 50% [21].

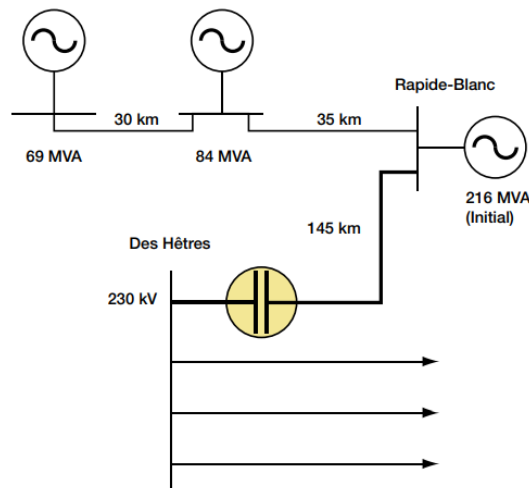


Figure 2.7 Single line diagram of series compensated power system in Hydro-Quebec [21].

Finland

In the Finish 400 kV transmission network, two series capacitors of 301 and 369 MVar were installed in 2009 in the Asmunti and Tuomela region. The goal of the compensation was to increase the cross border transmission capacity with Sweden by approximately 200 MW [22]. The transmission line was compensated for 70%.

India

The transmission system in India consists of several regional systems. With the aim to achieve a stronger, interconnected grid and to facilitate inter-regional power flows, several transmission corridors were planned. The East-West Interregional Link connects Rourkela and Raipur through a 412 km, 400 kV double circuit transmission line. This transmission line was compensated for 40% with the aim to enhance the transmission capacity.

To facilitate increased imports of hydro power from the neighbouring country Bhutan, the transmission capacity of the East-North Interconnector II was increased using series compensation (40%). The East-North Interconnector II is a 420 kV double circuit transmission line connecting Purnea and Gorakhpur.

Finally, in the Northern region several transmission lines were series compensated. The 400 kV double circuit transmission line between Bareilly and Mandaula as well as the 400 kV double circuit transmission line between Gorakhpur and Lucknow have a 30% compensation degree. Another 400 kV double circuit transmission line between Unnao and Bareilly has a compensation degree of 45%.

South Africa

In South Africa, a total of six fixed series capacitors were installed in 2012 in the 745 kV transmission system, see Figure 2.8 [23]. The Cape outages of 2006 resulted in more stringent security planning criteria. As a result of these criteria, the capacitors were required for strengthening of the Cape Corridor. To meet the stringent security criteria three options were considered: (i) commissioning of new 765 kV lines between Zeus and Perseus and between Hydra and Gamma, (ii) commissioning of a third 765 kV line between Beta and Alpha and a new 765 line between Hydra and Gamma and (iii) series compensation of existing 765 kV lines and commissioning of a new 765 kV line between Hydra and Gamma. The last option was the preferred option as it resulted in the best overall improvement in transfer limits, lowest costs, least environmental impact and significant reduction in transmission losses.

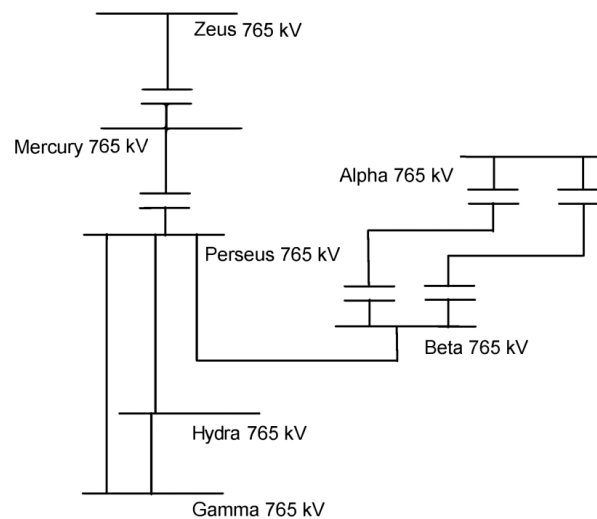


Figure 2.8 765 kV series compensated transmission corridor in South Africa [23].

Vietnam

A total of 18 installations with maximum capacity of 6,588 MVar were commissioned in the period from 2012 to 2016 for enhancing the transmission capability of the 500 kV transmission system in Vietnam, which is operated by the National Power Transmission Corporation. The goal of the series compensation was to enhance the operational reliability and efficiency and to facilitate increased power transfers to meet the forecasted annual economic growth of approx. 8%.

The aforementioned application examples illustrate the advantage and use of fixed series compensation. However, when series capacitors are in close electrical proximity of DFIG wind power plants, there is a risk for adverse interactions between the series capacitor and the DFIG wind turbine generators. This phenomenon is explained next.

2.3. DFIG-SERIES CAPACITOR INTERACTION

2.3.1. DESCRIPTION OF PHENOMENON

The schematic diagram of the DFIG is shown in Figure 2.9. The DFIG-series capacitor interaction can be explained by considering the DFIG's impedance model. The impedance of the main components of a DFIG can be grouped into two categories: the DFIG's grid side impedance Z_{GS} consists of the impedance of the filter and the inverter, whereas the DFIG's rotor side impedance Z_{RS} is formed by the impedance of the induction machine and the rectifier. During normal operation, the DC-link voltage is constant, and Z_{GS} and Z_{RS} can be considered to be connected in parallel as is shown in Figure 2.10 [24], [25].

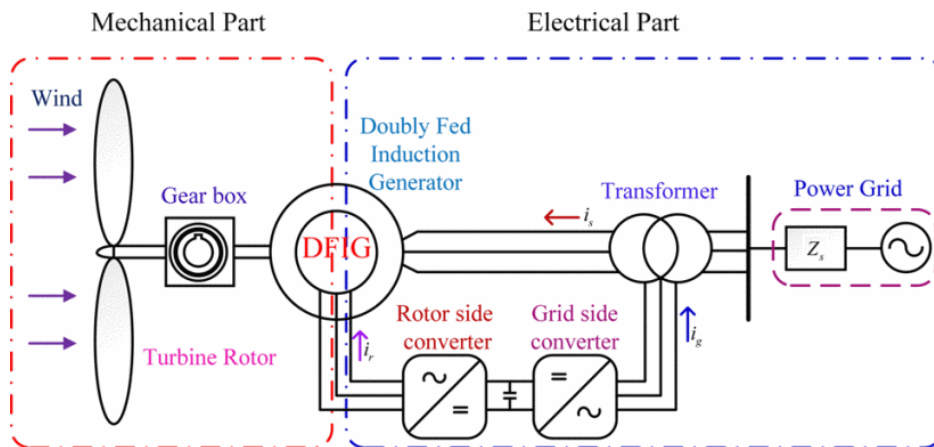


Figure 2.9 Schematic diagram of a DFIG WTG [26].

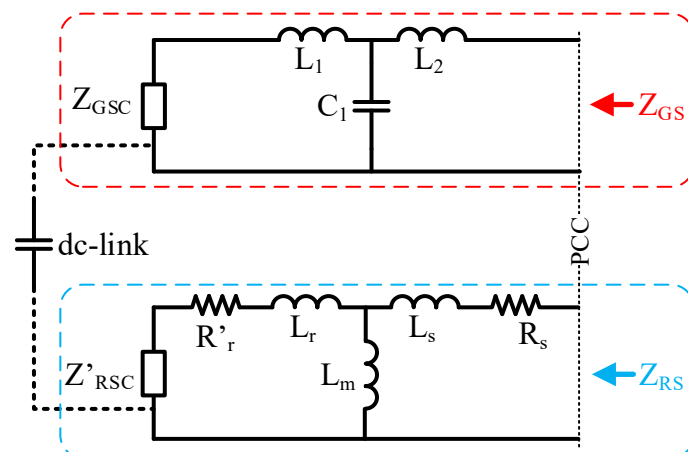


Figure 2.10 Electrical connection of the grid side and rotor side of the DFIG under normal operation (figure based on [24]).

In the DFIG of Figure 2.10, the DC-link capacitor connected between the rectifier or rotor side converter (RSC) and the inverter or grid side converter (GSC), decouples the RSC and GSC control and enables the independent operation of both converters. Furthermore, an LCL filter is used to enhance the power quality at the PCC. In this case, Z_{GS} as seen from the PCC is defined as given in (2.7).

$$Z_{GS} = \frac{Z_{L_2}Z_{C_1} + Z_{L_2}(Z_{L_1} + Z_{GSC}) + Z_{C_1}(Z_{L_1} + Z_{GSC})}{Z_{C_1} + Z_{L_1} + Z_{GSC}} \quad (2.7)$$

Z_{L_1}, Z_{L_2} : impedance of filter inductances L_1 and L_2
 Z_{C_1} : impedance of filter capacitance C_1
 Z_{GSC} : impedance of grid side converter

With slip χ as given in (2.8), Z_{RS} as seen from the PCC is defined as given in (2.9).

$$\chi = \frac{\omega_e - \omega_r}{\omega_e} \quad (2.8)$$

ω_e : electrical/stator speed (rad/s)
 ω_r : rotor speed (rad/s)

$$Z_{RS} = R_s + Z_{L_s} + \frac{Z_{L_m}(Z_{L_r} + R'_r + Z'_{RSC})}{Z_{L_m} + Z_{L_r} + R'_r + Z'_{RSC}} \quad (2.9)$$

$R'_r = \frac{R_r}{\chi}$
 $Z'_{RSC} = \frac{Z_{RSC}}{\chi}$
 R_s : induction machine stator winding resistance
 Z_{L_s} : impedance of induction machine stator leakage reactance
 Z_{L_r} : impedance of induction machine rotor leakage reactance
 Z_{L_m} : impedance of induction machine magnetising reactance
 R_r : induction machine rotor winding resistance
 R'_r : R_r referred to the stator side
 Z_{RSC} : impedance of rotor side converter
 Z'_{RSC} : Z_{RSC} referred to stator side

When the magnetising reactance is neglected, (2.9) simplifies to (2.10).

$$Z_{RS} = R_s + Z_{L_s} + Z_{L_r} + \frac{R_r + Z_{RSC}}{\chi} \quad (2.10)$$

As practical DFIGs generally have a large Z_{GS} , the impedance of the DFIG, Z_{DFIG} , can be approximated by Z_{RS} [25], [27], [28]. From (2.10) it is then observed that Z_{DFIG} is not constant and depends on χ . Under sub synchronous frequencies, χ can become negative, following which the damping of the DFIG system becomes negative. When the net damping, which is the sum of the DFIG damping and the damping provided by the transmission system, is negative, the power system will experience growing oscillations. For χ to be negative, sub synchronous

currents with a frequency lower than the rotor speed are required. These currents are produced following a disturbance in among others a series capacitor compensated transmission line.

The interaction between a DFIG and a series capacitor was discussed for the first time in 2003 [29], which was well before the adverse interactions occurred for real in the power system of Texas in 2009 [7]. The study in [29] presents an investigation of integrating between 500 MW and 1,000 MW of wind generation into the Dakota transmission system. The generated electrical energy would be transported across long distances and one alternative to facilitate the long distance transmission was through the use of series compensation. The influence of different degrees of series compensation was shown using damping torque analysis and a resonance at approx. 30 Hz was identified. Time domain simulations successfully validated the results. In [30], published in 2008, a static var compensator (SVC) and a thyristor controlled series capacitor (TCSC) controller were designed for mitigating this type of interaction. Whereas both FACTS controllers were able to successfully mitigate the DFIG-series capacitor interaction, the performance of the TCSC was found to be superior.

The interaction between a DFIG and a series capacitor is a form of self-excitation and is similar to IGE. Eigenvalue analysis performed in [31] on a DFIG connected to an infinite bus through a series compensated transmission line, identified four SSO modes. The state space model developed for the DFIG consisted of 20 state variables, i.e. four generator states (stator and rotor fluxes), five drive train states (rotating speeds of three masses and two relative angles between the masses), four controller states for the rectifier, one for the DC-link voltage, four controller states for the inverter and two states for the converter transformer current. The state space model of the transmission network consisted of the line currents and bus voltages. Using participation factor analysis, three modes (2.65, 3.23 and 6.74 Hz) were identified as torsional modes of the three mass drive train and the fourth mode (24.76 Hz) was identified as a network mode. The network mode was found to be mainly influenced by the series capacitor and the generator states of the DFIG. The participation factors of states related to the rectifier, the DC-link voltage and the inverter in the network mode were found to be practically zero. As the converter controllers do not participate in this network mode, defining such an interaction as SSCI is misplaced. Looking at the states that do participate in the network mode, this phenomenon is rather a form of self-excitation. Therefore, in the reclassification of SSO phenomena, this phenomenon is defined as *DFIG-SSR*. Finally, as was shown in [32], the full converter wind turbine generator is not susceptible to DFIG-SSR.

2.3.2. PRACTICAL CASE: TEXAS, USA

The first reported DFIG-SSR in a real power system occurred on 22 October 2009 in Texas. The configuration of the South Texas power system is shown in Figure 2.11. Two wind power plants are connected at the Zorillo substation, which is radially connected to the Ajo substation. The 345 kV transmission line from Nelson Sharpe to Rio Hondo consists of two line segments. The first segment connects substations Nelson Sharpe and Ajo. The second segment connects substations Ajo and Rio Hondo and has a 90% compensation degree.

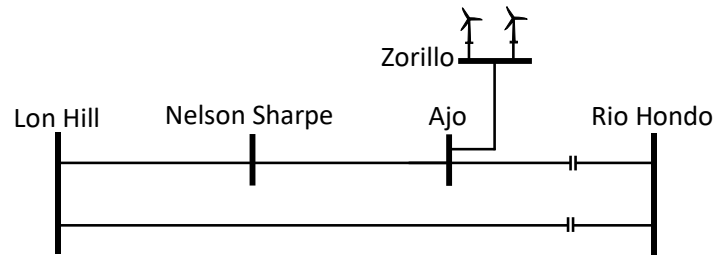


Figure 2.11 South Texas transmission system with coastal wind power plants [33].

On 22 October 2009, the Nelson Sharpe-Ajo line segment had a permanent fault and was isolated by the protection equipment. As a consequence, the new topology resulted in a radial connection of the wind power plant at Zorillo, through Ajo, to the series capacitor at Rio Hondo. In this new topology, the line segment Zorillo-Ajo-Rio Hondo had an equivalent degree of compensation of 75%. At these compensation degrees, the DFIG wind power plant acted as a negative resistance to the sub synchronous currents produced in the grid. Following the fault, the sub synchronous currents increased rapidly to 3 per unit in 200 milliseconds (see Figure 2.12). The series capacitor was bypassed after approx. three seconds, following which the oscillations subsided.

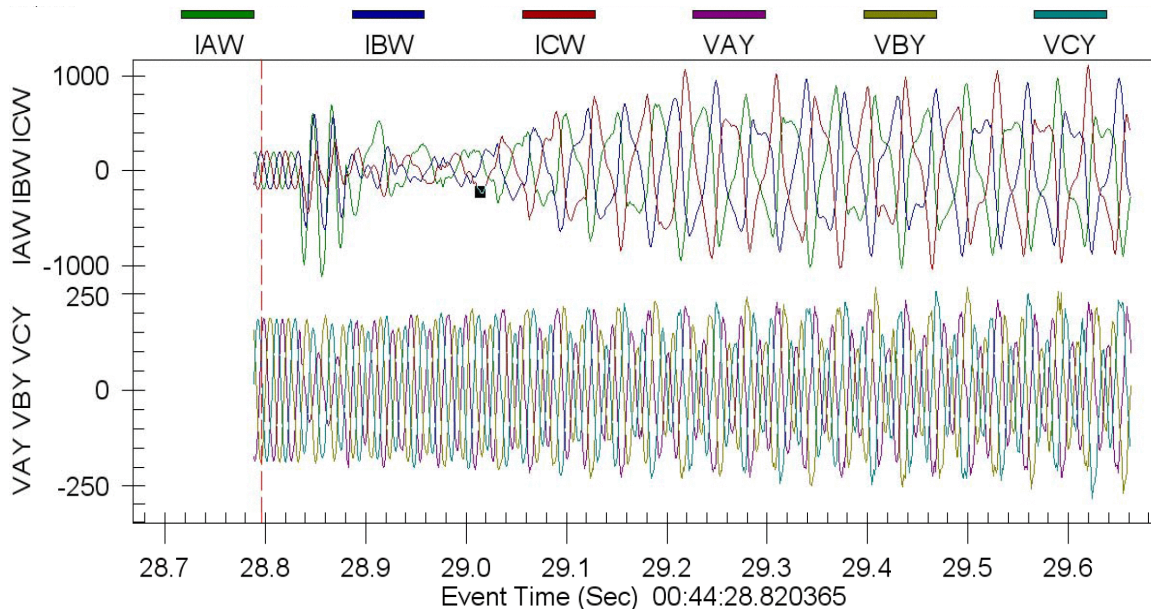


Figure 2.12 Oscilloscope record of 2009 sub synchronous event: first half second of resonance following initiating fault [33].

2.4. CONVERTER-GRID INTERACTION

2.4.1. DESCRIPTION OF PHENOMENON

The second SSO type occurs between an inverter and the grid. When the voltage source converter (VSC) is connected to a weak grid, control loop interactions become obvious. Under weak grid conditions, the phase and magnitude of the terminal voltage are sensitive to the power output. A small disturbance in the DC-link voltage control changes the inverter's power output, which further affects the phase and magnitude of the terminal voltage. The terminal voltage

phase and magnitude variations make the phase locked loop (PLL) and AC voltage control respond. In turn, actions of the PLL and AC voltage control lead to internal voltage phase and magnitude variations. Consequently, it leads to variations in active and reactive power outputs and affect the DC-link voltage control dynamics.

The resonance frequency of the SSO largely depends on the control philosophy and PLL parameters as will be explained next. Consider the d -axis control philosophies of an inverter as are shown in Figure 2.13. The outer loop control can be designed as an active power control or DC-link voltage control. The DC-link voltage control can be designed with or without DC-link dynamics. With losses neglected, the DC-link dynamics are described by (2.11).

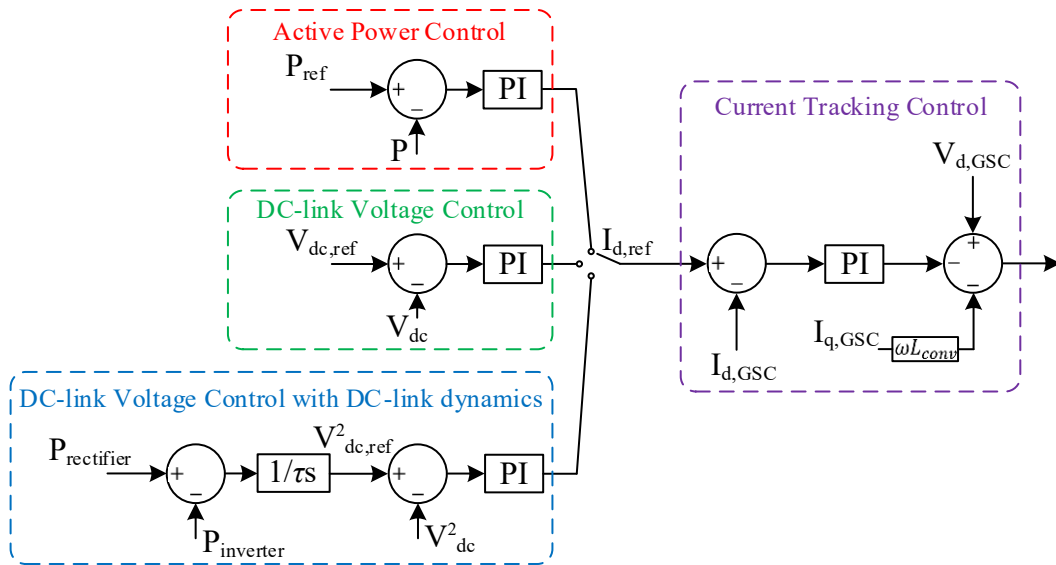


Figure 2.13 d -axis control philosophies for inverter control.

$$\frac{C}{2} \frac{dV_{DC}^2}{dt} = P_{rectifier} - P_{inverter}$$

C : DC-link capacitor

V_{DC} : DC-link voltage

$P_{rectifier}$: active power flowing into the DC-link

$P_{inverter}$: active power flowing out of the DC-link

(2.11)

Table 2.1 gives an overview of publications that describe the influence of different inverter's d -axis control concepts on the stability of the system. Eigenvalue analyses reported in the references of Table 2.1 showed that with reducing SCR some SSO modes move to the right half plane and cause instability, independent of the inverter d -axis control concept. It is worth noting that the visibility of these modes is only possible when the outer control loops and the PLL are modelled [34].

In [34] the inverter of the WTG was deployed with active power control. The stability of the system was investigated under different active power output levels and PLL bandwidths. It was found that when SCR=1.33, increasing power output and reducing PLL bandwidth made the low frequency mode (3-4 Hz) unstable. A more detailed investigation of the PLL's impact

on the stability of a VSC HVDC system is given in [35]. The inverter of the VSC HVDC system was deployed with an active power control. Also here it was concluded that when the SCR is higher than 1.32, a PLL with high bandwidth increases the stability. However, to eliminate voltage harmonics in a PLL, the PLL usually includes a low-pass filter, which in turn limits the PLL bandwidth. When the SCR was lower than 1.32, increasing the PLL bandwidth decreased the stability of the system and led to undamped oscillations of approx. 3 Hz. The maximum proportional gain of the PLL needed to transfer the rated power under different SCRs was also investigated. It was found that up to SCR=1.32 the HVDC could transfer the rated power across the full range of the PLL's proportional gain. With lower SCRs, the rated power transfer could only be achieved by reducing $K_{P,PLL}$. Although reduced $K_{P,PLL}$ enables operating the VSC HVDC in weak grid conditions, it has some disadvantages. When the SCR increases, low $K_{P,PLL}$ will result in poor damping capabilities. Furthermore, low $K_{P,PLL}$ will lead to a slower dynamic response, which may violate grid code requirements.

Table 2.1 Overview of research on the impact of various inverter d -axis control concepts on the stability of the system.

Ref	Active power control	DC-link voltage control	DC-link voltage control with DC-link dynamics
[34]	X		
[35]	X		
[36]	X		X
[37]	X		X
[38]			X
[39]			X
[40]			X
[41]		X	
[42]		X	
[43]		X	
[44]		X	

Active power control as well as DC-link voltage control (with DC-link dynamics modelled) for the inverter of a WTG are investigated in [36]. It was found that under weak grid conditions the active power control has a better stability performance than the DC-link voltage control. It was found in [37] that when the DC-link voltage control is used, the PLL bandwidth determines whether the low or sub synchronous frequency mode is dominant: a low PLL bandwidth (17 Hz) made the low frequency mode (approx. 5 Hz) unstable, whereas a high PLL bandwidth (70 Hz) deteriorated the stability of the sub synchronous mode (40 Hz). This conclusion was also reached for the DC-link voltage control in [38]. Participation factor analysis further revealed that when the PLL bandwidth was low (13 Hz), mainly the PLL and the AC voltage control participated in the low frequency mode (5 Hz). With a higher PLL bandwidth (34 Hz), the low frequency (5 Hz) as well as sub synchronous frequency (24 Hz) modes were linked to the DC-link dynamics, DC-link voltage control and the PLL. Independent of the PLL bandwidth, the DC-link dynamics, DC-link voltage control and the PLL had a large participation in the sub synchronous frequency mode. The influence of the bandwidths of the

DC-link voltage control and the PLL was investigated in [39]. It was found that when both bandwidths are close to each other, the low frequency mode (6 Hz) became unstable. In this reference, the bandwidth of the PLL was varied from 2 Hz to 24 Hz. When the PLL bandwidth was close to 10 Hz (which is the bandwidth of the DC-link voltage control), the low frequency oscillation mode became unstable. Finally, this type of interaction is not limited to direct drive permanent magnet synchronous generators (D-PMSG) or HVDC converters only. It was illustrated in [40] that a DFIG with DC-link voltage control is also prone to instability when the PLL bandwidth is close to the bandwidth of the DC-link voltage control. In this case the PLL with a bandwidth of 8 Hz led to unstable 4 Hz oscillations.

The DC-link voltage control discussed so far included the DC-link dynamics. The DC-link voltage control without DC-link dynamics is studied in [41]–[44]. The influence of different inner and outer control parameters on the oscillation mode are presented in [42]. The eigenvalue analysis for a D-PMSG was presented in [43] and revealed six SSO modes, of which one mode (32 Hz) becomes unstable with reducing grid strength. Participation factor analysis showed that the states of the generator and rectifier of the D-PMSG do not participate in this mode, whereas a large participation was observed for the states of the DC-link (DC-link voltage), the inverter (d -axis current tracking control) and the grid (d - and q -axis line currents). Further analysis of different SCRs showed that weak grids move the 32 Hz mode even more to the right half plane. The decreasing SCR also weakened the stability of a low frequency mode (approx. 8 Hz) without making it unstable.

Contrary to DFIG-SSR, this interaction is between the DC-link, converter controllers and the grid, and is an actual example of SSCI. To distinguish the converter-grid interaction (CGI) from other types of SSCI, it is defined here as *SSCI-CGI*. It is worth noting that although participation factor analysis reveal a large participation of the line impedance in the related oscillation mode, the impedance represents the equivalent of a power system. This is the reason why this phenomenon is defined here as *converter-grid interaction* and not as *converter-line interaction*.

Finally, the interaction of inverters with weak grids was first observed in railway grids in 1991 [45]. In railway systems, the inverter of locomotives can interact with weak power grids and lead to heavy SSO. Adaptation of the static frequency converter control parameters helped to mitigate the SSO. Standard EN 50388 [46] thoroughly addresses SSCI-CGI in railway grids.

2.4.2. PRACTICAL CASE: YORKSHIRE, UK

An SSCI-CGI event happened in the UK on 9 August 2019. The interaction in this case was triggered by a disturbance in the transmission system, which ultimately reduced the Hornsea One wind power plant's active power output from 799 MW to 62 MW. Hornsea One is an offshore wind power plant located 120 km from the coast of Yorkshire, UK, and consists of 174 wind turbines of 7 MW. The wind power plant is divided into three blocks of 400 MW each. Each block connects into its own offshore HVAC collector substation and all collector substations connect to a single HVAC reactive compensation station. From this station, the energy is transported to the onshore substation.

On 9 August 2019, the UK experienced significant storms, resulting in heavy rain and lightning. A lightning occurred at 16:52:33:490 and resulted in the tripping of a 400 kV

transmission line. The line was reconnected after 20 seconds. In the meantime, the resulting voltage dip due to the lightning caused the wind power plant to inject reactive power in the grid, as is expected by the grid code. In the following milliseconds, as the active power generated by the wind power plant decreased in order to accommodate the increased reactive power injection, protection systems tripped many wind turbines, reducing the active power generation to 62 MW at 16:52:33:835. Combined with other parallel events, this reduction disrupted the power supply of approx. 1 million electricity consumers.

According to the technical report of the wind power plant owner [47], the active power reduction resulted from an undamped electrical resonance in the sub synchronous frequency range, which in turn was caused by the lightning strike. The voltage and active power responses of Hornsea One are shown in Figure 2.14 [15], where a oscillation of approx. 10 Hz is visible in the voltage response.

Prior to the lightning and subsequent de-loading of Hornsea One, a poorly damped 10 Hz oscillation in the wind power plant's reactive power already existed, indicating a weak grid condition. The oscillation was triggered by a 2% voltage step change. It could therefore be reasonably argued that the transmission line outage following the lightning, weakened the grid even further and excited the SSO, leading to undamped voltage oscillations. More details on the event are reported in [15], [47].

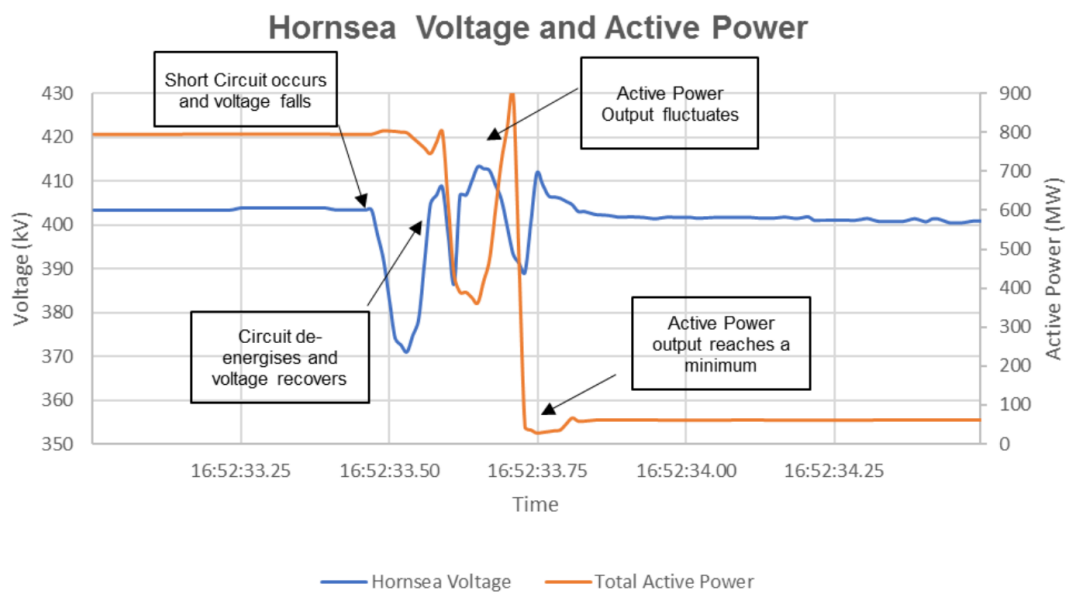


Figure 2.14 Voltage and active power at Hornsea One [15].

2.5. CONVERTER-CONVERTER INTERACTION

2.5.1. DESCRIPTION OF PHENOMENON

The converter-converter interaction (CCI) is another type of SSCI, where the interaction is between electrically close converters and is manifested as sub synchronous oscillations in the voltage/reactive power. The phenomenon is named *SSCI-CCI*.

From a conceptual perspective, the interaction can be caused when two converters try to control the voltage on the same bus, where both converters have different gains and time

constants. Following a small disturbance such as a step change in the bus voltage, both converters will aim to control the voltage back to its setpoint. However, as both converters have different gains and time constants, their control speed will be different and this could potentially lead to sub synchronous voltage oscillations. Practical as well as academic experience with SSCI-CCI is rarely published and is suggested as a future research direction.

2.5.2. PRACTICAL CASE: AUSTRALIA

A practical example of a SSCI-CCI event that happened in Australia on 31 March 2016 is reported in [48] and discussed next. The single line diagram of the power system is shown in Figure 2.15. The solar power plant is connected at the 22 kV bus and consists of 80 inverters with a combined active power output of approx. 53 MW. Two SVCs, each with a range of -29 MVar to +22 MVar, are also installed directly to the 22 kV bus without dedicated SVC transformers. Voltage control of the SVCs is achieved through an integral-only control structure, where the integral gain is limited due to the weak grid. The generated energy is transformed to 220 kV using two transformers. The 3 phase fault level at Bus A 220 kV is 347 MVA.

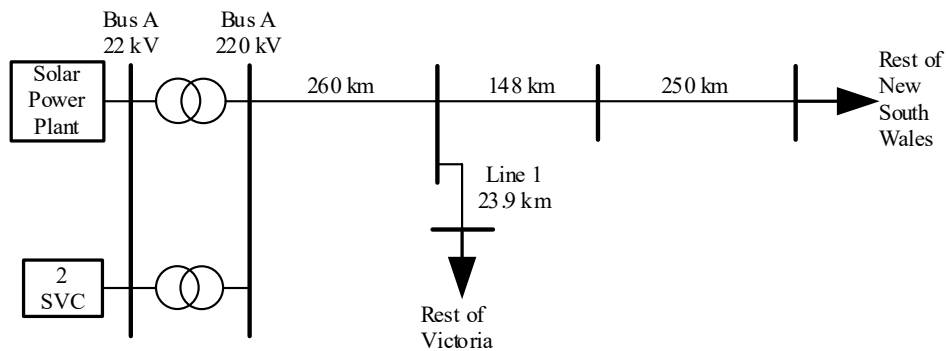


Figure 2.15 Single line diagram for the Australian SSCI-CCI example [48].

On 31 March 2016, Line 1 was out of service for maintenance. With line 1 out of service, the fault level at Bus A 220 kV decreased to 189 MVA, resulting in sustained voltage oscillations of 7.3 Hz with a peak to peak magnitude of 0.06 per unit (Figure 2.16). The oscillations only stopped after the system operator changed the operation mode of the SVCs to manual. Detailed time domain EMT simulations showed that the main devices actively involved in the control interaction were the SVCs and solar power plant inverter. Three different possible SVC control structures, i.e. proportional-only, proportional and integral, and proportional with lead-lags, were studied as potential mitigation solutions and none of these modifications were able to mitigate the interaction. Only with reduced proportional and integral gains of the SVCs' inverter level current control, SSCI-CCI was no longer observed.

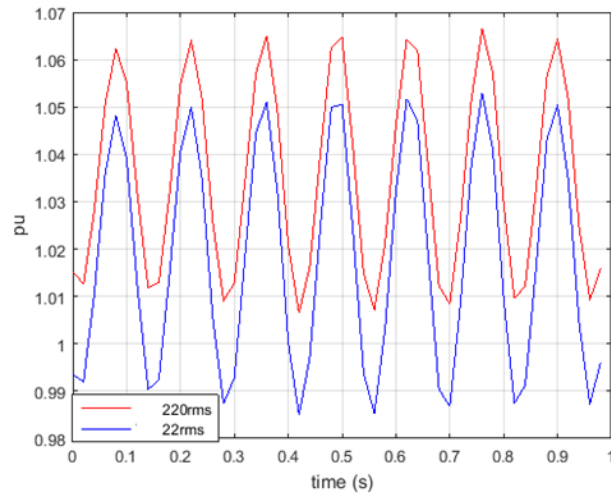


Figure 2.16 Voltage oscillations of 7.3 Hz following SSCI-CCI between the solar power plant and the two SVCs [48].

It is worth noting that the solar power plant was only installed in 2016, whereas the SVCs were operational years before the commissioning of the solar power plant. With only the SVCs in the system, no voltage oscillations were observed during line outages. The oscillations only appeared after the solar power plants were taken into operation.

2.6. PROPOSED RECLASSIFICATION OF SSO

As was discussed in the previous sections, new types of SSO have emerged in recent years. These phenomena (i.e. DFIG-SSR, SSCI-CGI and SSCI-CCI) are all electromagnetic in nature and as a result, the associated oscillations grow faster compared to classical electromechanical SSO phenomena. When considering the existing definition of SSO, it is concluded that the existing definition:

- excludes electromagnetic phenomena;
- excludes interactions between power electronic converters and passive elements;
- excludes interactions among power electronic converters.

Taking the above into consideration, the definition of SSO needs to be modified in such a way, that (i) it does not exclude electromagnetic phenomena and (ii) it includes the interactions related to power electronic converters. The following definition is proposed, in which the text in bold is added to the existing definition:

*SSO is a **sub synchronous electromechanical** interaction between (i) a turbine-generator and passive system elements such as series capacitors, (ii) a turbine-generator and active system elements such as power electronic equipment controls and static VAR system controls, **or (iii) active system elements and either other active system elements such as converters or passive system elements such as a weak grid.***

The next step is to include DFIG-SSR, SSCI-CGI and SSCI-CCI in the existing classification of Figure 2.1 (page 16), where the classification will be done based on interacting

devices. The proposed reclassification of SSO phenomena is shown in Figure 2.17. In this proposal, red boxes represent the new SSO categories, solid boxes represent electromechanical phenomena and dashed boxes represent electromagnetic phenomena. The interaction of either a conventional synchronous generator or a DFIG with a series capacitor is categorised as SSR. As DFIG-SSR is a form of self-excitation, it is categorised as such, together with torsional interaction and the induction generator effect. The interaction of a conventional synchronous generator with active system elements remains under the DDSSO category and no changes are made to the DDSSO classification. For the interaction of active system elements with either passive system elements or other active system elements a new category, ‘Sub Synchronous Control Interactions’, is proposed. This category is on the same hierarchical level as SSR and DDSSO. It should be kept in mind that control parameters, which can change significantly depending on the converter designs, largely influence the oscillation frequency. Especially for SSCI this could also lead to super synchronous oscillations.

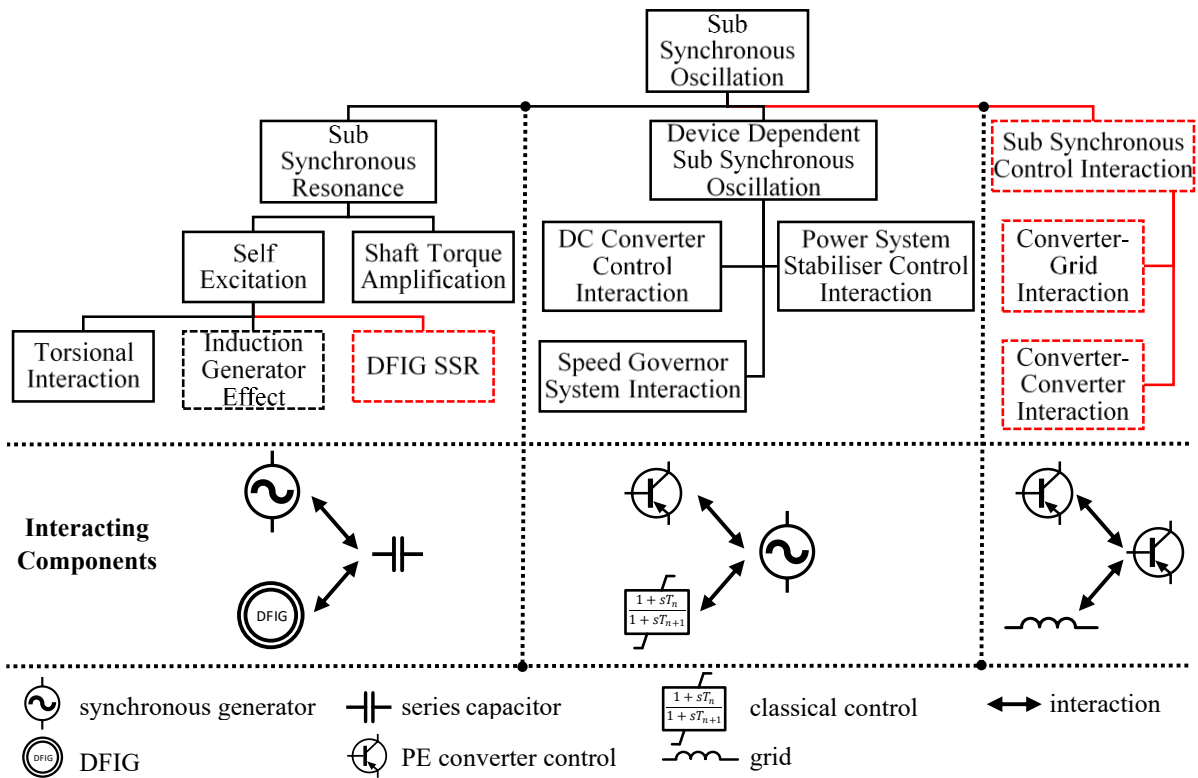


Figure 2.17 Proposed reclassification of SSO phenomena, taking into account three new SSO types: DFIG-SSR, SSCI-CGI and SSCI-CCI. Red boxes represent the new SSO categories, solid boxes represent electromechanical phenomena and dashed boxes represent electromagnetic phenomena.

The proposed SSO classification has some advantages compared to existing ones. The classifications of SSO given in [49] and [50] are incomplete as they do not consider converter-grid and converter-converter interactions. Furthermore, these references define the DFIG-SSR interaction as SSCI, which is inherently incorrect for the reasons given in Section 2.3. A completely new classification is proposed in [51], where oscillations were grouped in three categories: torsional, L-C and converter-grid oscillations. This classification has two major drawbacks. The first is that it moves away from the existing, well-established classification,

making the proposed one difficult to grasp. The second is that it considers the interaction among converters as converter-grid oscillation. The SSCI-CGI and SSCI-CCI phenomena are fundamentally different and cannot be grouped under the same category. Finally, in this reference the DFIG-SSR interaction is also incorrectly defined as SSCI. All these issues are correctly addressed in the classification proposed in Figure 2.17.

2.7. CONCLUSIONS

In recent years, the industry has been experiencing three new types of electromagnetic sub synchronous oscillations, which cannot be categorised under the existing SSO framework. Furthermore, the current SSO definition explicitly only considers electromechanical oscillations. Finally, there is a lack of consensus in academia and industry with regards to the terminology for the emerging phenomena, leading to addressing fundamentally different phenomena with the same terminology. These three reasons formed the basis for the new definition and classification of SSO presented in this Chapter.

In this Chapter a description as well as practical, industry examples of the three emerging SSO phenomena DFIG-SSR, SSCI-CGI and SSCI-CCI were given. The DFIG-SSR phenomenon occurs in the presence of a DFIG based wind power plant and a series capacitor. Eigenvalue analysis showed that the DFIG's converter controllers do not participate in the phenomenon and that therefore 'SSCI' is not a correct terminology for this phenomenon. Existing scientific literature also showed that the full converter wind turbine generator is not susceptible to the DFIG-SSR phenomenon.

The SSCI-CGI phenomenon occurs when an inverter is operating in weak grid conditions. Although this phenomenon is well known in railway grids, it is rather new in the context of power systems. Eigenvalue analysis showed that among others the inverter control and the grid participate in the resulting sub synchronous oscillations. In contrast to DFIG-SSR, this phenomenon does involve controllers. Therefore, the resulting interaction between the inverter and a grid is named *SSCI-CGI* in the proposed classification.

The last phenomenon is the adverse interaction among inverters. In the proposed classification this phenomenon is defined as *SSCI-CCI*, where 'CCI' is added to explicitly address the presence of multiple converters. Finally, to include these new electromagnetic phenomena in the existing framework of SSO, the SSO definition was extended.

The focus in this thesis is on the DFIG-SSR phenomenon. Therefore, Chapter 3 will investigate the limitations and recognised application boundaries of existing approaches for mitigating DFIG-SSR.

REFERENCES

- [1] IEEE Subsynchronous Resonance Working Group, “Terms, Definitions and Symbols for Subsynchronous Oscillations,” *IEEE Trans. Power Appar. Syst.*, vol. 104, no. 6, pp. 1326–1334, 1985.
- [2] IEEE Subsynchronous Resonance Working Group, “Reader’s Guide to Subsynchronous Resonance,” *IEEE Trans. Power Syst.*, vol. 7, no. 1, pp. 150–157, 1992.
- [3] P. M. Anderson, B. L. Agrawal, and J. E. Van Ness, *Subsynchronous Resonance in Power Systems*. New York: IEEE Publication, 1990.
- [4] M. Bahrman, E. V. Larsen, R. J. Piwko, and H. S. Patel, “Experience with HVDC — turbine-generator torsional interaction at Square Butte,” *IEEE Trans. Power Appar. Syst.*, vol. PAS-99, no. 3, pp. 966–975, May 1980.
- [5] Y. C. Choo, A. P. Agalgaonkar, K. M. Muttaqi, S. Perera, and M. Negnevitsky, “Analysis of subsynchronous torsional interaction of HVDC system integrated hydro units with small generator-to-turbine inertia ratios,” *IEEE Trans. Power Syst.*, vol. 29, no. 3, pp. 1064–1076, 2014.
- [6] C. Hong and H. Rao, “The study of SSTI between Guizhou-Guangdong II \pm 500 kV DC transmission link and steam-turbine-generators near the rectifier terminal,” in *2006 International Conference on Power System Technology, POWERCON2006*, 2007.
- [7] J. Adams, C. Carter, and S. H. Huang, “ERCOT experience with Sub-synchronous Control Interaction and proposed remediation,” in *Proceedings of the IEEE Power Engineering Society Transmission and Distribution Conference*, 2012, pp. 1–5.
- [8] L. Yunhong, L. Hui, C. Xiaowei, H. Jing, and Y. Li, “Impact of PMSG on SSR of DFIGs connected to series-compensated lines based on the impedance characteristics,” *J. Eng.*, vol. 2017, no. 13, pp. 2184–2187, 2017.
- [9] K. Narendra *et al.*, “New microprocessor based relay to monitor and protect power systems against sub-harmonics,” *2011 IEEE Electr. Power Energy Conf. EPEC 2011*, pp. 438–443, 2011.
- [10] L. Wang, X. Xie, Q. Jiang, H. Liu, Y. Li, and H. Liu, “Investigation of SSR in Practical DFIG-Based Wind Farms Connected to a Series-Compensated Power System,” *IEEE Trans. Power Syst.*, vol. 30, no. 5, pp. 2772–2779, 2015.
- [11] X. Xie, X. Zhang, H. Liu, H. Liu, Y. Li, and C. Zhang, “Characteristic Analysis of Subsynchronous Resonance in Practical Wind Farms Connected to Series-Compensated Transmissions,” *IEEE Trans. Energy Convers.*, vol. 32, no. 3, pp. 1117–1126, 2017.
- [12] Y. Li, L. Fan, and Z. Miao, “Replicating Real-World Wind Farm SSR Events,” *IEEE Trans. Power Deliv.* (early access), 2019.
- [13] Y. Xu and Y. Cao, “Sub-synchronous oscillation in PMSGs based wind farms caused by amplification effect of GSC controller and PLL to harmonics,” *IET Renew. Power Gener.*, vol. 12, no. 7, pp. 844–850, 2018.
- [14] S. H. Huang, J. Schmall, J. Conto, J. Adams, Y. Zhang, and C. Carter, “Voltage control challenges on weak grids with high penetration of wind generation: ERCOT experience,” *IEEE Power Energy Soc. Gen. Meet.*, pp. 1–7, 2012.
- [15] National Grid ESO, “Technical Report on the events of 9 August 2019,” London, 2019.

-
- [16] Y. Xu, S. Zhao, Y. Cao, and K. Sun, "Understanding Subsynchronous Oscillations in DFIG-based Wind Farms without Series Compensation," *IEEE Access*, vol. 7, pp. 107201–107210, 2019.
- [17] J. Miller, M. Brunet-watson, and J. Leighfield, "Review of Series Compensation for Transmission Lines," 2014.
- [18] M. Eremia and S. Nilsson, "Series Capacitive Compensation," in *Advanced Solutions in Power Systems: HVDC, FACTS, and AI Techniques*, Wiley-IEEE Press, 2016, pp. 339–407.
- [19] R. Gruenbaum, J. Rasmussen, and C. Li, "Series capacitors for increased power transmission capability of a 500 kV grid intertie," in *2012 IEEE Electrical Power and Energy Conference, EPEC 2012*, 2012, pp. 164–169.
- [20] ABB AB FACTS, "Series capacitor for increased hydro power transmission over a 230 kV grid," Västerås.
- [21] K. Gauthier and M. Alawie, "A special case of ferroresonance involving a series compensated line," in *2017 International Conference on Power System Transients*, 2017.
- [22] ABB AB FACTS, "Series capacitors for increased power transmission capacity in the Finnish 400 kV grid," Västerås, 2009.
- [23] R. Grünbaum, G. Ingeström, B. Ekehov, and R. Marais, "765 kV series capacitors for increasing power transmission capacity to the Cape Region," in *IEEE Power and Energy Society Conference and Exposition in Africa: Intelligent Grid Integration of Renewable Energy Resources, PowerAfrica 2012*, 2012.
- [24] Y. Song, X. Wang, and F. Blaabjerg, "Impedance-Based High-Frequency Resonance Analysis of DFIG System in Weak Grids," *IEEE Trans. Power Electron.*, vol. 32, no. 5, pp. 3536–3548, 2017.
- [25] I. Vieto and J. Sun, "Damping of subsynchronous resonance involving Type-III wind turbines," in *2015 IEEE 16th Workshop on Control and Modeling for Power Electronics, COMPEL 2015*, 2015.
- [26] R. Hiremath and T. Moger, "Comparison of LVRT Enhancement for DFIG-Based Wind Turbine Generator with Rotor-Side Control Strategy," in *International Conference on Electrical and Electronics Engineering, ICE3 2020*, 2020, pp. 216–220.
- [27] L. Fan and Z. Miao, "Nyquist-stability-criterion-based SSR explanation for type-3 wind generators," *IEEE Trans. Energy Convers.*, vol. 27, no. 3, pp. 807–809, 2012.
- [28] I. Vieto and J. Sun, "Impedance modeling of doubly-fed induction generators," in *2015 17th European Conference on Power Electronics and Applications, EPE-ECCE Europe 2015*, 2015.
- [29] P. Pourbeik, R. J. Koessler, D. L. Dickmader, and W. Wong, "Integration of Large Wind Farms into Utility Grids (Part 2 - Performance Issues)," in *2003 IEEE Power Engineering Society General Meeting, Conference Proceedings*, 2003, vol. 3, pp. 1520–1525.
- [30] R. K. Varma, S. Auddy, and Y. Semsedini, "Mitigation of subsynchronous resonance in a series-compensated wind farm using FACTS controllers," *IEEE Trans. Power Deliv.*, vol. 23, no. 3, pp. 1645–1654, 2008.
- [31] D. H. R. Suriyaarachchi, U. D. Annakkage, C. Karawita, and D. A. Jacobson, "A procedure to study sub-synchronous interactions in wind integrated power systems," *IEEE Trans. Power Syst.*,

- vol. 28, no. 1, pp. 377–384, 2013.
- [32] R. Nath and C. Grande-Moran, “Study of Sub-Synchronous Control Interaction due to the interconnection of wind farms to a series compensated transmission system,” *Proc. IEEE Power Eng. Soc. Transm. Distrib. Conf.*, pp. 1–6, 2012.
- [33] D. Kidd and P. Hassink, “Transmission operator perspective of Sub-Synchronous Interaction,” in *Proceedings of the IEEE Power Engineering Society Transmission and Distribution Conference*, 2012.
- [34] L. Fan, “Modeling Type-4 Wind in Weak Grids,” *IEEE Trans. Sustain. Energy*, vol. 10, no. 2, pp. 853–864, 2019.
- [35] J. Z. Zhou, H. Ding, S. Fan, Y. Zhang, and A. M. Gole, “Impact of short-circuit ratio and phase-locked-loop parameters on the small-signal behavior of a VSC-HVDC converter,” *IEEE Trans. Power Deliv.*, vol. 29, no. 5, pp. 2287–2296, 2014.
- [36] Y. Li, L. Fan, and Z. Miao, “Stability Control for Wind in Weak Grids,” *IEEE Trans. Sustain. Energy*, vol. 10, pp. 2094–2103, 2019.
- [37] L. Fan and Z. Miao, “Wind in Weak Grids: 4 Hz or 30 Hz Oscillations?,” *IEEE Trans. Power Syst.*, vol. 33, no. 5, pp. 5803–5804, 2018.
- [38] Y. Li, L. Fan, and Z. Miao, “Wind in Weak Grids: Low-Frequency Oscillations, Subsynchronous Oscillations, and Torsional Interactions,” *IEEE Trans. Power Syst. (early access)*, 2019.
- [39] Y. Huang, X. Yuan, J. Hu, and P. Zhou, “Modeling of VSC Connected to Weak Grid for Stability Analysis of DC-Link Voltage Control,” *IEEE J. Emerg. Sel. Top. Power Electron.*, vol. 3, no. 4, pp. 1193–1204, Dec. 2015.
- [40] J. Hu, Y. Huang, D. Wang, H. Yuan, and X. Yuan, “Modeling of grid-connected DFIG-based wind turbines for dc-link voltage stability analysis,” *IEEE Trans. Sustain. Energy*, vol. 6, no. 4, pp. 1325–1336, Oct. 2015.
- [41] N. P. W. Strachan and D. Jovcic, “Stability of a variable-speed permanent magnet wind generator with weak AC grids,” *IEEE Trans. Power Deliv.*, vol. 25, no. 4, pp. 2779–2788, 2010.
- [42] X. Li, J. Liang, G. Li, and T. Joseph, “Modeling and Stability Analysis of the Sub-synchronous Interactions in Weak AC Grids with Wind Power Integration,” *Proc. - 2018 53rd Int. Univ. Power Eng. Conf. UPEC 2018*, pp. 1–6, 2018.
- [43] B. Huang, H. Sun, Y. Liu, L. Wang, and Y. Chen, “Study on subsynchronous oscillation in D-PMSGs-based wind farm integrated to power system,” *IET Renew. Power Gener.*, vol. 13, no. 1, pp. 16–26, 2018.
- [44] H. Liu *et al.*, “Subsynchronous Interaction between Direct-Drive PMSG Based Wind Farms and Weak AC Networks,” *IEEE Trans. Power Syst.*, vol. 32, no. 6, pp. 4708–4720, 2017.
- [45] H. B. P. Schmidt, ““Die dezentrale Bahnenergieversorgung von 162/3-Hz Einphasenwechselstrombahnen über synchron-synchronumformer,” *Elektr. Bahnen*, vol. 11, no. 89, pp. 179–181, 1991.
- [46] GEL/9/3, “Standard EN 50388: Railway Applications. Power supply and rolling stock. Technical criteria for the coordination between power supply (substation) and rolling stock to achieve interoperability,” 2012.

-
- [47] National Grid ESO, “Appendices to the Technical Report on the events of 9 August 2019,” London, 2019.
- [48] L. Brand and L. Xu, “Challenges for SVCs and power electronic based system in close vicinity to each other,” in *CIGRE Session 2018*, 2018.
- [49] A. E. Leon and J. A. Solsona, “Sub-synchronous interaction damping control for DFIG wind turbines,” *IEEE Trans. Power Syst.*, vol. 30, no. 1, pp. 419–428, 2015.
- [50] L. G. Meegahapola, S. Bu, D. P. Wadduwage, C. Y. Chung, and X. Yu, “Review on Oscillatory Stability in Power Grids with Renewable Energy Sources: Monitoring, Analysis, and Control using Synchronphasor Technology,” *IEEE Trans. Ind. Electron.*, pp. 1–1, Jan. 2020.
- [51] J. Shair, X. Xie, L. Wang, W. Liu, J. He, and H. Liu, “Overview of emerging subsynchronous oscillations in practical wind power systems,” *Renew. Sustain. Energy Rev.*, vol. 99, pp. 159–168, 2019.

3. REVIEW OF MITIGATION SOLUTIONS FOR EMERGING SSO PHENOMENA

3.1. INTRODUCTION

Chapter 2 described the emerging SSO phenomena DFIG-SSR, SSCI-CGI and SSCI-CGI. The goal of this Chapter is to review the existing approaches in literature for mitigating DFIG-SSR and to investigate their limitations and recognised application boundaries. Some of these solutions also have the capability to mitigate SSCI. Whenever this is the case, it will be stated in this review. It is worth noting that not all of the mitigation solutions that are published in literature are actually implemented in practical applications. Furthermore, the commercial nature of vendors' intellectual property gives only limited, if any at all, insights in the exact solution implemented to meet the damping requirements as stipulated in grid codes. The selection criterion for including mitigation solutions available in scientific literature in the review below is based on whether the solution is only theoretical or also practical. Those theoretical solutions are included in the review, which deem to be most relevant and promising. These solutions are not yet implemented in practical applications mainly due to their technology readiness level. However, the solutions are emerging research lines and need to be mentioned. Practical solutions are selected if they are at least designed and considered for real SSO phenomena.

In this thesis, the mitigation solutions available in literature are categorised based on their geographical location of implementation. The Control Solution, Hardware Solution and System Level Coordination categories are proposed as shown in Figure 3.1. Control solutions are defined in this thesis as control modifications or new control concepts that are deployed in the rectifier or inverter control of the PEID. Examples of control solutions include a supplementary damping controller in the PEID control [1] and parameter tuning of the existing control [2]. Hardware solutions are defined as those solutions that require additional hardware to be installed at either the high voltage side of the coupling transformer (system operator's grid) or at the low voltage side of the coupling transformer.

Parts of this Chapter are published in V. N. Sewdien, X. Wang, J. L. Rueda Torres, and M. A. M. M. van der Meijden, "Critical Review of Mitigation Solutions for SSO in Modern Transmission Grids," *Energies*, vol. 13, no. 13, p. 3449, 2020.

Hardware solutions are divided into FACTS controllers and other VSC based methods. Examples of hardware solutions are a STATCOM [3] and a TCSC [4]. Finally, solutions based on system level coordination are defined as control actions that require coordination between the PEID behaviour and the changing grid response. Examples of such solutions are adaptive control (gain scheduling) based on wide area measurements [5] and protection [6]. The solutions of each category that are reviewed in this Chapter are shown in Figure 3.2.

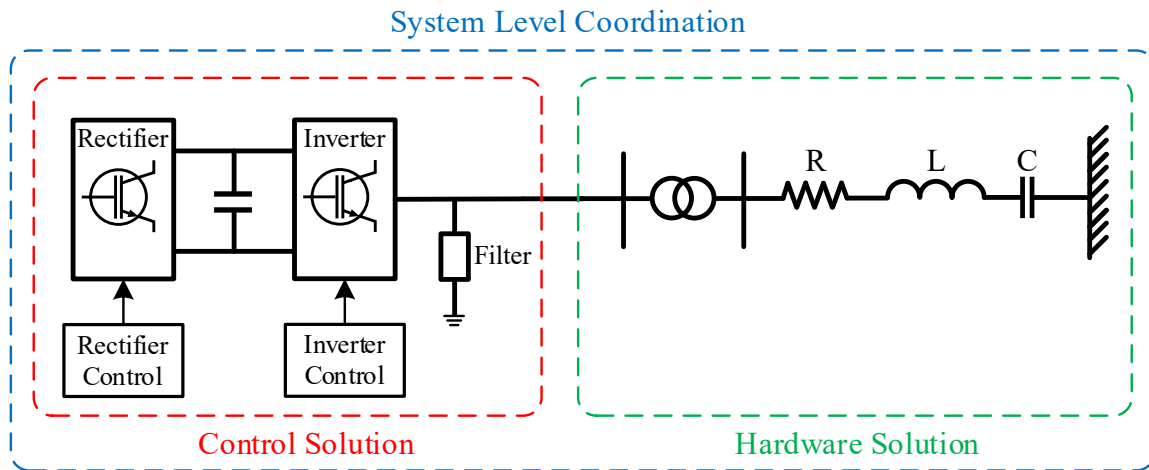


Figure 3.1 Proposed framework for mitigation solutions.

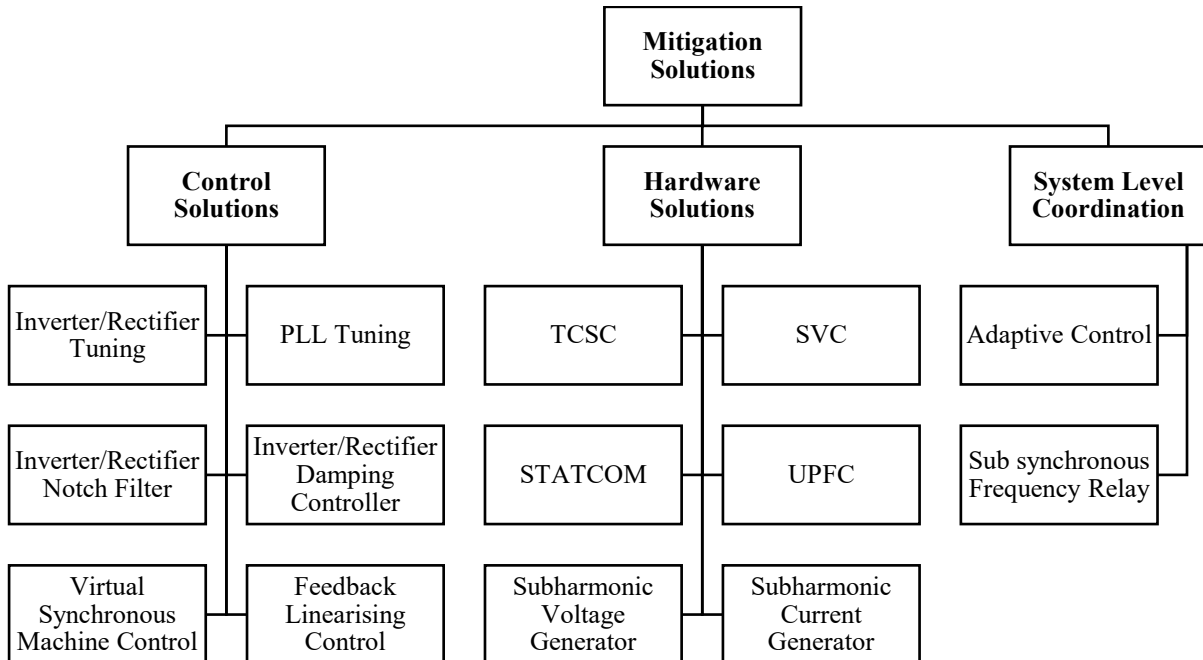


Figure 3.2 Overview of mitigation solutions for DFIG-SSR, SSCI-CGI and SSCI-CCI.

3.2. CONTROL SOLUTIONS

The control solutions category focuses on the rectifier and inverter control (see Figure 3.3) and consists of three main possibilities. The first and most straightforward is the tuning of the parameters of the converter control. It is the most practical and least intrusive option. The converter control parameters influence the PEID's impedance response and therefore the resonance behaviour of the overall system. In some cases, parameter tuning can alter the PEID's impedance response in such a way that adverse interactions can be mitigated. The goal of the parameter tuning is to tune the inherent design parameters to give the best damping performance. The second possibility is the modification of the converter's existing control scheme, where this modification can be achieved by adding supplementary control functions in the already existing converter control. Such supplementary control schemes can damp out oscillations that result from DFIG-SSR or even prevent sub synchronous currents from flowing in to the rotor. The third control solution possibility is the most intrusive one and consists of replacing the existing converter control scheme with an entirely new control concept. With the upcoming deployment of grid forming control, this category of control solutions is emerging.

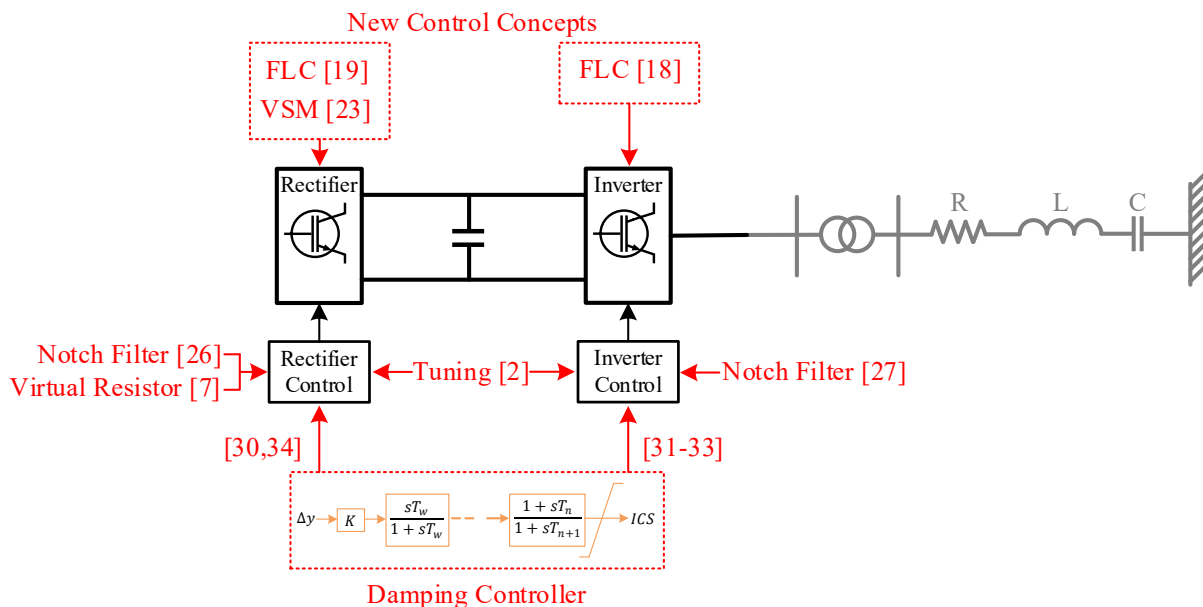


Figure 3.3 Overview of reviewed potential control solutions.

3.2.1. TUNING OF CONVERTER CONTROLLER PARAMETERS

The generic control schemes of the inverter and the rectifier are shown in Figure 3.4, respectively Figure 3.5. As was discussed in Chapter 2, the DFIG impedance has a major influence on DFIG-SSR. It was argued that Z_{DFIG} can be approximated by the rotor side impedance Z_{RS} [7]–[9]. From (2.10) it is clear that the rectifier impedance Z_{RSC} influences Z_{RS} . With Z_{RSC} being determined by its control parameters, it is evident that the rectifier control parameters influence DFIG-SSR.

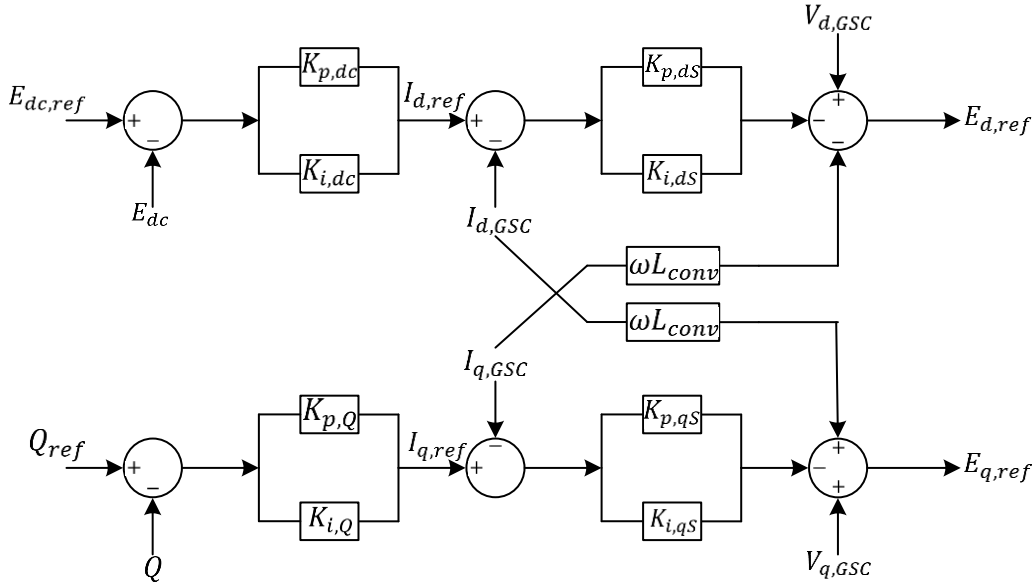


Figure 3.4 Generic inverter control of a DFIG.

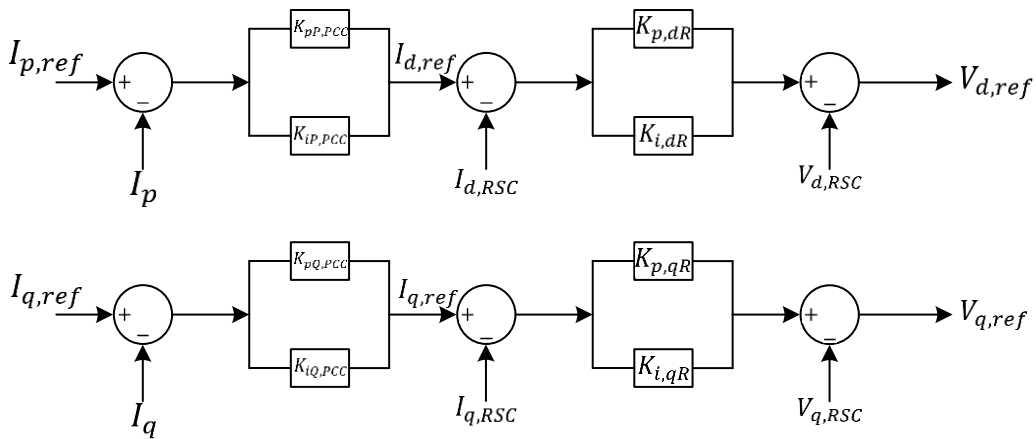


Figure 3.5 Generic rectifier control of a DFIG.

Practical controllers adopt a double-loop control (DLC) structure, and use vector control (VC) with a stator aligned reference frame, containing the d -axis and q -axis control. In renewable energy applications the goal is to harvest maximum active power and therefore the rectifier is generally equipped with a maximum power point tracking control. The goal of the rectifier is to extract this maximum active power (d -axis) and regulate the stator reactive power (q -axis). The d -axis control therefore is equipped with active power control (see Figure 2.13). With the rectifier in active power control, the inverter controls the DC-link through a DC-link voltage control (d -axis) and the terminal voltage (q -axis). In this way, the inverter regulates the power exchange with the grid at the PCC.

Tuning of control parameters is a cost-effective way to mitigate DFIG-SSR and tuning of the rectifier and inverter control parameters was performed for a real application in [2]. The tuning was performed based on a small-signal model of the DFIG connected to an infinite bus system. Eigenvalue analysis identified six SSO modes and the associated state variables were

found using participation factor analysis. The tuning was formulated as an optimisation problem, with the objective to maximise the damping of the identified six modes by considering different values for the eight proportional and eight integral gains of the inverter and rectifier controls (see Figure 3.4 and Figure 3.5). The optimisation results were validated using time domain simulations and it was found that the optimised set of parameters was able to damp all six SSO modes for a range of active power output levels.

To solve SSCI-CGI, parameter modification was carried out in [10]. To mitigate SSCI-CCI, tuning based on trial and error time domain simulations was performed in [11]. Finally, a new index to observe how the severity of the SSCI-CCI modes changes with varying control parameters was developed in [12]. The influence of the PLL gains on SSCI-CGI was investigated in [13]–[17] and it was shown that adequate PLL bandwidths can mitigate SSCI-CGI. Tuning PLL parameters for mitigating DFIG-SSR and SSCI-CCI is yet to be investigated.

In general, controller tuning is perceived as the preferred solution to mitigate SSO, as it does not require additional hardware devices or adaptation of existing control schemes. Yet, it is not always practical for two main reasons. First, controller tuning should result in a set of optimised parameters that is able to mitigate DFIG-SSR across a wide set of operational scenarios. This includes among others different levels of grid damping and different wind power plant dispatch levels. The optimisation that was performed in [2] resulted in a set of parameters where one of the DFIG-SSR modes was unstable for wind power plant dispatch levels below 25%. Second, controllers are designed to satisfy a wide range of operational and design requirements, such as fault ride through (FRT) capability and power quality. Optimising the PEID's response to mitigate DFIG-SSR or SSCI will come at the expense of e.g. decreased power quality or a slower dynamic response of the converter. The slower dynamic response due to tuning of the parameters is shown in Chapter 6.4.3. Hence, a multi-objective optimisation is needed for tuning the controller parameters of PEIDs in modern power grids.

3.2.2. FEEDBACK LINEARISATION CONTROL

The analysis performed in [2] showed that the optimisation of the DLC parameters was not able to define a set of parameters that mitigates DFIG-SSR across all credible operating conditions. To address this challenge, the partial Feedback Linearisation Control (FLC) was designed for the DFIG's inverter in [18]. This new control scheme replaced the inverter's classical DLC. The partial feedback linearisation is a model-based method to design non-linear controllers. The control is performed in two steps. First, the non-linear system is linearised via feedback to produce a linear system. In the next step, a linear controller is designed to operate the linearised system developed in the first step. The impedance of the DFIG with partial FLC was analysed and it was found that the damping was positive across the entire sub synchronous frequency range. Eigenvalue analysis further revealed that when using partial FLC, the overall system only had an unstable DFIG-SSR mode for compensation degrees higher than 90%. Finally, time domain EMT simulations showed that a DFIG equipped with partial FLC was able to provide adequate damping for DFIG-SSR, while respecting FRT requirements.

One of the main advantages of the partial FLC is that due to the conversion of a non-linear system into a partial linear one, it makes the system independent of the operating point. This is

advantageous for non-linear systems such as a DFIG. Also, the operating point-independent characteristic of the designed partial FLC addresses the optimisation deficiency of [2]. The partial feedback linearisation method was also used in [19] to design a non-linear damping controller in the DFIG's rectifier. The electrical damping of the DFIG with and without the damping controller was determined and compared. In the frequency range up to 20 Hz and between 50 and 60 Hz, the electrical damping response of the DFIG with damping controller was superior. Between 20 and 50 Hz the electrical damping response of the DFIG without damping controller was slightly better.

Although the FLC does not require access to the full model dynamics of the DFIG, its performance is directly influenced by the accuracy of the available DFIG model. The performance can be enhanced by reducing the uncertainties associated with model inaccuracies. One way to achieve this is through a sliding mode control (SMC) [20]. However, a shortcoming of the SMC is that it is operating condition-specific. Considering the same operating condition, the SMC has an improved performance compared to the FLC. To cope with uncertainties related to both the operating condition and model accuracy, the FLC and SMC are combined in [21], [22]. The effectiveness of FLC and SMC in mitigating SSCI is not yet reported.

3.2.3. VIRTUAL SYNCHRONOUS MACHINE

The virtual synchronous machine (VSM) control concept is a type of grid-forming (GF) control and PEIDs with this control concept exhibit dynamic characteristics similar to a conventional synchronous generator. The capability of the VSM control to mitigate DFIG-SSR was studied in [23], where it was implemented in the DFIG's rectifier. Eigenvalue analysis and detailed EMT time domain simulations showed that the VSM exhibited poorer performance, compared to VC. Based on eigenvalue analysis of both control concepts, it was found that VC maintained stability for higher levels of series compensation and lower wind speeds than VSM. When VC was used, the DFIG-SSR mode remained stable up to $k=28\%$. When VSM was used, the mode became unstable for $k>18\%$. The assessment of the wind speed showed that the influence of the wind speed on the difference in the stability margin of both concepts was rather small. With the VC, the DFIG-SSR mode was stable for wind speeds of 12 m/s and larger. With the VSM, stability was achieved for wind speeds of 12.5 m/s and larger.

Finally, under the same operating condition, the VC showed better damping of DFIG-SSR than the VSM. This can be explained by the fact that with VC, rotor current transients are fully controlled by the converter's inner current control, whereas with the proposed VSM, the control of the rotor current transients is achieved only through a current limiter [23]. The current limiting capability of the VSM was provided by a passive resistance, which inherently has a poorer transient performance than an active DLC based current control.

VSM control concepts are developed for HVDC applications in [24] and for multi-terminal DC systems in [25]. However, their capability to mitigate SSCI still needs to be investigated.

3.2.4. DIGITAL FILTERS

Digital filters block sub synchronous currents from flowing in to the rotor and consequently, negative resistances are not observed. To mitigate DFIG-SSR, a second-order

notch filter in the rectifier was designed in [26], while in [27] a location-dependent performance index was developed with the aim to identify the best location in the converter control for placing a digital filter. Using this index, the rectifier's d -axis inner current loop and the inverter's d -axis outer voltage loop were identified as the most suitable locations. Time domain EMT simulations showed the capability of the designed filter to mitigate DFIG-SSR for a fixed operating condition. Superior performance was observed when the notch filter was implemented in the rectifier as well as in the inverter, instead of only in the rectifier. A major drawback of the designed notch filter is that it is tuned for a small frequency range (6.17-8.42 Hz), whereas the frequency at which DFIG-SSR occurs can be outside this range. This limitation could explain why the use of notch filters for this purpose is limited in practice.

To increase the rectifier damping within a predefined frequency range, a scheme based on a virtual resistor in the rectifier is designed in [7]. The performance of this scheme was compared with controller parameter tuning (as discussed in Section 3.2.1) and with a virtual resistor in the inverter. The results showed that the virtual resistor in the rectifier yields the best performance, as the damping is directly influenced. The damping can also be influenced indirectly by adding an integral gain in the current control of the rectifier [28], which has the same effect of adding a virtual series inductance. As a result, the resonance frequency will decrease and DFIGs have a larger damping at lower frequencies.

3.2.5. SUPPLEMENTARY DAMPING CONTROLLER

A supplementary damping controller (SDC) is an auxiliary controller that can be added in the rectifier or inverter of a PEID or in the inverter of FACTS controllers (FACTS controllers are discussed in Section 3.3.1) with the goal to damp oscillations. The control structure of a generic lead-lag SDC is shown in Figure 3.6. It is worth noting that other types of SDCs such as a multi-band or artificial intelligence based SDCs also exist. The design and application description of these types is limited and is a research gap in existing literature. However, within the objective of the current research, the generic lead-lag SDC is sufficient for the fundamental qualitative assessment.

Consider the SDC of Figure 3.6. The input Δy of the SDC passes through a gain, a washout filter and lead-lag compensation blocks. The output of the SDC is denoted as 'input control signal' (ICS) and is fed into the rectifier and/or inverter as an additional signal.

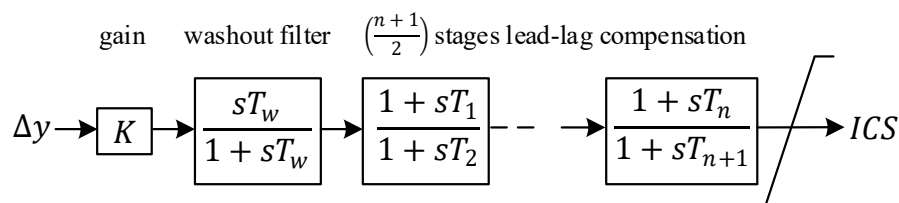


Figure 3.6 Control structure of a generic supplementary damping controller.

Several signals can be used for Δy . Examples include the active power output [29], the DFIG's rotor speed deviation $\Delta\omega_m$ [30], the line current I_{line} [29] and the voltage across the series capacitor V_C . In [31] an SDC is developed using the observed-state feedback control. The

advantage of this method is that the SDC is not limited to any specific input and therefore local measured signals can be used. The corresponding ICS was supplied to the inverter's q -axis outer control.

The ICS of the SDC can be supplied as a feedback signal to either the inverter (e.g. [31]–[33]) or the rectifier (e.g. [30], [34]), whereas the SDC developed in [35] provides the feedback signal to both. When the influence of the SDC location on the damping capability is assessed, the inverter is perceived as a more suitable location. The DFIG's inverter with SDC is conceptually similar to a STATCOM with its inverter, of which the latter is known to have excellent damping capabilities [36].

The efficiency of the SDC depends to a large extent on the proper design of SDC parameters. Two widely used methods for the design of SDC parameters are the residue-based method using the B and C matrices of the linearised system equations [37] and parameter optimisation based on time domain simulations [38]. The residue based analysis in [39] showed that an SDC utilising $\Delta\omega_m$ or I_{line} as the input, destabilises any present supersynchronous mode. When using V_C as input to the SDC, both sub- and super-synchronous oscillation modes can be stabilised. While most of the research work focused on mitigating DFIG-SSR in a single wind power plant, SDCs are designed for multiple wind power plants in [1] to mitigate different DFIG-SSR modes.

When assessing the effectiveness of the residue-based and time domain optimisation methods, one major limitation is observed: both methods are unable to efficiently consider a wide range of operating conditions in the SDC parameter tuning process. To tackle this, three solutions are reported in literature. First, an improved particle swarm optimisation considering different levels of series compensation is proposed in [34]. Second, a probabilistic SDC design method is proposed in [40]. And lastly, to obtain the optimised performance across multiple operating conditions, concepts for real-time adaptive damping controllers were developed using the wind speed [41], the level of series compensation [42] and the number of in-service wind turbines [43].

While these tuning methods can identify the SDC parameters that mitigate DFIG-SSR under different wind speeds and series compensation levels, they fail to incorporate the different grid topologies in their optimisation problem. It is useful to include different grid damping levels in the formulation of the optimisation problem, as different grid topologies and load levels (i.e. grid damping) are realistic and expected operational variables.

3.3. HARDWARE SOLUTIONS

Hardware solutions encompass those solutions that require hardware to be installed in the system operator's grid (see Figure 3.7). These solutions can be broadly divided into FACTS controllers and other VSC based methods.

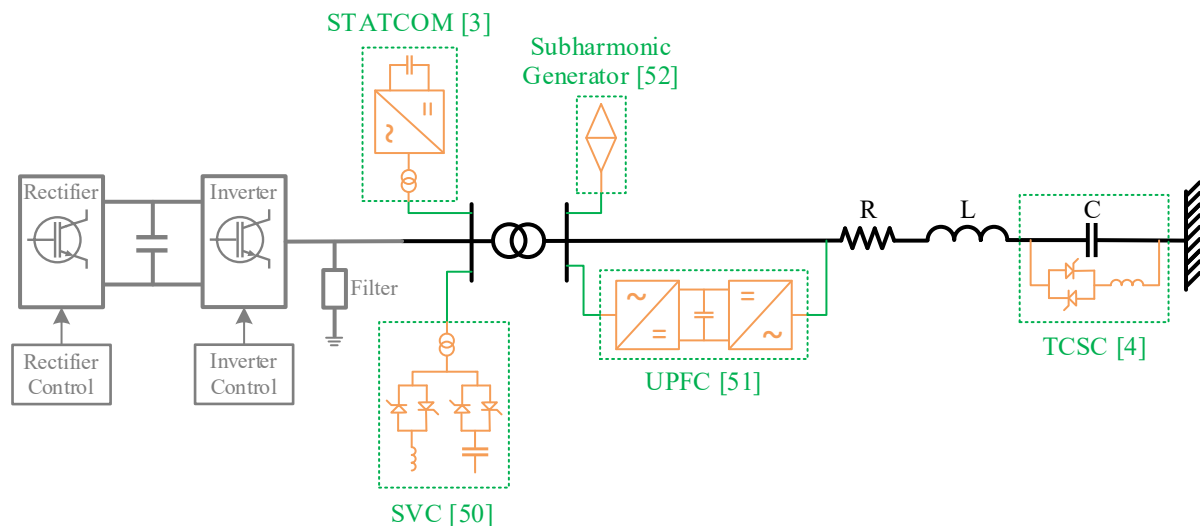


Figure 3.7 Overview of reviewed hardware solutions.

3.3.1. FACTS

FACTS controllers are generally used to assist in the control of voltages and power flows in AC power systems. The IEEE defines FACTS as “*alternating current transmission systems incorporating power electronic-based and other static controllers to enhance controllability and increase power transfer capability*” [44], [45]. Based on a survey conducted among different system operators and network owners, an overview of different installed FACTS controllers was created, which is shown in Table 3.1 [46]. Where known, the number of FACTS controllers is mentioned in brackets. These FACTS controllers have a wide range of application, including damping of oscillations (Colombia), compensation of voltage unbalances due to traction load (South Africa), reduction of transmission losses (India) and increased power transfer capability (Peru). A detailed description of FACTS controllers is given in [47].

FACTS controllers that are installed with the aim of mitigating DFIG-SSR have to be equipped with an SDC to provide the required damping. An exception is the TCSC, which, when the control scheme is designed for this purpose, provides immunity against DFIG-SSR. The constant reactance control scheme was designed for the TCSC that was commissioned at the 500 kV Slatt substation [48]; the synchronous voltage reversal control strategy was deployed in the TCSC that was installed in the 345 kV Kanawha River substation [49]. Whereas DFIG-SSR risk would limit the degree of compensation that is achievable using fixed series capacitors (see Chapter 5.3.2), the TCSC’s immunity against DFIG-SSR removes this limit for practical applications. Successful mitigation of DFIG-SSR using a TCSC is described in [4].

An SVC with an SDC was developed in [50]. The SVC was installed at the low voltage side of the coupling transformer and its primary goal was to provide voltage support. The input of the SDC was the active power flow through the transmission line, which was calculated from the measured current and voltage at the SVC connection point. The damping control scheme included a functionality to adapt the gain as a function of the wind speed. This adaptive functionality made the SDC effective in damping DFIG-SSR across the full wind speed spectrum.

Table 3.1 Overview of FACTS controllers in 12 regions [46].

Region	FACTS	Region	FACTS
Australia (South)	SVC	India	STATCOM (7) SVC (1) TCSC (6)
Chile	STATCOM SVC	Japan	STATCOM
China	SVC UPFC	Norway	STATCOM (1) SVC (10)
Colombia	STATCOM (1) SVC (3)	Peru	STATCOM(1) SVC (11)
Germany	TCSC (1)	South Africa	STATCOM (1) SVC (3)
Gulf Cooperation Council	SVC TCSC	South Korea	STATCOM (6) SVC (3) UPFC (1)

When comparing the performance of the series connected TCSC with the shunt connected SVC, it was observed that the series device is superior in mitigating DFIG-SSR. This is confirmed by [51], where the shunt and series inverter of an unified power flow controller (UPFC) were equipped with an SDC. The UPFC was designed as a static synchronous series capacitor (SSSC) and a STATCOM. The SSSC and STATCOM were coupled together through a common DC-link. The series inverter belongs to the SSSC, whereas the shunt inverter belongs to the STATCOM. Both inverters are able to operate independently. The UPFC was installed in the transmission line on the high voltage side of the coupling transformer with the goal to mitigate DFIG-SSR. It was found that the SDC in the series inverter was able to damp out oscillations faster than the SDC in the shunt inverter, whereas the best damping response was obtained when SDCs were installed in both inverters. The analyses were performed for different wind speeds and degrees of compensation.

An SDC-equipped STATCOM was designed in [3] for mitigating DFIG-SSR. The STATCOM was installed on the low voltage side of the coupling transformer. The input for the SDC was chosen to be the rotor speed deviation $\Delta\omega_m$. The STATCOM controller produces a modulation index and phase angle difference signal and the best stabilising performance was achieved when the ICS was added to the modulation index. Eigenvalue analysis showed that without the STATCOM, undamped oscillations would occur for compensation degrees in excess of 50%. With the developed STATCOM, instability only occurred when the transmission line was compensated for 90% and the power level was maximum (500 MW). A major challenge with this solution is the requirement to establish a stable communication link between the DFIG and the STATCOM to transfer the rotor speed deviation with as little latency as possible.

Although FACTS controllers are able to mitigate DFIG-SSR, a major drawback of any FACTS based solution is that it requires capital intensive investments. If on top of the DFIG-SSR mitigation, additional system services such as voltage support are required, the SVC and STATCOM are good solutions. In all other cases, more cost-effective solutions exist. When

a risk for DFIG-SSR is identified in the design stage, the fixed series capacitor can be designed using the phase imbalance concept (as will be discussed in Chapter 5) or be replaced by a TCSC. Replacing an FSC before the end of its lifetime is not a cost-effective measure.

Some observations can be made with regards to the applicability of the control solutions presented in Section 3.2 in FACTS controllers. First, parameter tuning of FACTS controllers is already being used. Especially when a FACTS controller is added with the goal of mitigating DFIG-SSR, its performance is tuned with this objective in mind. Second, FACTS controllers such as STATCOMs can already be designed with supplementary controllers such as an SDC. Thirdly, the design of grid forming control for FACTS controllers is an emerging research topic, albeit that descriptions of grid forming control based FACTS controllers in real applications are rare. An industrialised energy storage system (which is fundamentally similar to a STATCOM) equipped with the VSM grid forming control concept is operational in Australia. The damping behaviour of the device is not reported, but the grid forming capabilities were validated using field tests and are described in [52]. Finally, no design or application descriptions of FLC and digital filters in FACTS controllers were found in literature. This is identified as another research gap.

For SSCI-CGI, the probability of the adverse interactions is inversely proportional to the grid strength. Therefore, FACTS controllers that increase the system strength also contribute to mitigate SSCI, albeit that publications covering this are rare. Caution should be taken as FACTS controllers installed for mitigating SSCI-CGI could lead to SSCI-CCI as was discussed in Chapter 2.5.

3.3.2. OTHER VSC-BASED SOLUTIONS

Except for the TCSC, FACTS controllers mitigate DFIG-SSR through an SDC, which in real power systems would only be a secondary goal of such a device. Commissioning a FACTS controller only for DFIG-SSR mitigation is not a cost-effective solution. Therefore, other independent VSC based methods were developed. A grid side sub synchronous damping controller was developed in [53]. It was installed at the high voltage side of the coupling transformer. This controller is a shunt device and consists of a controlled current source, governed by a damping calculator and a VSC based subharmonic current generator. The calculator extracts the sub synchronous modes from the bus voltage and line current. Control signals based on the extracted sub synchronous modes are used as input to the current generator, which then injects subharmonic currents in the power system to stabilise DFIG-SSR. Eigenvalue analysis and time domain simulations showed the stable behaviour of this solution across a wide range of operating conditions. Time domain simulations were performed for different operating conditions such as switching of the series capacitor, abrupt wind speed changes, three phase faults and changes in the degree of compensation. The controller showed satisfactory performance under all of these operating conditions.

One of the major drawbacks of this solution is that it has limited controllability compared to a STATCOM or an SVC. The STATCOM and SVC provide controllability at the fundamental frequency and provide damping for sub synchronous oscillations. The fundamental frequency operation enables these FACTS controllers to also contribute to system strength, making them capable of addressing DFIG-SSR as well as SSCI. The grid side sub

synchronous damping controller on the other hand is a special purpose controller that operates only in the sub synchronous frequency range and can only be used to tackle DFIG-SSR [53]. The grid side sub synchronous damping controller is expected to be implemented in the Guyuan power system in China.

An innovative solution for mitigating classical SSR using a battery energy storage system (BESS) was designed in [54], where an SDC was added to the inverter of the BESS. Although this solution was designed to mitigate classical SSR, the concept could also be used for mitigating DFIG-SSR. The BESS can then also provide frequency support, where operational procedures would be needed that describe the priority for either DFIG-SSR mitigation or frequency support, in case both events happen simultaneously.

3.4. SYSTEM LEVEL COORDINATION

With the increasing number of electrically close PEIDs, SSO solutions based on tuning of individual control parameters may eventually get exhausted. In such cases, system level coordination can help to mitigate SSO in a rather unconventional way. For this solution, control actions are taken based on some level of coordination between the PEID and the power system and/or atmospheric conditions. As illustrated in Figure 3.8, the control based on system level coordination can be implemented in the PEID or in the grid. Examples of such solutions are active disturbance rejection control (ADRC), multiple model adaptive control (MMAC) and protection.

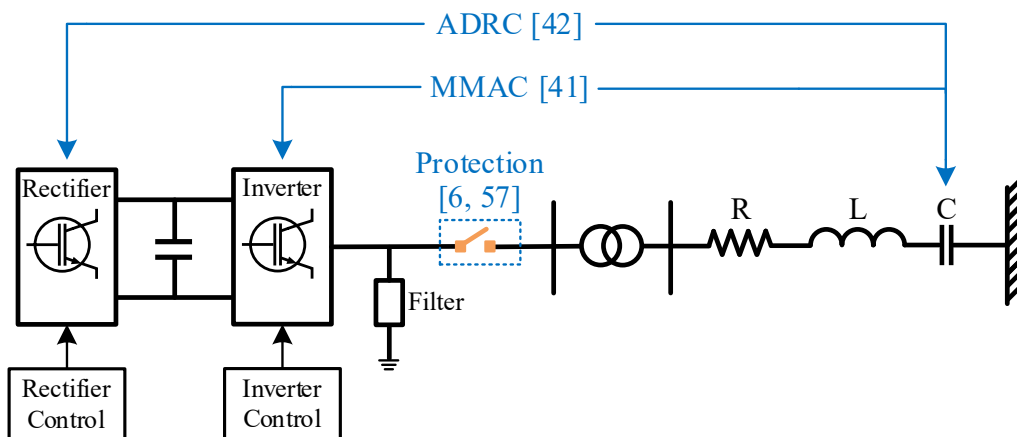


Figure 3.8 Overview of reviewed system level coordination-based solutions.

3.4.1. ADAPTIVE CONTROL

Adaptive controllers have the capability to change their controller parameters to adapt to changes in a process that occur with time. In the context of SSO, such changes consist of variations in the wind speed, the level of series compensation and the grid impedance. By now, it is known that the damping requirements for DFIG-SSR vary as a function of the wind speed and the degree of series compensation. High wind speeds impose lower damping requirements than low wind speed conditions. On the other hand, the higher the degree of series compensation, the higher the damping requirements for suppressing DFIG-SSR. Finally, as was

shown in Chapter 2.4, the SSCI-CGI mode is highly sensitive to the grid impedance (SCR), and using adaptive PLL parameters, it was possible to keep the SSCI-CGI mode stable under different grid strength conditions.

An MMAC approach was used in [41] to design an SDC for mitigating DFIG-SSR. The SDC has the same structure as Figure 3.6. The MMAC consisted of two layers. The first layer contained multiple SDCs, where the parameters of each SDC were optimised to deliver adequate damping under predefined wind speeds and compensation degrees. Different permutations of wind speed and compensation degree resulted in a wide range of operating conditions, where for each operating condition an optimised SDC was designed using the root locus method.

The second layer was the supervisory controller and was used to determine the operating condition of the system. After the supervisory controller determined the operating condition, the first level controller selected the corresponding SDC parameters. The degree of series compensation was determined based on the capacitor voltage and the wind speed was assumed to be given. The capacitor voltage was used as input for the SDC and the ICS was fed into the terminal voltage control of the inverter. Eigenvalue analysis and time domain EMT simulations confirmed the effective mitigation of DFIG-SSR under a wide range of operating conditions. However, a major drawback in the implementation of this concept is that the wind speed is assumed to be known, which is not a valid assumption for real applications. Without knowledge of the wind speed, the MMAC strategy will not work. The gain scheduling control developed in Chapter 6 of this thesis tackles this shortcoming by forecasting the wind speed.

Another solution based on adaptive control is developed in [42], where the authors developed the “active disturbance rejection control” (ADRC) to operate adequately across different levels of series compensation. The control was implemented in the d -axis and q -axis inner loop of the DFIG rectifier. A final example of adaptive control is given in [43] and takes into account the compensation degree as well as the outage status of the WTGs in the wind power plant. This adaptive damping controller was implemented in the wind park control.

The adaptive control concepts discussed so far were implemented in the PEID in either the DFIG’s inverter and rectifier control or in the wind park control. In [5], a synchrophasor data based gain scheduling control of an SDC in a TCSC was designed. The power system consisted of several DFIG-based wind power plants and the SDC and TCSC were designed to mitigate DFIG-SSR as well as torsional interactions. The SDC gains were dynamically adjusted based on measurements at several wind power plants and it was concluded that the proposed concept performed better than local TCSC control. Although its superior performance, the proposed solution required a wide-area measurement system, which is not common practice for many system operators. Furthermore, the reliability, accuracy and speed of the communication link will have a critical impact on the TCSC’s damping response and need further investigation. Considering the aforementioned adaptive controllers, the main challenge is how to timely and adequately determine the grid damping, the wind speed, and the number of in-service WTGs.

Finally, in [55] an adaptive PLL was proposed for mitigating SSCI-CGI, in which the inverter’s PLL gains were adjusted in real-time as a function of the grid impedance. The adaptive characteristic ensured that a predefined stability margin was maintained across different grid strength conditions. A method was also proposed to calculate the actual grid impedance at fundamental frequency using the measured voltages and currents. The major

drawback of this approach is that the calculated grid impedance always lags behind the actual grid impedance due to the required calculation time. In the case of SSCI-CGI, the gain scheduling algorithm may not be able to timely and accurately calculate the grid impedance. It is envisaged that the gain scheduling approach for SSO mitigation will have an improved performance if the grid impedance could be forecasted, or at least if its influence could be *a priori* taken into account. For sake of completeness, a method for the online measurement of the PEID impedance at sub and super synchronous frequencies was developed in [56].

A final note of caution for solutions based on adaptive control is that control parameters are adjusted during the course of operation. It needs to be ensured that the changes in parameter values do not result in small-signal instability.

3.4.2. PROTECTION

The last resort against unstable DFIG-SSR and SSCI is protection. A sub synchronous frequency relay can be used for disconnecting either the wind power plant (in case of DFIG-SSR and SSCI) or the series capacitor (in case of DFIG-SSR). The relay developed in [6] was capable of detecting multiple oscillations between 5 and 25 Hz and issued either alarms or trip commands.

Another protection algorithm for tripping a wind power plant subjected to DFIG-SSR was developed in [57]. The concept was based on three processes. In the first process, offline frequency scans were performed across multiple credible operating conditions to determine decision-making thresholds such as minimum damping. In the second process, continuous online monitoring of system variables was performed. In the last process, the monitored variables were continuously compared with the predefined thresholds. When limit violations were detected, a trip command was issued to the wind power plant. Using this method, oscillations could be detected within 25 ms and the trip signal could be issued in the following 50 ms. The DFIG-SSR detection algorithm in [58] achieved a detection time of maximum 29 ms. A real example where protection solved SSCI-CCI is described in [12].

From the system operation perspective, protection solutions are the most intrusive, as they abruptly disconnect generation and/or change the system topology, thereby transforming a small-signal stability problem to a (more difficult to manage) large disturbance. Therefore, protection solutions should be used as the last resort to mitigate SSO.

3.5. CONCLUSIONS

The goal of this Chapter was to review existing approaches for mitigating DFIG-SSR and to investigate their limitations and recognised application boundaries. Table 3.2 gives an overview of the investigated mitigation solutions and summarises for each of these solutions their capability to mitigate DFIG-SSR and SSCI. Depending on their location of implementation, the investigated mitigation solutions were categorised in three classes: control solutions, hardware solutions and system level coordination. Control solutions were defined as control modifications or new control concepts that are deployed in the rectifier or inverter control of the PEID. Likewise, hardware solutions were defined as those solutions that require

additional hardware to be installed in either the high voltage side or the low voltage side of the coupling transformer. Finally, solutions based on system level coordination were defined as controls that require coordination between the PEID behaviour and the changing grid response or atmospheric conditions.

Table 3.2 Overview of Mitigation Solutions.
X: cannot mitigate SSO, ✓: can mitigate SSO, ?: more research needed.

Mitigation Solution	DFIG-SSR	SSCI-CGI	SSCI-CCI
Control Solutions			
GF Virtual Synchronous Machine	X	?	?
Feedback Linearising Control	✓	?	?
Rectifier Control Tuning	✓	X	X
Inverter Control Tuning	X	✓	✓
Inverter PLL Tuning	X	✓	?
Rectifier Notch Filter	✓	X	X
Inverter Notch Filter	✓	X	X
Rectifier Damping Control	✓	X	X
Inverter Damping Control	✓	X	?
Hardware Solutions			
TCSC	✓	X	X
SVC	✓	✓	X
STATCOM	✓	✓	X
UPFC	✓	✓	X
Subharmonic Voltage Generator	✓	X	X
Subharmonic Current Generator	✓	X	X
System Level Coordination			
Adaptive Control	✓	✓	?
Protection	✓	✓	✓

The review of the existing mitigation solutions helped to shape the current research in different ways. First, the phase imbalance compensation concept is another approach for fixed series compensation and was originally designed in the 1990s to mitigate classical SSR. The capability of this niche concept to mitigate DFIG-SSR is rarely reported in academic literature. In Chapter 5 it will be investigated to what extent the phase imbalance compensation concept can be used as a potential hardware solution to mitigate DFIG-SSR.

Second, adaptive control is increasingly being investigated as a potential solution for various phenomena. Section 3.4.1 identified the research gaps and drawbacks in existing adaptive control philosophies. These include (i) the necessity to have in advance knowledge of the wind speed and grid damping for correct operation of the adaptive control, (ii) the need for a wide area measurement system and (iii) validation that the adaptive characteristic of the multiple-model adaptive control does not result in small-signal instability. These issues have not been addressed yet and will be investigated in Chapters 6-8. These Chapters will describe

the development of a system level coordination solution based on an adaptive control strategy for mitigating DFIG-SSR, taking into account the research gaps and drawbacks mentioned above.

Finally, system operators in multiple jurisdictions are incorporating grid forming control requirements in their grid codes. Several grid forming control schemes exist and the limited amount of published research revealed that the Virtual Synchronous Machine scheme was not able to mitigate DFIG-SSR. With grid forming control becoming more prominent, research is needed to identify whether other grid forming schemes can act as a control solution for mitigating DFIG-SSR. This is left as a topic for future research.

The next Chapter will describe the different methodologies and simulation models that are used in this research.

REFERENCES

- [1] A. E. Leon, "Integration of DFIG-Based Wind Farms into Series-Compensated Transmission Systems," *IEEE Trans. Sustain. Energy*, vol. 7, no. 2, pp. 451–460, 2016.
- [2] A. Chen, D. Xie, D. Zhang, C. Gu, and K. Wang, "PI parameter tuning of converters for sub-synchronous interactions existing in grid-connected DFIG wind turbines," *IEEE Trans. Power Electron.*, vol. 34, no. 7, pp. 6345–6355, 2019.
- [3] A. Moharana, R. K. Varma, and R. Seethapathy, "SSR alleviation by STATCOM in induction-generator-based wind farm connected to series compensated line," *IEEE Trans. Sustain. Energy*, vol. 5, no. 3, pp. 947–957, 2014.
- [4] L. Piyasinghe, Z. Miao, J. Khazaei, and L. Fan, "Impedance model-based SSR analysis for TCSC compensated type-3 wind energy delivery systems," *IEEE Trans. Sustain. Energy*, vol. 6, 2015.
- [5] P. Mahish and A. K. Pradhan, "Mitigating Subsynchronous Resonance Using Synchrophasor Data Based Control of Wind Farms," *IEEE Trans. Power Deliv.*, vol. 35, no. 1, 2020.
- [6] K. Narendra *et al.*, "New microprocessor based relay to monitor and protect power systems against sub-harmonics," *2011 IEEE Electr. Power Energy Conf. EPEC 2011*, pp. 438–443, 2011.
- [7] I. Vieto and J. Sun, "Damping of subsynchronous resonance involving Type-III wind turbines," in *2015 IEEE 16th Workshop on Control and Modeling for Power Electronics, COMPEL*, 2015.
- [8] L. Fan and Z. Miao, "Nyquist-stability-criterion-based SSR explanation for type-3 wind generators," *IEEE Trans. Energy Convers.*, vol. 27, no. 3, pp. 807–809, 2012.
- [9] I. Vieto and J. Sun, "Impedance modeling of doubly-fed induction generators," in *2015 17th European Conference on Power Electronics and Applications, EPE-ECCE Europe 2015*, 2015.
- [10] National Grid ESO, "Technical Report on the events of 9 August 2019," London, 2019.
- [11] L. Brand and L. Xu, "Challenges for SVCs and power electronic based system in close vicinity to each other," in *CIGRE Session 2018*, 2018.
- [12] Y. Xu and Y. Cao, "Sub-synchronous oscillation in PMSGs based wind farms caused by amplification effect of GSC controller and PLL to harmonics," *IET Renew. Power Gener.*, vol. 12, no. 7, pp. 844–850, 2018.
- [13] Y. Li, L. Fan, and Z. Miao, "Stability Control for Wind in Weak Grids," *IEEE Trans. Sustain. Energy*, vol. 10, pp. 2094–2103, 2019.
- [14] L. Fan and Z. Miao, "Wind in Weak Grids: 4 Hz or 30 Hz Oscillations?," *IEEE Trans. Power Syst.*, vol. 33, no. 5, pp. 5803–5804, 2018.
- [15] Y. Huang, X. Yuan, J. Hu, and P. Zhou, "Modeling of VSC Connected to Weak Grid for Stability Analysis of DC-Link Voltage Control," *IEEE J. Emerg. Sel. Top. Power Electron.*, vol. 3, no. 4, pp. 1193–1204, Dec. 2015.
- [16] J. Hu, Y. Huang, D. Wang, H. Yuan, and X. Yuan, "Modeling of grid-connected DFIG-based

- wind turbines for dc-link voltage stability analysis,” *IEEE Trans. Sustain. Energy*, vol. 6, no. 4, pp. 1325–1336, Oct. 2015.
- [17] J. Z. Zhou, H. Ding, S. Fan, Y. Zhang, and A. M. Gole, “Impact of short-circuit ratio and phase-locked-loop parameters on the small-signal behavior of a VSC-HVDC converter,” *IEEE Trans. Power Deliv.*, vol. 29, no. 5, pp. 2287–2296, 2014.
- [18] M. A. Chowdhury, M. A. Mahmud, W. Shen, and H. R. Pota, “Nonlinear Controller Design for Series-Compensated DFIG-Based Wind Farms to Mitigate Subsynchronous Control Interaction,” *IEEE Trans. Energy Convers.*, vol. 32, no. 2, pp. 707–719, 2017.
- [19] M. A. Chowdhury and G. M. Shafiullah, “SSR Mitigation of Series-Compensated DFIG Wind Farms by a Nonlinear Damping Controller Using Partial Feedback Linearization,” *IEEE Trans. Power Syst.*, vol. 33, no. 3, pp. 2528–2538, 2018.
- [20] C. Karunanayake, J. Ravishankar, and Z. Y. Dong, “Nonlinear SSR Damping Controller for DFIG based Wind Generators Interfaced to Series Compensated Transmission Systems,” *IEEE Trans. Power Syst. (early access)*, vol. 35, no. 2, pp. 1156–1165, 2019.
- [21] P. Li, J. Wang, L. Xiong, and M. Ma, “Robust Nonlinear Controller Design for Damping of Sub-Synchronous Control Interaction in DFIG-Based Wind Farms,” *IEEE Access*, vol. 7, 2019.
- [22] P. Li, L. Xiong, F. Wu, M. Ma, and J. Wang, “Sliding mode controller based on feedback linearization for damping of sub- synchronous control interaction in DFIG-based wind power plants,” *Electr. Power Energy Syst.*, vol. 107, pp. 239–250, 2019.
- [23] K. Gu *et al.*, “SSR Analysis of DFIG-Based Wind Farm With VSM Control Strategy,” *IEEE Access*, vol. 7, pp. 118702–118711, 2019.
- [24] J. Roldán-Pérez, J. A. Suul, S. D’Arco, A. Rodríguez-Cabero, and M. Prodanovic, “Virtual synchronous machine control of VSC HVDC for power system oscillation damping,” *Proc. IECON 2018 - 44th Annu. Conf. IEEE Ind. Electron. Soc.*, pp. 6026–6031, 2018.
- [25] Y. Cao *et al.*, “A Virtual Synchronous Generator Control Strategy for VSC-MTDC Systems,” *IEEE Trans. Energy Convers.*, vol. 33, no. 2, pp. 750–761, 2018.
- [26] H. He, D. Lv, L. Wen, W. Lu, H. Geng, and J. Gao, “Analysis and Suppression Strategies of Sub-synchronous Resonance on DFIG,” *Proc. - 2018 IEEE Int. Power Electron. Appl. Conf. Expo. PEAC 2018*, pp. 1–5, 2018.
- [27] H. Liu, X. Xie, Y. Li, H. Liu, and Y. Hu, “Mitigation of SSR by embedding subsynchronous notch filters into DFIG converter controllers,” *IET Gener. Transm. Distrib.*, vol. 11, no. 11, 2017.
- [28] Y. Meng, X. Pan, H. Ma, K. Li, J. Yu, and X. Wang, “Analysis and mitigation of subsynchronous resonance based on integral control for DFIG-based wind farm,” *IET Gener. Transm. Distrib.*, vol. 13, no. 9, pp. 1718–1725, 2019.
- [29] U. Karaagac, S. O. Faried, J. Mahseredjian, and A. A. Edris, “Coordinated Control of Wind Energy Conversion Systems for Mitigating Subsynchronous Interaction in DFIG-Based Wind Farms,” *IEEE Trans. Smart Grid*, vol. 5, no. 5, pp. 2440–2449, 2014.

-
- [30] Z. Bin *et al.*, “An active power control strategy for a DFIG-based wind farm to depress the subsynchronous resonance of a power system,” *Int. J. Electr. Power Energy Syst.*, vol. 69, 2015.
- [31] H. A. Mohammadpour, A. Ghaderi, H. Mohammadpour, and E. Santi, “SSR damping in wind farms using observed-state feedback control of DFIG converters,” *Electr. Power Syst. Res.*, vol. 123, pp. 57–66, 2015.
- [32] H. A. Mohammadpour, E. Santi, and A. Ghaderi, “Analysis of sub-synchronous resonance in doubly-fed induction generator-based wind farms interfaced with gate – controlled series capacitor,” *IET Gener. Transm. Distrib.*, vol. 8, no. 12, pp. 1998–2011, 2014.
- [33] Y. Li, L. Fan, and Z. Miao, “Replicating Real-World Wind Farm SSR Events,” *IEEE Trans. Power Deliv.* (early access), 2019.
- [34] J. Yao, X. Wang, J. Li, R. Liu, and H. Zhang, “Sub-Synchronous Resonance Damping Control for Series-Compensated DFIG-Based Wind Farm With Improved Particle Swarm Optimization Algorithm,” *IEEE Trans. Energy Convers.*, vol. 34, no. 2, 2019.
- [35] A. E. Leon and J. A. Solsona, “Sub-synchronous interaction damping control for DFIG wind turbines,” *IEEE Trans. Power Syst.*, vol. 30, no. 1, pp. 419–428, 2015.
- [36] M. S. El-Moursi, B. Bak-Jensen, and M. H. Abdel-Rahman, “Novel STATCOM controller for mitigating SSR and damping power system oscillations in a series compensated wind park,” *IEEE Trans. Power Electron.*, vol. 25, no. 2, pp. 429–441, 2010.
- [37] P. Dattaray, D. Chakravorty, P. Wall, J. Yu, and V. Terzija, “A Novel Control Strategy for Subsynchronous Resonance Mitigation Using 11 kV VFD-Based Auxiliary Power Plant Loads,” *IEEE Trans. Power Deliv.*, vol. 33, no. 2, pp. 728–740, 2018.
- [38] H. A. Mohammadpour, M. M. Islam, E. Santi, and Y. J. Shin, “SSR Damping in Fixed-Speed Wind Farms Using Series FACTS Controllers,” *IEEE Trans. Power Deliv.*, vol. 31, no. 1, 2016.
- [39] L. Fan and Z. Miao, “Mitigating SSR using DFIG-based wind generation,” *IEEE Trans. Sustain. Energy*, vol. 3, no. 3, pp. 349–358, 2012.
- [40] X. Bian, Y. Ding, Q. Jia, L. Shi, X.-P. Zhang, and K. L. Lo, “Mitigation of sub-synchronous control interaction of a power system with DFIG-based wind farm under multi-operating points,” *IET Gener. Transm. Distrib.*, vol. 12, no. 21, pp. 5834–5842, 2018.
- [41] H. Ghaffarzadeh and A. Mehrizi-sani, “Mitigation of Subsynchronous Resonance Induced by a Type III Wind System,” *IEEE Trans. Sustain. Energy*, vol. 11, no. 3, pp. 1717–1727, 2020.
- [42] Y. Xu and S. Zhao, “Mitigation of subsynchronous resonance in series-compensated dfig wind farm using active disturbance rejection control,” *IEEE Access*, vol. 7, pp. 68812–68822, 2019.
- [43] M. Ghafouri, U. Karaagac, J. Mahseredjian, and H. Karimi, “SSCI Damping Controller Design for Series Compensated DFIG based Wind Parks Considering Implementation Challenges,” *IEEE Trans. Power Syst.*, vol. 34, no. 4, pp. 2644–2653, 2019.
- [44] E. Larsen and T. Weaver, “FACTS Overview, IEEE FACTS Working Group and CIGRE FACTS

- Working Group,” 1995.
- [45] E. Larsen and F. Sener, “FACTS applications, IEEE FACTS Working Group and IEEE FACTS Application Task Force,” 1996.
- [46] V. N. Sewdien, “Operation of FACTS Controllers,” in *Flexible AC Transmission Systems*, S. Nilsson and B. Andersen, Eds. Cham: Springer Nature, 2020, pp. 1063–1070.
- [47] B. Andersen and S. Nilsson, *Flexible AC Transmission Systems*. Cham: Springer, 2020.
- [48] J. F. Hauer, “Modulation and SSR tests performed on the BPA 500 kV thyristor controlled series capacitor unit at Slatt substation,” *IEEE Trans. Power Syst.*, vol. 11, no. 2, pp. 801–806, 1996.
- [49] L. Ängquist, G. Ingeström, and H.-Å. Jönsson, “Dynamic Performance of TCSC Schemes,” in *Proceedings of the 1996 CIGRE Session*, 1996.
- [50] H. Xie and M. M. De Oliveira, “Mitigation of SSR in presence of wind power and series compensation by SVC,” in *2014 International Conference on Power System Technology*, 2014.
- [51] S. Golshannavaz, F. Aminifar, and D. Nazarpour, “Application of UPFC to enhancing oscillatory response of series-compensated wind farm integrations,” *IEEE Trans. Smart Grid*, vol. 5, no. 4, pp. 1961–1968, 2014.
- [52] S. Cherevatskiy *et al.*, “Grid Forming Energy Storage System addresses challenges of grids with high penetration of renewables (A case study),” in *CIGRE Session 2020*, 2020.
- [53] X. Zhang, X. Xie, J. Shair, H. Liu, Y. Li, and Y. Li, “A Grid-side Subsynchronous Damping Controller to Mitigate Unstable SSCI and its Hardware-in-the-loop Tests,” *IEEE Trans. Sustain. Energy*, vol. 11, no. 3, pp. 1548–1558, 2020.
- [54] J. Khazaei, A. Asrari, P. Idowu, and S. Shushekar, “Sub-Synchronous Resonance Damping using Battery Energy Storage System,” *2018 North Am. Power Symp. NAPS 2018*, pp. 1–6, 2019.
- [55] L. Huang, H. Xin, Z. Wang, W. Huang, and K. Wang, “An Adaptive Phase-Locked Loop to Improve Stability of Voltage Source Converters in Weak Grids,” in *IEEE Power and Energy Society General Meeting*, 2018.
- [56] I. Vieto, P. Huang, T. Reinikka, H. Nademi, C. Buchhagen, and J. Sun, “Online measurement of offshore wind farm impedance for adaptive control of hvdc transmission systems,” in *2019 IEEE 20th Workshop on Control and Modeling for Power Electronics*, 2019.
- [57] F. Salehi, I. Brandao Machado Matsuo, A. Brahman, M. Aghazadeh Tabrizi, and W.-J. Lee, “Sub-Synchronous Control Interaction Detection: A Real-Time Application,” *IEEE Trans. Power Deliv.*, vol. 35, no. 1, pp. 106–116, 2020.
- [58] H. Li *et al.*, “An Improved Fast Detection Method on Subsynchronous Resonance in a Wind Power System with a Series Compensated Transmission Line,” *IEEE Access*, vol. 7, 2019.

4. MODELS AND METHODOLOGIES

4.1. INTRODUCTION

This Chapter discusses the development of the DFIG wind turbine generator model, the study model based on the single machine infinite bus system and the IEEE 39-bus system, all in PSCAD. The study model will be used for the development and assessment of the mitigation solutions. The IEEE 39-bus system is a larger power system used to apply the developed concepts and validate the findings from the study model. The wind turbine generator model is developed in Section 4.2. The impedance based stability method will be used as screening tool and is discussed in Section 4.3. Guidelines for numerical simulations, needed to capture the impedance response of the DFIG, are developed in Section 4.4. Section 4.5 introduces the time domain EMT analysis as a tool for detailed analysis of DFIG-SSR. Finally, the study model and the IEEE 39-bus system are presented in Section 4.6.

4.2. WIND TURBINE GENERATOR MODEL

As part of the MIGRATE project, root mean square (RMS) and EMT DFIG models were developed in respectively Power Factory and PSCAD. The developed models are generic and their controls are based on the IEC Standard 61400-27-1 [1]. Since the controls of the generic models in the Standard are developed for RMS applications, modifications as described in [2], [3] were necessary to extend the models for EMT simulations. Two variations of the EMT model were developed: the detail model and the average model. The detail model includes the power electronic switches and the associated pulse width modulation (PWM) technique and is suitable for dynamic and harmonic analysis. In the average model, the converters are replaced with equivalent voltage sources. This model preserves the dynamic behaviour of the machine, however, the harmonic behaviour of the converters is lost and the average model is therefore not suitable for harmonic analysis. For other types of analysis, the average model has the advantage that it simplifies the simulation model, thus speeding up the simulation.

Although the focus of this thesis is not the DFIG design, a high level description of the EMT models developed in MIGRATE will be given next. The generic PSCAD DFIG model presented here was developed for a single 3.6 MW machine connected to a 50 Hz equivalent voltage source. The DFIG is an electromechanical system with electrical, mechanical and controls components, as is shown in Figure 4.1. The DFIG model was developed as a two part system, with a mechanical subsystem in charge of converting the maximum power available from the wind into torque, and an electrical subsystem in charge of delivering the power into the electrical system. The interface component in this system is the induction generator, which converts the mechanical energy into electrical energy.

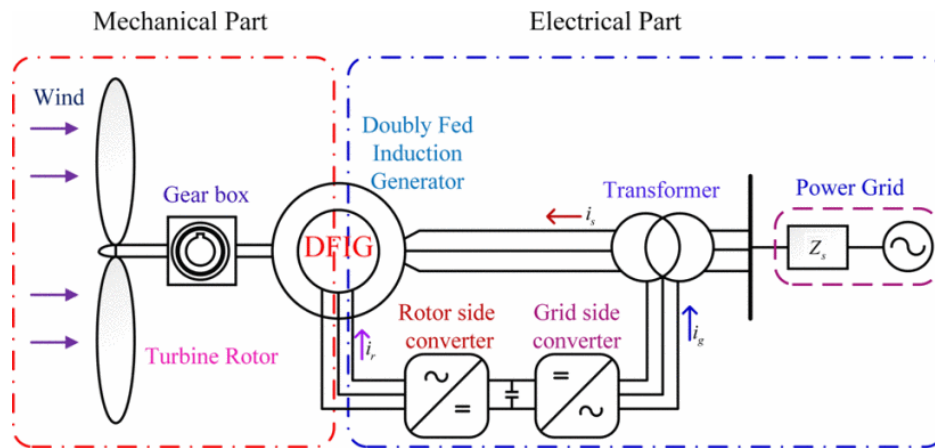


Figure 4.1 Schematic diagram of a DFIG WTG [4].

The inverter (GSC) is in charge of maintaining the DC-link voltage. The inverter control uses the dq -reference frame, where the inverter is set to operate in DC-link voltage control mode (d -axis) and reactive power control mode (q -axis). The reactive power control is set to inject zero reactive power into the system during normal operation. Low pass filters with a characteristic frequency of 600 Hz were added to improve the quality of dq -quantities by filtering out some of the high frequency harmonics introduced by the power electronic converters. Converter reference voltages are obtained through classical DLC and the three phase reference voltage waveforms for the PWM are obtained from the $dq-abc$ transformation of the converter reference voltages. The three phase voltage references are used in the PWM control, which in turn issues the firing pulses to the two-level insulated gate bipolar transistor (IGBT) bridges.

The rectifier (RSC) is in charge of injecting the appropriate currents to the rotor circuit of the induction machine, such that the desired active and reactive power are obtained at the stator terminals of the machine. The d -axis rotor current component contributes to the torque, whereas the q -axis component contributes to the reactive power. This means that controlling the rotor d -axis and q -axis currents leads to the control of the stator real and reactive power. To obtain the d -axis and q -axis components of the rotor current, it is necessary to determine the relative difference between the stator flux and rotor position (slip angle). The position of the rotating flux vector is obtained via a PLL locked to the stator voltage after subtracting the voltage drop across the stator resistance.

According to most new grid code requirements, wind turbines must remain connected to the grid during grid disturbances and provide voltage support during and after the faults. As a DFIG has the stator connected to the grid, it makes the rotor winding sensitive to the high currents induced during grid disturbances and faults. The rotor windings are connected to the grid via a back-to-back converter, which is very sensitive to over-currents. The most common means to avoid injecting such induced currents into the power electronic converters is to short the rotor terminals via a resistance. Such shorting mechanism is normally known as a crowbar. The duration of the crowbar activation depends on grid code requirements. For grids with low wind penetration the injection of reactive current during the faults is normally not required. In this case the crowbar is usually activated for the whole duration of the fault. For more restrictive policies in terms of reactive current injection, duration of crowbar activation has to be minimised given that the controllability of reactive power injection is lost as long as the rotor terminals are shorted. Therefore, protection by means of the DC-link chopper prevents overcharging the DC-link capacitor. Summarising, the chopper is used to protect the DC-link from overvoltages and the crowbar circuit is used to protect the rectifier against current surges coming from the machine rotor side circuit.

To reduce the voltage harmonics introduced by the two-level converter, an AC filter is used on the inverter side. Several filter topologies and methods on how to calculate filter parameters exist and the filter design in the developed model follows the requirements as given in [5]. The relevant parameters of the DFIG are given in Appendix A.

4.3. SCREENING: IMPEDANCE BASED STABILITY ANALYSIS

The analysis of any SSO phenomenon contains two main steps: screening and detailed analysis. Screening is a relatively fast method to assess the stability of SSO modes across a wide range of operating conditions, including various generation dispatch scenarios, grid topologies and controller parameters. Different permutations of these conditions can result in thousands of simulation cases to be assessed. The screening step identifies a subset of simulation cases with a high risk for instability. The identification is done based on observing the value of a predefined index. Whenever the index of a simulation case violates a predefined threshold, the case is investigated in more detail. Methodologies for detailed analysis are discussed in Section 4.5.

The unit interaction factor (UIF) [6] is a well-known screening method for DDSSO involving line commutated converter (LCC) HVDC. When the calculated UIF is larger than 0.1, the DDSSO risk is high and detailed studies are required. Another DDSSO screening method is the radiality factor [7]. In contrast to UIF, the radiality factor can also be used for DDSSO involving VSC HVDC. Like for the UIF, the threshold value for the radiality factor is determined based on extensive sensitivity studies and was set at 0.2. Simulation cases with a radiality factor smaller than 0.2 are considered acceptable low risk cases.

Two well-known screening methods for DFIG-SSR risks are the dynamic frequency scanning technique [8] and the impedance based stability analysis [9]. The impedance based stability analysis will be used in this thesis and is described next. Its advantage over the dynamic frequency scanning method is that the impedance based method can accurately identify the

resonance frequency of the overall system and quantify the distance to instability at this frequency using the phase margin.

4.3.1. METHODOLOGY

From the phenomena shown in Figure 2.17, the impedance based stability analysis is mainly used to screen for DFIG-SSR, SSCI-CGI and SSCI-CCI. In this concept, the effective impedances of the DFIG and the AC network as viewed from the PCC are obtained through impedance modelling [10] or through numerical simulations. Impedance modelling requires full access to all the converter control and design details. However, vendors only deliver black-box simulation models, which makes the use of impedance modelling by utilities practically impossible. Numerical simulations based on perturbation analysis can be used on white-box as well as black-box models. Therefore numerical simulations are used in this work to obtain the DFIG impedance and is further described in Section 4.4.

The effective impedances of the DFIG and the AC network are determined for specific operating conditions and considering multiple contingency scenarios that could result in radial or near radial connection of the DFIG to series compensated lines. The effective DFIG impedance is viewed in conjunction with the impedance scan of the AC network, which then gives insight in the distance to instability for different operating conditions.

The impedance based stability analysis evaluates the stability of the overall system using the source and load impedance. For a system with a source and load impedance connected at the PCC as shown in Figure 4.2, the current I can be calculated by (4.1).

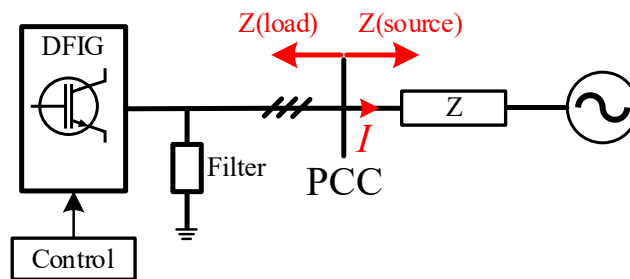


Figure 4.2 Equivalent representation of source and load system for impedance based stability analysis.

$$I(s) = \frac{E_s}{Z_{load}(s)} \cdot \frac{1}{[1 + Z_{source}(s)/Z_{load}(s)]} \quad (4.1)$$

Provided that E_s and the load subsystem (Z_{load}) are open loop stable, the impedance based stability can be assessed based on the term: $[1 + Z_{source}(s)/Z_{load}(s)]$. The open loop bode plots of Z_{source} and Z_{load} can provide the phase margin for assessing the stability of the overall system in closed loop.

In the context of DFIG-SSR screening Z_{load} is the DFIG impedance Z_{DFIG} and is influenced by the machine parameters, circuit parameters and DFIG converter controls. The source impedance Z_{source} is the equivalent impedance of the AC network and includes network

elements such as generators, transformer impedances, load and non-transformer branch impedances. Z_{load} and Z_{source} are superimposed on one another, to assess the stability for different operating conditions, such as variation of controller gains in the DFIG converters and variations in wind speeds.

4.3.2. LIMITATIONS AND ASSUMPTIONS

The primary assumption of the impedance based method is the open loop stability of the DFIG and the AC grid. The results from this method are dependent on where the two systems are partitioned. The choice of partitioning point can have an impact on the stability margin. Furthermore, the network equivalent Z_{source} in this technique is not representative of the dynamic behaviour of nearby non-linear controlled devices such as FACTS and HVDC systems. Finally, for the DFIG-SSR assessment all the DFIG machines are considered as one collector system, connected to the rest of the grid. Thus, the distinction between the different machines cannot be addressed with this method, unless the partition point is considered at the individual DFIG level. The impact of different partition points is discussed in Chapter 8.

4.3.3. MODELLING REQUIREMENTS

The application of the impedance based stability method requires an EMT representation of the considered source and load subsystems. The DFIG wind park module should contain a good representation of all electrical components and control loops, whose dynamics are of relevance for the SSO frequency range. With all the control loops modelled, average representations for PEIDs can be used to investigate DFIG-SSR. The EMT representation of the electrical grid should as well take components into account, whose dynamics are expected to fall in the relevant frequency range for the SSO. Nearby devices as well as other generating units (e.g. HVDC links, wind power plants and STATCOMs) should also be represented. To capture the dynamics of the active devices in the grid, several sets of source impedances are required, where each set is a permutation of the expected setpoints of the active devices.

4.3.4. EVALUATION CRITERIA

To assess the risk for DFIG-SSR, the open loop impedance plots for the DFIG and the AC grid are superimposed on one another. The frequency where both impedance plots intersect is identified as the resonance frequency f_r . The phase margin (PM) is a measure for the distance to instability and is calculated at the resonance frequency according to (4.2).

$$\begin{aligned} |Z_{grid}(f_r)| &= |Z_{DFIG}(f_r)| \\ PM &= 180^\circ - |\angle Z_{grid}(f_r) - \angle Z_{DFIG}(f_r)| \end{aligned} \quad (4.2)$$

f_r : frequency at which Z_{grid} and Z_{DFIG} intersect

PM : phase margin at f_r

The smaller PM, the closer the system is to instability. A threshold for the PM to indicate marginal stability for practical applications is yet to be defined. This is at the discretion of the utility and depends on the accuracy of the obtained impedances and the confidence of the utility in the simulation models. The more conservative the utility, the higher the phase margin threshold below which detailed studies are demanded.

Figure 4.3 illustrates the evaluation of DFIG-SSR using the impedance based stability analysis. The source and load impedance responses are shown in Figure 4.4 and are obtained using numerical simulations (discussed in Section 4.4). The magnitude responses intersect at 10 Hz, indicating a potential for adverse interactions. The phase margin is calculated using (4.2) and the phase angles of the source and load impedances. In this case, the phase margin is 30° and depending on the utility's practice, this case may or may not qualify for detailed analysis. In this work, detailed analysis will be performed for phase margins lower than 10° .

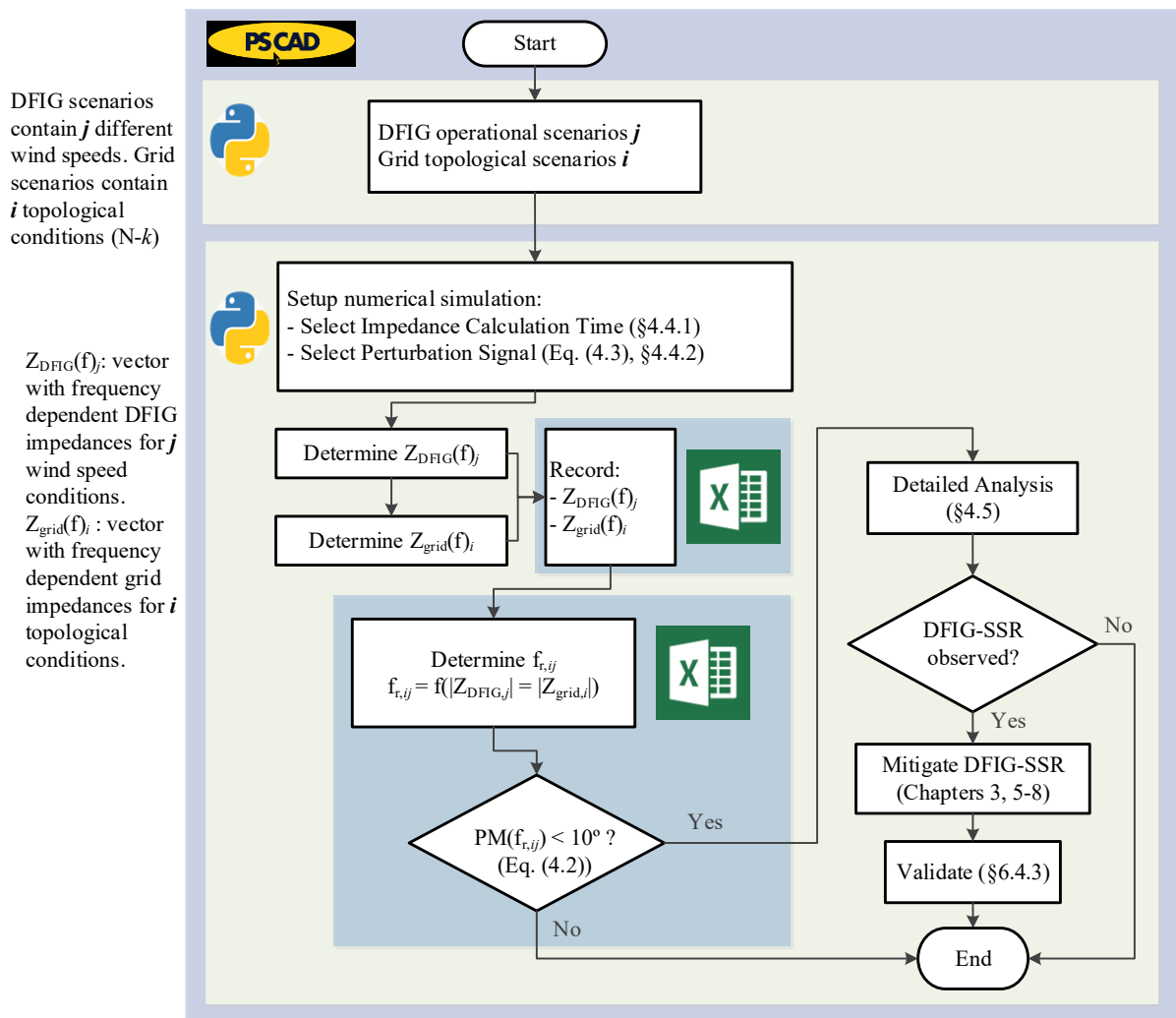


Figure 4.3 Evaluation of DFIG-SSR using the impedance based stability analysis.

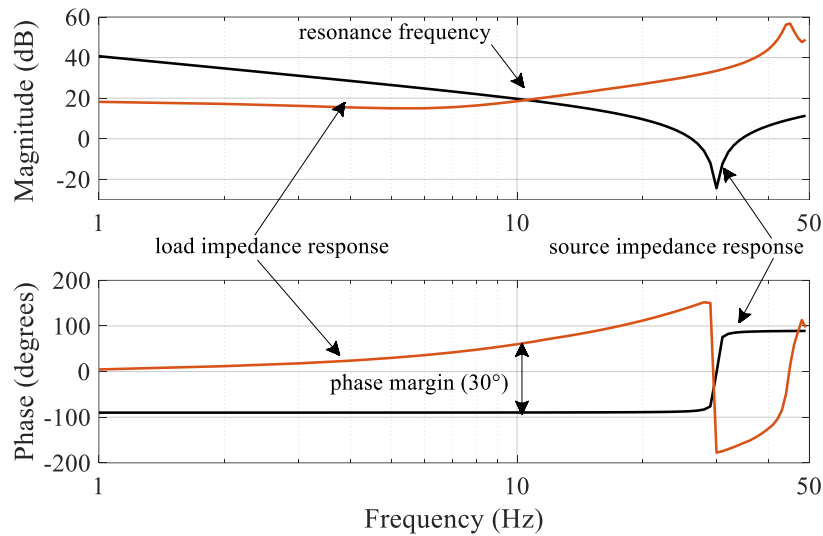


Figure 4.4 Example of DFIG-SSR evaluation using the impedance based stability method.

4.4. IMPEDANCE CALCULATION: NUMERICAL SIMULATIONS

In most cases, intellectual property issues prohibit the exchange of detailed white-box models of the electrical grid and DFIG, hindering the application of analytical approaches such as the state-space based approach to assess DFIG-SSR. In this Section, a numerical approach to obtain the DFIG and grid impedances based on the availability of black-box EMT models is outlined. The methodology is based on the frequency dependent characteristic of both subsystems and aims to create a frequency dependent positive sequence impedance representation of the electrical grid and the DFIG as seen from their PCC.

PEIDs are highly non-linear and determining their impedance needs to be done carefully. Numerical simulations are one of the widely used methods in industry to calculate the PEID impedance. The method is a type of small-signal analysis and is based on injecting small perturbation voltages at different frequencies in the PEID and measuring the corresponding voltages and currents (denoted as V and I in Figure 4.5).

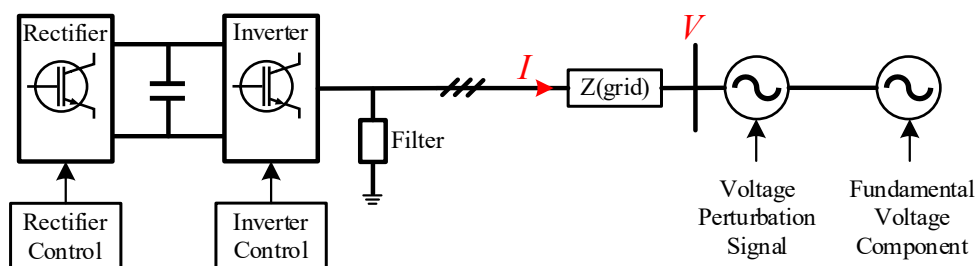


Figure 4.5 Numerical simulation set up for impedance calculation.

Through Fourier analysis, the voltage and current components at the perturbation frequency are extracted and the PEID impedance at that frequency is obtained. Due to non-linearity in the PEID's circuit and control, the measured current will also contain non-characteristic harmonics. Under most circumstances, these harmonics can be ignored in small-signal analysis. However,

with asymmetric dq -control the non-characteristic harmonics cannot be ignored. This is further discussed in Section 4.4.4.

Considering a balanced perturbation, the voltage perturbation signal is defined by (4.3).

$$\begin{aligned}
 V_{a,p} &= \sum_{\psi} V_p \cos(\omega_{p,\psi} t + \phi_{\psi}) \\
 V_{b,p} &= \sum_{\psi} V_p \cos\left(\omega_{p,\psi} t + \phi_{\psi} - \frac{2\pi}{3}\right) \\
 V_{c,p} &= \sum_{\psi} V_p \cos\left(\omega_{p,\psi} t + \phi_{\psi} + \frac{2\pi}{3}\right)
 \end{aligned} \tag{4.3}$$

$\boldsymbol{\psi}$: vector with a number of perturbation frequencies
 V_p : magnitude of perturbation voltage
 $\omega_{p,\psi}$: perturbation frequency
 ϕ_{ψ} : phase shift associated to $\omega_{p,k}$

When the voltage perturbation signal consists of white noise, vector $\boldsymbol{\psi}$ contains the frequencies that make up the white noise signal. When determining the impedance using the perturbation method, the impedance calculation time, the perturbation signal and type of simulation model have to be selected. Sections 4.4.1, 4.4.2 and 4.4.3 provide recommendations and guidelines for the selection of respectively the time for impedance calculation, the composition of the perturbation signal and the selection of the adequate simulation model. The procedure is depicted in Figure 4.6.

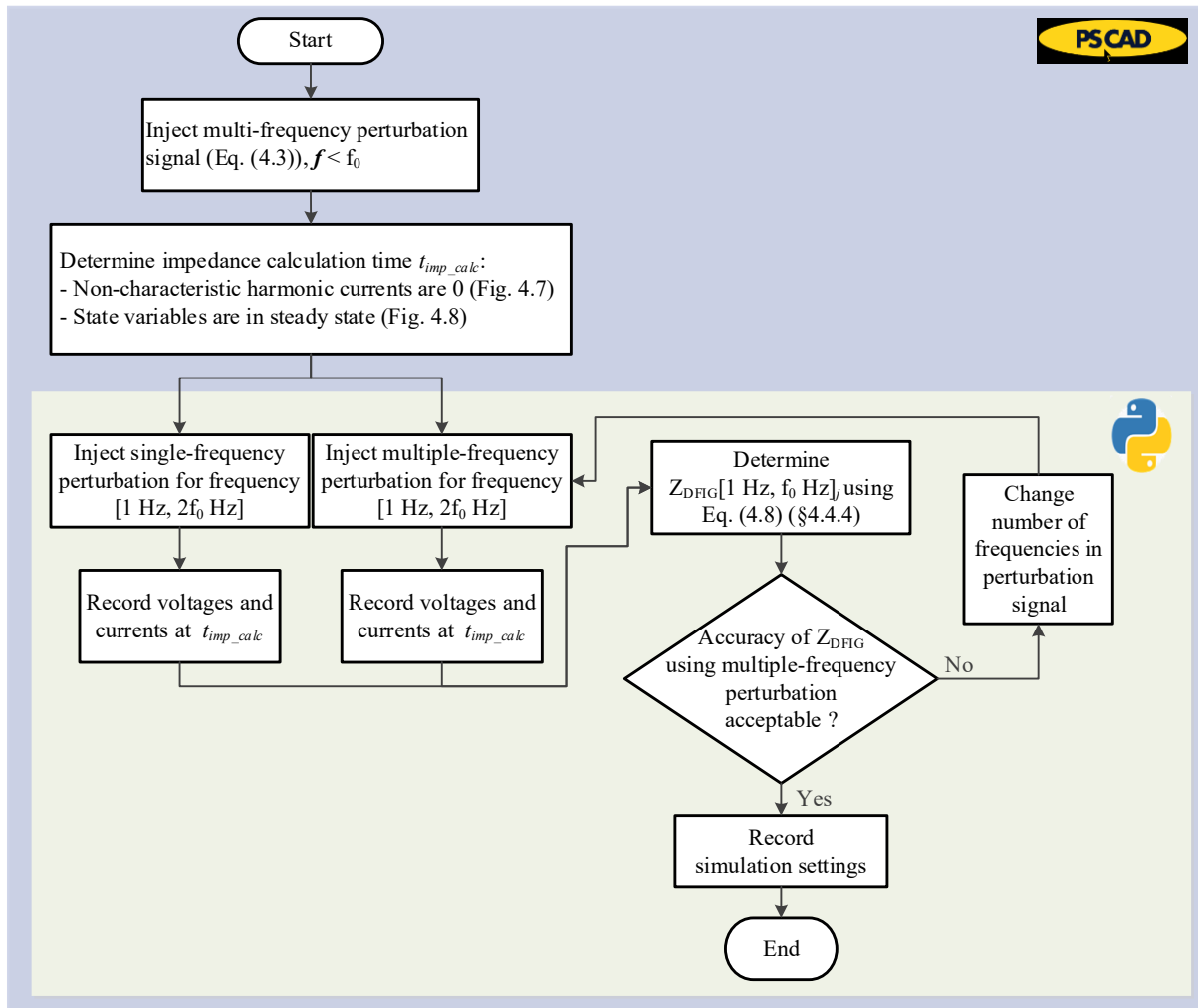


Figure 4.6 Procedure for identification of the perturbation signal and the impedance calculation time.

4.4.1. IMPEDANCE CALCULATION TIME

When determining the DFIG impedance using the perturbation method, three stages can be distinguished in the recorded time domain signal as shown in Figure 4.7. In stage I, the model initialises and no perturbation signal is injected. The duration of this stage depends on the start-up sequence of the DFIG simulation model. In the developed model, this stage lasts for less than one second. Stage II is characterised by the ramp up of the perturbation signal. Depending on the objective of the study, the perturbation frequency consists of either a single frequency perturbation or a perturbation based on white noise excitation. If the impedance is captured in stage II, an oscillatory behaviour will be observed in the impedance angle. This is caused by the fact that the perturbation signal and state variables are not yet settled in stage II, as well as due to cross coupling effects of non-characteristic harmonics caused by the perturbation signal. Stage III commences when the perturbation signal as well as the state variables are settled to a steady state value. The impedance should be captured in stage III.

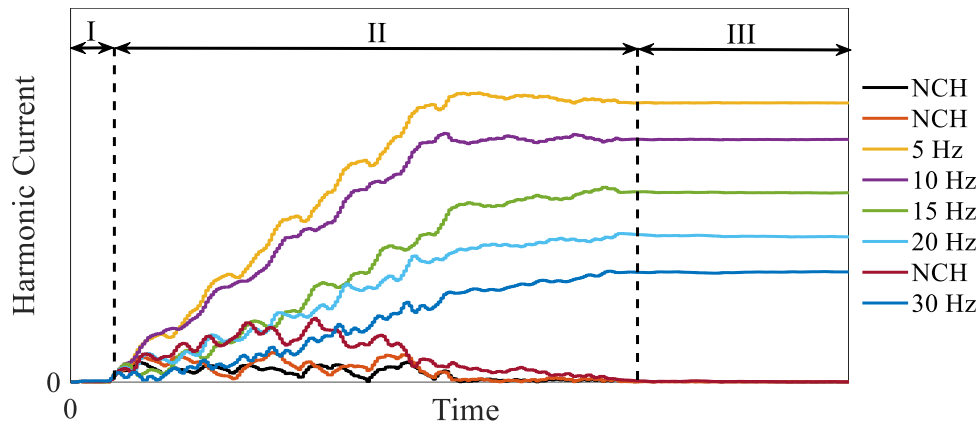


Figure 4.7 Current measurement following a white noise perturbation (NCH=non-characteristic harmonics).

The perturbation signal used for the measurement of the current in Figure 4.7 contains five subsynchronous frequencies, i.e. $\psi = [5, 10, 15, 20, 30 \text{ Hz}]$. As is observed, the perturbation signal is not injected in stage I. Stage II starts with the ramping up of the perturbation signal. The cross coupling of frequencies in stage II is observed by the presence of non-characteristic harmonics. Once the perturbation signal and state variables have reached steady state, stage III commences.

To illustrate the influence of the time selected for capturing the DFIG impedance, two different timings are considered based on examining the time trajectory of the generator speed state variable, see Figure 4.8. Two timings are selected: 3 seconds (stage II) and 30 seconds (stage III). The impedance response is captured at both timings and is shown in Figure 4.9. As is shown, the impedance angle exhibits an oscillatory behaviour when the impedance is captured after 3 seconds. On the other hand, when the impedance response is determined after the state variable is settled, a stable response is obtained. In summary, necessary conditions for selecting adequate impedance calculation timings include steady state perturbation signals and state variables.

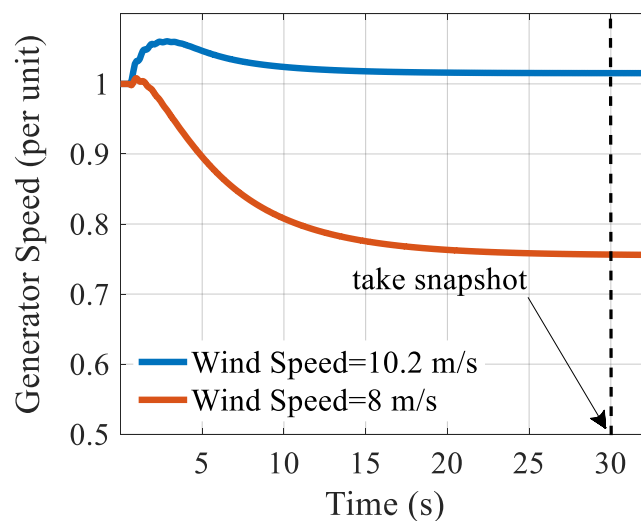


Figure 4.8 Evolution of the generator speed state variable over time.

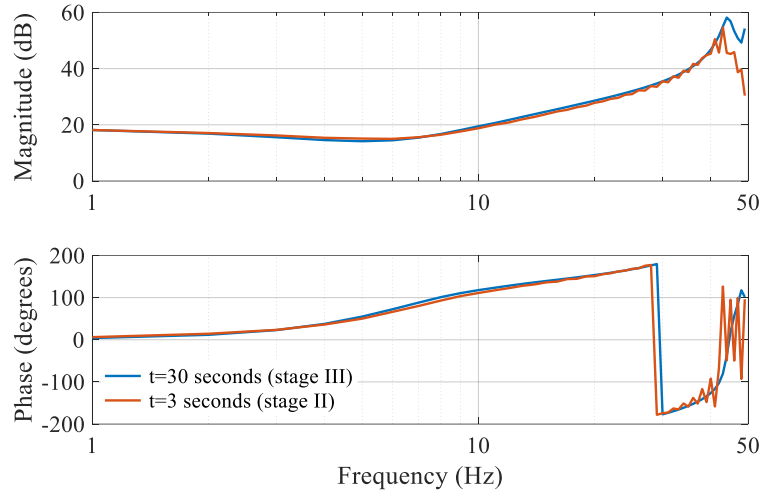


Figure 4.9 DFIG impedance response captured in stage II and stage III.

4.4.2. PERTURBATION SIGNAL

Due to the presence of non-linear elements in the DFIG and the AC grid, the magnitude of the perturbation signal should be modulated to ensure linear operating conditions. Under nominal conditions, the DFIG controller is designed to only respond to positive sequence quantities. Considering that the DFIG impedance is required for at least the sub synchronous frequency range, i.e. 1-49 Hz, the perturbation signal as defined in (4.3) consists of three variables for each of the frequencies of interest. These variables are the magnitude of the perturbation voltage (V_p), the initial phase shift of the signal (ϕ) and the number of frequencies that are injected simultaneously (ψ). Following the recommendations given in [11], V_p is set to 5% of the nominal voltage and ϕ is set to 0° . No recommendations were given for k . Therefore, the accuracy of the frequency scanning using ψ frequencies is assessed next. The obtained DFIG impedance is compared when the perturbation signal contains 1, 2, 5 and 25 frequencies. The result is shown in Figure 4.10. The difference in the phase angle between 1 and 25 injected frequencies at e.g. 20 Hz is 30.4° . The corresponding difference between 1 and 2 and 1 and 5 injected frequencies is respectively 4.7° and 4.3° . For further analysis throughout this work, the DFIG impedance is measured using a perturbation signal with $\psi = 5$. This simplification is justified as the obtained DFIG impedance is only used for screening purposes. Detailed analysis will be performed with the detail DFIG EMT model that takes all non-linearities into account.

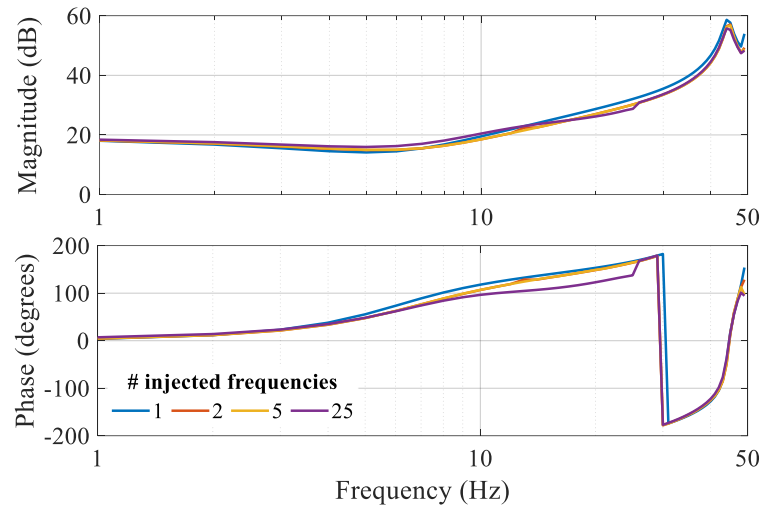


Figure 4.10 Impact of the number of frequencies in the white noise perturbation on the measured DFIG impedance.

4.4.3. SIMULATION MODEL

An average model of the converter can be used when a faster simulation time is desired, and when the focus of the simulation is not on the firing controls or on the effects of the higher harmonics produced by the power electronics converter. In the average model, the AC side is interfaced with voltage sources set to generate the three phase voltage references, while on the DC side a current is injected such that the power balance is preserved. As the damping is crucial for DFIG-SSR analysis, a ‘dummy’ resistance is added in the converter of the average model. The purpose of this resistance is to model the switching losses of the IGBTs. Its value is determined iteratively such that the losses of both models are identical. This resistance only provides an attempt to achieve the same level of damping provided by the switching losses in the full model.

To evaluate the impact of the model simplification, the impedance responses of both models are obtained and shown in Figure 4.11. The impedance response of the average model can be considered close enough to the response of the detail model, with some deviations. These deviations can be attributed to:

- The use of a static ‘dummy’ resistance, determined at the fundamental frequency. Increased model accuracy can be obtained when this resistance is frequency dependent.
- The altered reactance of the average model due to the omission of the IGBTs. However, the influence of this altered reactance on the oscillation frequency is negligible.

Considering the increased simulation speed and the negligible loss in accuracy, the average model is used for further screening analysis. The detail model will be used for validation purposes, as it contains more accurate damping characteristics. It is worth mentioning that the choice of the model does not influence the validity of the methods and frameworks designed in this thesis.

Finally, to further decrease the required simulation time, simulations were performed using snapshots. Several comparisons of the average model impedance response obtained using snapshots and using standard initialisation were performed. These comparisons showed the exact same impedance responses, thereby justifying the use of the snapshots.

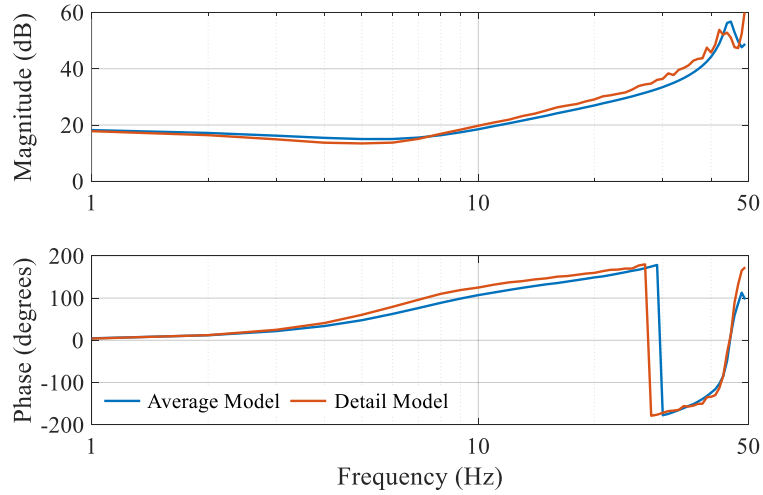


Figure 4.11 DFIG impedance response using the average and detail EMT model.

4.4.4. CROSS COUPLING

In the previously described small-signal analysis, the DFIG impedance is determined based on perturbation signals at different sub synchronous frequencies. In such an analysis, the current with the same frequency component as the perturbation voltage is extracted and the impedance at the corresponding frequency is calculated. This is performed for the frequency range of interest, i.e. 1-49 Hz for DFIG-SSR analysis.

Non-characteristic harmonics are usually numerically insignificant and are ignored. However, under certain circumstances the non-characteristic harmonics may have to be considered. For a voltage perturbation with frequency f_p , asymmetric dq -control introduces a coupled non-characteristic harmonic f_{nc} , where the frequency coupling is governed according to $f_p + f_{nc} = 2f_0$ [12]. In [12] it was concluded that the coupling resulting from the asymmetric dq -control causes the DFIG's current response to a voltage perturbation at f_p to be dependent on the grid impedance Z_{grid} . To account for the coupling, the DFIG impedance behaviour is described using the 2×2 matrix given in (4.4).

$$Z_{DFIG} = \begin{bmatrix} Z_{DFIG}(f_p) & Z_{DFIG}(f_p \rightarrow f_{nc}) \\ Z_{DFIG}(f_{nc} \rightarrow f_p) & Z_{DFIG}(f_{nc}) \end{bmatrix} = \begin{bmatrix} \frac{V(f_p)}{I(f_p)} & \frac{V(f_p)}{I(f_{nc})} \\ \frac{V(f_{nc})}{I(f_p)} & \frac{V(f_{nc})}{I(f_{nc})} \end{bmatrix} \quad (4.4)$$

$Z_{DFIG}(f_p)$: Impedance of DFIG at f_p due to perturbation at f_p

$Z_{DFIG}(f_p \rightarrow f_{nc})$: Impedance of DFIG at f_{nc} due to perturbation at f_p

$Z_{DFIG}(f_{nc} \rightarrow f_p)$: Impedance of DFIG at f_p due to perturbation at f_{nc}

$Z_{DFIG}(f_{nc})$: Impedance of DFIG at f_{nc} due to perturbation at f_{nc}

For balanced three phase grids the coupling between frequencies is absent and Z_{grid} is defined as given by (4.5).

$$Z_{grid} = \begin{bmatrix} Z_{grid}(f_p) & 0 \\ 0 & Z_{grid}(f_{nc}) \end{bmatrix} \quad (4.5)$$

When using the perturbation analysis for the model shown in Figure 4.5, the voltage-current relation is obtained according to (4.6).

$$\begin{bmatrix} V(f_p) \\ 0 \end{bmatrix} = \begin{bmatrix} Z_{DFIG}(f_p) + Z_g(f_p) & Z_{DFIG}(f_p \rightarrow f_{nc}) \\ Z_{DFIG}(f_{nc} \rightarrow f_p) & Z_{DFIG}(f_{nc}) + Z_g(f_{nc}) \end{bmatrix} \begin{bmatrix} I(f_p) \\ I(f_{nc}) \end{bmatrix} \quad (4.6)$$

Expressing $I(f_{nc})$ in terms of $I(f_p)$ and solving (4.6) for the system impedance Z_{SYSTEM} , where the system impedance is $V(f_p)/I(f_p)$, equation (4.7) is obtained.

$$Z_{SYSTEM}(f_p) = \underbrace{Z_{grid}(f_p)}_{grid} + \underbrace{Z_{DFIG}(f_p) - \frac{Z_{DFIG}(f_p \rightarrow f_{nc}) \cdot Z_{DFIG}(f_{nc} \rightarrow f_p)}{Z_{DFIG}(f_{nc}) + Z_{grid}(f_{nc})}}_{DFIG} \quad (4.7)$$

With $V(f_p)$ and $I(f_p)$ measured and $Z_{grid}(f_p)$ and $Z_{grid}(f_{nc})$ known, the equivalent impedance $\overline{Z_{DFIG}}(f_p)$ of the DFIG at frequency f_p is calculated as given in (4.8).

$$\overline{Z_{DFIG}}(f_p) = Z_{DFIG}(f_p) - \frac{Z_{DFIG}(f_p \rightarrow f_{nc}) \cdot Z_{DFIG}(f_{nc} \rightarrow f_p)}{Z_{DFIG}(f_{nc}) + Z_{grid}(f_{nc})} \quad (4.8)$$

The calculation of the DFIG impedance in this thesis always takes the cross coupling into account according to (4.8).

4.5. DETAILED ANALYSIS

In the analysis of SSO phenomena, the screening step identifies those scenarios that potentially could lead to instability. These scenarios, defined in this thesis as those operating conditions with a phase margin lower than 10° , need to be thoroughly assessed using detailed analysis. Two main methods exist for performing detailed analysis of DFIG-SSR: eigenvalue analysis and EMT analysis. These are discussed next.

4.5.1. EIGENVALUE ANALYSIS

Eigenvalue analysis provides the damping and frequency of the oscillation modes at a given operating point. This method is based on a representation of both mechanical and electrical systems in one set of differential equations. The state matrix can be calculated by writing the linearised forms of these equations. Analysis of the eigenvalues of the state matrix provides information regarding the stability of the system [13]. A real eigenvalue corresponds to a non-oscillatory mode, whereas a complex eigenvalue occurs in a conjugate pair and corresponds to an oscillatory mode. The real component of the complex eigenvalue gives the damping and the

imaginary component gives the oscillation frequency. A negative real part signifies a stable mode (damped oscillation), whereas a positive real part represents an unstable mode (oscillation of increasing amplitude). The participation matrix, which combines the right and left eigenvectors of the state matrix, allows identifying the association between the state variables and the modes. The impact of converter parameters on the oscillation modes can be assessed by observing the loci of eigenvalues while parameters are changed.

It should be kept in mind that the eigenvalue method is based on the assumption of a linear system behaviour. The results are only valid for small disturbances, as nonlinearities of the system are not included in the small-signal model. Switching devices are represented by approximated linear transfer function and the effect of the switching on the system behaviour is neglected.

Compared to detailed time domain EMT simulations, the main advantages of the eigenvalue method are its ability to provide a holistic view of all oscillation modes of the system and to identify the source of and devices participating in these oscillations. As was discussed in Chapter 2, the eigenvalue method was used in [14] to demonstrate that the controllers of a DFIG do not participate in DFIG-SSR. On the other hand, one of the major drawbacks of the eigenvalue method is the need to have full access to otherwise proprietary data, such as converter control schemes and parameters of the DFIG. This is one of the main reasons why the use of the eigenvalue method is limited for practical applications.

4.5.2. EMT ANALYSIS

EMT analysis use step-by-step numerical integration to solve a set of differential equations. Unlike the eigenvalue method, EMT analysis can provide insights in the exact non-linear behaviour of the system, provided that the modelling is done adequately. An EMT model includes detailed models of machines, transformers, transmission lines and power electronic converters. The DFIG EMT model includes a detailed model of the generator, the turbine-generator protection and converter control. The converter control is modelled in full detail and the final developed model can be exchanged with third parties as a black-box model without losing simulation accuracy, thereby protecting the intellectual property of the vendor. This is the main advantage over the eigenvalue method and the reason why EMT simulations are practical for interaction studies.

However, a disadvantage of the EMT analysis is that it only provides time domain response results, which make it difficult to get insight in the mechanisms behind SSO phenomena. Another disadvantage is that EMT simulations are computationally expensive, where a single EMT simulation for large electrical systems can take several hours.

In the subsequent Chapters, EMT analysis will be used as a tool for the detailed analysis, for the following two reasons. First, the fault ride through capability of the DFIG equipped with the developed mitigation solutions will be investigated. The eigenvalue method is based on small-signal disturbances and will not be able to capture the non-linearities. Second, the EMT model was already developed for screening purposes. As the mechanisms behind DFIG-SSR were already reported in [14], the added value in developing a small-signal model is limited.

4.6. GRID MODELS

4.6.1. SINGLE MACHINE INFINITE BUS MODEL

The mitigation solutions are initially developed using a single machine infinite bus (SMIB) model. This model, defined as the study model throughout this thesis, is depicted in Figure 4.12. The compensated transmission line has a compensation degree of 36%, which corresponds to a resonance frequency of 30 Hz.

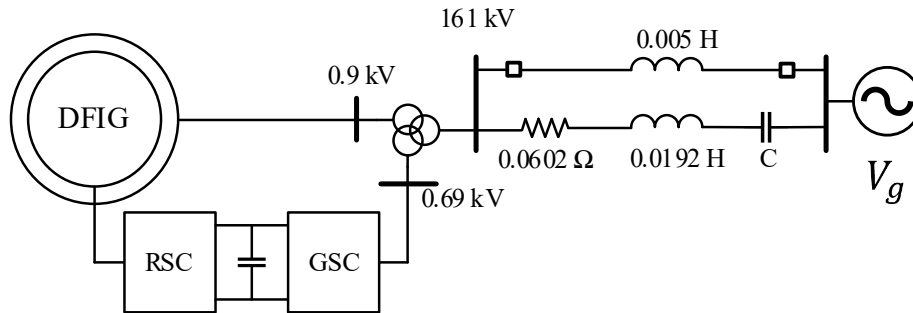


Figure 4.12 Study model for DFIG-SSR mitigation.

The impedance based stability method was used to obtain the impedance response of the study model and to analyse its stability. The impedance responses are obtained for the double circuit and radial operation of the DFIG and are shown in Figure 4.13. In radial operation, the uncompensated transmission line is switched off. In double circuit operation, the magnitude plots of the DFIG and the grid do not intersect and therefore there is no risk for DFIG-SSR. In radial operation, the magnitude plots intersect at approx. 10 Hz. The phase margin at this frequency is -17° , indicating a high risk for DFIG-SSR. The next step in the analysis would be to perform detailed EMT time domain simulations to confirm the presence of DFIG-SSR.

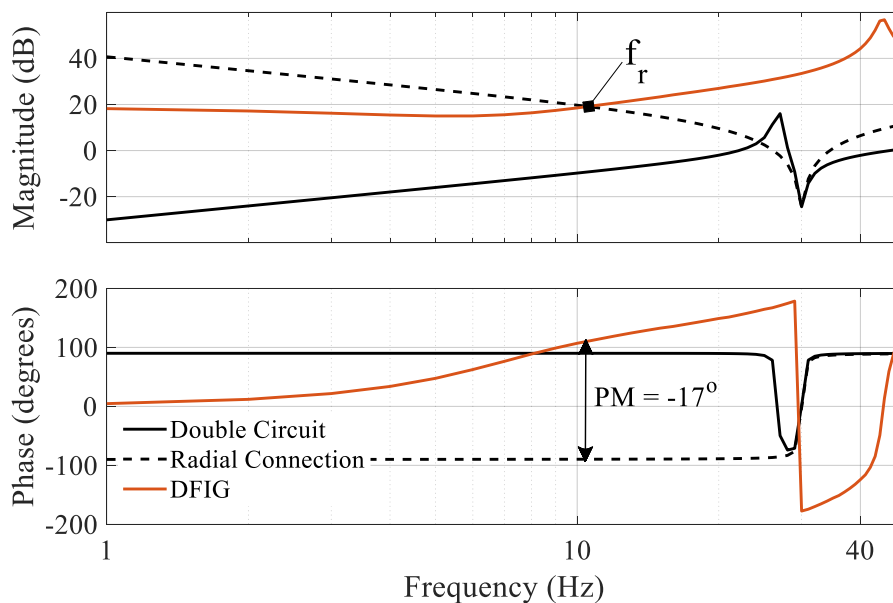


Figure 4.13 Impedance responses of the study model for double circuit and radial operation.

4.6.2. IEEE 39-BUS SYSTEM

The IEEE 39-bus system shown in Figure 4.14 is used to validate the developed mitigation solutions. The EMT model of the IEEE 39-bus system developed in [15] is modified to accommodate DFIG-SSR analysis. The following modifications are implemented:

- The synchronous generator at bus 9 is replaced with a DFIG wind power plant. A machine multiplier component, denoted as ‘ Σ ’ in Figure 4.14, is used to scale up the DFIG and simulate a collection of machines;
- A series capacitor is added to the existing transmission line between bus 9 and bus 29, where the compensation degree is variable;
- Finally, the transmission line connecting buses 26 and 29 is modified to connect bus 9 to bus 29, creating a double circuit connection between bus 9 and bus 29. With the uncompensated transmission line out of service, DFIG-SSR could occur.

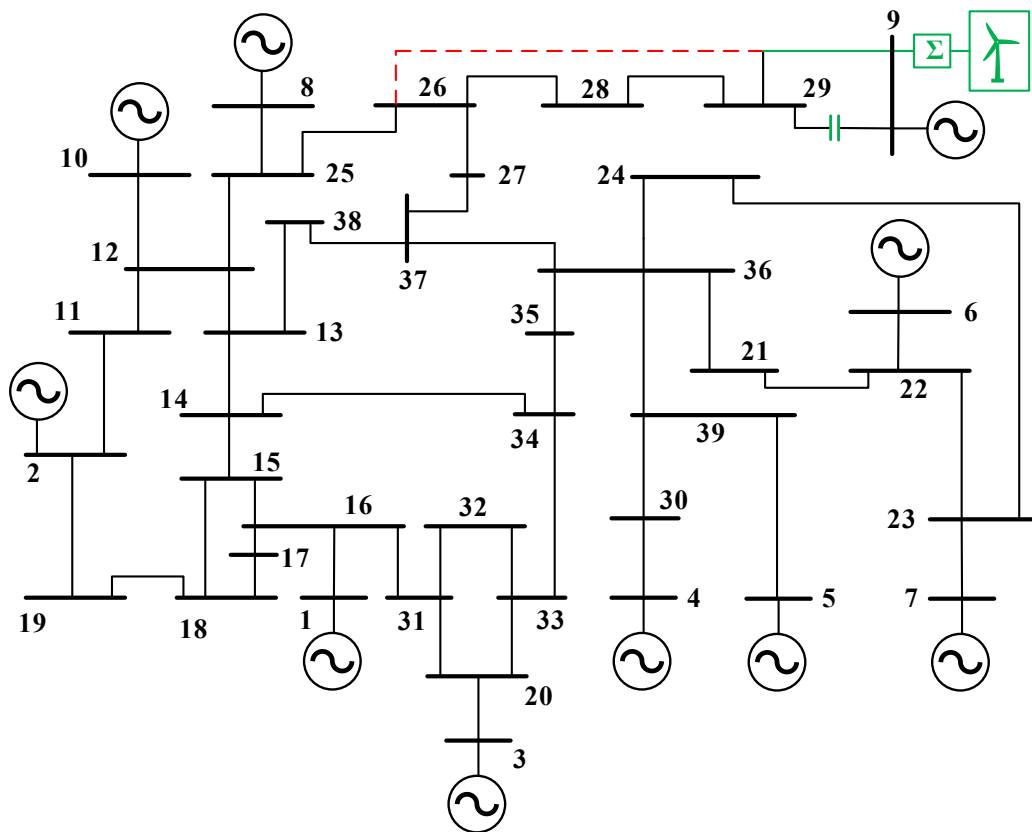


Figure 4.14 Modified IEEE 39-bus system. Components added to the system are in green; components removed are in red.

4.7. CONCLUSIONS

This Chapter presented the models and methodologies that are used for the analysis of DFIG-SSR and for the development of the mitigation solutions. The DFIG EMT model was developed in PSCAD and consists of an average model and a detail model. Furthermore, two grid models are developed to be used in the subsequent analysis. The study model is a single machine infinite bus system and is used for the investigation of DFIG-SSR and for the

development and assessment of mitigation solutions. The developed mitigation solutions are then validated on the second grid model, which is the IEEE 39-bus system.

This Chapter also provided guidelines for the SSO analysis. The impedance based stability analysis is used to screen for DFIG-SSR risks. The source and load impedances are obtained using numerical simulations, where the impedance is calculated after state variables have reached a steady state. The perturbation signal consists of 5 frequencies, has a magnitude of 5% of the fundamental component and has 0° phase shift. As the perturbation signal introduces a cross coupling, the DFIG impedance will always take the cross coupling into account according to (4.8). Finally, the average model is used for development of mitigation solutions due to its faster simulation time. However, it has a lower phase angle in the frequency range up to 30 Hz. To account for this, mitigation solutions will be validated using the detailed model.

REFERENCES

- [1] IEC, “International Standard 61400-27-1: Wind Turbines - Part 27-1: Electrical Simulation Models - Wind Turbines,” Geneva, 2015.
- [2] MIGRATE, “MIGRATE Project Type 3 and Type 4 EMT Model Documentation,” 2017.
- [3] Energynautics, “MIGRATE Project, Type-3 and Type-4 EMT – Model Documentation,” Darmstadt, Germany, 2017.
- [4] R. Hiremath and T. Moger, “Comparison of LVRT Enhancement for DFIG-Based Wind Turbine Generator with Rotor-Side Control Strategy,” in *International Conference on Electrical and Electronics Engineering, ICE3 2020*, 2020, pp. 216–220.
- [5] T. C. Y. Wang, Z. Ye, G. Sinha, and X. Yuan, “Output filter design for a grid-interconnected three-phase inverter,” in *PESC Record - IEEE Annual Power Electronics Specialists Conference*, 2003, vol. 2, pp. 779–784.
- [6] R. J. Piwko and E. V. Larsen, “HVDC system control for damping of subsynchronous oscillations,” *IEEE Trans. Power Appar. Syst.*, vol. PAS-101, no. 7, pp. 2203–2211, 1982.
- [7] M. S. Annakkage, C. Karawita, and U. D. Annakkage, “Frequency scan-based screening method for device dependent sub-synchronous oscillations,” *IEEE Trans. Power Syst.*, vol. 31, no. 3, pp. 1872–1878, May 2016.
- [8] B. Badrzadeh, M. Sahni, Y. Zhou, D. Muthumuni, and A. Gole, “General methodology for analysis of sub-synchronous interaction,” *IEEE Trans. Power Syst.*, vol. 28, no. 2, pp. 1858–1869, 2013.
- [9] J. Sun, “Impedance-based stability criterion for grid-connected inverters,” *IEEE Trans. Power Electron.*, vol. 26, no. 11, pp. 3075–3078, 2011.
- [10] I. Vieto and J. Sun, “Impedance modeling of doubly-fed induction generators,” in *2015 17th European Conference on Power Electronics and Applications, EPE-ECCE Europe 2015*, 2015.
- [11] J. Sun, “Guidelines for the Application of Impedance Modeling and Analysis Methods for Offshore Wind and HVDC Systems,” 2016.
- [12] W. Ren and E. Larsen, “A Refined Frequency Scan Approach to Sub-Synchronous Control Interaction (SSCI) Study of Wind Farms,” *IEEE Trans. Power Syst.*, vol. 31, no. 5, pp. 3904–3912, 2016.
- [13] P. Kundur, N. J. Balu, and M. G. Lauby, *Power System Stability and Control*. McGraw-Hill Education, 1994.
- [14] D. H. R. Suriyaarachchi, U. D. Annakkage, C. Karawita, and D. A. Jacobson, “A procedure to study sub-synchronous interactions in wind integrated power systems,” *IEEE Trans. Power Syst.*, vol. 28, no. 1, pp. 377–384, 2013.
- [15] PSCAD, “IEEE-39 Bus System.”

5. PHASE IMBALANCE COMPENSATION CONCEPT

5.1. INTRODUCTION

The classification of solutions proposed in Chapter 3 for mitigating DFIG-SSR identifies hardware solutions, solutions based on system level coordination, and control solutions. This Chapter focuses on the hardware solutions category. Fixed series compensation has traditionally been used to increase the transfer capacity of a transmission line in a cost effective manner. However, one of the major drawbacks of fixed series compensation is the risk for sub synchronous resonance. Fixed series compensation can be achieved through the classical series compensation concept or the phase imbalance compensation concept. In contrast to the classical series compensation concept, the phase imbalance concept implements an asymmetrical compensation throughout the three phases. This Chapter investigates if and under which conditions the latter can be used for mitigating DFIG-SSR.

As discussed in Chapter 2.3.1, the DFIG-SSR phenomenon is a form of self-excitation and is similar to the induction generator effect. The resistance of the rotor to sub synchronous currents, as viewed from the armature, is negative for a design dependent frequency range. If the net resistance is negative, sub synchronous currents within this frequency range flowing into the armature will be amplified. This adverse interaction can be mitigated by increasing the damping (e.g. through modification of control parameters), or by weakening the rotating MMF produced by the sub synchronous currents in the armature. The phase imbalance compensation concept was initially proposed in [1] for mitigating classical SSR and works on the principle of weakening the rotating MMF. It can be implemented as a series or a parallel scheme.

The published research on the phase imbalance compensation concept is limited. A theoretical case study is presented in [2], where the series phase imbalance concept was implemented to mitigate torsional interactions between a series capacitor compensated transmission line and the shaft system of a turbine-generator.

Parts of this Chapter are published in V. N. Sewdien, J. L. Rueda Torres, and M. A. M. M. van der Meijden, "Evaluation of Phase Imbalance Compensation for Mitigating DFIG-Series Capacitor Interaction," *Energies*, vol. 13, no. 17, p. 4512, 2020.

The radial transmission line had a compensation degree of 13%, which, in a system with a fundamental frequency of 50 Hz, corresponds to a resonance frequency of 18 Hz. The net damping of the transmission system and the turbine-generator at one of the electromechanical modes was negative, which resulted in torsional interactions. These interactions were mitigated by using series phase imbalance compensation in one of the three phases of the transmission line. Furthermore, time domain simulations showed that when the series imbalance compensation was implemented in two phases, it became less effective in mitigating the adverse interactions. The reason for this reduced effectiveness is explored in this Chapter.

In the analysis presented in [3] the parallel phase imbalance concept was deployed in one phase to mitigate torsional interactions between a series compensated transmission line and the torsional masses of turbine-generators. The transmission line was compensated for 65%, corresponding to a resonance frequency of 40 Hz. The parallel imbalance compensation was achieved using a TCSC. The TCSC was further equipped with an SDC to damp out low frequency oscillations (1.2 Hz in this case). A similar analysis is reported in [4] for damping interarea oscillations of 0.78 Hz and 0.46 Hz.

Finally, in [5] the series phase imbalance compensation scheme was implemented in two phases to mitigate DFIG-SSR. The transmission line was compensated for 50%.

Although the aforementioned references have studied some implementation aspects of the series and parallel schemes of the phase imbalance compensation concept, research that methodically investigates the influence of the phase imbalance concept on the impedance behaviour of the grid as well as the resonance frequency of the overall system is lacking. The goal of this Chapter is to systematically and thoroughly investigate to which extent phase imbalance compensation is able to mitigate DFIG-SSR through weakening of the rotating MMF. To this end, two main research gaps are addressed in this Chapter. First, the influence of the series and parallel phase imbalance compensation on the resonance frequency will be investigated. The impact of deploying the imbalance compensation in one or two phases on the system's stability will also be assessed. Second, it will be investigated under which conditions the series and parallel phase imbalance compensation concepts can be used to mitigate DFIG-SSR.

Detailed simulations will be performed using the study model defined in Chapter 4 and shown again for convenience in Figure 5.1. The IEEE 39-bus system, including the modifications described in Chapter 4, is used for the purpose of validating the developed solution on a larger power system.

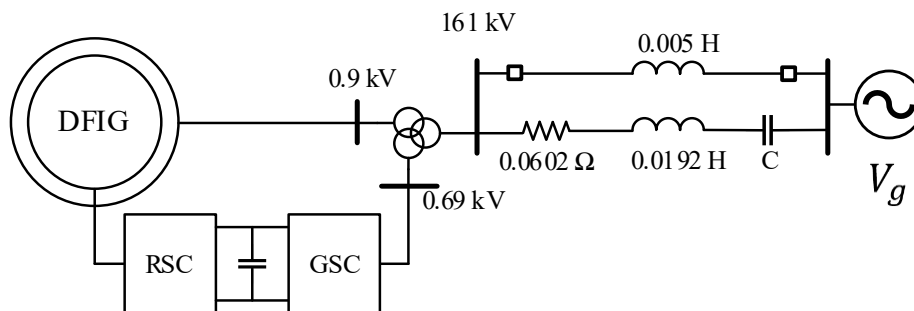


Figure 5.1 Study model for DFIG-SSR mitigation.

5.2. SERIES PHASE IMBALANCE COMPENSATION

5.2.1. CONCEPT DESCRIPTION

The series phase imbalance compensation (PIC) concept is shown in Figure 5.2. In this concept, the capacitor C that is used to compensate the transmission line in the classical compensation concept is complemented by an additional inductor L_A and an additional capacitor C_A . The series PIC can be implemented in one or two phases. The inductor L is the inductance of the uncompensated transmission line.

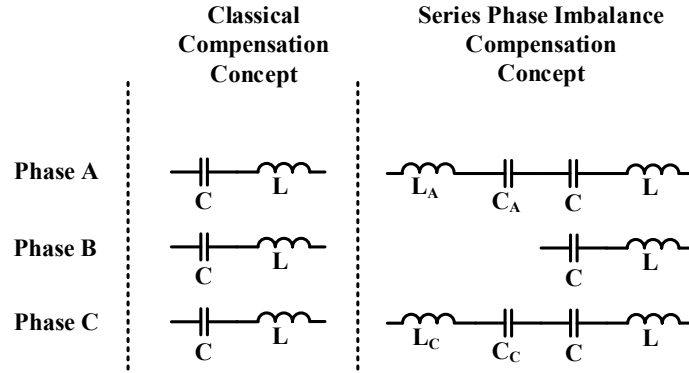


Figure 5.2 Overview of the classical and series phase imbalance compensation schemes.

In the series PIC, the phase wide series compensation is implemented in such a way that the impedance of each phase at the fundamental frequency remains the same under both compensation schemes, i.e. $Z'(\omega_0) = Z''(\omega_0)$, where the prime symbol denotes quantities in the classical compensation scheme and the double prime symbol denotes quantities in the series PIC. In order to achieve this impedance requirement, assume phase A. The relation between capacitor C_A and inductor L_A is derived as follows.

$$\begin{aligned}
 Z''_A(\omega_0) &= Z'_A(\omega_0) \\
 \omega_0(L + L_A) - \frac{C + C_A}{\omega_0 C C_A} &= \omega_0 L - \frac{1}{\omega_0 C} \\
 \omega_0^2 L_A + \frac{1}{C} &= \frac{C + C_A}{C C_A} \therefore \omega_0^2 L_A + \frac{1}{C} = \frac{1}{C} + \frac{1}{C_A}
 \end{aligned} \tag{5.1}$$

The same applies for phase C and solving (5.1) for ω_0 ultimately leads to (5.2). This equation defines the relation between the additional inductance and capacitance for each phase with series PIC. For each phase, a single degree of freedom exists.

$$\omega_0 = \sqrt{1/L_A C_A} = \sqrt{1/L_C C_C} \tag{5.2}$$

The additional capacitors and inductors lead to an imbalanced compensation, and therefore the resonance frequency of each phase will be different. With series PIC deployed in phases A and C (see Figure 5.2), $\omega''_{r,A} \neq \omega''_{r,B} \neq \omega''_{r,C}$. The resonance frequency is then defined as (5.3),

(5.4) and (5.5) for respectively phases A , B and C . As no additional impedances are included in phase B , it should be noted that $\omega''_{r,B} = \omega'_{r,B}$.

$$\omega''_{r,A} = \sqrt{\frac{1}{L_{eq,A}C_{eq,A}}} = \sqrt{\frac{1}{(L + L_A)\frac{CC_A}{C + C_A}}} \quad (5.3)$$

$$\omega''_{r,A} = \sqrt{\frac{C + C_A}{CC_A(L + L_A)}}$$

$$\omega''_{r,B} = \omega'_{r,B} = \sqrt{\frac{1}{LC}} \quad (5.4)$$

$$\omega''_{r,C} = \sqrt{\frac{C + C_C}{CC_C(L + L_C)}} \quad (5.5)$$

Figure 5.3 conceptually shows the vector and phasor diagrams of the phase impedances at sub synchronous frequency $\omega'_{r,B}$ for the classical as well as the series PIC concepts. In the classical compensation concept, the phase impedances are identical. At $\omega'_{r,B}$ these impedances are equal to the damping (Figure 5.3a) and result in a balanced phasor (Figure 5.3c). For the series PIC, the phase impedances at $\omega''_{r,B}$ are different (Figure 5.3b), which lead to an unbalanced phasor (Figure 5.3c).

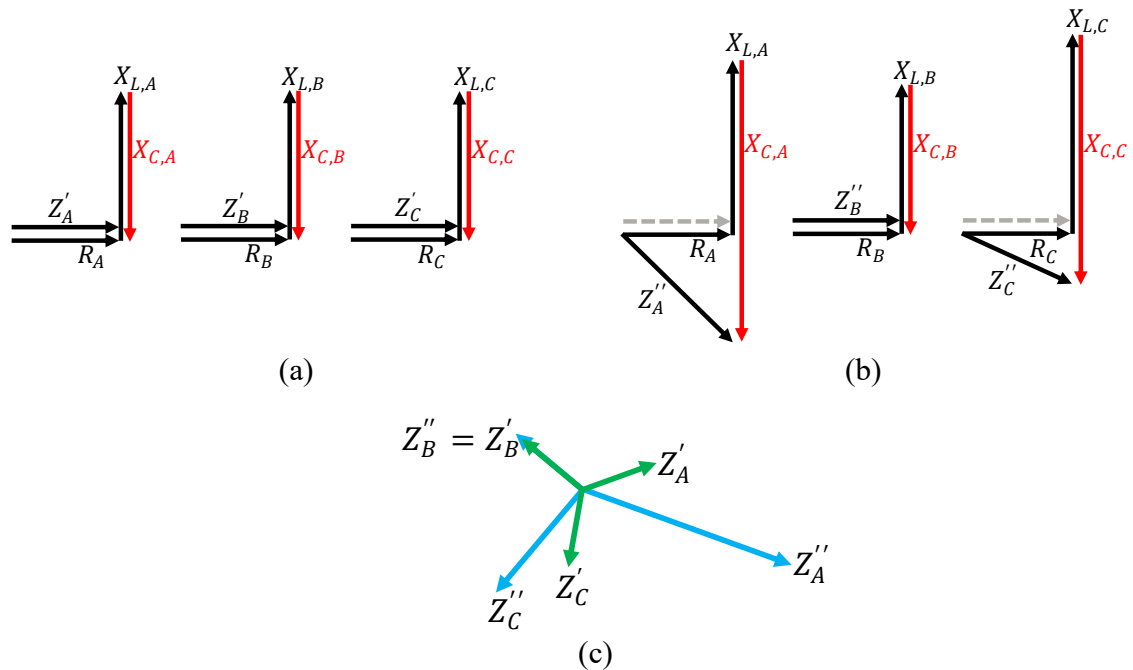


Figure 5.3 Vector diagram of the phase impedances at sub synchronous frequency for (a) classical series compensation and (b) phase imbalance compensation. For both cases, the phasor diagram of the impedance is shown as well (c). At sub synchronous frequencies, the phases that are compensated using the imbalance concept have different impedances compared to the respective phases that use the classical compensation concept.

The unbalanced phase impedances create a non-uniformly distributed MMF at $\omega''_{r,B}$. This MMF is defined as given in (5.6).

$$\begin{aligned} MMF_{total} &= \sum_{i=A}^c MMF_i \\ MMF_A &= K\hat{I}_A \cos(\omega t) \cos \theta \\ MMF_B &= K\hat{I}_B \cos(\omega t) \cos \theta \\ MMF_C &= K\hat{I}_C \cos(\omega t) \cos \theta \end{aligned} \quad (5.6)$$

Without series compensation, $MMF(\omega''_{r,B})$ is zero. With the classical compensation, $MMF(\omega'_{r,B})$ in each phase is identical, as the maximum current \hat{I} in each phase is the same (due to the same Z' in each phase). On the other hand, for each phase that implements an asymmetrical compensation, \hat{I} is different depending on Z'' , which in turn is a function of the degree of asymmetry in that respective phase. As such, the PIC is able to alter $MMF(\omega''_{r,B})$ at sub synchronous frequencies, and, therefore, potentially mitigate DFIG-SSR: the larger Z'' , the smaller \hat{I} and the smaller $MMF(\omega''_{r,B})$. With decreasing $MMF(\omega''_{r,B})$, the resulting sub synchronous oscillations will be smaller.

In the following, it is investigated to what extent the series PIC concept is able to eliminate DFIG-SSR. The impedance of the DFIG (see Chapter 4) plays a key role in this investigation. In order to gain an understanding of how the series PIC alters the resonance behaviour of the power system, an analytical, mathematical model is derived that describes the relation between the inductance and capacitance of the imbalanced phase and the corresponding resonance frequency. The starting point for this derivation is $\omega''_{r,B}$, as $\omega''_{r,B} = \omega'_{r,B}$. Assume phase A. If $\omega''_{r,A}$ differs from $\omega''_{r,B}$ by $\Delta\omega_r$, then the relation between $\omega''_{r,A}$ and $\omega''_{r,B}$ is given by (5.7).

$$\omega''_{r,A} = \omega''_{r,B} + \Delta\omega_r = \omega'_{r,B} + \Delta\omega_r = \sqrt{\frac{C + C_A}{CC_A(L + L_A)}} \quad (5.7)$$

Substituting (5.2) in (5.7) yields (5.8).

$$\omega'_{r,B} + \Delta\omega_r = \sqrt{\frac{C + C_A}{CC_AL + \frac{C}{\omega_0^2}}} \therefore \omega'_{r,B}{}^2 + 2\Delta\omega_r\omega'_{r,B} + \Delta\omega_r{}^2 = \frac{C + C_A}{CC_AL + \frac{C}{\omega_0^2}} \quad (5.8)$$

Solving (5.8) for C_A results in (5.9).

$$C_A = C \left[\left(\frac{\omega'_{r,B} + \Delta\omega_r}{\omega_0} \right)^2 - 1 \right] \frac{1}{1 - LC(\omega'_{r,B} + \Delta\omega_r)^2} \quad (5.9)$$

Substituting $LC = \frac{1}{\omega'_{r,B}{}^2}$ in (5.9) gives (5.10).

$$C_A = C \left[\left(\frac{\omega'_{r,B} + \Delta\omega_r}{\omega_0} \right)^2 - 1 \right] \frac{1}{1 - \left(\frac{\omega'_{r,B} + \Delta\omega_r}{\omega'_{r,B}} \right)^2} \quad (5.10)$$

Finally, solving (5.10) results in (5.11).

$$C_A(\Delta\omega_r) = C \left[\frac{(\omega'_{r,B} + \Delta\omega_r)^2}{\omega_0^2 - \left(\frac{\omega_0(\omega'_{r,B} + \Delta\omega_r)}{\omega'_{r,B}} \right)^2} - \frac{1}{1 - \left(\frac{\omega'_{r,B} + \Delta\omega_r}{\omega'_{r,B}} \right)^2} \right] \quad (5.11)$$

The relation between C_A , $\Delta\omega_r$ and k is derived by substituting $\omega_r = \sqrt{k\omega_0^2}$ in (5.11), which ultimately results in (5.12).

$$C_A(k, \Delta\omega_r) = C \left[\frac{(\sqrt{k\omega_0^2} + \Delta\omega_r)^2}{\omega_0^2 - \left(\frac{\omega_0(\sqrt{k\omega_0^2} + \Delta\omega_r)}{\sqrt{k\omega_0^2}} \right)^2} - \frac{1}{1 - \left(\frac{\sqrt{k\omega_0^2} + \Delta\omega_r}{\sqrt{k\omega_0^2}} \right)^2} \right] \quad (5.12)$$

The degree of asymmetry Q for phase A is then defined as given in (5.13). The same relation holds for phase C .

$$Q(k, \Delta\omega_r) = \frac{C_A(k, \Delta\omega_r)}{C} \quad (5.13)$$

$$Q(k, \Delta\omega_r) = \frac{(\sqrt{k\omega_0^2} + \Delta\omega_r)^2}{\omega_0^2 - \left(\frac{\omega_0(\sqrt{k\omega_0^2} + \Delta\omega_r)}{\sqrt{k\omega_0^2}} \right)^2} - \frac{1}{1 - \left(\frac{\sqrt{k\omega_0^2} + \Delta\omega_r}{\sqrt{k\omega_0^2}} \right)^2}$$

Figure 5.4 graphically illustrates (5.13) and shows the degree of asymmetry Q required to achieve different compensation levels k and different values of Δf_r . As Q , which is always positive, results in an additional series capacitor, the resonance frequency f_r will always increase: Δf_r is always positive and it is therefore not possible to reduce the resonance frequency below $\omega''_{r,B}$ using the series PIC scheme. Furthermore, for any given k , Δf_r is inversely proportional to Q .

From Figure 5.4 it is also observed that an imposed Δf_r in the series PIC can be achieved by modifying either k or Q in the design phase. For fixed Q , modification of k (which is a quantity at f_0) results in an altered active power transfer limit and altered Δf_r . For fixed k , modification of Q results only in an altered sub synchronous behaviour (i.e. altered Δf_r), as $Z''(\omega_0) = Z'(\omega_0)$ should be respected for each value of Q .

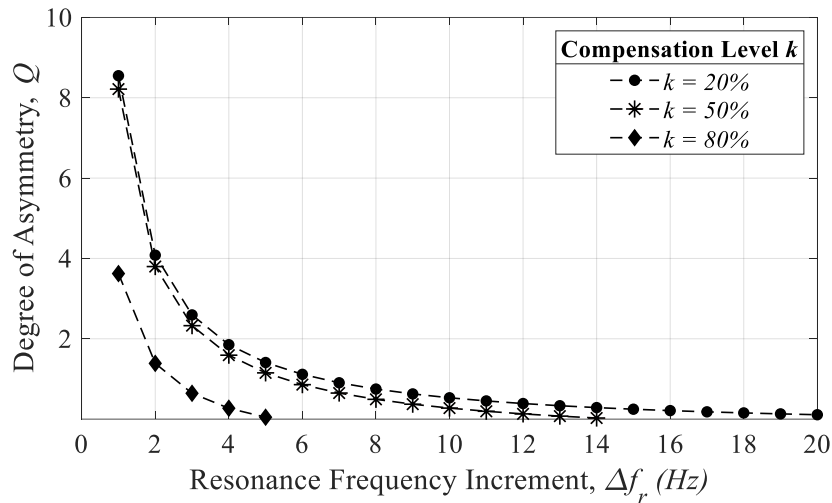


Figure 5.4 Influence of k and Δf_r on the required degree of asymmetry Q .

5.2.2. SERIES PIC EVALUATION FOR DFIG-SSR MITIGATION

To investigate the effectiveness of the series PIC scheme in mitigating DFIG-SSR, the study model as described in Chapter 4 and shown in Figure 5.1 is used. In this model, the resonance frequency f_r is arbitrarily set to 30 Hz ($k=36\%$).

Prior to evaluating the effectiveness of the series PIC in mitigating DFIG-SSR, its influence on the impedance characteristic of the transmission line in the study model is assessed. To this end, low Q values are chosen as their effect on the impedance characteristic is more pronounced. The results of this assessment are shown in Figure 5.5. In Figure 5.5a phase A is equipped with the one phase series PIC and the phase A impedances under 0.1, 0.25, and 0.5 degrees of asymmetry are shown. It is observed that higher Q values indeed decrease Δf_r , which is in line with (5.13) and the findings from Figure 5.4. In Figure 5.5b the series PIC is implemented in phases A and C with Q_A and Q_C respectively 0.2 and 0.5. Substituting these values in (5.13) results in Δf_r of 14 Hz and 10 Hz for respectively phase A and phase C. The same results are achieved using the perturbation method based frequency scanning and are shown in Figure 5.5b.

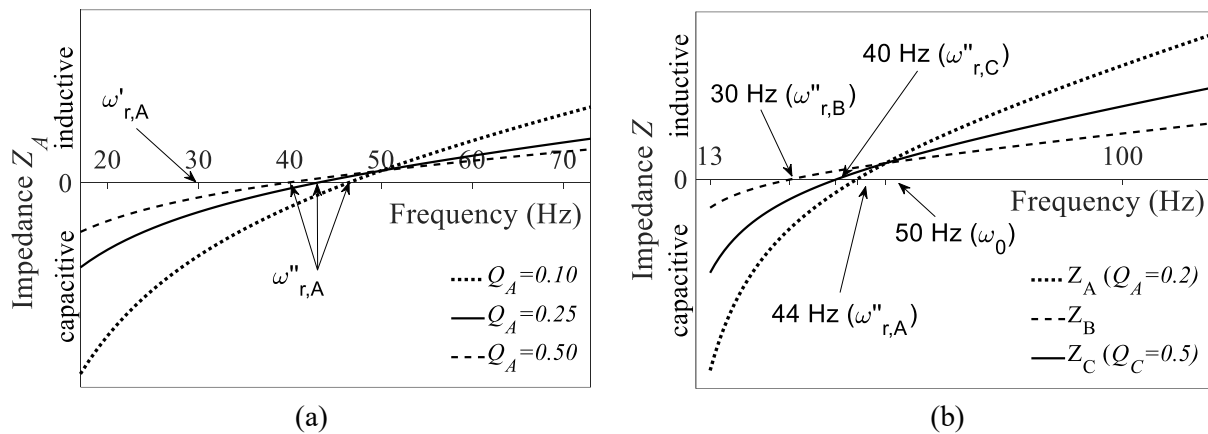


Figure 5.5 Influence of the degree of asymmetry Q on the resonance frequency as seen from the point of common coupling. (a) one phase series PIC in phase A; (b) two phase series PIC in phases A and C.

When the DFIG is added to the transmission system, the impedance of the overall system is changed, following which the actual f_r will be different from 30 Hz. Connecting the DFIG to the classical series compensated transmission line results in a resonance frequency of the overall system of 10 Hz, denoted as $f_{r,classical}$ in Figure 5.6. The inductances of the transformers and the DFIG machine, the inductance and shunt capacitance of the inverter filter, and the controller parameters are the reasons for the reduction in f_r . When phase A is compensated using series PIC with $Q=0.5$, f_r increases to 13 Hz and is denoted as $f_{r,series PIC}$ in Figure 5.6.

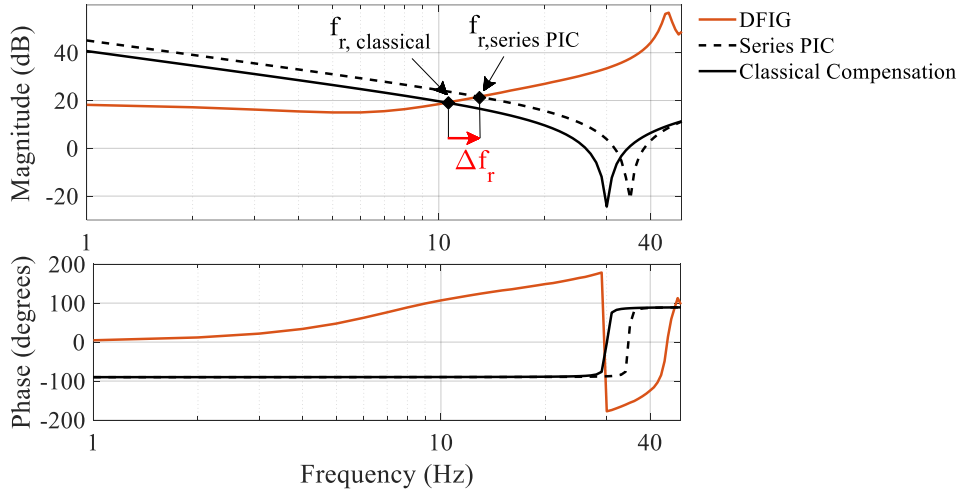


Figure 5.6 Positive sequence impedance and resonance frequency of the overall system using classical compensation and series PIC. The series PIC is implemented in phase A with Q of 0.5.

To identify degrees of asymmetry capable of mitigating DFIG-SSR, two sets of optimisations were performed. In the first optimisation, the imbalance compensation was only implemented in phase A. The objective function of this optimisation is given by (5.14), where parameter η represents the oscillation energy and is introduced to monitor the performance of the optimisation. In the second optimisation, the imbalance compensation was implemented in phases A and C. The objective function is given by (5.15). In both cases, the starting time t_1 is set at a time when the state variables have reached steady state, similar to Chapter 4.3.1. An optimisation is chosen over a brute force approach, as the former can quickly and efficiently search through wide parameter ranges.

$$\begin{aligned} \text{minimise } \eta &= \int_{t_1}^{t_1+3} (P_{ref}(t) - P_{measured}(t)_{Q_A})^2 dt \\ \text{subject to } &0.01 < Q_A < 100 \end{aligned} \quad (5.14)$$

$$\begin{aligned}
 & \text{minimise } \eta = \int_{t_1}^{t_1+3} (P_{ref}(t) - P_{measured}(t)_x)^2 dt \\
 & \text{subject to} \\
 & \mathbf{x}_{min} \leq \mathbf{x} \leq \mathbf{x}_{max} \\
 & \text{where} \\
 & \mathbf{x} = [Q_A, Q_C] \\
 & 0.01 < Q_A, Q_C < 100
 \end{aligned} \tag{5.15}$$

Based on extensive empirical analysis (as will be shown in Chapter 6 for controller tuning of the rectifier), it was found that DFIG-SSR can be considered mitigated when η is smaller than 0.07, as this represents a case with negligible oscillation energy. The empirical method for determining a threshold is also used in screening methods for DDSSO, e.g. unit interaction factor [6] and radiality factor [7].

Figure 5.7 illustrates a successful case where DFIG-SSR is mitigated and shows the response of the DFIG to a fault before and after tuning of the rectifier parameters[†]. After one second a switching action caused a radial connection of the DFIG with the series capacitor, resulting in DFIG-SSR for the case without tuning. The value of parameter η , in this case, is 0.01. As a reference, $\eta=0.215$ under the classical series compensation scheme

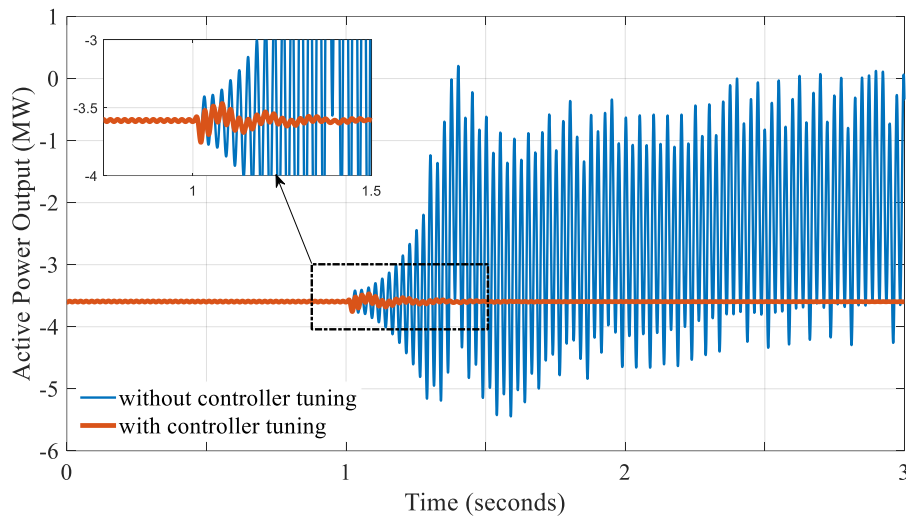


Figure 5.7 Successful rectifier controller tuning ($\eta = 0.01$).

The optimisation results are given in Figure 5.8a for the one phase PIC and in Figure 5.8b for the two phase PIC.

[†] Rectifier tuning is extensively discussed in Chapter 6.

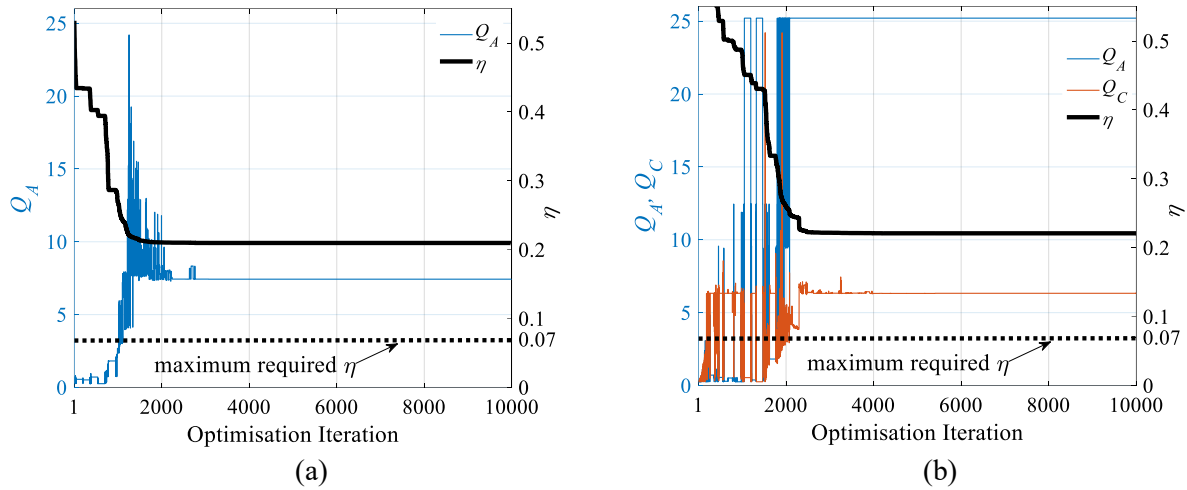


Figure 5.8 Optimisation of Q with the goal to mitigate DFIG-SSR. Imbalance compensation is applied in (a) one phase and (b) two phases.

In none of the optimisations η converged to a value smaller than 0.07 and consequently no adequate degree of asymmetry capable of mitigating DFIG-SSR was identified. Even more so, for the investigated DFIG, the series PIC consistently performed either the same as or worse than the classical series compensation scheme. This is concluded by observing the phase margins in Figure 5.9. For all the considered cases, the phase margin decreases even further compared to the classical compensation scheme.

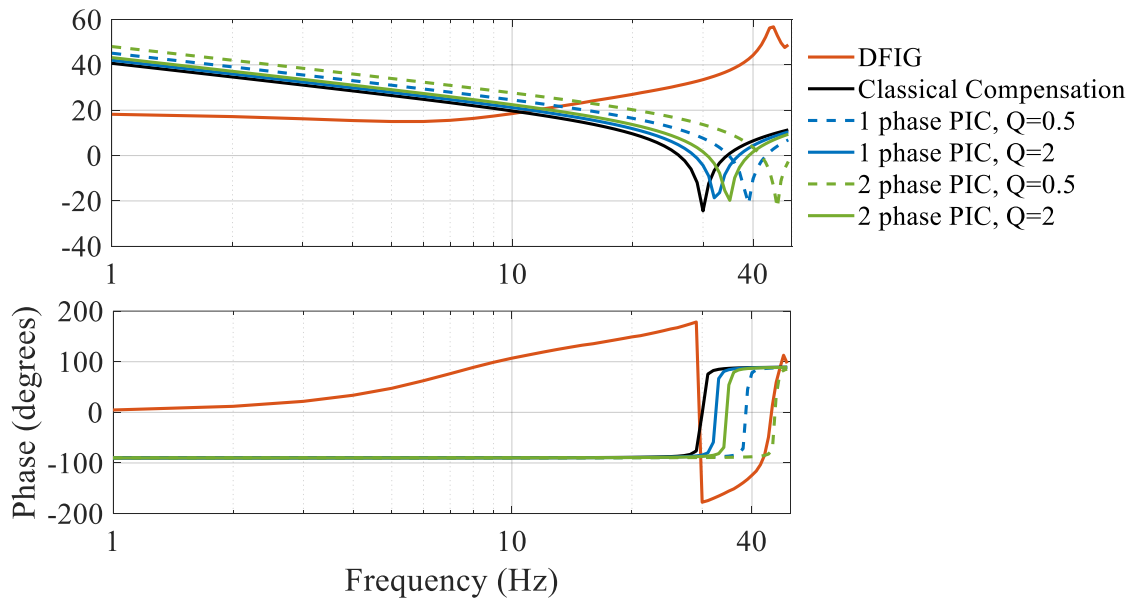


Figure 5.9 Positive sequence impedance of DFIG and compensated transmission line. The transmission line is compensated using the classical and series PIC concepts.

Two other conclusions can be drawn from Figure 5.9. First, independent of whether the series PIC is implemented in one or two phases, a smaller Q results in larger Δf_r . Considering the impedance of the DFIG, such an increase reduces the phase margin and consequently further deteriorates the stability. Second, independent of Q , series PIC implemented in 2 phases

consistently results in a larger Δf_r compared to one phase series PIC. Again, considering the impedance of the DFIG, larger Δf_r leads to reducing phase margins.

Another way to assess the influence of Q on DFIG-SSR in more detail, is to observe how the MMF at f_r , $MMF(f_r)$, develops with changes in Q . Using (5.6), $MMF(f_r)$ can be observed by observing the peak current \hat{I} : the higher \hat{I} , the stronger $MMF(f_r)$ and the larger the resulting η , i.e. the poorer the capability for mitigating DFIG-SSR. Different levels of asymmetry in phase A were evaluated. Table 5.1 provides the resonance frequency and maximum phase current \hat{I}_A for each of these Q_A . For comparison purposes, the results from the classical compensation scheme are included as well. Two observations can be made. First, it is confirmed again that f_r increases with Q , which is in line with (5.13). Detailed time domain EMT simulations for the classical and series phase imbalance concepts are shown in Figure 5.10, showing that the series PIC indeed increases the frequency of the observed resonance. Second, with decreasing Q_A (i.e. increasing f_r), \hat{I}_A increases, implying that with smaller degrees of asymmetry, $MMF(f_r)$ gets larger. This Q_A - \hat{I} - $MMF(f_r)$ relation explains why η is relatively large for small values of Q_A and small for larger values of Q_A .

Table 5.1 Maximum current at f_r for phase A for different levels of asymmetry Q .

Q_A	$f_{r,A}$ (Hz)	$\hat{I}_{f_{r,A}}$ (kA)
0.1	20	0.383
0.2	16	0.368
0.5	14	0.279
2.5	13	0.231
5.0	12	0.226
classical compensation	10	0.214

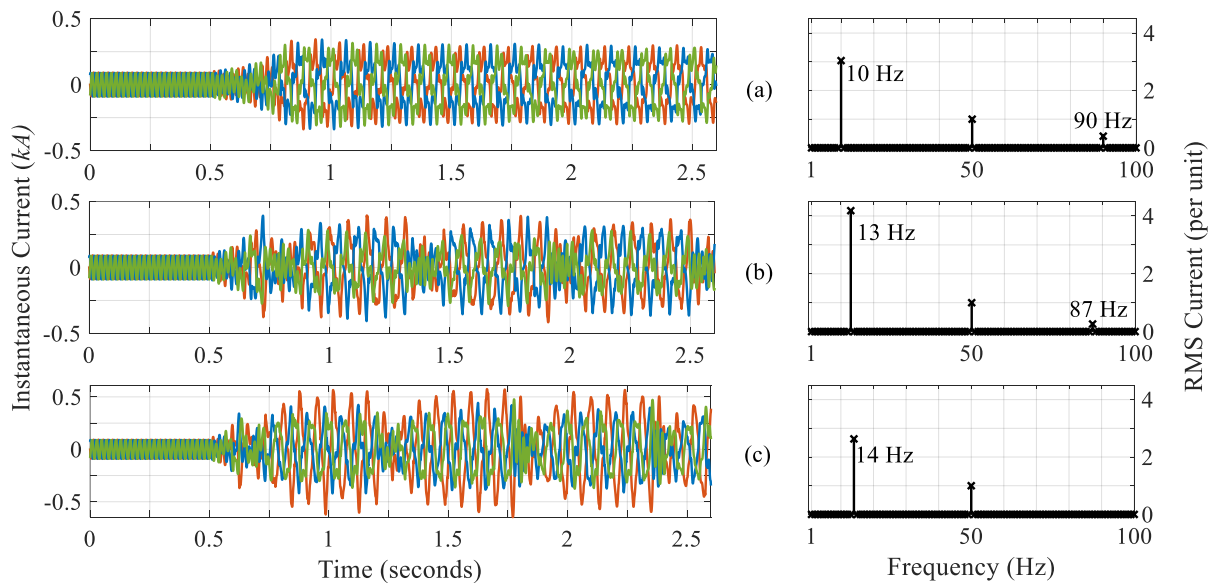


Figure 5.10 Detailed time domain EMT simulations for series PIC. (a) classical compensation, (b) one phase series PIC with Q of 0.5 and (c) two phase series PIC with Q of 0.5.

Finally, to explain why \hat{I} is increasing as Q_A decreases, it is necessary to investigate the damping characteristic of the DFIG. Using the perturbation based dynamic frequency scan (see Chapter 4.4), the damping of the DFIG was estimated at wind speeds 6 m/s (i.e. below nominal wind speed), 10 m/s (i.e. at nominal wind speed) and 20 m/s (i.e. above nominal wind speed). The results are shown in Figure 5.11, leading to the following two conclusions. First, considering f_r of 10 Hz, any Δf_r achieved by means of series imbalance compensation where f_r'' remains in the negative resistance region, will deteriorate the damping provided by the DFIG. To achieve an f_r'' outside the negative resistance region requires Q values which are not economical for practical applications. The negative resistance region, defined as the sub synchronous frequency range where the DFIG's damping is negative, is given in Table 5.2 for different wind speeds. Second, for the same Q , the damping worsens with decreasing wind speeds. This is related to the slip, as was discussed in Chapter 2.3.1. Therefore, the design of a mitigation solution based on the PIC needs to be validated across operating conditions with all possible expected wind speeds.

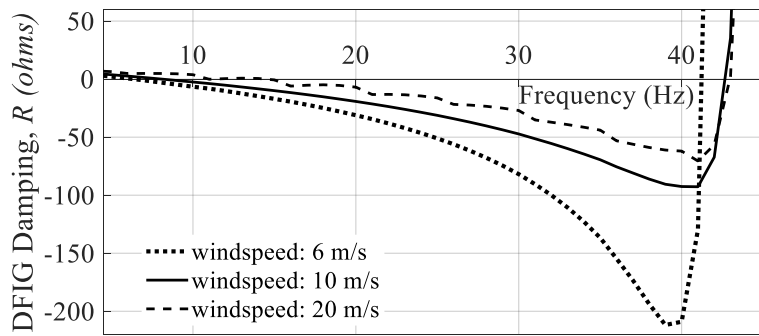


Figure 5.11 DFIG damping under different wind speed conditions.

Table 5.2 Negative resistance region of DFIG under different wind speed conditions.

Wind speed (m/s)	f_{min} (Hz)	f_{max} (Hz)
5	6	41
6	7	41
7	7	42
8	8	42
9	8	43
10	8	43
15	10	43

The analysis conducted so far focused on the capability of the series PIC to mitigate DFIG-SSR. The analytical model developed for the series PIC enabled to understand how the resonance frequency of the compensated line varies for different degrees of asymmetry. Taking the DFIG impedance and the study model into account, it is concluded that neither the one phase nor the two phase series PIC can mitigate DFIG-SSR. It was found that the shift in resonance frequency is always positive, independent of the degree asymmetry. Furthermore, the change in resonance frequency was found to be inversely proportional to the degree of

asymmetry. Finally, the resulting increase in resonance frequency is larger when the series PIC is implemented in two phases. As the negative resistance of the DFIG becomes more negative with an increase in the resonance frequency, it can be concluded that as long as the resonance frequency resulting from the series PIC is within the negative resistance region of the DFIG, the stability of the system decreases even further compared to when classical compensation is used. The deterioration of the stability is more pronounced when the series PIC is deployed in two phases.

The next Section will investigate the capability of the parallel PIC in mitigating DFIG-SSR.

5.3. PARALLEL PHASE IMBALANCE COMPENSATION

5.3.1. CONCEPT DESCRIPTION

The parallel scheme is the second type of PIC and is illustrated in Figure 5.12. In this scheme, the capacitor C of the classical compensation concept is divided in C_1 and C_2 , where C , C_1 , and C_2 are governed by $C = \frac{C_1 C_2}{C_1 + C_2}$.

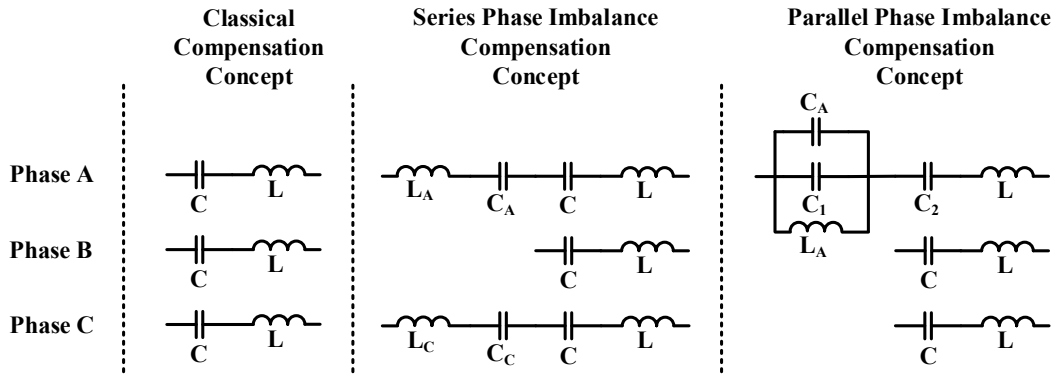


Figure 5.12 Series and parallel phase imbalance compensation schemes.

In line with the impedance requirement imposed on the series PIC, the parallel PIC should also ensure that the impedance of all three phases at 50 Hz is identical. Considering the parallel PIC as implemented in Figure 5.12, the impedance requirement is translated to $X_A''(\omega_0) = X_B'(\omega_0)$. The equivalent reactance $X_{eq,1}(\omega_0)$ of the parallel resonance circuit of phase A is defined as given in (5.16).

$$\left. \begin{aligned} X_{C,eq}(\omega_0) &= -\frac{1}{\omega_0(C_A + C_1)} \\ X_{L,A}(\omega_0) &= \omega_0 L_A \\ X_{eq,1} &= \frac{X_{L,A} X_{C,eq}}{X_{L,A} + X_{C,eq}} \end{aligned} \right\} \Rightarrow X_{eq,1}(\omega_0) = \frac{\omega_0 L_A \frac{-1}{\omega_0(C_A + C_1)}}{\omega_0 L_A - \frac{1}{\omega_0(C_A + C_1)}} \quad (5.16)$$

$$= \frac{-L_A}{\omega_0 L_A (C_A + C_1) - \frac{1}{\omega_0}}$$

The total reactance $X_A''(\omega_0)$ of phase A is given by (5.17).

$$X_A''(\omega_0) = X_{eq,1}(\omega_0) - \frac{1}{\omega_0 C_2} + \omega_0 L = \omega_0 L - \frac{1}{\omega_0 C_2} - \frac{L_A}{\omega_0 L_A (C_A + C_1) - \frac{1}{\omega_0}} \quad (5.17)$$

The impedance requirement $X_A''(\omega_0) = X_B''(\omega_0)$ leads to (5.18).

$$\begin{aligned} \omega_0 L - \frac{1}{\omega_0 C_2} - \frac{L_A}{\omega_0 L_A (C_A + C_1) - \frac{1}{\omega_0}} &= \omega_0 L - \frac{1}{\omega_0 C} \\ \frac{L_A}{\omega_0 L_A (C_A + C_1) - \frac{1}{\omega_0}} &= \frac{1}{\omega_0 C} - \frac{1}{\omega_0 C_2} \\ \frac{L_A}{L_A (C_A + C_1) - \frac{1}{\omega_0^2}} &= \frac{C_2 - C}{CC_2} \end{aligned} \quad (5.18)$$

Solving (5.18) for L_A leads to (5.19). Next, solving (5.19) for ω_0^2 leads to (5.20).

$$L_A = \frac{C_2 - C}{CC_2} L_A (C_A + C_1) - \frac{C_2 - C}{CC_2} \frac{1}{\omega_0^2} \quad (5.19)$$

$$\frac{1}{\omega_0^2} = L_A C_A + L_A C_1 - L_A \frac{C_2 C}{C_2 - C} \quad (5.20)$$

$$C = \frac{C_1 C_2}{C_1 + C_2} \therefore C_1 = \frac{C_2 C}{C_2 - C} \quad (5.21)$$

Substituting C_1 as defined by (5.21) into (5.20), gives (5.22). It is worth noting that the impedance requirement results in the same L_A - C_A relation for the series and parallel schemes. In contrast to the series PIC, each phase now has two degrees of freedom, namely C_1/C_2 and C_A/C_1 .

$$\omega_0 = \sqrt{1/L_A C_A} \quad (5.22)$$

The impedance of phase A with classical compensation, series PIC, and parallel PIC is shown in Figure 5.13. In line with the previous simulations, k in the classical compensation scheme is chosen to produce a series resonance at 30 Hz. The series PIC is implemented in one phase with a Q -value (C_A/C) of 0.5. The parallel PIC is also implemented in one phase, with C_1/C_2 and Q (C_A/C_1) of 0.5. This figure indeed illustrates that the impedance at ω_0 is the same for all three compensation concepts and that the steady state behaviour at ω_0 is identical for the aforementioned compensation concepts.

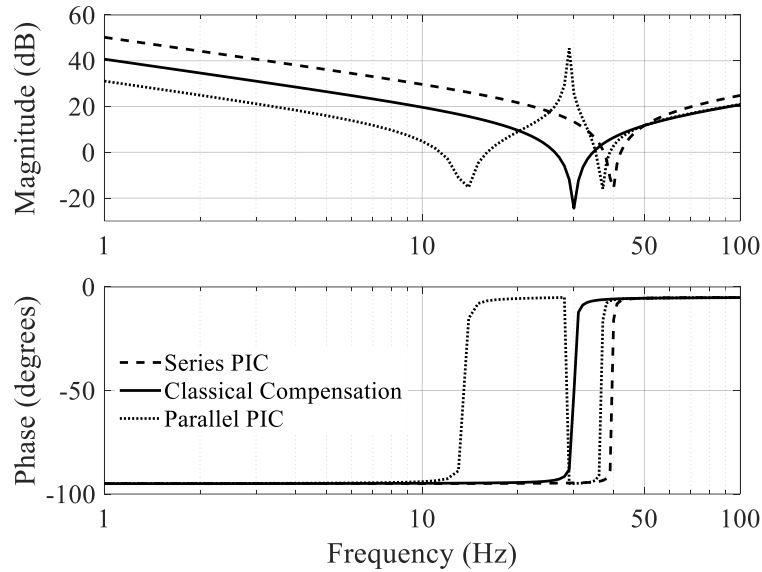


Figure 5.13 Impedance of phase A compensated using the classical and series and parallel phase imbalance concepts.

The parallel PIC concept is a combination of parallel and series resonance schemes and creates multiple resonance frequencies. In bode plots, a series resonance is observed at the frequency where the magnitude curve dips and the phase curve crosses zero with a positive slope. Likewise, a parallel resonance occurs at the frequency where the magnitude curve peaks and the phase curve crosses zero with a negative slope. For the parallel PIC described above, one parallel resonance at 29 Hz and two series resonances at 14 Hz and 37 Hz are identified in the sub synchronous frequency range.

The next Section will evaluate for several parallel PIC schemes their capability to mitigate DFIG-SSR.

5.3.2. PARALLEL PIC EVALUATION FOR DFIG-SSR MITIGATION

The impedance based stability method is used next to screen for potential DFIG-SSR risks. The frequencies f_r at which the magnitude curves of the DFIG and the transmission grid intersect can potentially lead to DFIG-SSR. When the phase margin at these frequencies is negative, DFIG-SSR will occur. The phase margin is a measure to quantify the system's stability, where the larger the phase margin, the more stable the system will be.

The positive sequence impedances of the DFIG and the transmission grid are shown in Figure 5.14. The grid impedance is shown for compensation using the classical and the one phase series and parallel compensation schemes and is identical to Figure 5.13. A number of observations can be made. First, when the grid is compensated using the classical compensation concept, the overall system has a resonance at approx. 10 Hz, denoted as $f_{r,classical}$ in the figure. Second, when series PIC is used for the compensation, the resonance frequency of the overall system increases to approx. 13 Hz, denoted as $f_{r,series\ PIC}$. The phase margin also reduces from -17° using classical compensation to -34° using series PIC, implying that the latter is more unstable than the former. These observations are in line with the conclusions of Section 5.2.2. Finally, for the considered parallel PIC scheme (i.e. $\frac{C_1}{C_2} = \frac{C_A}{C_1} = \frac{1}{2}$), the impedance based stability

analysis identified one series resonance and one parallel resonance in the overall system. The series resonance, denoted as $f_{r,parallel PIC 1}$, occurs at 9 Hz and has a phase margin of -10° . The parallel resonance is denoted as $f_{r,parallel PIC 2}$ and occurs at 29 Hz. The corresponding phase margin is -88° .

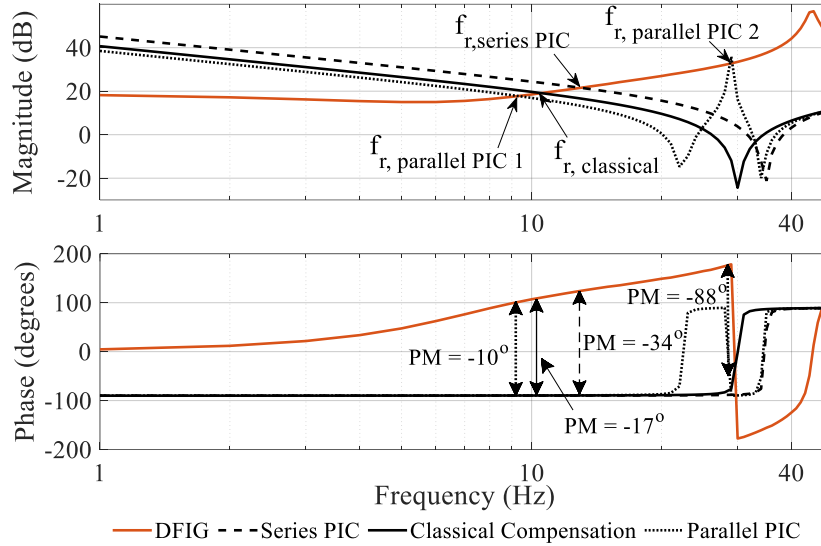


Figure 5.14 Positive sequence impedance of DFIG and compensated grid.

All of the identified resonances are unstable as their phase margins are negative. Detailed analysis using time domain EMT simulations confirm this. Figure 5.15 shows the instantaneous three phase current waveforms and the accompanying harmonic spectrum for series compensation using the classical, series PIC, and parallel PIC concepts. The resonance frequencies identified using the impedance based stability analysis match the resonance frequencies observed using the detailed EMT simulations. For the parallel PIC, both the series and parallel resonances are observed. The series resonances introduce an additional frequency component in the super synchronous frequency range. This coupling frequency occurs due to the asymmetry in the dq coordinate control and equals $2f_0 - f_r$.

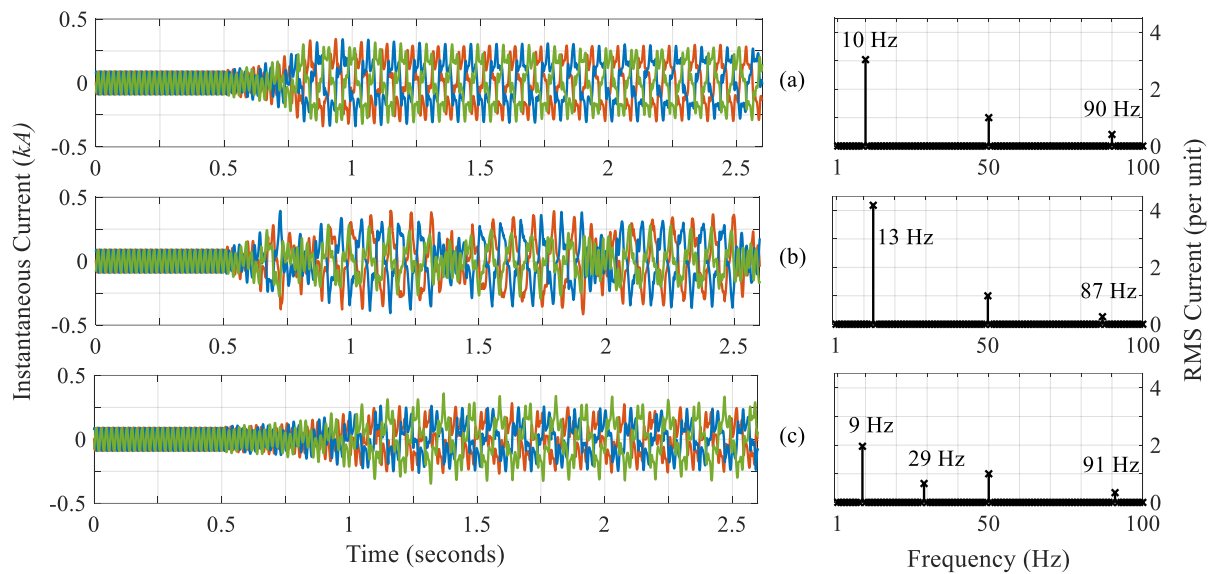


Figure 5.15 Measured instantaneous current and its harmonic spectrum. (a) classical compensation, (b) one phase series PIC and (c) one phase parallel PIC.

The previous analysis focused on the performance comparison of the classical and series and parallel PIC compensation concepts. The next analysis aims at identifying the influence of the ratios C_A/C_1 and C_1/C_2 in the parallel PIC on the impedance behaviour of the grid and how they interact with the DFIG impedance. To this end, screening studies are performed using C_A/C_1 -ratios of 0.25, 0.5, 1, and 2 and C_1/C_2 -ratios of 0.5, 1, and 2. The screening results are depicted in Figure 5.16 and show that for all the investigated cases, a series resonance of approx. 9 Hz may exist in the overall system. Furthermore, the frequency of the parallel resonance in the compensated grid is mainly influenced by the C_A/C_1 ratio, whereas its magnitude is mainly affected by C_1/C_2 . Finally, apart from the series resonance at 9 Hz, the screening revealed a total of three parallel resonances as given in Table 5.3.

Table 5.3 Identified parallel resonances.

f_r (Hz)	C_A/C_1	C_1/C_2
22	0.25	0.5
29	0.5	0.5
29	0.5	1.0

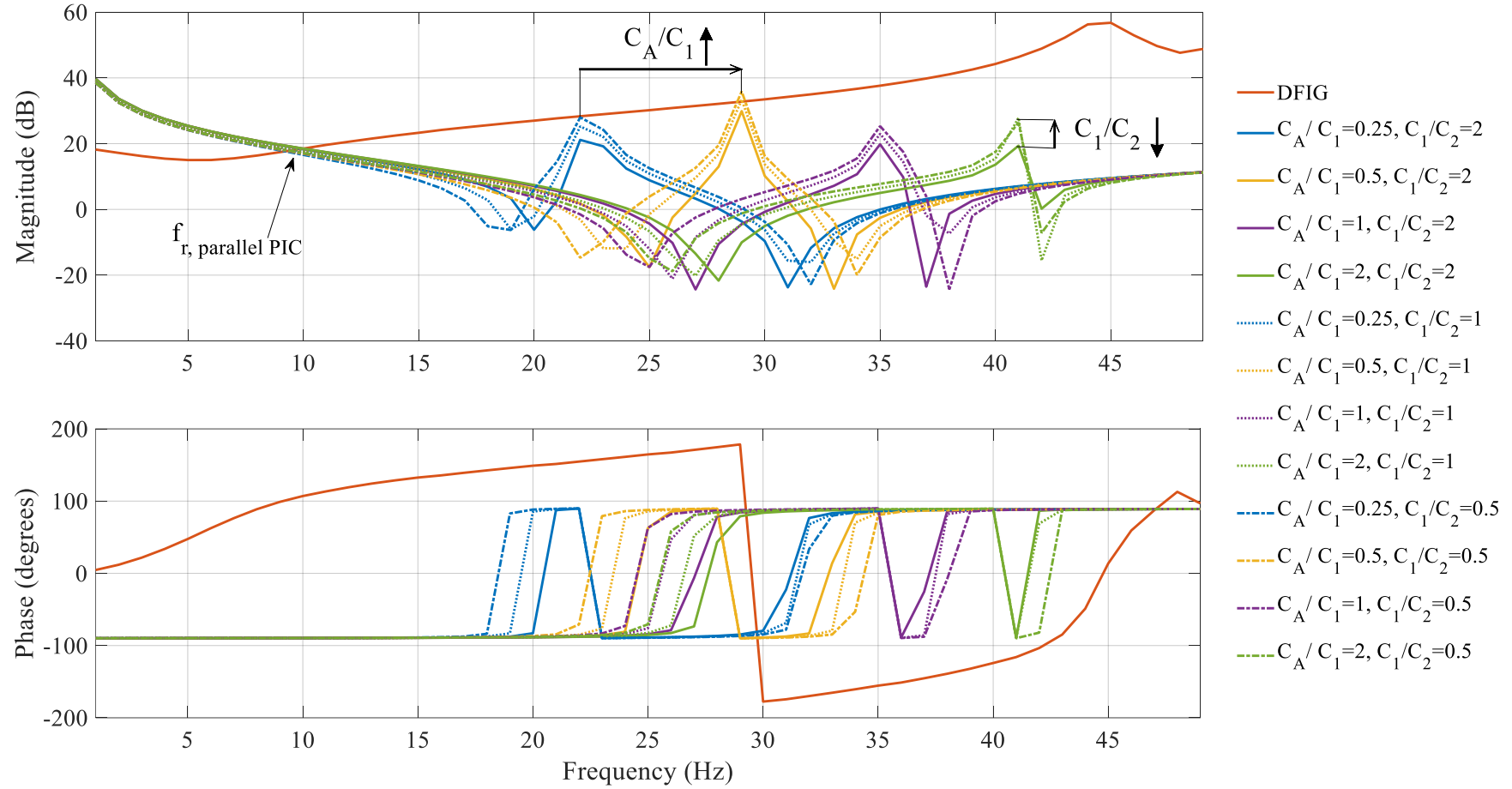


Figure 5.16 DFIG-SSR screening results for different parallel PIC cases.

Figure 5.17 looks more detailed into the series resonance and it is found that for all the analysed cases, the phase margin is between -10° and -17° , indicating instability. The figure also shows that the C_1/C_2 -ratio has a larger impact on the overall system's resonance frequency than the C_A/C_1 -ratio. Furthermore, stability will only be achieved when the overall system's resonance frequency is lower than 8 Hz, as the corresponding phase margin is 0° . Lowering the C_1/C_2 -ratio could move the resonance frequency to a value lower than 8 Hz. As decreasing C_1/C_2 increases the magnitude of the parallel resonance (see Figure 5.16), the C_A/C_1 -ratio is fixed at 2.0 for further analysis (C_A/C_1 -ratio of 2.0 has the largest difference between the impedance magnitudes of the grid and DFIG at the parallel resonance and therefore the lowest risk for creating a parallel resonance with decreasing ratios of C_1/C_2). Reducing the C_1/C_2 -ratio even further, the series resonance frequency remains around 9 Hz. As indicated in Figure 5.18, the phase margin increases from -17° under C_1/C_2 -ratio 2 to approx. -6.5° under C_1/C_2 -ratio 0.001. For comparison purposes, the impedance for the case C_1/C_2 0.001, C_A/C_1 0.25 is also provided. In this case, the phase margin increases further to -4° , whereas an unstable resonance appears at 23 Hz with a phase margin of approx. -68° . Therefore, it is concluded that the one phase parallel PIC is not able to sufficiently damp the 9 Hz series resonance.

Figure 5.19 provides a more detailed overview of the three parallel resonances that were identified in Figure 5.16. These resonances occur at the following frequencies:

- 22 Hz for C_A/C_1 of 0.25 and C_1/C_2 of 0.5;
- 29 Hz for C_A/C_1 of 0.5 and C_1/C_2 of 0.5;
- 29 Hz for C_A/C_1 of 0.5 and C_1/C_2 of 1.0.

When analysing the phase margins, it is found that only the resonance at 22 Hz has a positive phase margin (115°), and therefore is stable. Both resonances at 29 Hz have a negative phase margin and are unstable. This is confirmed by detailed time domain EMT simulations performed for all the twelve combinations of C_A/C_1 and C_1/C_2 shown in Figure 5.16. The instantaneous three phase current waveforms and the accompanying harmonic spectra are shown in Figure 5.20, Figure 5.21 and Figure 5.22.

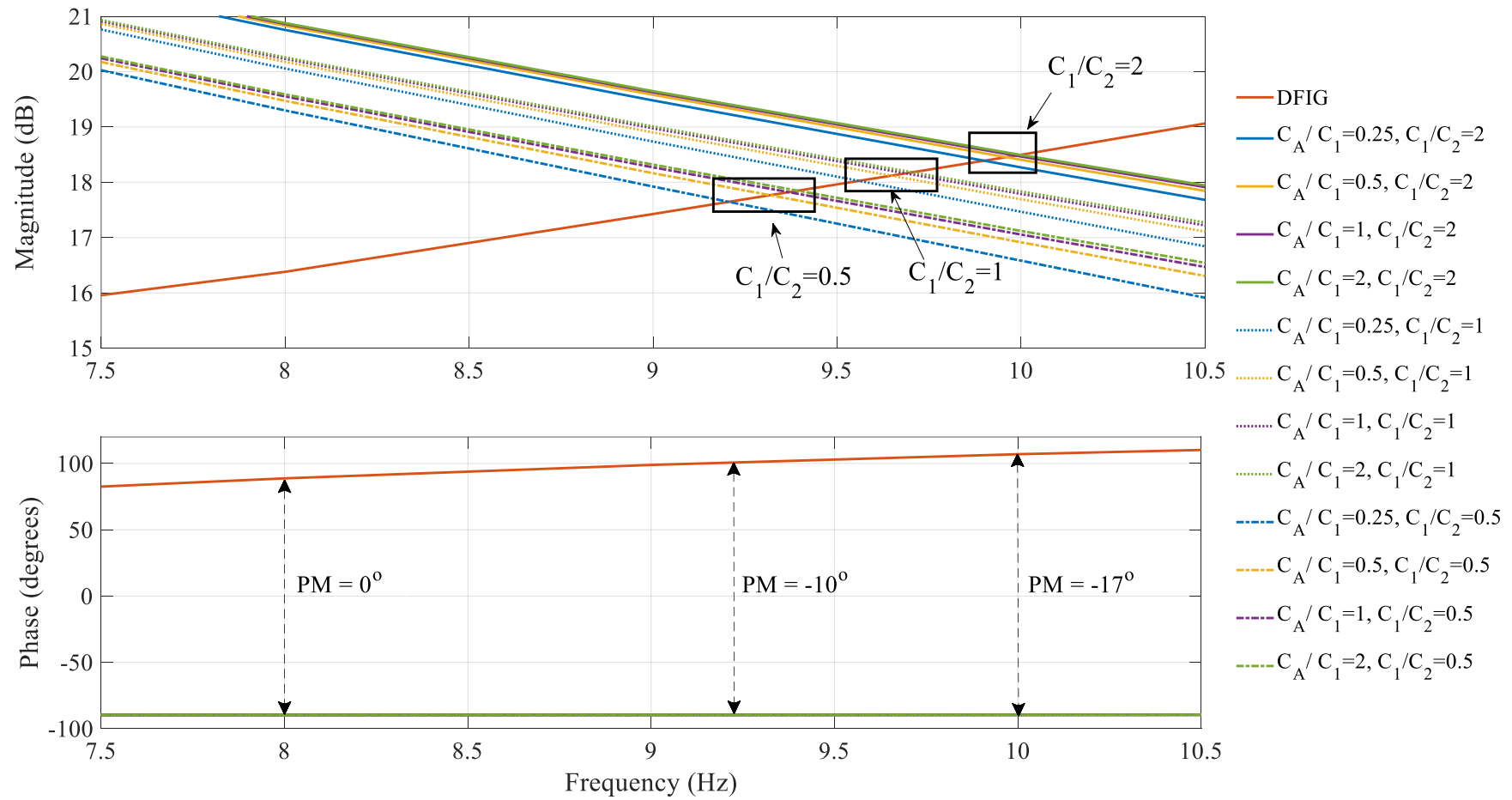


Figure 5.17 DFIG-SSR screening results for series resonance.

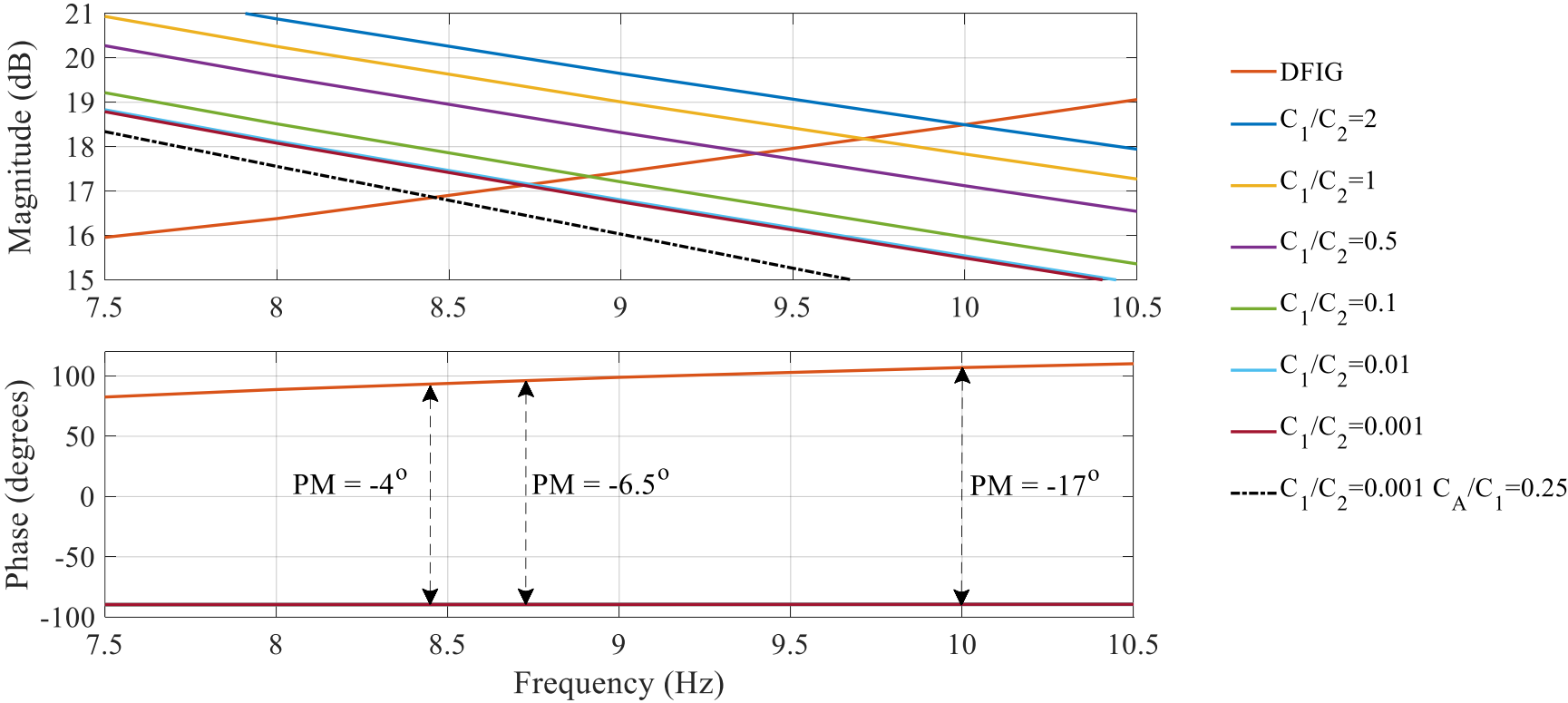


Figure 5.18 DFIG-SSR screening results for C_A/C_1 -ratio 2 under varying C_1/C_2 -ratios.

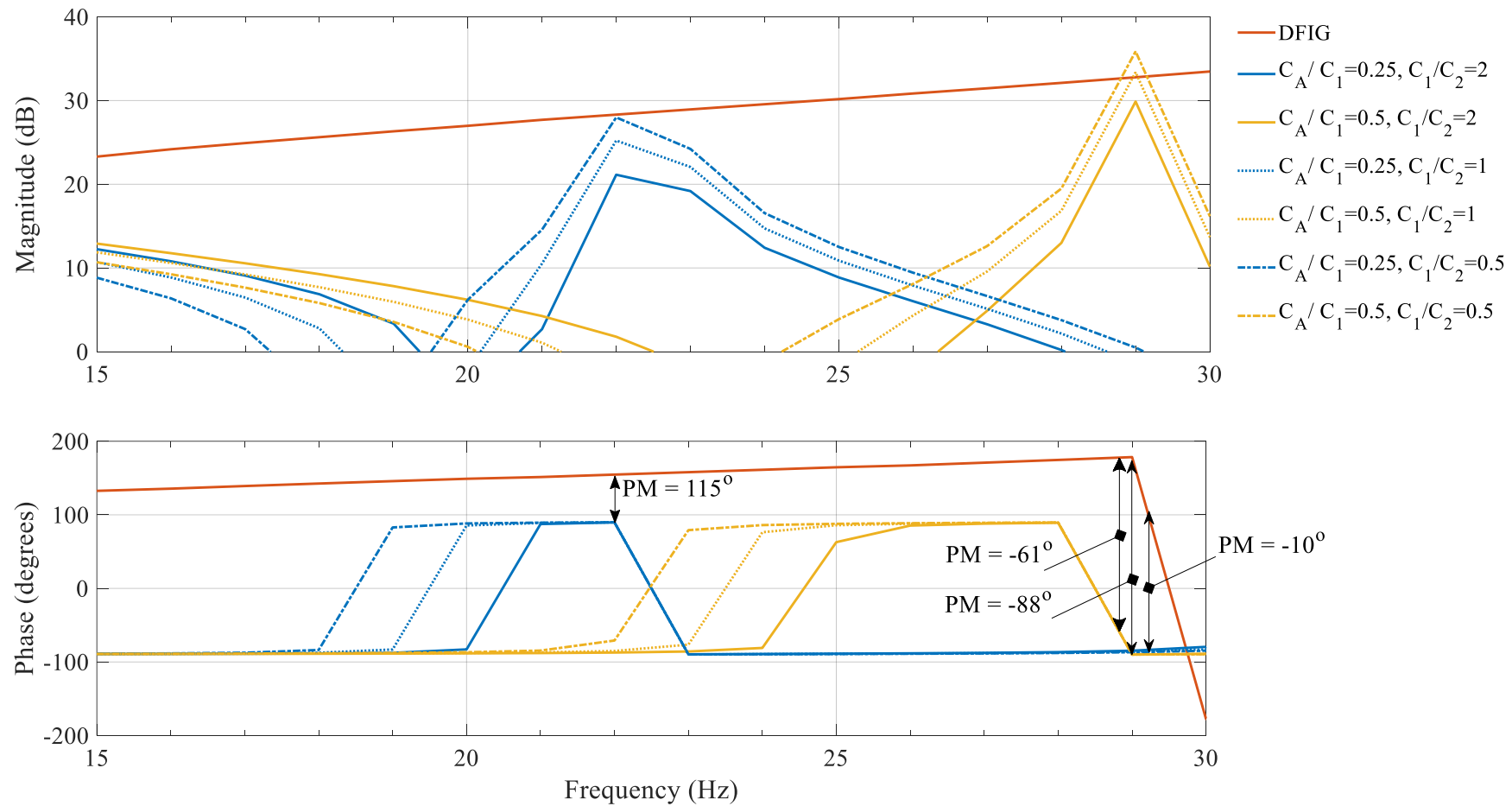


Figure 5.19 DFIG-SSR screening results for parallel resonances.

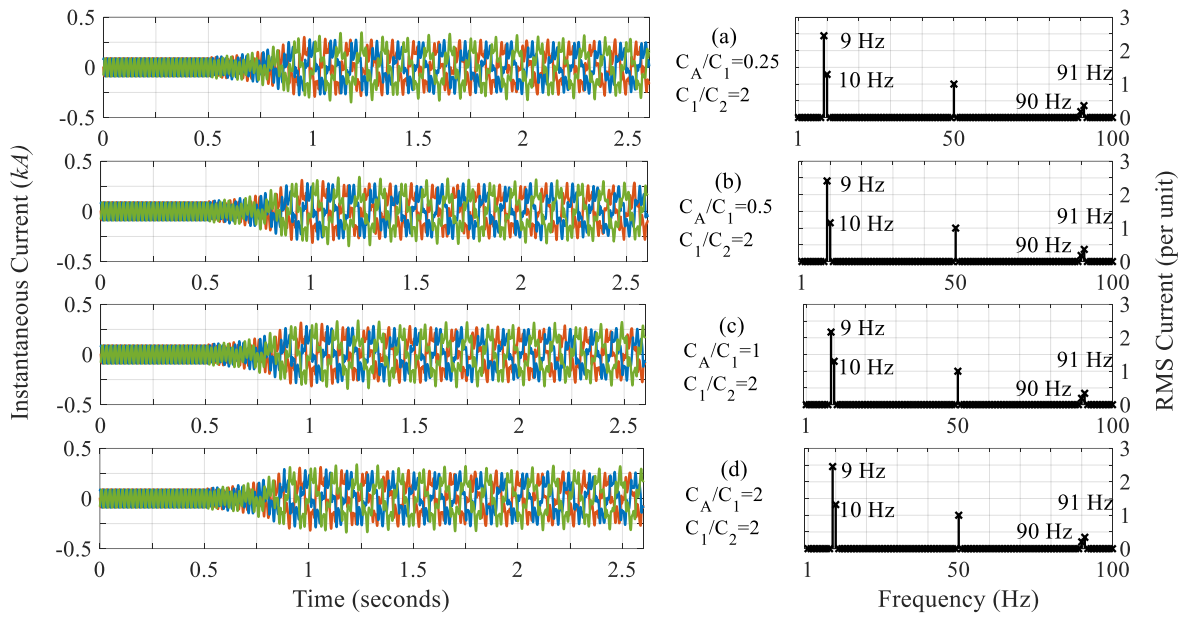


Figure 5.20 Detailed time domain EMT simulations for one phase parallel PIC with C_1/C_2 -ratio of 2.

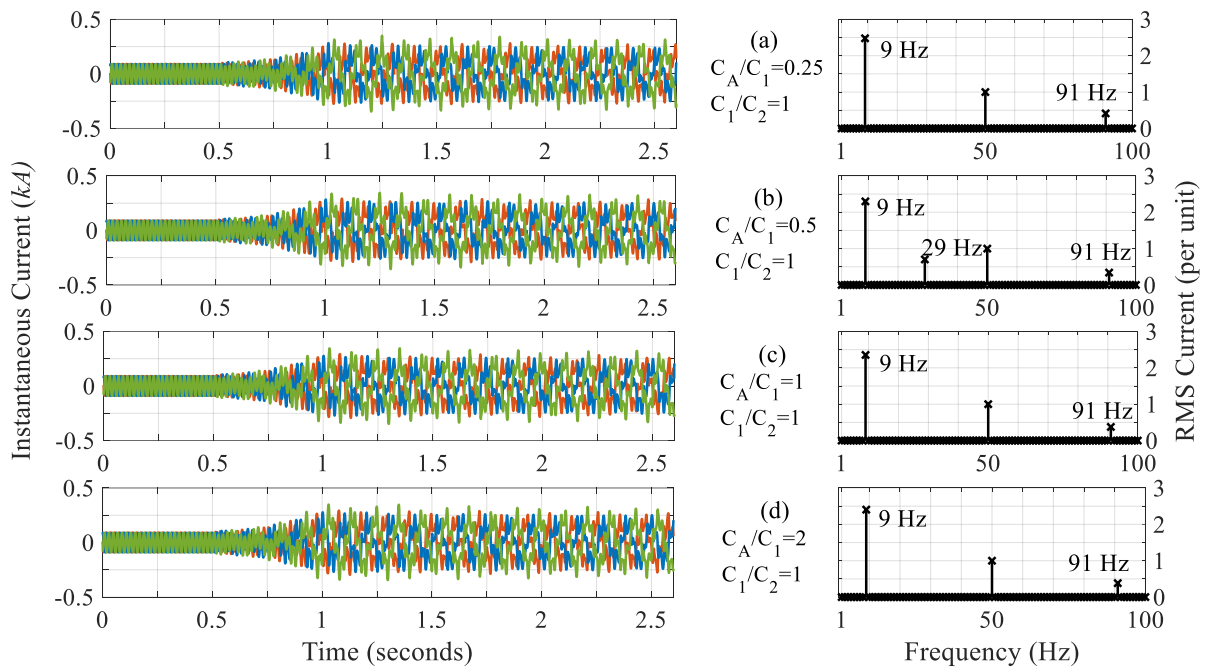


Figure 5.21 Detailed time domain EMT simulations for parallel PIC with C_1/C_2 -ratio of 1.

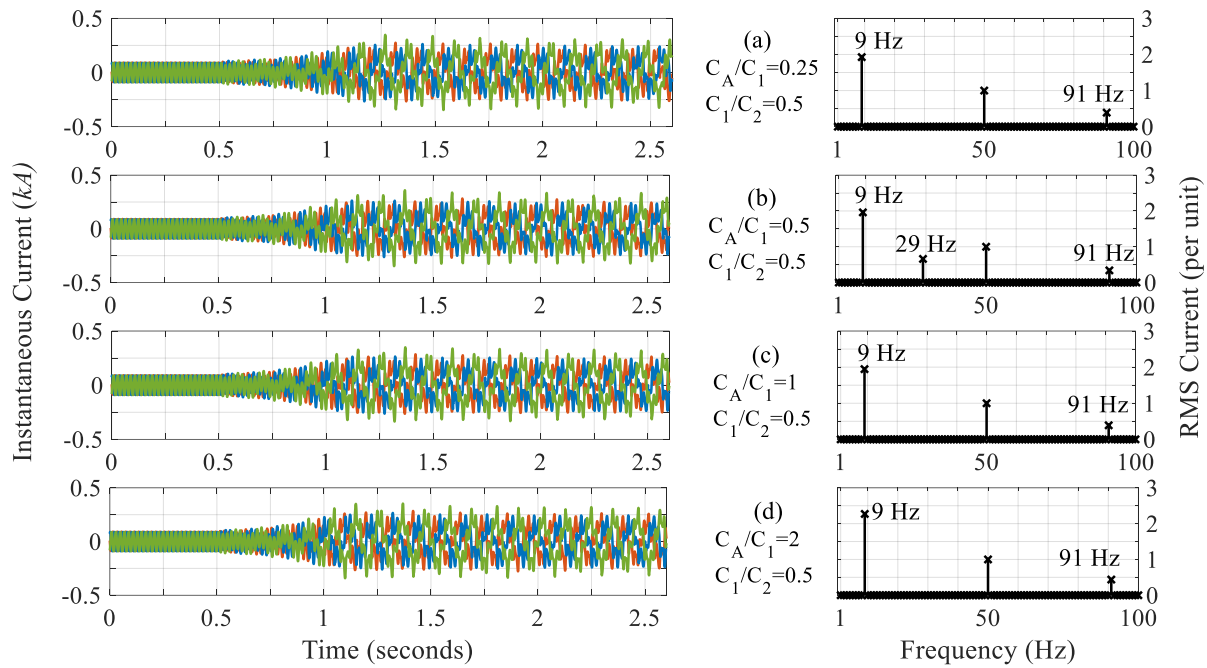


Figure 5.22 Detailed time domain EMT simulations for parallel PIC with C_1/C_2 -ratio of 0.5.

The analysis performed so far shows that with a compensation degree of 36%, neither the series phase imbalance compensation concept nor the one phase parallel phase imbalance compensation concept were able to mitigate DFIG-SSR. The series PIC concept always resulted in an increase of the overall system's resonance frequency. Taking into account the damping profile of the DFIG (Figure 5.11), such an increase worsens the damping characteristic of the overall system and therefore further deteriorates the stability. The one phase parallel PIC concept on the other hand is able to decrease the overall system's series resonance frequency, albeit that this decrease is marginal. Under all the investigated cases this resonance remains unstable. The parallel PIC further introduces a parallel resonance in the frequency range between 20 and 30 Hz. It was shown that depending on the ratios of C_1/C_2 and C_A/C_1 the parallel resonance can be stable.

Further analysis revealed that the series resonance frequency of the overall system is mainly determined by the DFIG's impedance and the grid's degree of compensation. This series resonance will be stable if the phase margin is positive, which occurs at a frequency smaller than 8 Hz (see Figure 5.17). To illustrate the influence of the various compensation concepts on DFIG-SSR, for each compensation concept the compensation degree resulting in a series resonance of 7 Hz is sought. This is carried out for C_1/C_2 of 1 and C_A/C_1 of 2 in case of the parallel PIC and for C_A/C of 2 in case of the series PIC. Under these circumstances, compensation degrees in excess of those identified will result in resonance frequencies with negative phase margins, and will therefore be unstable.

Figure 5.23 shows for each of the compensation concepts the compensation degree resulting in marginal stability. The active power transfers associated with the identified compensation degrees are indicated as well. Taking into account the impedance profile of the DFIG and the study model, two main conclusions can be drawn from this figure. First, compared to the classical compensation concept, the series PIC concept has a worse

performance, where the two phase series PIC is less stable than the one phase series PIC. Second, the parallel PIC has a better performance than the classical compensation, where the best performance is achieved for the two phase parallel PIC. This essentially means that where DFIG-SSR would limit k to 15% for classical compensation, the two phase parallel PIC enables compensation up to 25%. The associated active power transfer increases from 1.17 per unit to 1.34 per unit. Detailed time domain EMT simulations confirm the stability of the identified degrees of compensation, as is shown in Figure 5.24.

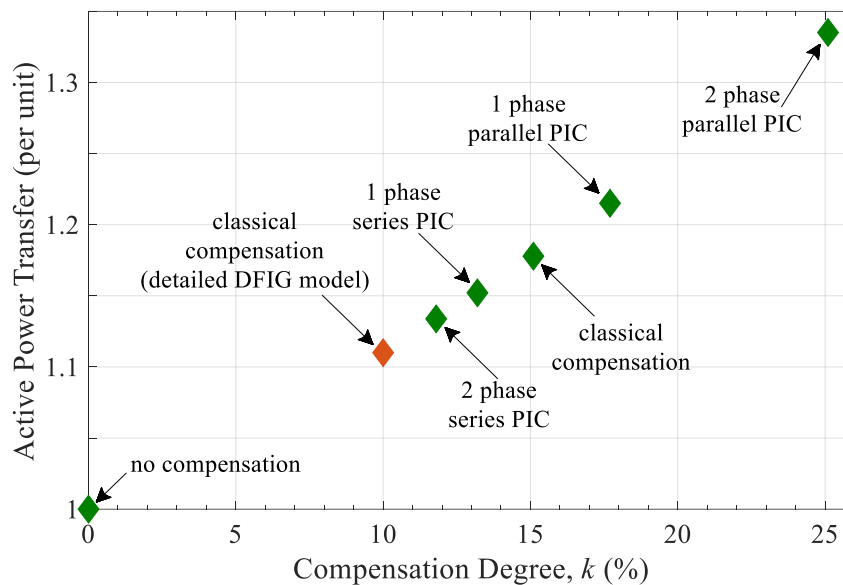


Figure 5.23 Compensation degrees for different series compensation concepts leading to marginal stability of the system with the average DFIG model shown in Figure 5.1. The classical compensation case using the detailed DFIG model is included.

With the identified marginal stability cases, it becomes clear that the parallel PIC can mitigate DFIG-SSR when the required compensation is below the compensation degree resulting in marginal stability. In Figure 5.25 time domain EMT results are shown for a grid with 19% compensation. In line with the results from Figure 5.23, the classical compensation concept is unstable, whereas the two phase parallel PIC scheme shows a stable response.

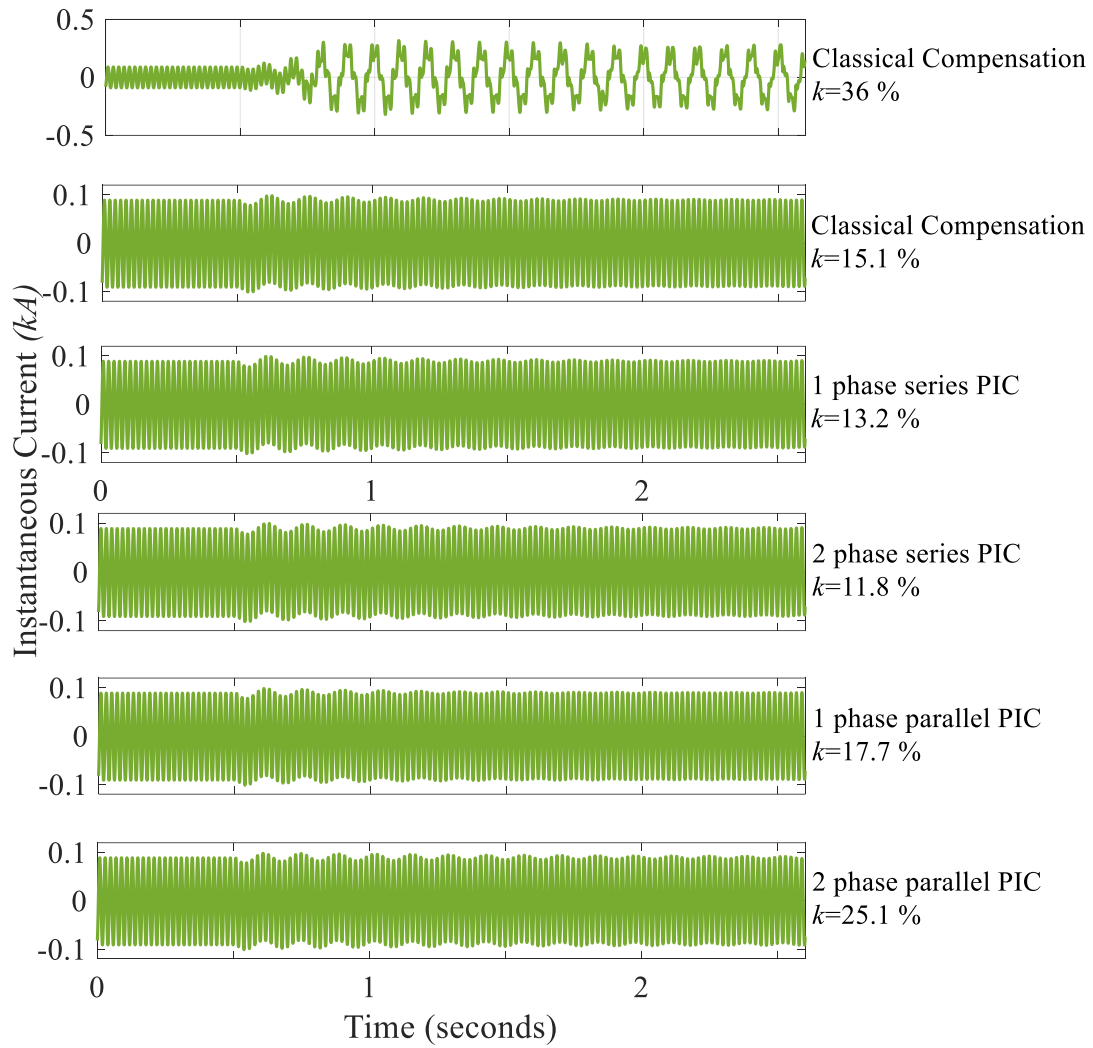


Figure 5.24 Phase C instantaneous currents for compensation degrees resulting in marginal stability.

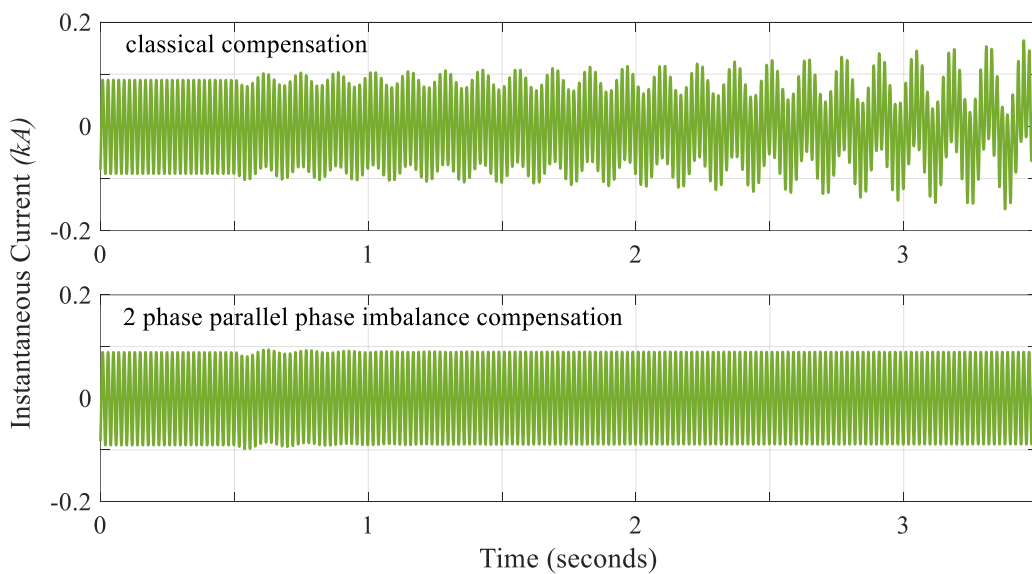


Figure 5.25 Phase C instantaneous currents for 19% compensation using the classical as well as two phase parallel PIC compensation.

The analysis conducted for the parallel PIC showed that, in contrast to the series PIC, the resonance frequency can be reduced. This reduction is more pronounced when the parallel PIC is deployed in two phases. Based on the identification of marginal stability cases of the study model, it is concluded that the parallel PIC has a positive impact on mitigating DFIG-SSR. Furthermore, the two phase parallel PIC has a superior performance compared to the one phase parallel PIC.

5.4. SYSTEM STRENGTH ASSESSMENT

The analysis performed so far considered a fixed system strength, which is approximated by the equivalent inductance as seen from the PCC in the study model. The larger this inductance, the lower the system strength. For several system strength conditions, the DFIG-SSR assessment is shown in Figure 5.26. The goal was to assess how the stability of the overall system changes with varying system strength conditions. The series compensation is achieved through classical series compensation with $k=28\%$ (marginal stability case for $L=0.01$ H). For constant k and decreasing system strength, f_r increases, while the phase margin decreases.

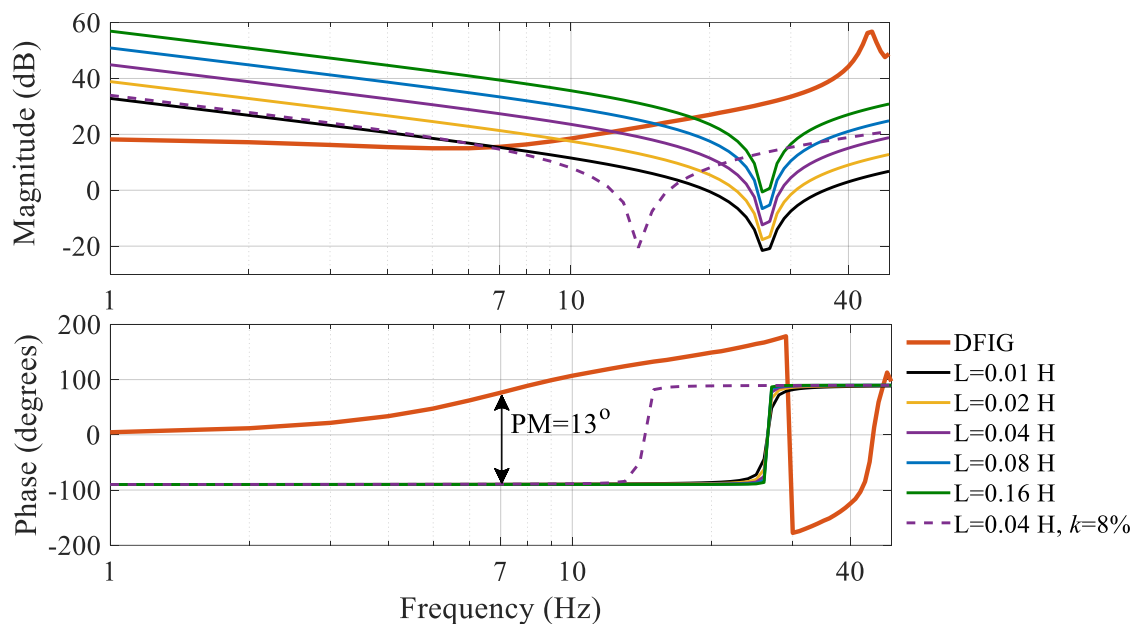


Figure 5.26 DFIG-SSR screening results for different system strength conditions. Series compensation is achieved through classical compensation with $k=28\%$.

The degrees of compensation k leading to marginal stability of the different system strength cases are shown in Figure 5.27. To avoid DFIG-SSR, the maximum allowed k should be reduced with decreasing system strength. Similar analyses were conducted for the different PIC schemes. For all the schemes, it was found that the compensation degree leading to marginal stability decreases with reducing system strength. This is shown in Figure 5.28.

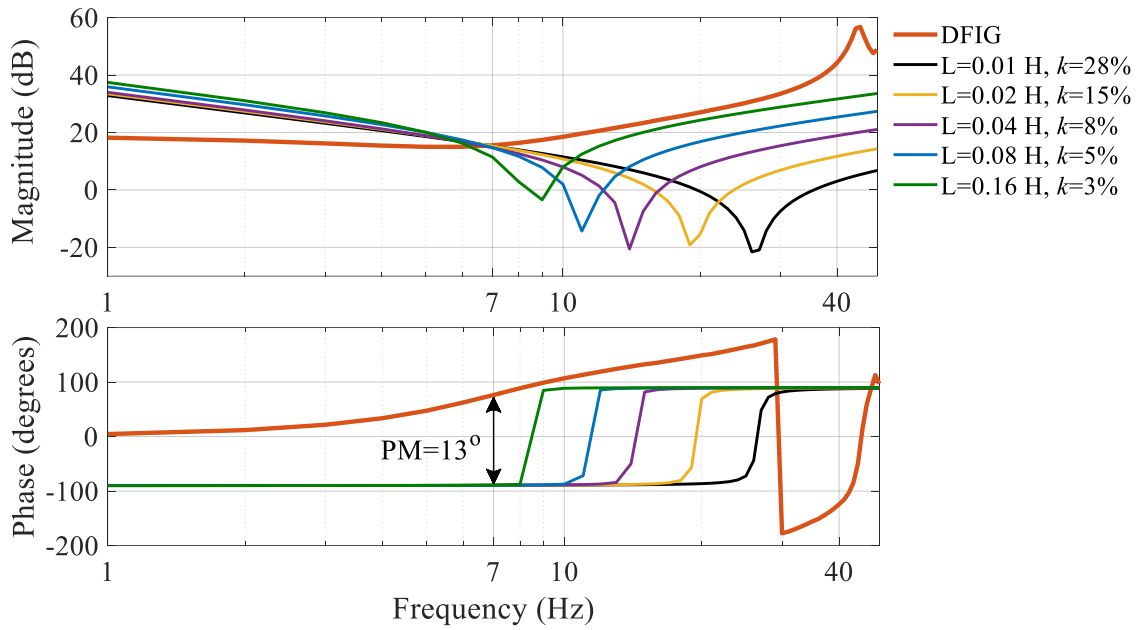


Figure 5.27 DFIG-SSR screening results for marginal stability under different system strength conditions. Series compensation is achieved using the classical compensation concept.

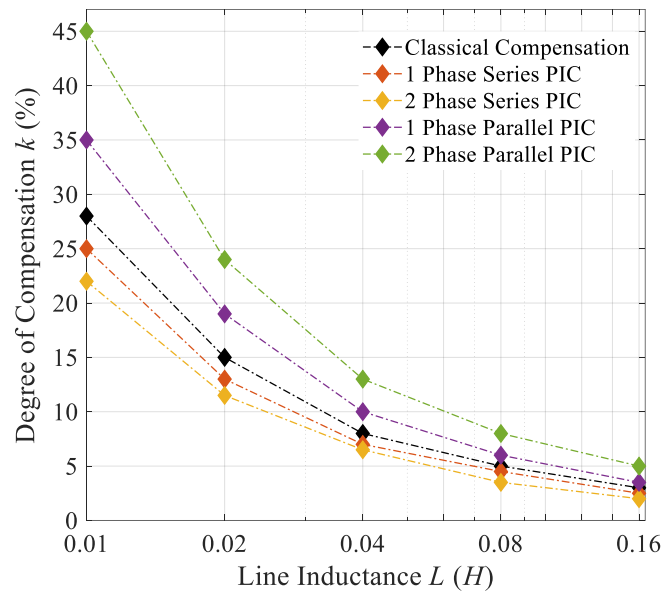


Figure 5.28 Compensation degrees for different series compensation concepts leading to marginal stability under different system strength conditions.

5.5. AVERAGE VERSUS DETAIL DFIG EMT MODEL

The evaluation performed so far was carried out using the average DFIG EMT simulation model. This Section evaluates how the modelling details of the DFIG influences the stability of the DFIG-SSR mode. To this extent, the impedance responses of the classical compensated grid and the average and detail DFIG EMT simulation models are obtained and depicted in Figure 5.29.

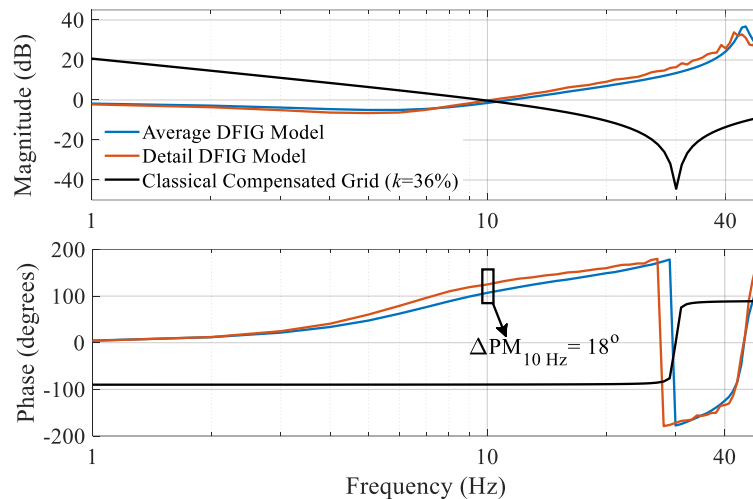


Figure 5.29 DFIG-SSR assessment for classical series compensation using the average and detail DFIG EMT simulation model.

Although the resonance frequency remains 10 Hz, independent of the DFIG model, the phase margin at this frequency is 18° lower when using the detail DFIG EMT model. This means that mitigation measures designed with the detail model will need to be more stringent compared to when the average model is used. This is confirmed in the process of identifying and comparing the marginal stability using the detail DFIG EMT model ($k=10\%$) and the average model ($k=15.1\%$). Figure 5.30 shows the time domain EMT simulation results using the detail DFIG EMT simulation model. It shows that the average DFIG model overestimates the phase margin, which is in line with the discussions in Chapter 4.3.3.

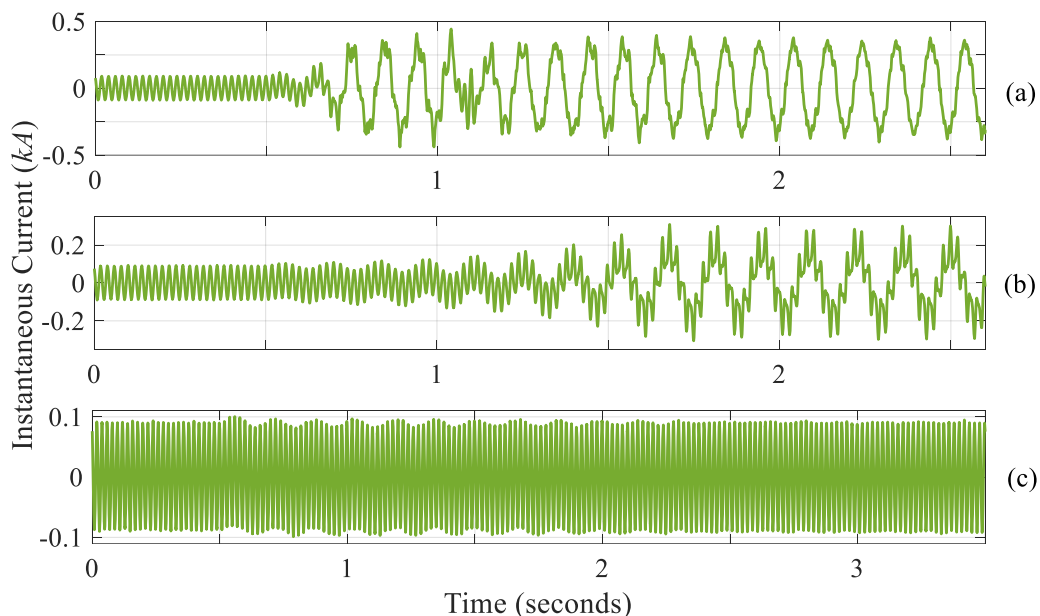


Figure 5.30 Phase C instantaneous currents for classical compensation using the detail DFIG model. (a) $k=36\%$; (b) 15.1% ; (c) 10% .

5.6. METHODOLOGY FOR PIC EVALUATION

5.6.1. DESCRIPTION OF METHODOLOGY

Based on the investigation steps so far, a methodology for evaluating PIC as a DFIG-SSR mitigation solution is developed and is depicted in Figure 5.31. The process starts with the screening studies, which require the impedances of the DFIG and the grid for a wide range of topological conditions. Using the impedance based stability analysis, the risk for DFIG-SSR is investigated. When the magnitude plots intersect in the sub synchronous frequency range, there is a potential risk for DFIG-SSR. If the minimum phase margin at this frequency is larger than 10° , the risk is low and the analysis can be stopped. Phase margins lower than 10° pose a realistic risk for DFIG-SSR and would require detailed analysis and, if DFIG-SSR is observed, mitigation solutions. The 10° threshold is chosen based on industrial practices, but it can be any positive value at which the system operator feels confident. At this stage, different PIC schemes are evaluated using similar analysis as performed in Sections 5.2 and 5.3. When the resulting phase margin is larger than a predefined threshold, the most effective PIC can be selected and validated. This new threshold can be different from 10° and depends on the likelihood that DFIG-SSR occurs when the PIC scheme is used. If the phase margin remains lower than this threshold, the PIC schemes are not able to mitigate DFIG-SSR and other solutions as discussed in Chapter 3 need to be investigated. At this stage, the PIC evaluation is concluded.

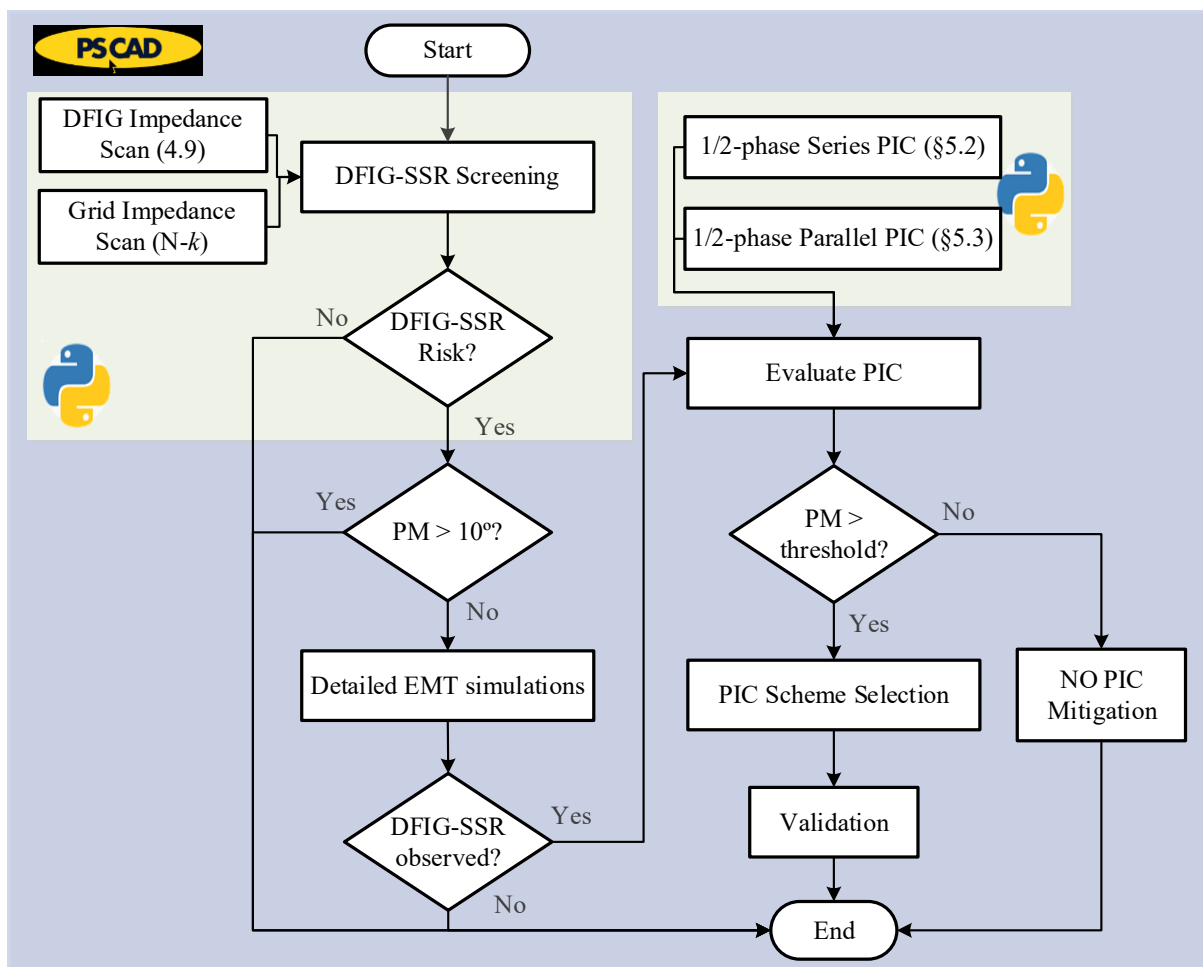


Figure 5.31 Methodology for DFIG-SSR mitigation using phase imbalance compensation.

5.6.2. DFIG-SSR MITIGATION IN IEEE 39 BUS SYSTEM

The methodology described in Section 5.6.1 is now used in the IEEE 39-bus system to mitigate DFIG-SSR. The first step consists of performing the screening studies. The DFIG impedance is obtained using the perturbation method described in Chapter 4. Following the practical guidelines for DFIG-SSR studies by ERCOT, the grid impedance is obtained for several grid topological conditions up to $N-5$ [8]. For several of these topologies, the impedance responses of the DFIG and the grid intersect at approx. 12 Hz. The specific $N-5$ grid topology shown in Figure 5.32 results in a phase margin of -3° , which is below the 10° threshold, indicating a high DFIG-SSR risk. This case is investigated in more detail.

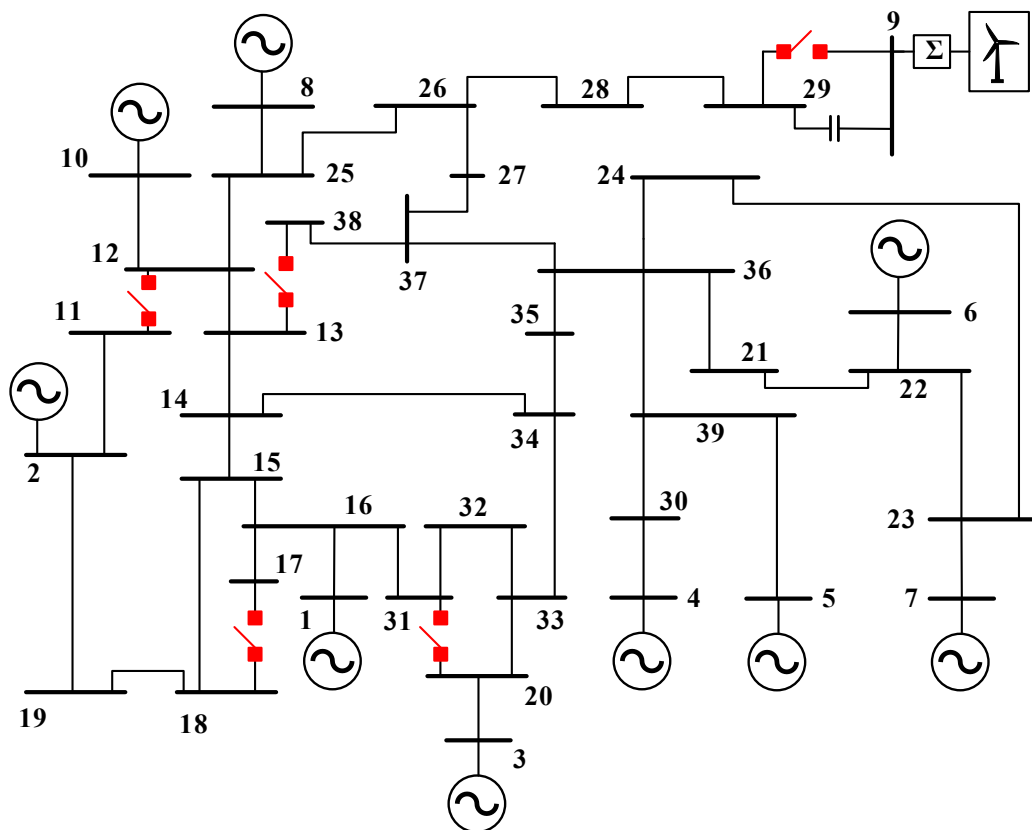


Figure 5.32 Identification of a $N-5$ grid topology resulting in DFIG-SSR.

Detailed time domain EMT simulations confirm the presence of DFIG-SSR as is shown in Figure 5.34. In the next stage, the series and parallel PIC schemes are evaluated and their capability to mitigate the observed DFIG-SSR is assessed. Figure 5.33 shows the impedance responses of the DFIG (in red) and the IEEE 39-bus system under classical compensation (black) and under series (in green) and parallel (in blue) PIC configurations for different degrees of asymmetry. It is observed that the series PIC increases and the parallel PIC decreases the resonance frequency, confirming the findings of Sections 5.2 and 5.3.

The two phase parallel PIC with $C_1/C_2 = C_A/C_1 = 0.5$ increases the phase margin to $+28^\circ$. The detailed time domain EMT simulations of Figure 5.34 show the final validation and illustrate the effective mitigation of DFIG-SSR using these degrees of asymmetry.

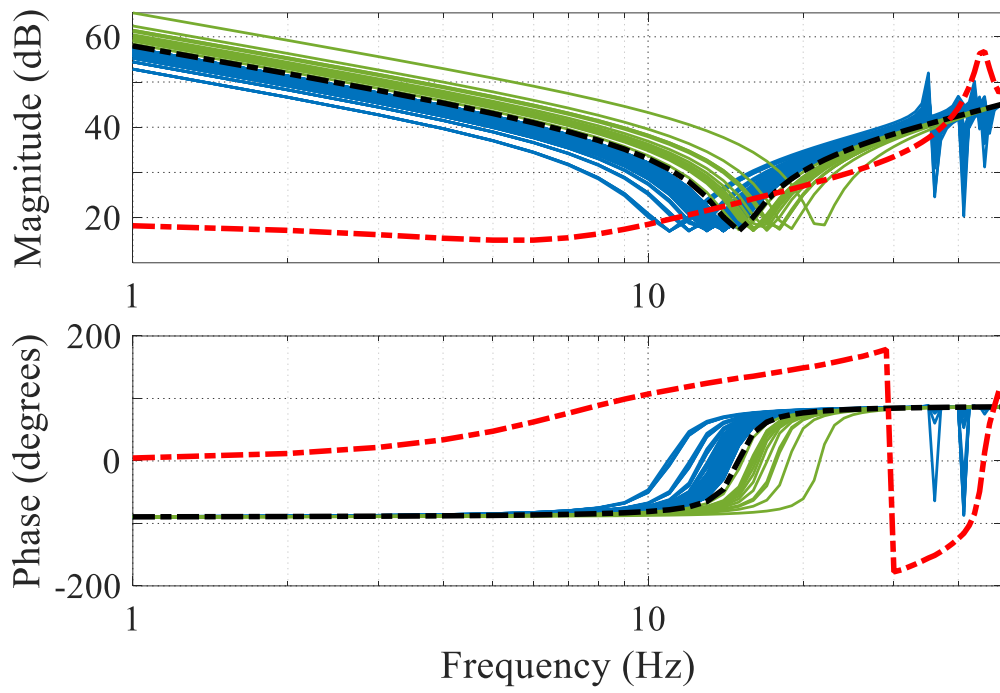


Figure 5.33 Impedance responses of DFIG (red) and the IEEE 39 bus system. The black curves represent the response of the N -5 grid using classical compensation. Green and blue curves represent respectively series and parallel PIC.

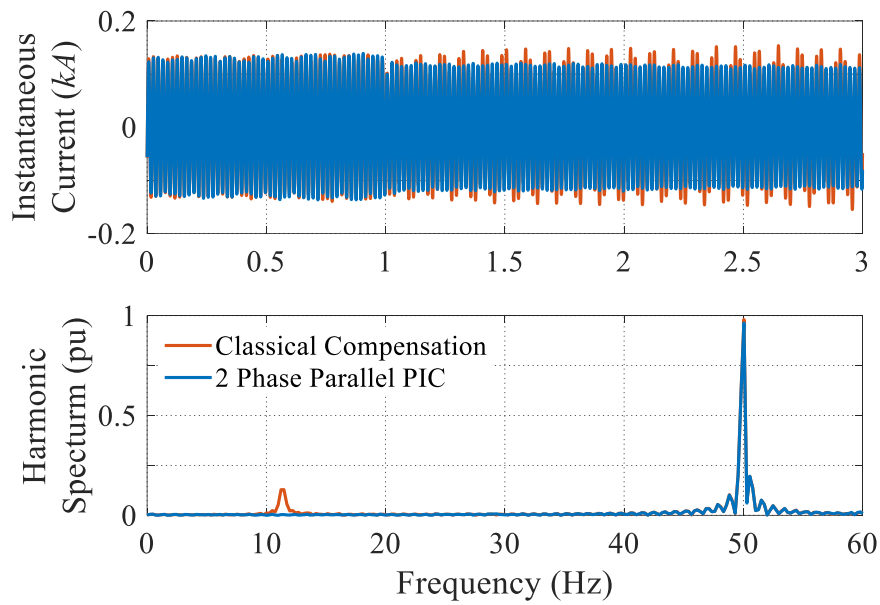


Figure 5.34 Phase A instantaneous currents for the N -5 topology in the IEEE 39-bus system.

5.7. MITIGATING TORSIONAL SSR WITH PIC

As was discussed in Section 5.2.2, the series PIC was not able to mitigate DFIG-SSR, as the resulting shift in f_r deteriorates the electrical damping even further. However, in [1] it was shown that the series PIC scheme successfully mitigated torsional SSR. The capability of the series PIC scheme to mitigate torsional SSR is explained next.

For a wind power plant in China, torsional interaction (SSR) analyses were performed. Using the complex torque coefficient method, electrical damping coefficients under different wind power output levels were calculated. These are shown in Figure 5.35 [9].

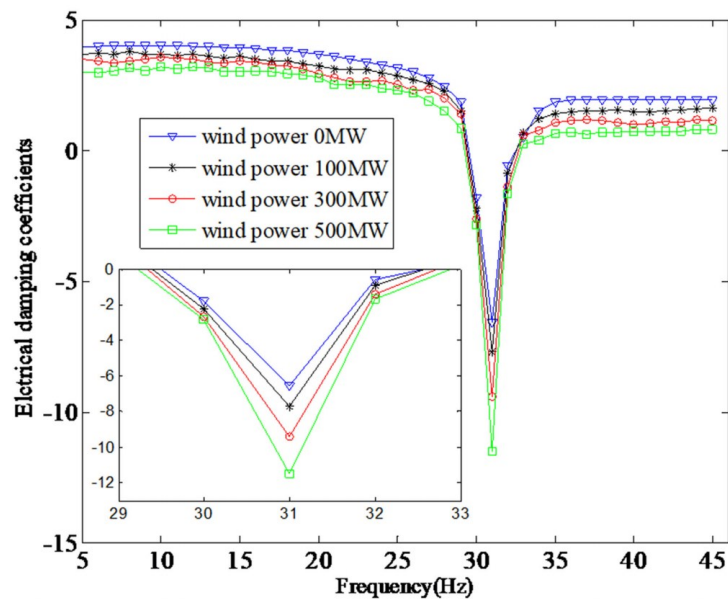


Figure 5.35 Electrical damping coefficients under different wind generation levels [9].

The possibility of a torsional interaction with f_r of 31 Hz was identified. At this frequency, the damping coefficients were negative. Compared to the DFIG damping (Figure 5.11), the negative resistance region in Figure 5.35 is limited to a 4 Hz interval. The negative resistance region of the DFIG was identified for different wind power output levels (i.e. different wind speeds), which varied from approx. 10-43 Hz for high wind speeds to 6-41 Hz for low wind speeds. The negative resistance region in Figure 5.35 is 29-33 Hz. Increasing f_r in this case with as little as 2 Hz would result in positive damping and eliminate the adverse torsional SSR interaction. The series PIC is capable of achieving this shift in f_r and therefore could be a potential solution for mitigating the torsional SSR interaction. In this specific example, an UPFC was considered as a mitigation solution.

In another example, SSR analysis was carried out to investigate the torsional characteristics of the Hanul nuclear power plant in Japan [10]. Increased probability of torsional interaction between the turbine-generator and a fixed series capacitor was identified, where depending on the operating condition, f_r ranged between 35 and 39 Hz. A 2-5 Hz shift in f_r would result in positive damping and therefore eliminate the adverse torsional interactions. Here as well, the series PIC could be one of the potential solutions to achieve this. To mitigate the torsional interactions in this example, a TCSC was evaluated as a mitigation solution.

As a comparison, to mitigate DFIG-SSR using the series scheme a 30 Hz increase in the resonance frequency would be required.

5.8. CONCLUSIONS

The goal of this Chapter was to evaluate to which extent the phase imbalance compensation concept, as an alternative for classical compensation, could mitigate DFIG-SSR. The phase imbalance concept can be implemented as a series or parallel scheme in one or two phases of the transmission line.

The series PIC scheme consists of a series resonance circuit. For this scheme, an analytical model was developed and validated using time domain EMT simulations. This model enabled to understand how the resonance frequency of the compensated transmission line varies for different degrees of asymmetry. An index in the form of the oscillation energy was developed to quantify the intensity of DFIG-SSR. This index was then used to evaluate the stability of the overall system under different levels of asymmetry. To prevent biased conclusions, optimisations of the degree of asymmetry were performed with the goal of minimising the oscillation energy. The results showed that independent of the degree of asymmetry, the shift in resonance frequency that is introduced by the series scheme is always positive and that the shift is inversely proportional to the degree of asymmetry. Finally, the resulting increase in the resonance frequency is larger when the series scheme is implemented in two phases instead of one phase.

As the negative resistance of the DFIG becomes more negative with an increase in the resonance frequency, it is concluded that as long as this increased resonance frequency resulting from the series scheme remains within the negative resistance region of the DFIG, the stability of the system decreases even further, compared to when classical compensation is used. The deterioration of the stability is even more pronounced when the series scheme is deployed in two phases. For the DFIG impedance and the study model with $k=36\%$, it is therefore concluded that neither the one phase nor the two phase series PIC can mitigate DFIG-SSR.

The parallel scheme on the other hand is a hybrid compensation concept consisting of a series and parallel resonance circuit. As a result, the compensated line introduces multiple series and parallel resonance frequencies. The analysis conducted for the parallel scheme showed that in contrast to the series scheme, the lower series resonance frequency can be reduced. This reduction is more pronounced when the parallel scheme is deployed in two phases instead of one phase. The resonance circuits of the parallel scheme can be tuned in such a way that the lowest resonance frequency occurs outside the DFIG's negative resistance region. This tuning requires special attention to ensure that the parallel resonance is also mitigated. A methodology was developed using the obtained insights to effectively design the PIC concept for mitigating DFIG-SSR and was implemented on the IEEE 39-bus system.

Based on the identification of compensation degrees leading to marginal stability of the study model, it is concluded that the parallel scheme has a positive impact on mitigating DFIG-SSR. Furthermore, the two phase parallel scheme has a superior performance compared to the one phase parallel scheme. The influence of the system strength on DFIG-SSR was also

investigated. It was found that independent of the compensation concept, decreasing system strength reduces the compensation degree required for marginal stability.

Finally, a comprehensive reasoning was provided for why the PIC can mitigate torsional SSR. Compared to a DFIG, a conventional synchronous machine's negative resistance region in the sub synchronous frequency range is small. With adequate degrees of asymmetry, the resonance frequency can either be increased using the series scheme or decreased using the parallel scheme to a frequency outside the negative resistance region, and thereby successfully mitigating the adverse interactions.

With the hardware solution covered in this Chapter, the next Chapter will focus on the design of a system level coordination based mitigation solution for DFIG-SSR.

REFERENCES

- [1] A.-A. Edris, "Series compensation schemes reducing the potential of subsynchronous resonance," *IEEE Trans. Power Syst.*, vol. 5, no. 1, pp. 219–226, 1990.
- [2] A. A. Edris, "Subsynchronous resonance countermeasure using phase imbalance," *IEEE Trans. Power Syst.*, vol. 8, no. 4, pp. 1438–1447, 1993.
- [3] D. Rai, G. Ramakrishna, S. O. Faried, and A. A. Edris, "Enhancement of power system dynamics using a phase imbalanced series compensation scheme," *IEEE Trans. Power Syst.*, vol. 25, no. 2, pp. 966–974, 2010.
- [4] D. Rai, S. O. Faried, G. Ramakrishna, and A. A. Edris, "Damping inter-area oscillations using phase imbalanced series compensation schemes," *IEEE Trans. Power Syst.*, vol. 26, no. 3, pp. 1753–1761, 2011.
- [5] U. Karaagac, S. O. Faried, J. Mahseredjian, and A. A. Edris, "Coordinated Control of Wind Energy Conversion Systems for Mitigating Subsynchronous Interaction in DFIG-Based Wind Farms," *IEEE Trans. Smart Grid*, vol. 5, no. 5, pp. 2440–2449, 2014.
- [6] R. J. Piwko and E. V. Larsen, "HVDC system control for damping of subsynchronous oscillations," *IEEE Trans. Power Appar. Syst.*, vol. PAS-101, no. 7, pp. 2203–2211, 1982.
- [7] M. S. Annakkage, C. Karawita, and U. D. Annakkage, "Frequency scan-based screening method for device dependent sub-synchronous oscillations," *IEEE Trans. Power Syst.*, vol. 31, no. 3, pp. 1872–1878, May 2016.
- [8] J. Adams, V. A. Pappu, and A. Dixit, "Ercot experience screening for Sub-Synchronous Control Interaction in the vicinity of series capacitor banks," *IEEE Power Energy Soc. Gen. Meet.*, pp. 1–5, 2012.
- [9] H. Jiang *et al.*, "Application of UPFC to mitigate SSR in series-compensated wind farms," *J. Eng.*, vol. 2019, no. 16, pp. 2505–2509, 2019.
- [10] M. Q. Tran *et al.*, "Analysis and mitigation of subsynchronous resonance in a Korean power network with the first TCSC installation," *Energies*, vol. 12, no. 15, 2019.

6. SYSTEM LEVEL COORDINATION

6.1. INTRODUCTION

The mitigation solutions to address DFIG-SSR were categorised in Chapter 3 in hardware solutions, solutions based on system level coordination and control solutions. In the previous Chapter a method was designed to mitigate DFIG-SSR using the phase imbalance compensation concept.

This Chapter introduces the design framework of a DFIG-SSR mitigation solution based on system level coordination. The solution is a prediction based gain scheduling control which addresses the drawbacks of existing adaptive control solutions. These drawbacks are summarised in Section 6.1.2 and include among others the need for *a priori* knowledge of operating conditions and the need for a wide area measurement system. As will be explained in Section 6.2, the proposed gain scheduling solution consists of a gain identification and scheduling module, a prediction module, and a real-time operation module. The gain identification module is discussed in Section 6.3. Section 6.4 presents the development of a lookup table as well as its validation. Finally, Section 6.5 concludes this Chapter.

Adaptive and predictive control are rather niche concepts for system operations and are introduced first.

6.1.1. TENNET'S CONTROL ROOM OF THE FUTURE PROGRAM

The Dutch-German transmission system operator TenneT recently started the Control Room of the Future program, aiming to develop concepts and methodologies required to operate the power system of the future. This future is characterised by a major shift in the role of the control room operator, in which the operator will be supervising instead of operating the power system. Within this program, several methodologies and technologies will be developed to monitor and, where possible, mitigate operational challenges. The maturity trend of each of these methodologies and technologies are defined using six key pillars: Data, Software, Hardware, Decision Support, Output and Training and Testing (Figure 6.1).

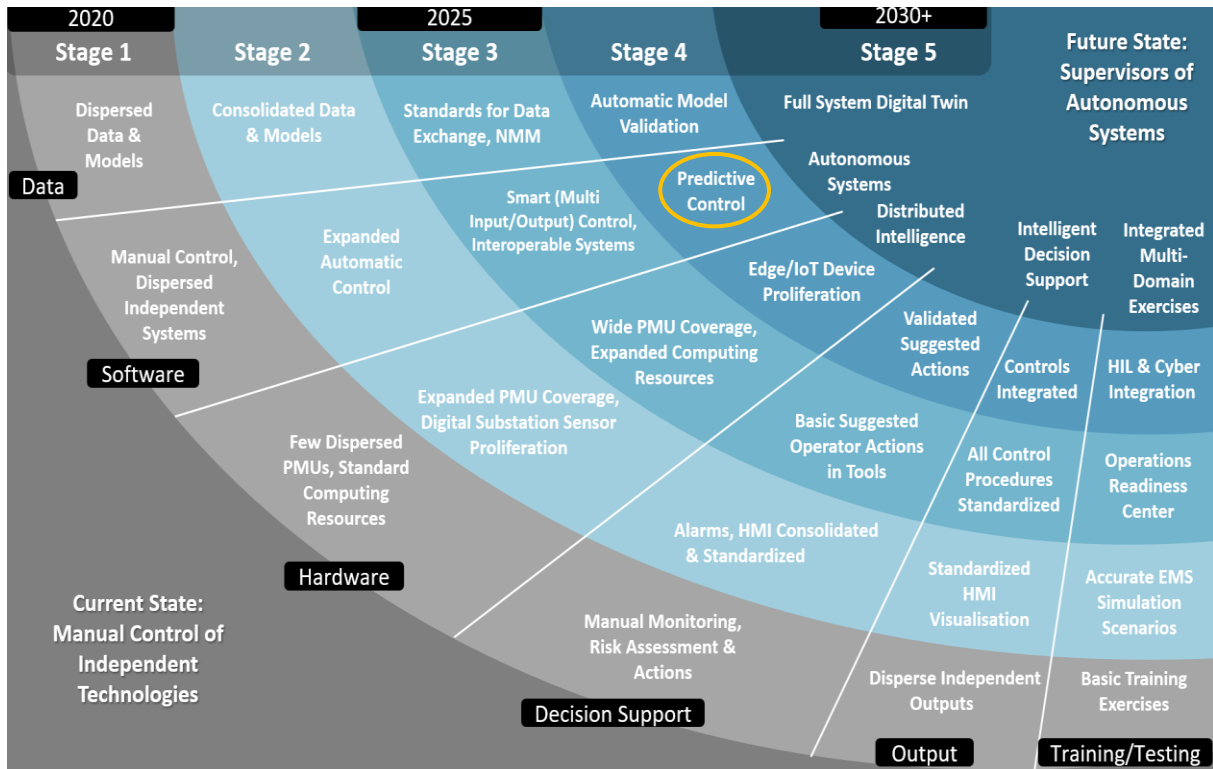


Figure 6.1 Generalised high-level overview of the stage breakdown of the pillars of TenneT’s control room of the future program. Predictive control is perceived as an advanced operational method to ensure operational security [1].

In safety critical environments the trend for technologies and methodologies is to move from manual to automatic to smart, then predictive and finally autonomous control. Automatic control is already well established in today’s power system. An example of automatic control is the primary control used to arrest the frequency after a disturbance. Predictive control is perceived as a more advanced concept, where control actions are scheduled prior to system changes or disturbances. As such, a necessary requirement for predictive control is that it should be adaptive. Some examples of adaptive controls are given next.

6.1.2. EXAMPLES OF ADAPTIVE CONTROL

To mitigate SSCI-CGI, an adaptive control strategy was proposed in [2]. In this strategy, an additional proportional controller with gain K (indicated in orange in Figure 6.2) was introduced in the q-axis outer loop control of the inverter.

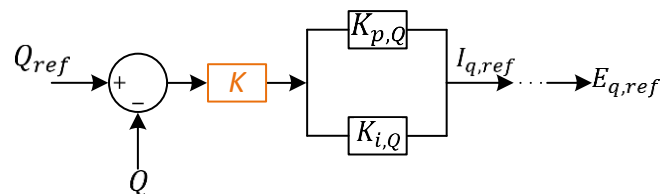


Figure 6.2 Adaptive control proposed in [2]. Control block in orange is adaptive.

To effectively mitigate SSCI-CGI, K is required to be low for weak grid conditions (as explained in Chapter 2.4.1). A constant low gain, however, would compromise the performance at high grid strength conditions. Therefore, the adaptive control strategy proposed in [2] recommends that the gain K is scheduled based on the grid strength. The Automated Stability Phasor-based Algorithm System (ASPAS) is a method to determine the grid strength online and is already implemented in the power system of Spain [3], [4]. ASPAS provides the system operator with real-time information about topology and network conditions and acts on the control of the LCC HVDC link that connects Mallorca to the Spanish mainland. The ASPAS actions successfully mitigate LCC commutation failures and unstable oscillatory behaviour.

Whereas ASPAS was used to determine the grid strength of the onshore power system, an online measurement concept for determining offshore wind power plant impedance is proposed in [5]. Using the obtained impedance characteristic of the offshore system, adaptive controls are designed for the control of an HVDC converter that guarantees stable operation in the face of variable network configurations and wind power plant operating conditions. The concept was developed to tackle subsynchronous as well as supersynchronous control interactions between a converter and a weak grid.

To achieve an optimised performance of the inverter of a full converter wind turbine generator during large load changes, the DC-link voltage control was designed as an adaptive controller in [6]. In this control, the proportional gain of the DC-link voltage control was scheduled according to the error between the reference and measured DC-link voltage. A threshold was defined below which the gains were fixed. Above this threshold, the gains were varied according to the polarity of the voltage error, where a positive voltage error led to the acceleration of the wind turbine and a negative error resulted in deceleration.

To cope with SSCI-CGI due to high power transfers in weak grids, an advanced vector control strategy based on a gain scheduling approach is proposed for a VSC HVDC in [7]. This control strategy was obtained by introducing four additional decoupling gains in the inverter's outer control loop. The values for these gains were determined for each possible operating condition using a tuning algorithm. Eigenvalue analysis showed that all poles remained in the left half plane when the active power was gradually increased in a very weak grid ($SCR < 1$), implying a stable control.

In Chapter 3 the research gaps and drawbacks in existing adaptive control philosophies were identified. These include (i) the necessity to have in advance knowledge of the wind speed and grid damping for correct operation of the adaptive control, (ii) the need for a wide area measurement system and (iii) validation that the adaptive characteristic of the multiple-model adaptive control does not result in small-signal instability. The developed prediction based gain scheduling control introduced in Section 6.2 addresses these issues. It solves the need for *a priori* knowledge of wind speeds through forecasting. The wide area measurement system is not needed in the developed solution, as the gains are determined for the worst $N-5$ operating condition. Finally, small disturbances such as changing wind speeds and periodic variations in the converter controller parameters could trigger instability. The proposed validation procedure ensures that the adaptive behaviour of the developed control does not lead to small-signal instability.

6.2. PROPOSED SYSTEM LEVEL SOLUTION

The system level solution that is developed in this work is a prediction based gain scheduling control (PGSC) and consists of three modules. The first module is the gain identification and scheduling module; the second module contains a prediction algorithm to forecast the scheduling variables; the last module is the real-time operation module. An overview of the processes and time frames associated with each module is depicted in Figure 6.3.

As was shown in Chapter 5, the wind speed has a determining influence on the occurrence of DFIG-SSR, where the influence of lower wind speeds is more pronounced. At low wind speeds, the damping of the DFIG as seen from the PCC is negative at subsynchronous frequencies. Due to this negative damping, subsynchronous currents will be undamped and potentially harm the wind power plant. The developed solution forecasts the wind speed for near real-time operational time frames (Module 2). The forecasted wind speed is then used to determine the value of some controller gains. The selected gains are then scheduled in the DFIG's control. The values of the gains are determined using extensive offline EMT simulation based optimisations (Module 1). Finally, in real-time operation the actual wind speed is fed to the simulation model. In this situation, the DFIG's gains are scheduled using the forecasted wind speed, while the DFIG will observe the actual wind speed. As such, the performance of the proposed prediction based gain scheduling control heavily depends on the accuracy of the prediction algorithm.

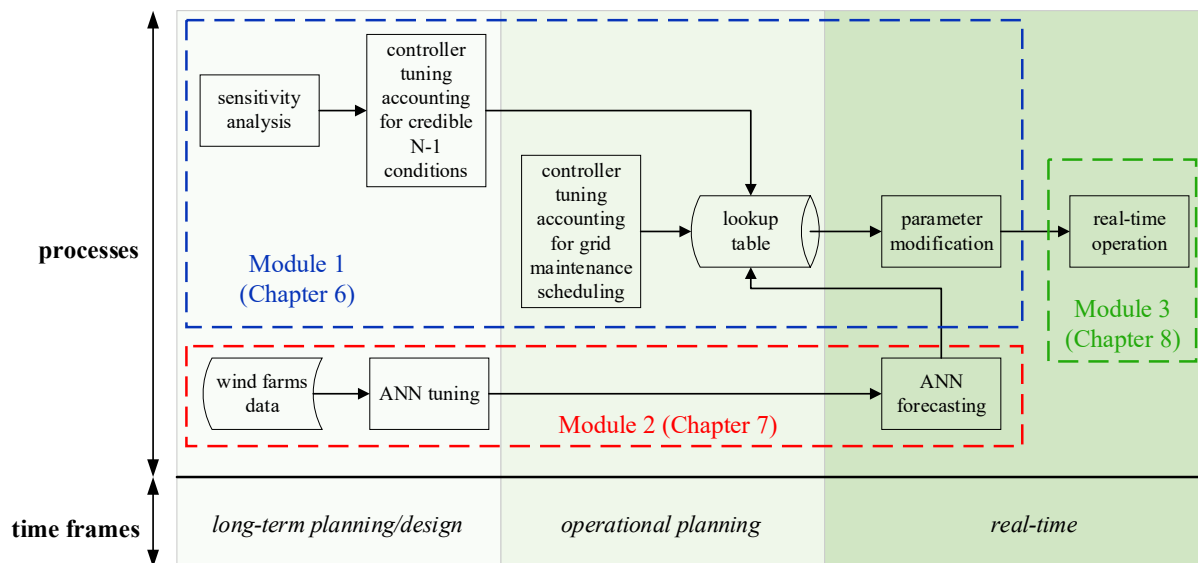


Figure 6.3 Overview of prediction based gain scheduling control for DFIG-SSR mitigation.

6.2.1. MODULE 1: GAIN IDENTIFICATION AND SCHEDULING

In the proposed gain scheduling solution, the values of the gains are selected from a lookup table. The lookup table consists of different gains for selected controller parameters and operating conditions and is populated using extensive offline EMT simulation based optimisations. The operating conditions considered here encompass different wind speeds. First, the relevant controller parameters are identified using sensitivity analysis (Section 6.3).

The impedance based stability analysis method is used to evaluate the sensitivity analysis: controller parameters that influence the impedance characteristic of the DFIG are selected for the lookup table. Furthermore, relevant guidelines are provided to perform such simulations. Next, for the parameters selected through the sensitivity and impedance based stability analyses, multiple optimisations are performed to identify parameter values that mitigate DFIG-SSR under different wind speed conditions. The parameters and their associated values for each wind speed make up the lookup table (Section 6.4).

The forecasted wind speed provided by Module 2 is used to select the gains associated with that wind speed. These gains are then deployed on the DFIG. A retuning of the parameters is only necessary when planned outages lead to phase margins lower than the most critical $N-5$ contingency.

6.2.2. MODULE 2: PREDICTION ALGORITHM

When analysing the time series of the observed wind speeds, it was found that the difference in wind speed between two consecutive time instances could reach 15 m/s, as is shown for a twelve hour period in Figure 6.4. If these wind speed differences cross the cut-in or cut-off wind speeds, the simulation model showed instable behaviour when the associated gains were changed abruptly. After several trial and error simulations, it was found that when the gains were ramped over a time window of maximum 46.5 seconds, the simulation model was stable.

To account for the time needed for ramping, a prediction algorithm is developed that forecasts the wind speed. The forecast attribute gives ample time to implement the required ramp for each scheduling action and is therefore essential in the developed solution. In Module 2 a forecasting algorithm is developed in Python version 3.7.1 [9], where the algorithm's parameters are determined based on how they influence the forecast accuracy of the forecast model. The forecast model is built using an artificial neural network (ANN) and is schematically shown in Figure 6.5.

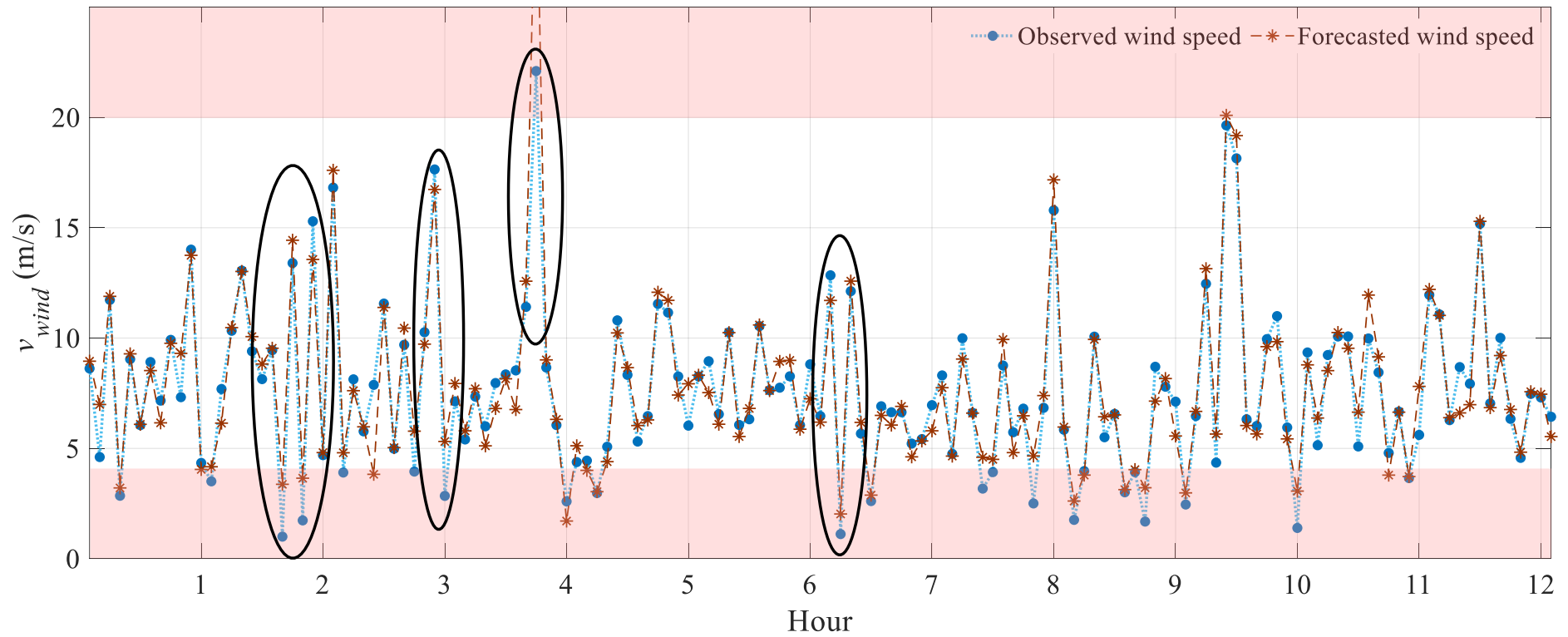


Figure 6.4 Observed and forecasted wind speeds for twelve hours. Red shaded areas represent the cut-in and cut-off wind speed regions. Black ellipses highlight the time instances at which the EMT model was unstable due to high wind speed changes for consecutive time instances.

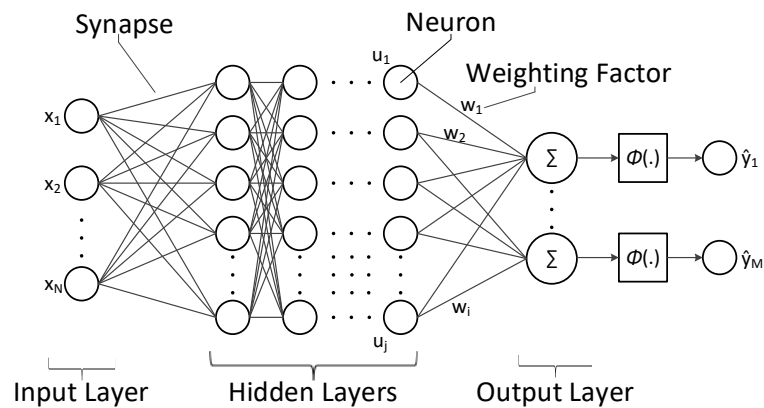


Figure 6.5 General architecture of an artificial neural network.

As the PGSC's performance directly depends on the accuracy of the forecast model, Chapter 7 develops and optimises a feedforward ANN based forecast model. The development of the model and optimisation of its parameters consist of three main steps. First, the combined influence of the input data, batch size, number of neurons and hidden layers, and the training data on the forecast accuracy is investigated for forecast horizons of 5, 15, 30 and 60 minutes. Next, the optimiser and loss function leading to the most accurate forecasts are identified. Finally, it is investigated if the most accurate optimiser-loss function combination is influenced by the choice of the performance metric. With the aim of ensuring robustness of the achieved results, the abovementioned investigations are performed using data of twelve different wind power plants.

6.2.3. MODULE 3: REAL-TIME OPERATION

With the gains associated to the forecasted wind speed, the DFIG is subjected to the actual, observed wind speed in the real-time operation module. For each time instant, an EMT simulation is performed to validate whether DFIG-SSR is indeed mitigated or not. In each EMT simulation a disturbance leads to the radial connection of the DFIG with the series capacitor. For convenience, the study model on which the analyses will be performed is shown again in Figure 6.6. The performance of the PGSC is deemed adequate when it is able to successfully mitigate DFIG-SSR. The assessment is performed using five years of wind speed data. Chapter 8 describes the performance of the PGSC and presents some practical considerations with regards to the proposed solution.

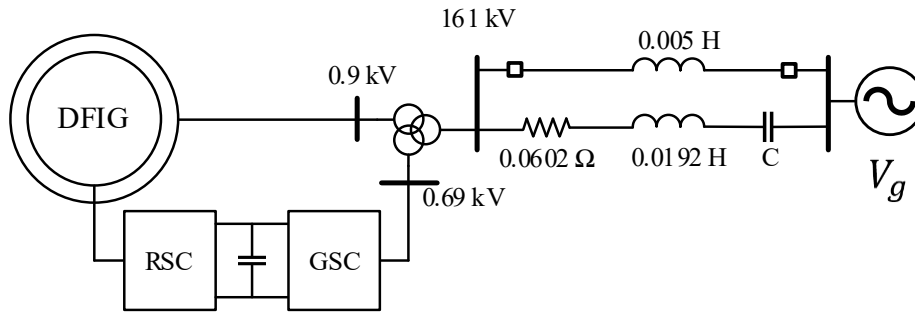


Figure 6.6 Study model for development of DFIG-SSR mitigation solutions.

Next, the development of the gain identification and scheduling module is presented.

6.3. GAIN IDENTIFICATION

In the proposed gain scheduling solution, the lookup table is an offline populated table consisting of different values for predefined controller parameters and operating conditions. The operating conditions considered here encompass different wind speeds. The goal of this Section is to present the method developed to populate such a lookup table. The different controller parameters that will be adaptive, are identified using one factor at a time sensitivity analysis (explained in more detail further down in this Section).

The influence of some controller parameters on DFIG-SSR was already investigated in existing literature and is summarised in Table 6.1. The considered parameters can be grouped in four classes: system characteristics, inverter-PLL parameters and rectifier and inverter parameters. The rectifier and inverter parameters are according to the double loop control structure shown in Chapter 3.2.1 and repeated for convenience in respectively Figure 6.7 and Figure 6.8.

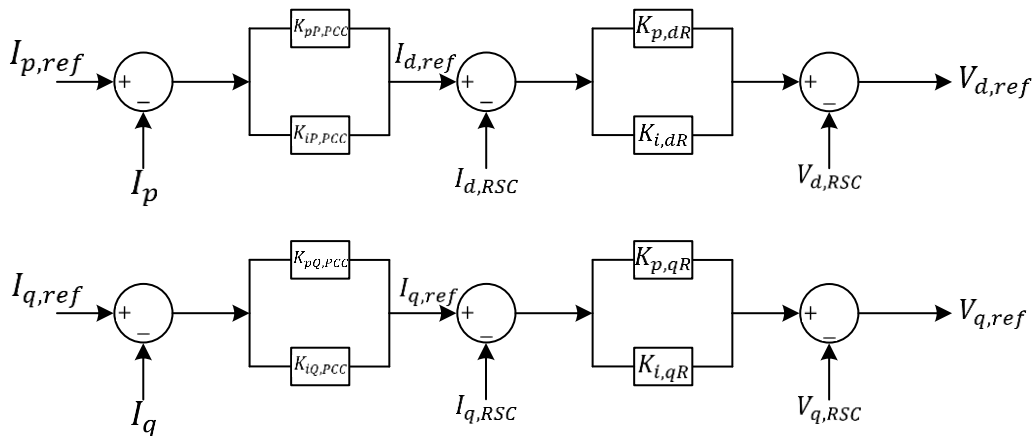


Figure 6.7 Generic rectifier control of a DFIG.

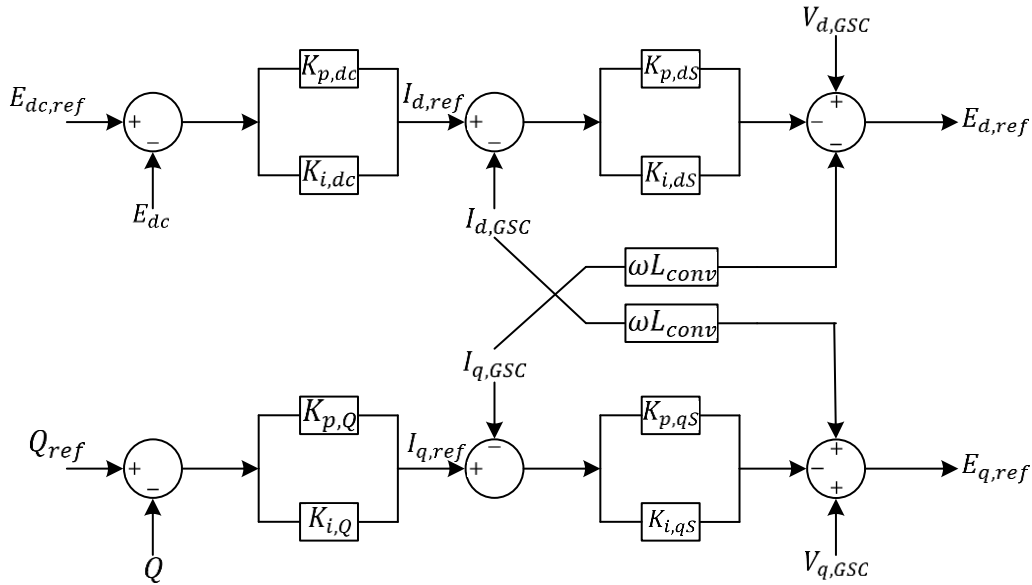


Figure 6.8 Generic inverter control of a DFIG.

As was shown in Figure 5.11, lower wind speeds deteriorate the stability of the DFIG-SSR mode. This is observed by the lower damping. The phase margin at 10 Hz reduces from $+20^\circ$ at wind speed 20 m/s to -38° at wind speed 6 m/s. This relation between the wind speed and the stability was also found in [10]. The impact of the grid strength on DFIG-SSR was shown in Figure 5.26. Under a fixed compensation degree, a decrease in grid strength (i.e. increase in equivalent line inductance) increases the resonance frequency in the overall system. The increasing resonance frequency decreases the phase margin, *ergo* decreasing grid strength reduces the stability. This is also in line with [10]. Finally, eigenvalue analysis performed in [11] showed that with increasing number of online wind turbine generators the real part of the eigenvalue related to the DFIG-SSR mode increases, implying that increasing wind turbine generators decreases the stability.

The influence of the rectifier PI parameters $K_{p,dR}$ and $K_{pP,PCC}$ on DFIG-SSR are reported in respectively [11] and [12]. For both cases, the stability of the DFIG-SSR mode is inversely proportional to these proportional gains. The influence of other parameters is not reported. According to [12], the inverter's double loop control PI parameters do not influence DFIG-SSR. Finally, the PI parameters of the inverter PLL are analysed in [10] and it was concluded that the stability is enhanced when the PLL's proportional gain is reduced, whereas the influence of the integral gain was only marginal.

As is visible from Table 6.1, it is not yet clear how each rectifier parameter influences the stability of the DFIG-SSR mode. This information is needed for selecting the parameters for the gain scheduling solution. To get insight in the parameters' influence, the one-factor-at-a-time sensitivity analysis (OFAT-SA) method is used. In this method, each time the value of a single parameter is increased by 10% and the changes in the resonance frequency and associated phase margin are recorded. The OFAT-SA is conducted for all rectifier and inverter (including PLL) parameters shown in Table 6.1. The results are then compared with the base case to reveal the sensitivities of the parameters. The impedance based stability analysis described in

Chapter 4.3 is a well suited technique for OFAT-SA [13] and will be used in the sensitivity analysis.

Table 6.1 Parameter influence on DFIG-SSR and SSCI.

Class	Parameter	DFIG-SSR	SSCI
System characteristics	Wind speed	Decrease results in less stability [10]	Decrease results in less stability [14]
	Grid strength	Decrease results in less stability [10]	Decrease results in less stability [14]–[19]
	# turbines	Decrease results in more stability [11]	Decrease results in more stability [16]
Rectifier parameters	$K_{p,dR}$	Decrease results in more stability [11]	As the DC bus decouples the rectifier and the inverter, the rectifier has insignificant participation in the adverse interactions with the grid [14], [18]
	$T_{i,dR}$	<i>research gap</i>	
	$K_{p,qR}$	<i>research gap</i>	
	$T_{i,qR}$	<i>research gap</i>	
	$K_{pP,PCC}$	Decrease results in more stability [12]	
	$T_{iP,PCC}$	<i>research gap</i>	
	$K_{pQ,PCC}$	<i>research gap</i>	
Inverter-PLL parameters	$T_{iQ,PCC}$	<i>research gap</i>	
	$K_{p,PLL}$	Decrease results in more stability [10]	Under weak grid conditions a decrease results in more stability [17], [18], [20]
Inverter parameters	$T_{i,PLL}$	No influence on stability [10]	Decrease results in minor stability increase [20]. Also, an increase increases the oscillation frequency [20], [21]
	$K_{p,dS}$	The inverter has insignificant influence on DFIG-SSR [12]	Decrease results in less stability [16], [20] and lower resonance frequencies [14]
	$T_{i,dS}$		Increase results in more stability [14]
	$K_{p,qS}$		<i>research gap</i>
	$T_{i,qS}$		Increase results in more stability [16]
	$K_{p,dc}$		Increase results in less stability [14] and lower resonance frequencies [16]
	$T_{i,dc}$		<i>research gap</i>
	$K_{p,Q}$		<i>research gap</i>
$T_{i,Q}$	<i>research gap</i>		

The obtained impedance responses showing the OFAT-SA results for the inverter are shown in Figure 6.9, where it is observed that 10% changes in inverter parameters have a negligible impact on the DFIG's impedance, i.e. the resonance frequency and associated phase margin do not change for different inverter parameter variations. Also, with varying PLL parameters, the phase margin of the DFIG remains unchanged, showing that the observed interaction is indeed DFIG-SSR and not SSCI-CGI.

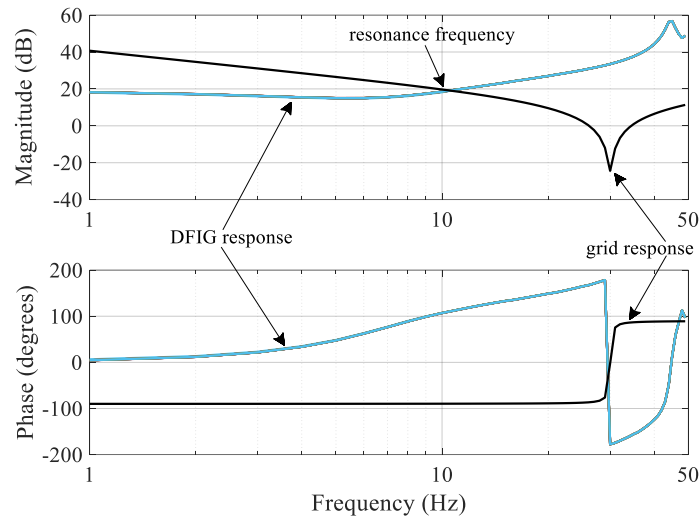


Figure 6.9 Impedance response of the grid and DFIG under inverter parameter variations.

The OFAT-SA results for the rectifier are shown in Figure 6.10. It shows that although the resonance frequency remains unchanged at 10 Hz, the rectifier parameters do influence the phase margin.

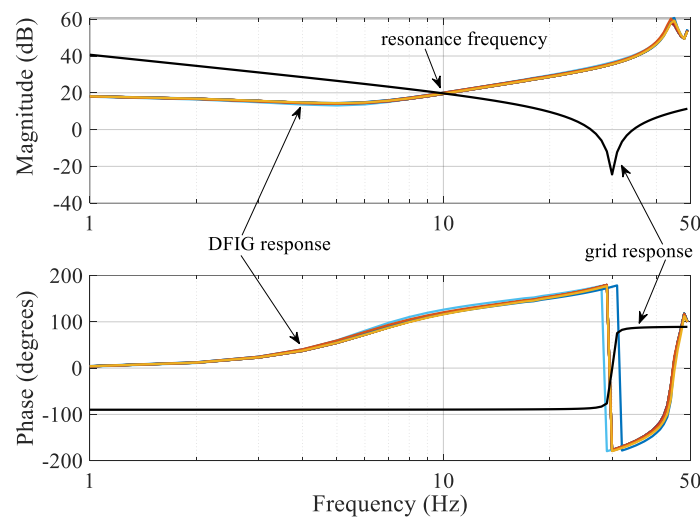


Figure 6.10 Impedance response of grid and DFIG under rectifier parameter variations.

Further examination revealed that all rectifier DLC parameters influence the phase margin at 10 Hz as shown in Figure 6.11. From these, the following six rectifier control parameters changed the phase margin with more than 1° and will be used for the gain scheduling module:

- d-axis proportional gain of the inner control $K_{p,dR}$;
- q-axis proportional gain of the inner control $K_{p,qR}$;
- q-axis integral time constant of the inner control $T_{i,qR}$;
- d-axis integral time constant of the outer control $T_{iP,PCC}$;
- q-axis proportional gain of the outer control $K_{pQ,PCC}$, and
- q-axis integral time constant of the outer control $T_{iQ,PCC}$.

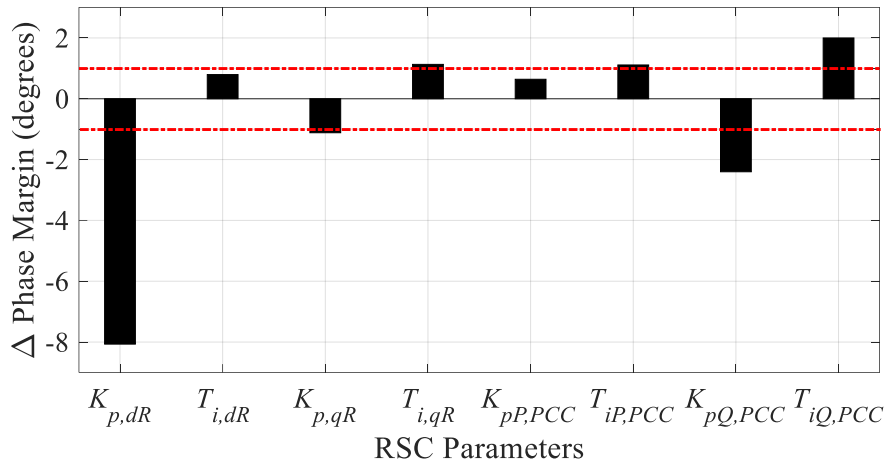


Figure 6.11 Influence of 10% increase in rectifier parameters on the phase margin at 10 Hz. Negative phase margins imply deterioration of stability. Positive phase margins imply enhancement of stability.

These six parameters are combined in the vector \mathbf{x} and multiple optimisations will be performed in the next Section with the goal to identify parameter values that mitigate DFIG-SSR for different wind speeds.

6.4. DEVELOPMENT OF LOOKUP TABLE

6.4.1. OPTIMISATION

The parameter tuning is formulated as a single objective bound constrained optimisation problem. The goal of the optimisation is to minimise the oscillation energy defined by (6.1). The genetic algorithm [22] is deemed to be a suitable solver for such optimisation problems and was also used in [23]–[26] to tune converter parameters and to determine parameters of damping controllers. The settings of the genetic algorithm are given in Table 6.2 and were adopted from [27]. The use of other algorithms and a comparative assessment of their performance as well as the influence of the solver and its settings as given in Table 6.2 on the optimisation performance are out of the scope of this work.

$$\begin{aligned}
 &\text{minimise } \eta = \int_{t_1}^{t_2} (P_{ref} - P_{actual}(t)_x)^2 dt \\
 &\text{subject to} \\
 &\mathbf{x}_{min} \leq \mathbf{x} \leq \mathbf{x}_{max} \\
 &\text{where} \\
 &\mathbf{x} = [K_{p,dR}, K_{p,qR}, K_{pQ,PCC}, T_{i,qR}, T_{iP,PCC}, T_{iQ,PCC}] \\
 &0 < K_{p,dR}, K_{p,qR}, K_{pQ,PCC} \leq 5 \\
 &0 < T_{i,qR}, T_{iP,PCC}, T_{iQ,PCC} \leq 0.5
 \end{aligned} \tag{6.1}$$

In general, the upper and lower bounds of the optimisation variables are defined by the vendor of the DFIG. In the range between the upper and lower bound, the model is expected to have a satisfactory overall performance. In the current model, these bounds were given and

guarantee satisfactory performance of the model with regards to harmonics and changes in operational conditions such as the wind speed and grid topology.

Table 6.2 Genetic algorithm solver settings.

Parameter	Value
Maximum number of iterations	10,000
Initial Population	100
Population of the Surviving Generation	80
Population of the Mating Pool	40
Elite Population	10
Maximum Deviation Rate	10
Binary Mutation Rate	5
Real part Mutation Rate	5
Pairing Method	Random

The simulation model is first initialised until steady state is reached after 35 seconds. The oscillation energy is calculated between 35-38.5 seconds, after which the simulation is terminated. The switching event leading to the radial connection of the DFIG occurs at 36 seconds. The optimisations were performed for each wind speed, where the optimisation stopping criterium was defined as a maximum of 10,000 iterations.

Through extensive empirical analysis it was concluded that when $\eta < 0.07$, DFIG-SSR can be considered to be mitigated. In the subsequent analysis, 0.07 is used as a threshold to assess the suitability of α in mitigating DFIG-SSR.

6.4.2. LOOKUP TABLE

The optimisation discussed in Section 6.4.1 is used to obtain values for the six rectifier parameters ($K_{p,dR}$, $K_{p,qR}$, $K_{pQ,PCC}$, $T_{i,qR}$, $T_{iP,PCC}$ and $T_{iQ,PCC}$) that mitigate DFIG-SSR. The optimisation is performed for wind speeds between 4 m/s (cut-in speed) and 20 m/s (cut-off speed). For each wind speed, the optimisation resulted in a six dimensional solution space essentially proving that DFIG-SSR can be mitigated as long as the parameter values are within this solution space. In the context of the proposed gain scheduling control, the wind speed determines the value of the each of the six rectifier parameters. With the aim of further minimising the number of parameters, it was possible to manually minimise the solution space from six dimensions to two dimensions as is shown in Figure 6.12. The reduction of the number of parameters will not be always possible and depends on the allowed upper and lower bounds of the optimisation variables. As such, only the two rectifier parameters $T_{iP,PCC}$ and $T_{iQ,PCC}$ need to be scheduled according to the expected wind speed. Further reduction was not possible, implying that for the developed DFIG, no unique set of the six rectifier parameters exists that is capable of mitigating DFIG-SSR under all possible wind speed conditions. The proposed gain scheduling solution is based on forecasted wind speeds. The forecasting algorithm will be developed in Chapter 7.

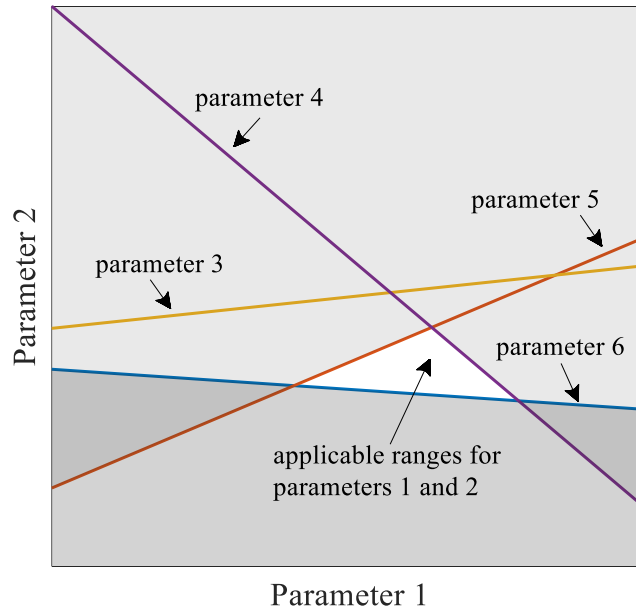


Figure 6.12 Parameter reduction for gain scheduling.

Based on the optimisation and reduction techniques, the control rule for $T_{iP,PCC}$ and $T_{iQ,PCC}$ is formulated as (6.2), with values as given in Table 6.3. For wind speeds lower than 4 m/s and higher than 20 m/s the controller parameters are changed to their initial values. The parameters' values are graphically depicted as a function of the wind speed in Figure 6.13. It is worth noting that the value of these tuned parameters are larger than their initial values in the base case. This is in line with the sensitivity results, i.e. increasing T_i lead to an increase in PM (Figure 6.11).

$$T_i = \begin{cases} T_{i,low} & 4 \leq v_{wind} < 6, v_{wind} \in \mathbb{N} \\ \frac{1}{3}(T_{i,high} - T_{i,low}) \cdot v_{wind} + c & 6 \leq v_{wind} \leq 9, v_{wind} \in \mathbb{N} \\ T_{i,high} & 9 < v_{wind} \leq 20, v_{wind} \in \mathbb{N} \end{cases} \quad (6.2)$$

Table 6.3 Values for the constants of control rule (6.2).

T_i	Initial Value	$T_{i,low}$	$T_{i,high}$	c
$T_{iP,PCC}$	0.02	0.171	0.483	-0.453
$T_{iQ,PCC}$	0.02	0.368	0.103	0.898

Further analysis on the scheduling of these controller parameters revealed that the maximum ramp needed to ensure a stable operation of the DFIG occurred when $T_{iP,PCC}$ needed to be reduced as a result of decreasing wind speeds. This was only the case when the initial wind speeds were higher than 14 m/s.

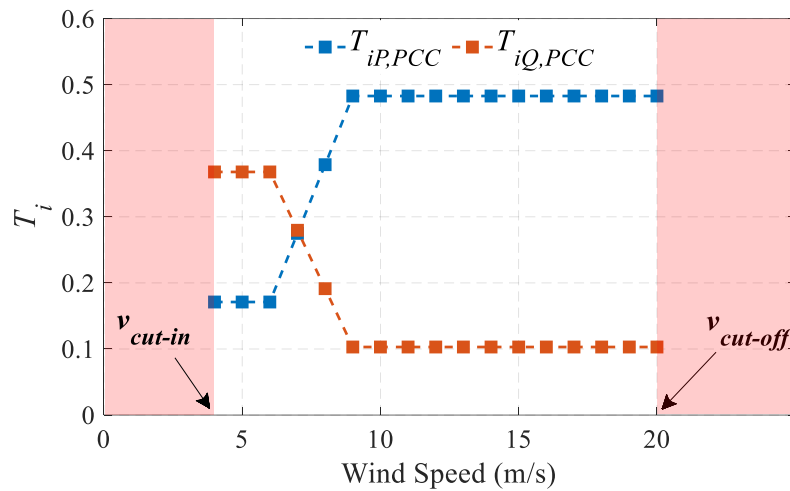


Figure 6.13 Graphical representation of the parameters' values as a function of the wind speed.

6.4.3. VALIDATION

Next, for all wind speeds three validation steps are performed. Below the results are given when the DFIG is operated with wind speed 9 m/s. The goal of the first validation is to confirm that the optimisation and reduction results summarised by (6.1) and (6.2) are indeed able to mitigate DFIG-SSR. Figure 6.14 shows the impedance response for the base case without parameter tuning and for the case with scheduled parameters according to (6.2). Figure 6.15 shows the corresponding detailed time domain EMT simulation results using the study model. It is concluded that the optimised set of parameters can successfully mitigate DFIG-SSR.

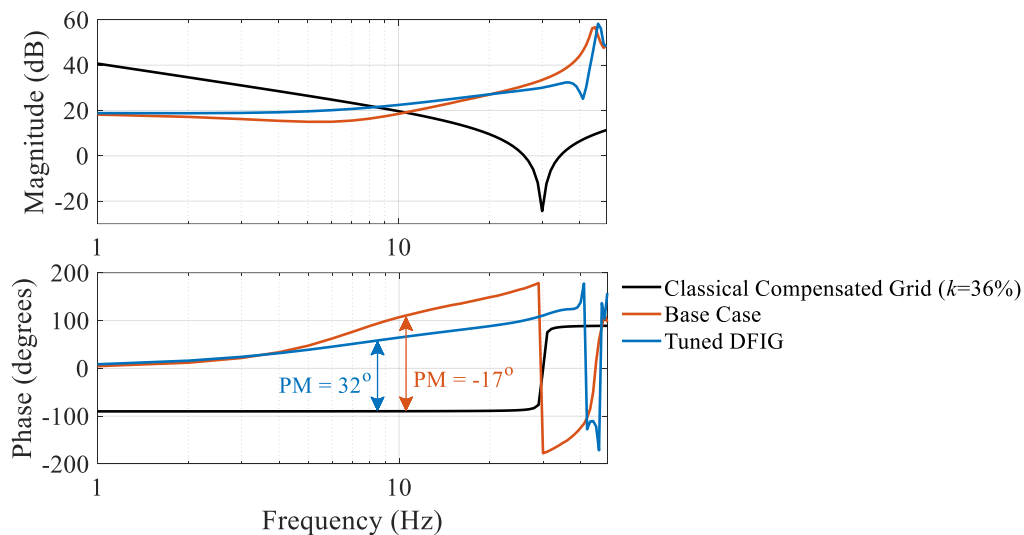


Figure 6.14 Impedance response of the grid and DFIG before and after parameter tuning.

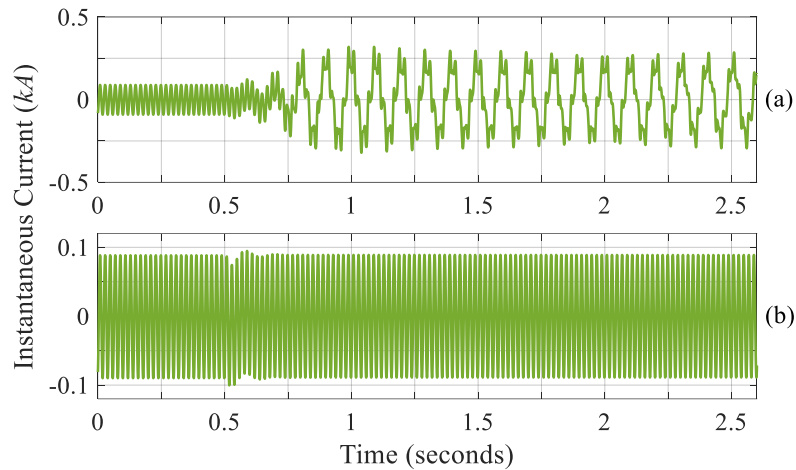


Figure 6.15 Validation of parameter optimisation and reduction results for wind speed 8 m/s. Phase *C* instantaneous currents for (a) base case and (b) tuned parameters according to (6.2).

The second validation is performed to ensure that the optimised parameters do not violate fault ride through (FRT) requirements as stipulated in grid codes. Parameter tuning solutions in literature are rarely accompanied by FRT-validations and as was discussed in Chapter 3, this validation step is crucial to ensure operational reliability.

The FRT performance of the DFIG was evaluated against the FRT requirement as stipulated in the Network Code on Requirements for Generators in Europe [28]. The FRT performance was obtained by simulating a three-phase short circuit of 100 ms at the sending end bus of the study model (Figure 6.6). Figure 6.16 shows the FRT behaviour of the DFIG with and without parameter tuning. The imposed FRT requirement is also shown. The first observation is that for both cases the FRT requirements are met. The second observation is that the tuned parameters introduce a 2 cycle oscillation. This oscillation is well damped and is therefore not considered to be critical.

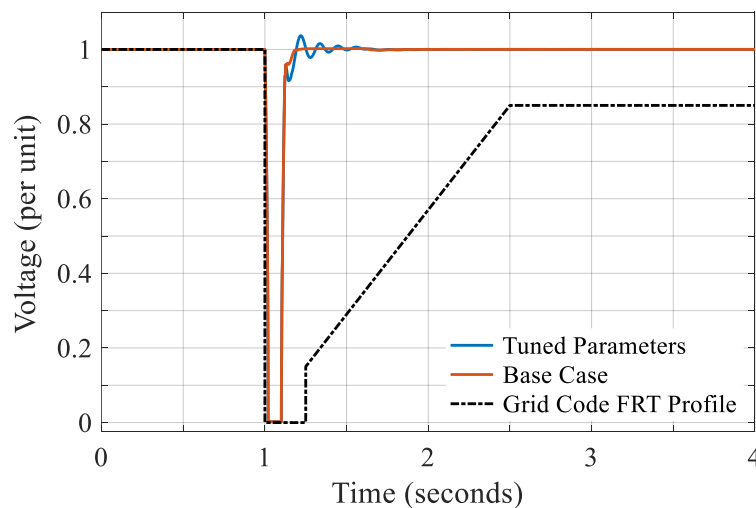


Figure 6.16 Validation of FRT performance against grid code requirements.

Finally, the last validation was performed with the aim to confirm that periodic changes of the controller parameters do not lead to small-signal instability when the DFIG is already in

operation. To investigate this, the DFIG was initialised with wind speed 9 m/s. The wind speed was increased and decreased according to the wind speed profile shown in Figure 6.17a. The rectifier parameters are changed at the indicated times. The active power output (Figure 6.17b) and DC-link voltage (Figure 6.17c) responses are shown for the cases with and without parameter tuning. The DFIG with tuned parameters performs as expected and no small-signal instability is observed. Furthermore, the performance difference between both cases is only minor.

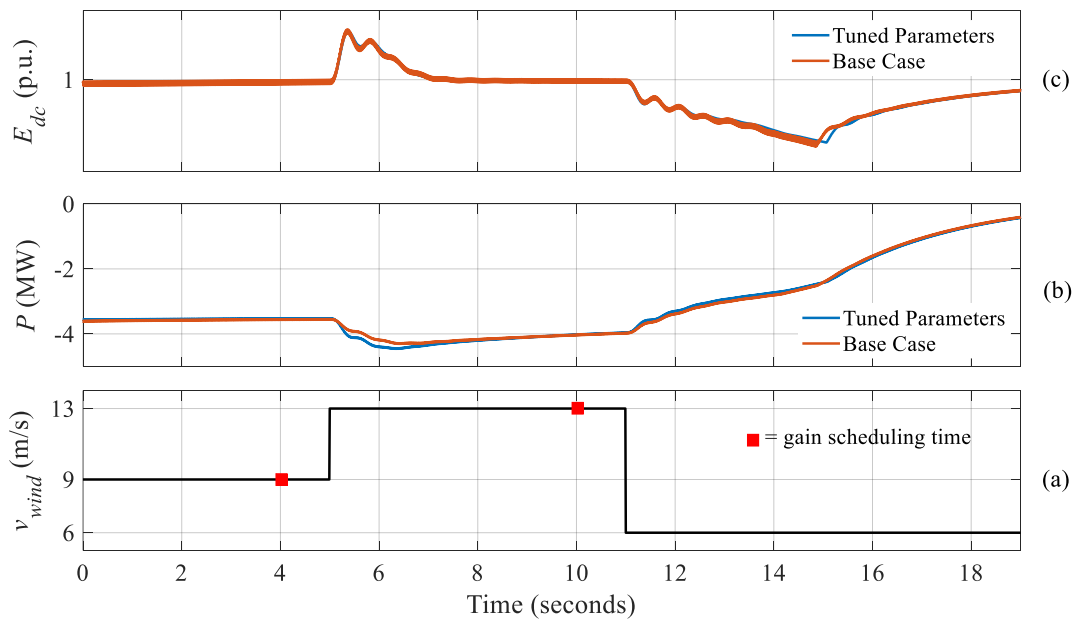


Figure 6.17 Validation of small-signal stability assessment using fictive wind speeds.

The three validation steps show that the tuned parameters are able to mitigate DFIG-SSR without violating operating criteria. The validation steps were performed for all wind speeds as well as for various step changes in the wind speed.

6.5. CONCLUSIONS

This Chapter introduced the design framework of a mitigation solution based on system level coordination. The solution is a prediction based gain scheduling control and consists of three modules. The first module is the gain identification and scheduling module; Module 2 contains a prediction algorithm; the last module is the real-time operation module. This Chapter focused on the development of the first module.

Using monothetic sensitivity analysis the influence of the rectifier, inverter and inverter-PLL parameters on the impedance of the DFIG were assessed. The impedance based stability analysis showed that the influence of the inverter and its PLL on DFIG-SSR was negligible. On the other hand, rectifier parameters were found to have an influence and were used in the optimisation process. In this process, a loss function was formulated based on the oscillation energy. The optimisation resulted in a six dimensional solution space for each wind speed, which was then manually further reduced to a two dimensional solution space. Finally, the

obtained tuned parameters were validated in three steps using time domain EMT simulations. The first validation step aimed at confirming that the tuned parameters were able to effectively mitigate DFIG-SSR. The second step ensured that imposed fault ride through requirements are not violated when the tuned parameters are used. In the final step it was successfully illustrated that the gain scheduling resulting from the expected change in wind speed was stable in the small-signal sense.

The next Chapter will focus on the development of the short-term wind speed forecasting model, which is the second module in the proposed gain scheduling solution.

REFERENCES

- [1] TenneT TSO B.V., “Control Room of the Future R&D Roadmap,” 2021.
- [2] N. P. W. Strachan and D. Jovcic, “Stability of a variable-speed permanent magnet wind generator with weak AC grids,” *IEEE Trans. Power Deliv.*, vol. 25, no. 4, pp. 2779–2788, 2010.
- [3] J. Martin, “How to improve human decisions with PMU’s automatic system for the control of stability of a HVDC link in Red Electrica de España,” in *CIGRE Session 2020*, 2020.
- [4] P. Maibach, A. Hernandez, J. Peiro, C. Smith, V. Sewdien, and J. van Putten, “Capabilities of Power Electronic Devices in Enabling the Energy Transition and Mitigating System Operational Challenges (accepted for publication),” *CIGRE Sci. Eng. J.*, vol. 19, 2020.
- [5] I. Vieto, P. Huang, T. Reinikka, H. Nademi, C. Buchhagen, and J. Sun, “Online measurement of offshore wind farm impedance for adaptive control of hvdc transmission systems,” in *2019 IEEE 20th Workshop on Control and Modeling for Power Electronics*, 2019.
- [6] X. Yuan, F. Wang, D. Boroyevich, R. Burgos, and Y. Li, “DC-link voltage control of a full power converter for wind generator operating in weak-grid systems,” *IEEE Trans. Power Electron.*, vol. 24, no. 9, pp. 2178–2192, 2009.
- [7] A. Egea-Alvarez, S. Fekriasl, F. Hassan, and O. Gomis-Bellmunt, “Advanced Vector Control for Voltage Source Converters Connected to Weak Grids,” *IEEE Trans. Power Syst.*, vol. 30, no. 6, pp. 3072–3081, Nov. 2015.
- [8] D. Wilson, “Icelandic Operational Experience of Synchrophasor-based Fast Frequency Response and Islanding Defence,” in *Proceedings of the 2018 CIGRE Session*, 2018.
- [9] “Python Language Reference, version 3.6.3.” Python Software Foundation, Available at <https://www.python.org/>.
- [10] W. Jin and Y. Lu, “Stability Analysis and Oscillation Mechanism of the DFIG-Based Wind Power System,” *IEEE Access*, vol. 7, pp. 88937–88948, 2019.
- [11] X. Xie, L. Wang, X. Liu, and Q. Jiang, “Centralised solution for subsynchronous control interaction of doubly fed induction generators using voltage-sourced converter,” *IET Gener. Transm. Distrib.*, vol. 9, no. 16, pp. 2751–2759, 2015.
- [12] L. Fan, C. Zhu, Z. Miao, and M. Hu, “Modal analysis of a DFIG-based wind farm interfaced with a series compensated network,” *IEEE Trans. Energy Convers.*, vol. 26, no. 4, pp. 1010–1020, 2011.
- [13] T. Rauhala and P. Järventausta, “Frequency scanning techniques for analysis of the effect of device dependent subsynchronous oscillations on subsynchronous damping,” in *16th Power Systems Computation Conference, PSCC 2008*, 2008, pp. 1–7.
- [14] B. Huang, H. Sun, Y. Liu, L. Wang, and Y. Chen, “Study on subsynchronous oscillation in D-PMSGs-based wind farm integrated to power system,” *IET Renew. Power Gener.*, vol. 13, no. 1, pp. 16–26, 2018.

-
- [15] Y. Chen, Y. Liu, H. Sun, B. Huang, and L. Wang, "SSCI Problem of D-PMSGs Based Wind Farm Considering Frequency Characteristics of Grid Impedance," *2018 Int. Conf. Power Syst. Technol. POWERCON 2018 - Proc.*, no. 201804270000930, pp. 1826–1831, 2019.
- [16] H. Liu *et al.*, "Subsynchronous Interaction between Direct-Drive PMSG Based Wind Farms and Weak AC Networks," *IEEE Trans. Power Syst.*, vol. 32, no. 6, pp. 4708–4720, 2017.
- [17] J. Z. Zhou, H. Ding, S. Fan, Y. Zhang, and A. M. Gole, "Impact of short-circuit ratio and phase-locked-loop parameters on the small-signal behavior of a VSC-HVDC converter," *IEEE Trans. Power Deliv.*, vol. 29, no. 5, pp. 2287–2296, 2014.
- [18] L. Fan, "Modeling Type-4 Wind in Weak Grids," *IEEE Trans. Sustain. Energy*, vol. 10, no. 2, pp. 853–864, 2019.
- [19] L. Papangelis, M. S. Debry, T. Prevost, P. Panciatici, and T. Van Cutsem, "Stability of a voltage source converter subject to decrease of short-circuit capacity: A case study," *20th Power Syst. Comput. Conf. PSCC 2018*, pp. 1–7, 2018.
- [20] Y. Xu and Y. Cao, "Sub-synchronous oscillation in PMSGs based wind farms caused by amplification effect of GSC controller and PLL to harmonics," *IET Renew. Power Gener.*, vol. 12, no. 7, pp. 844–850, 2018.
- [21] Y. Li, L. Fan, and Z. Miao, "Wind in Weak Grids: Low-Frequency Oscillations, Subsynchronous Oscillations, and Torsional Interactions," *IEEE Trans. Power Syst.* (early access), 2019.
- [22] R. L. Haupt and S. E. Haupt, *Practical Genetic Algorithms*. New York: Wiley-Interscience, 1998.
- [23] A. Chen, D. Xie, D. Zhang, C. Gu, and K. Wang, "PI parameter tuning of converters for sub-synchronous interactions existing in grid-connected DFIG wind turbines," *IEEE Trans. Power Electron.*, vol. 34, no. 7, pp. 6345–6355, 2019.
- [24] R. Thirumalaivasan, M. Janaki, and N. Prabhu, "Damping of SSR using subsynchronous current suppressor with SSSC," *IEEE Trans. Power Syst.*, vol. 28, no. 1, pp. 64–74, 2013.
- [25] T. Rajaram, J. M. Reddy, and Y. Xu, "Kalman Filter Based Detection and Mitigation of Subsynchronous Resonance with SSSC," *IEEE Trans. Power Syst.*, vol. 32, no. 2, pp. 1400–1409, 2017.
- [26] Z. Bin *et al.*, "An active power control strategy for a DFIG-based wind farm to depress the subsynchronous resonance of a power system," *Int. J. Electr. Power Energy Syst.*, vol. 69, 2015.
- [27] H. A. Mohammadpour, M. M. Islam, D. Coats, E. Santi, and Y. J. Shin, "Sub-synchronous resonance mitigation in wind farms using gate-controlled series capacitor," *2013 4th IEEE Int. Symp. Power Electron. Distrib. Gener. Syst. PEDG 2013 - Conf. Proc.*, no. 1, pp. 2–7, 2013.
- [28] European Commission, "COMMISSION REGULATION (EU) 2016/631 of 14 April 2016 establishing a network code on requirements for grid connection of generators," *Off. J. Eur. Union*, no. L 112, pp. 1–68, 2016.

7. FORECASTING MODULE DEVELOPMENT

7.1. INTRODUCTION

The previous Chapter presented the overall functionalities of the predictive gain scheduling control. It also elaborated on the identification of control parameters of the rectifier for the gain scheduling, as well as on determining the wind speed dependent gain values.

The goal of the current Chapter is to develop an accurate wind speed forecasting algorithm by assessing the influence of several forecasting related parameters on the prediction accuracy and by tuning these parameters to yield a minimum prediction error. As will be shown in this Chapter, forecasting algorithms found in existing literature only perform a limited tuning of some of the forecasting algorithm's parameters, whereas tuning of the optimiser and loss function for wind speed forecasting applications is not yet reported. The wind speed forecast model developed in this Chapter is based on an artificial neural network and the tuning is achieved in three steps. In the first step the combined influence of the input data, batch size, number of neurons in hidden layers, number of hidden layers, and the training data on the forecast accuracy across forecast horizons of 5, 15, 30 and 60 minutes is analysed. These parameters make up the structure of the artificial neural network. In the second step, the optimiser and loss function leading to the most accurate forecasts are identified. The optimiser and loss function are variables of the forecast algorithm itself. Finally, it will be investigated if the most accurate optimiser-loss function combination identified in the second step is influenced by the choice of the performance evaluation metric. The forecasting module is developed in Python and analyses will be performed using data of twelve wind power plants.

Parts of this Chapter are published in V. N. Sewdien, R. Preece, J. L. Rueda Torres, E. Rakhshani, and M. A. M. M. van der Meijden, "Assessment of Critical Parameters for Artificial Neural Networks based Short-Term Wind Generation Forecasting," *Renew. Energy*, vol. 161, pp. 878–892, 2020.

7.2. FORECASTING IN THE OPERATIONAL PLANNING PROCESS

In the operational planning process, RES related forecasting is performed with different purposes and across different time horizons. A summary of such forecast horizons and their applications is summarised in Table 7.1.

Table 7.1 Forecast time horizons in operational planning.

Forecasting Time Horizon	Range	Application
Long-term	Days to weeks ahead	<ul style="list-style-type: none"> • Maintenance schedules of transmission lines during low forecasted renewable energy generation; • Maintenance schedules of e.g. wind turbines in order to minimise revenue losses for wind power plant owners.
Short-term: Day Ahead	24 hours ahead	<ul style="list-style-type: none"> • Operational decision making with regards to the dispatch of renewable energy sources; • Dynamic assessment of operating reserves requirements (e.g. for balancing).
Short-term: Near Real Time	Between 24 hours and 5 minutes ahead	<ul style="list-style-type: none"> • Adjustments of real time dispatch; • Dynamic assessment of operating reserves requirements (e.g. for ramp management); • More accurate security analysis.

Depending on the time horizon of interest, forecast models are generally divided in two categories: physical models and statistical models. Physical models use atmospheric quantities (e.g. wind speed and direction, temperature and pressure), physical properties (e.g. terrain ruggedness and wind power plant layout) and numerical weather predictions (NWP) as inputs for complex meteorological forecast models. Physical models are very accurate for forecast horizons exceeding six hours [1]. However, one of the main challenges with this approach is that it requires specialised equipment for the acquisition and processing of the atmospheric and physical data [2].

Statistical models are purely mathematical models and mainly use past observed data, sometimes complemented with NWP information. Statistical models consists of among others spatial correlation models, models based on probabilistic methods and models based on machine learning. Machine learning methods are widely used [3], where artificial neural networks (ANN) are among the top used techniques for short-term forecasting [2], [4]. The review performed in [5] even concluded that ANN based forecasting methods are the most accurate ones, provided that the ANN network configuration is optimised.

The gain scheduling mitigating solution developed in this thesis is based on short-term forecasting of the wind speed. With ANNs being among the top used techniques for this purpose, it will be used for the wind speed prediction required for the proposed solution. The

next Section provides a brief summary of the basic form and function of an ANN, while more details can be found in [6].

7.3. ARTIFICIAL NEURAL NETWORKS

An ANN acts as a black-box that maps inputs to outputs. It learns this input-output mapping by training and optimisation. Figure 7.1 illustrates the general structure of an ANN. It consists of an input layer, one or more hidden layers, an output layer and several synapses with their associated weighting factors. Each layer contains a number of neurons. A synapse is the link between two neurons of different layers.

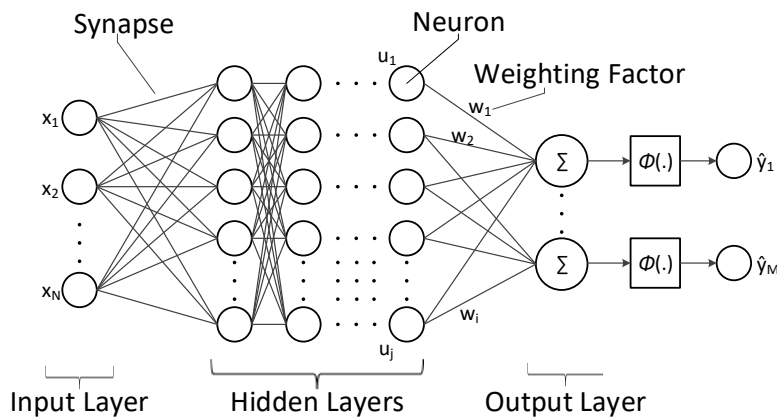


Figure 7.1 Generic architecture of an artificial neural network.

With respect to the application of an ANN for short-term wind speed prediction, the input layer can consist of either previously observed wind speeds or numerical weather prediction data, where each input variable is assigned to a single neuron in the input layer. The neurons in the input layer are connected to the hidden layer and although the number of neurons in each hidden layer can be chosen arbitrarily, some sort of optimisation is required as this number influences the forecast accuracy. An activation function $\phi(\tau)$ is used to define the output of neurons for the next layer according to (7.1). The dimension of the output layer is determined by the number of outputs being forecasted.

$$\hat{y}_M = \phi \left(\sum_{i,j=1}^{i,j} w_i u_j \right) \quad (7.1)$$

\hat{y}_M : forecasted value

ϕ : activation function

w_i : weighting factor of synapse

u_j : neuron in hidden layer

The activation function implemented in the ANN of this work is the rectifier function [7] and is mathematically described as given in (7.2). The rectifier function is widely used due to its low forecast error and high sparsity [8], [9].

$$\phi(\tau) = \max(0, \tau) \quad (7.2)$$

Based on the objective function of the ANN's optimiser, the weighting factors are updated using the feedforward back propagation (FFBP) technique [10]. The algorithm for the FFBP technique can be decomposed in four steps as is explained next.

Consider the ANN as depicted in Figure 7.2. It consists of one input layer with three input neurons, two hidden layers with four neurons each and one output layer with two neurons. Weight $w_{i,j}$ represents the weighting factor of the synapse connecting neuron i to neuron j . For simplicity reasons, the activation function $\phi(\cdot)$ is shown only for the output layer. However, all neurons of the hidden and input layers have an activation function in the same structure as is shown for the output layer.

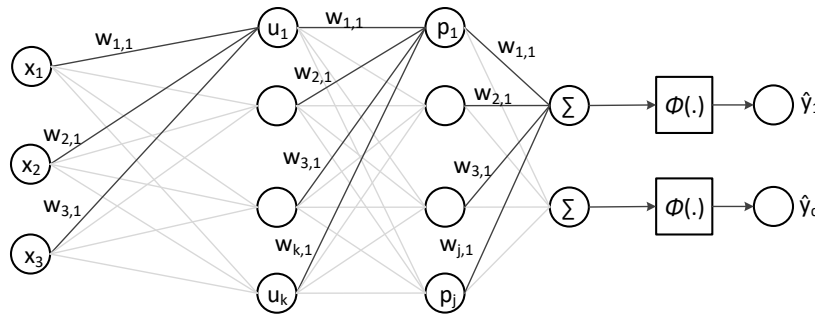


Figure 7.2 ANN for development of feedforward back propagation algorithm.

The first step of the FFBP technique consists of establishing the value of the output neuron \hat{y}_q in terms of input neurons x_n . The value of neurons u_1, u_2, u_3 and u_4 of the first hidden layer are calculated as

$$\begin{cases} u_1 = \phi(x_1 \cdot w_{1,1} + x_2 \cdot w_{2,1} + x_3 \cdot w_{3,1}) \\ u_2 = \phi(x_1 \cdot w_{1,2} + x_2 \cdot w_{2,2} + x_3 \cdot w_{3,2}) \\ u_3 = \phi(x_1 \cdot w_{1,3} + x_2 \cdot w_{2,3} + x_3 \cdot w_{3,3}) \\ u_4 = \phi(x_1 \cdot w_{1,4} + x_2 \cdot w_{2,4} + x_3 \cdot w_{3,4}) \end{cases} \quad (7.3)$$

With N neurons in the input layer and k neurons in the first hidden layer, (7.3) becomes

$$u_k = \phi \left(\sum_{n=1}^N w_{n,k} \cdot x_n \right) \quad (7.4)$$

Similarly, the value of neurons p_j in the second hidden layer are calculated using (7.5).

$$\begin{cases} p_1 = \phi(u_1 \cdot w_{1,1} + u_2 \cdot w_{2,1} + u_3 \cdot w_{3,1} + u_4 \cdot w_{4,1}) \\ p_2 = \phi(u_1 \cdot w_{1,2} + u_2 \cdot w_{2,2} + u_3 \cdot w_{3,2} + u_4 \cdot w_{4,2}) \\ p_3 = \phi(u_1 \cdot w_{1,3} + u_2 \cdot w_{2,3} + u_3 \cdot w_{3,3} + u_4 \cdot w_{4,3}) \\ p_4 = \phi(u_1 \cdot w_{1,4} + u_2 \cdot w_{2,4} + u_3 \cdot w_{3,4} + u_4 \cdot w_{4,4}) \end{cases} \quad (7.5)$$

With k neurons in the first hidden layer and j neurons in the second hidden layer, (7.5) becomes

$$p_j = \phi\left(\sum_{k=1}^K w_{k,j} \cdot u_k\right) \quad (7.6)$$

By substituting (7.4) in (7.6), neuron p_j of the second hidden layer can be expressed in terms of the input neurons x_n as shown in (7.7).

$$p_j = \phi\left(\sum_{k=1}^K w_{k,j} \cdot \phi\left(\sum_{n=1}^N w_{n,k} \cdot x_n\right)\right) \quad (7.7)$$

The values of neurons \hat{y}_q in the output layer are calculated using (7.8) and can be generalised to (7.9).

$$\begin{cases} y_1 = \phi(p_1 \cdot w_{1,1} + p_2 \cdot w_{2,1} + p_3 \cdot w_{3,1} + p_4 \cdot w_{4,1}) \\ y_2 = \phi(p_1 \cdot w_{1,2} + p_2 \cdot w_{2,2} + p_3 \cdot w_{3,2} + p_4 \cdot w_{4,2}) \end{cases} \quad (7.8)$$

$$\hat{y}_q = \phi\left(\sum_{j=1}^J w_{j,q} \cdot p_j\right) \quad (7.9)$$

Finally, when substituting (7.7) in (7.9), the generic mathematical expression of the output neurons in terms of the input neurons is obtained:

$$\hat{y}_q = \phi\left(\sum_{j=1}^J w_{j,q} \cdot \phi\left(\sum_{k=1}^K w_{k,j} \cdot \phi\left(\sum_{n=1}^N w_{n,k} \cdot x_n\right)\right)\right) \quad (7.10)$$

Equation (7.11) describes the concept of the feedforward forecasting algorithm.

In the second step, the error between the forecasted output \hat{y}_q and its actual observed value y_q is determined using a loss function. As \hat{y}_q is determined among others by the weights w_i , the loss function is indirectly also a function of $w_{i,j}$. A very basic loss function is given in (7.12). The error $J(\theta)$ is then back propagated to the output layer, hence the ‘back propagation’ terminology in FFBP. Loss functions are further discussed in Section 7.6.3.

$$\hat{y}_q = \phi \left(\sum_{j=1}^J w_{j,q} \cdot \phi \left(\sum_k^K w_{k,j} \dots \dots \left(\phi \left(\sum_{n=1}^N w_{n,k} \cdot x_n \right)_{HL\ 1} \right)_{HL\ p-1} \right)_{HL\ p} \right)_{output\ layer} \quad (7.11)$$

- \hat{y}_q : forecasted value of the q^{th} neuron in the output layer
 J : number of neurons in hidden layer p
 $w_{j,q}$: weighting factor of synapse that connect the j^{th} neuron of hidden layer p to the q^{th} neuron of the output layer
 K : number of neurons in hidden layer $p-1$
 N : number of neurons in input layer
 $HL1$: first hidden layer
 p : number of hidden layers

$$J(\theta) = y - \hat{y}(\theta) \quad (7.12)$$

- J : forecast error
 θ : vector containing all weighting factors w_i
 y : observed output
 \hat{y} : forecasted output

In the third step, the back propagation continues to the hidden layers. In the final step, the weights are updated, with the aim of minimising $J(\theta)$. The algorithm stops when a predefined number of optimisation iterations has been reached. Usually, the objective function has the target to minimise (7.13): the error between N pairs of forecasted and observed values.

$$\varepsilon = \frac{1}{N} \sum_{i=1}^N J(\theta)_i \quad (7.13)$$

At the start of each training process, the weights w_i need to be initialised. A widely used initialisation method is the Xavier initialisation [11]. However, as was shown in [12], the Xavier scheme is not appropriate for the current application, as the scheme loses its strengths when used with non-linear activation functions such as the rectifier activation function. In [12] the He initialisation scheme is shown to be appropriate for non-linear activation functions and is used throughout this work. The influence of weight initialisation methods on the forecast accuracy is out of the scope of this work.

7.4. DATA

Depending on the geographical location of a wind power plant, the same forecast algorithm will result in different forecast accuracies [13]. To ensure robustness of the forecast results obtained in this thesis, the analyses are carried out for twelve different wind power plants, each

with their own geographical characteristics. By doing so, the achieved results can be considered general enough to be applied on wind power plants with a wide range of geographical characteristics. The wind speed data is retrieved from the WIND Prospector Toolkit of USA's National Renewable Energy Laboratory [14]–[17] and belongs to the wind parks shown in Figure 7.3 and Table 7.2. The dataset of each location consists of measured wind speeds with a 5 minutes resolution for the time span 2007–2012.

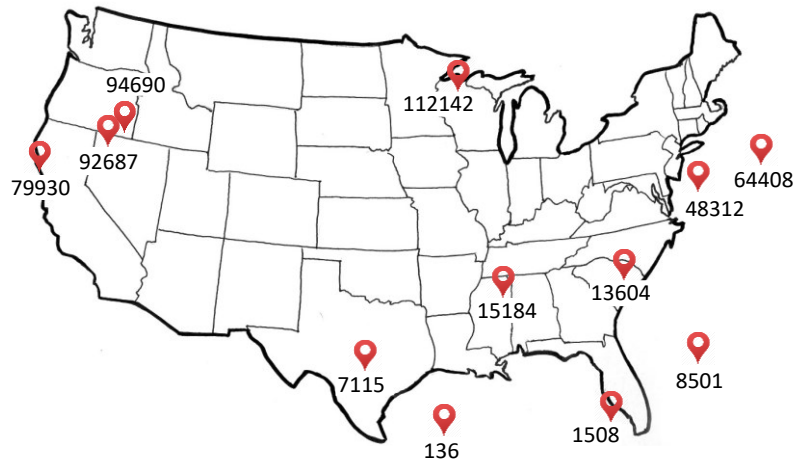


Figure 7.3 Location and site identification numbers of the considered wind power plants.

Table 7.2 Geographical coordinates of considered wind power plants.

Site ID	Longitude	Latitude
136	-93.660828	25.789566
1508	-82.809998	26.368622
7115	-99.497406	30.336601
8501	-77.39856	29.295036
13604	-88.724579	33.849228
15184	-80.262238	33.363693
48312	-73.391205	37.496029
64408	-70.430237	38.473736
79930	-123.977585	39.193207
92687	-118.889999	41.542522
94690	-118.084106	41.870815
112142	-90.955688	46.140095

7.5. TUNING OF ANN STRUCTURE AND ALGORITHM

As stated in Section 7.2, ANNs are among the most accurate methods for forecasting wind speeds, provided that the parameters of the ANN structure are optimised for forecast horizons (FH) 5, 15, 30 and 60 minutes. To develop a custom forecasting module for the gain scheduling algorithm, the influence of different ANN and FFBP algorithm parameters on the forecast accuracy is investigated next. The obtained results will be used to developed a tuned forecasting

module. Currently, five minutes forecasts are mainly useful in security constrained economic dispatch markets and for ramp forecasting in power systems with high penetration of RES [18]. FH 15, FH 30 and FH 60 are useful for intraday and balancing markets, where quarter-hourly and hourly products are traded.

7.5.1. STATE OF THE ART

The ANN parameters that are of interest are the amount of historical data (i.e. historical data size, HDS), the batch size (BS), the number of hidden layers (HL), number of neurons per hidden layer (N_{HL}) and the amount of training data (TD).

Whereas previous publications investigated the influence of the amount of historical data on the forecast accuracy, only few analysed the impact of HDS combined with other aspects of the ANN's structure. In [19] the influence of the HDS for a single one-hour forecast of wind generation was investigated. The forecasting algorithm contained one hidden layer with three neurons, and TD 57 %. It was found that the optimum HDS was dependent on the learning rate of the algorithm. In [20] the influence of HDS on the forecast accuracy for FH 30 was investigated. The implemented forecasting algorithm contained one hidden layer, whereas HDS was varied from three to eight. The highest forecast accuracy was achieved for the ANN with HDS 8. In [21] the influence of HL and HDS on the forecast accuracy was investigated. A simple ANN with HDS 2 and no hidden layers achieved the highest forecast accuracy.

The aim in the above mentioned references was to identify the ANN with the highest forecast accuracy across one specific forecast horizon. Furthermore, the solution space considered in these references was rather limited, as maximum two ANN parameters were varied. Therefore, there are still unresolved questions around the impact of proper tuning of the ANN's parameters on the forecast accuracy and how the tuning results differ across different forecast horizons. Thus, the first goal of this Chapter is to examine the combined influence of the amount of historical data, batch size, number of hidden layers, number of neurons per hidden layer, and the amount of training data on the forecast accuracy for forecast horizons 5, 15, 30, and 60 minutes ahead. This influence on the forecast accuracy will be considered by observing the mean absolute error (MAE).

7.5.2. SIMULATION RESULTS

The influence of the following parameters on the forecast accuracy is investigated:

- HDS: 5, 10, 20[†];
- HL: 1, 2, 3[‡];
- N_{HL} : 100 % (i.e. equal to the number of neurons in the input layer) and 50 % (i.e. equal to the average of the neurons in the input and output layer);
- TD: 50 % and 80 % of the test data;
- BS, i.e. amount of samples after which the weighting factors are updated: 5, 10, 20.

[†] Higher number of inputs did not influence the forecast error positively

[‡] More hidden layers did not influence the forecast error positively

For each FH, several permutations of the above mentioned parameters were produced for analysing their impact on the forecast accuracy. The analyses were carried out for twelve different wind power plants. For each of these sites and for each FH, Figure 7.4 depicts the first quartile of the MAE.

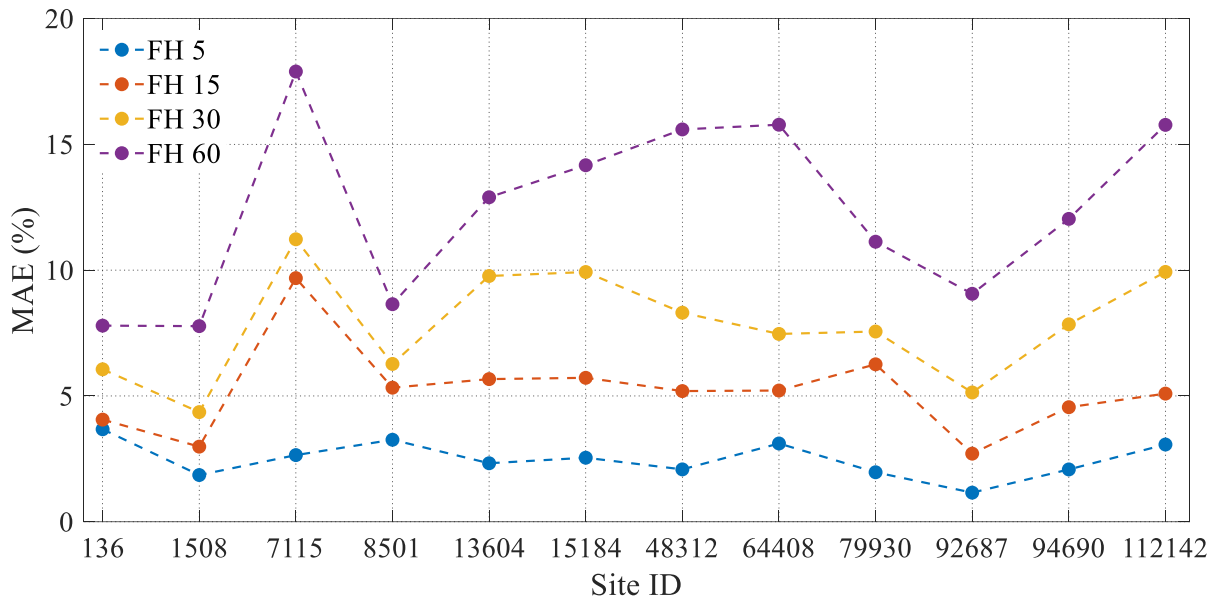


Figure 7.4 First Quartile of MAE for twelve wind power plants across four forecast horizons.

Two interesting observations can be made from Figure 7.4. First, for each of the sites, increasing forecast horizons consistently lead to increasing forecast errors. As the predictability of the state of any highly complex system decreases with increasing look ahead time, the forecast error increases. Similar conclusions were also reached in [22], [23]. Second, for the same forecast horizon the forecast errors are different across the different sites. When comparing different sites, it is observed that forecasts with longer look ahead times of a site perform better than forecasts with shorter look ahead times of another site: the 60 minutes forecast of site 136 has a better performance than the 30 minutes forecast of site 7115, whereas the 30 minutes forecast of site 1508 and the 15 minutes forecast of site 92687 outperform respectively the 15 minutes forecast of site 8501 and the 5 minutes forecast of site 8501. This is not an attribute of the forecast model, but is due to the geographical characteristics and ruggedness of the site. The ruggedness is expressed using the ruggedness index (RIX) and higher RIX values lead to increased forecast errors [24]. A similar conclusion regarding the sensitivity of the forecast error to the RIX was also achieved in [25].

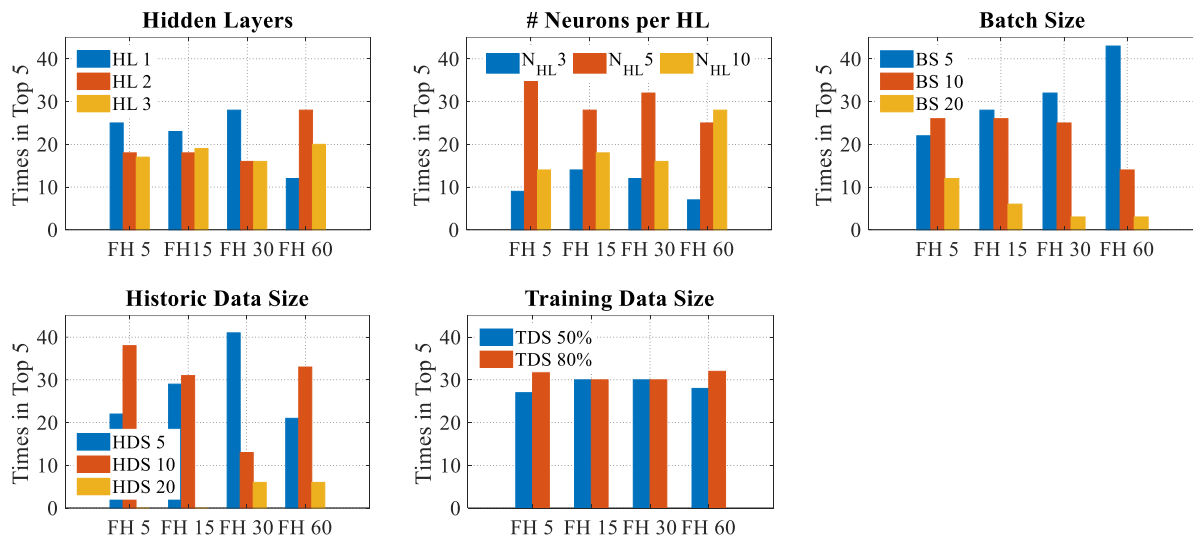


Figure 7.5 Parametric evaluation of ANN based forecast model.

Maximising the system's predictability with increasing forecast horizons increases the complexity of forecasting algorithms. Two factors that contribute to the algorithm's complexity are the architecture of the ANN (i.e. the number of hidden layers, the number of neurons per hidden layer and the historical data size) and the training algorithm (i.e. the batch size and the test data size). Figure 7.5 shows for the four FH how often each of the parameters ended up in the top 5 MAE. The higher the presence of a parameter in the top 5, the higher its influence on the forecast error. The analysis gives insights in how the complexity of the forecasting algorithm changes as a function of the forecast horizon.

In terms of the size of the training data set, it can be concluded that TD has an insignificant sensitivity for the forecast horizon and that either 50 % or 80 % of the test data can be used for learning purposes. The advantage of a lower TD is that the lower the size of the training data set, the earlier a forecast model can be fully operational. In this research the test data consisted of one year of data, which results in a 6 months period before the model could be deployed and be fully operational.

In terms of the number of hidden layers, up to FH 30 one hidden layer provided sufficient complexity to minimise the forecast error (41.7 % of the top 5 cases for FH 5, 38.3 % for FH 15 and 46.7 % for FH 30 contained one hidden layer). Two hidden layers claimed a share of 46.7 % in the top 5 MAE for FH 60. The complexity is even further increased by assigning 10 neurons per hidden layer for FH 60 (in 46.7 % of the top 5 cases), as opposed to 5 neurons for FH 5 (in 61.7 % of the top 5 cases). Finally, the share of BS 5 in the top 5 cases consistently increases with increasing forecast horizons (from 36.7 % for FH 5 to 71.7 % for FH 60). This means that compared to FH 5 the algorithm needs to update its weights more often for FH 60. The increased complexity, observed by increased HL and N_{HL} and reduced BS, confirms that the longer the look ahead time of the forecast model, the more complex the ANN structure and training algorithm will be.

Regarding the historical data size, it is observed that HDS 5 and HDS 10 lead to the most accurate results. Furthermore, a steady increase in the share of HDS 5 is observed until FH 30. The share of HDS 5 in the top 5 for FH 60 decreases to 35 %, whereas HDS 10 increases to

55 %. The reason for this could be the need for increased observed data required for capturing the dynamics associated with FH 60, which is confirmed when examining the variance: data sets associated with FH 60 have a larger variance than datasets associated with FH 5. The lowest forecast errors and associated ANN parameters for each site and forecast horizon are given in Appendix B.

7.6. TUNING OF FFBP ALGORITHM

In the ANN, the optimiser and loss function are important parts of the forecast algorithm. The goal of a loss function is to determine the difference between an observed and its forecasted value. The optimiser minimises the selected loss function by updating a set of weights θ . The influence of different optimiser-loss function pairs on the accuracy of wind speed forecasting is not yet examined. A majority of the considered references do not specify the optimiser and loss function of the implemented forecasting algorithm. When these are specified, no justification for the selection is provided. For example, the mean square error is used as the loss function in [19], [21]. The ANNs in [26]–[29] implemented the Levenberg-Marquardt algorithm as optimiser, whereas ADALINE was used in [21]. Neither the optimiser nor the loss function are given for the forecast model developed in [20]. The influence of the optimisers and loss functions on the forecast accuracy remains unknown. The second aim of this Chapter is to explore how different combinations of optimisers and loss functions influence the error of wind speed forecasting.

Finally, the third aim of this Chapter is to investigate whether a dependency exists between the performance evaluation metrics and the most accurate optimiser-loss function combination.

7.6.1. FORECAST EVALUATION METRICS

Several metrics exist in literature for evaluating the performance of forecast models and usually multiple metrics are used to evaluate a forecast model. The most used ones are the mean absolute error (MAE) as defined by (7.14), the root mean squared error (RMSE) as defined by (7.15) and the mean absolute percentage error (MAPE) as defined by (7.16).

Mean Absolute Error (MAE):

$$MAE = \frac{1}{N} \sum_{i=1}^N |y_i - \hat{y}_i| \quad (7.14)$$

Root Mean Square Error (RMSE):

$$RMSE = \sqrt{\frac{1}{N} \sum_{i=1}^N (y_i - \hat{y}_i)^2} \quad (7.15)$$

Mean Absolute Percentage Error (MAPE, also known as the bias error):

$$MAPE = \frac{100}{N} \sum_{i=1}^N \left| \frac{y_i - \hat{y}_i}{y_i} \right| \quad (7.16)$$

In (7.14) – (7.16) N is the number of samples in the data set, y_i and \hat{y}_i are respectively the observed and forecasted value at timestep i .

In order to evaluate the performance of different forecast models, their accuracies are compared with each other. However, this only makes sense when the input data is exactly the same across all models. Evaluating a model's performance using forecast accuracies at different geographical locations does not lead to meaningful conclusions, as the accuracies are influenced by the geographical characteristics of the wind power plants under consideration. To illustrate the impact of the performance metric choice on the most accurate optimiser-loss function pair, all three performance metrics are used.

7.6.2. OPTIMISERS

The goal of ANN based forecast models is to converge to a set of weights θ that comply with the objective to minimise $J(\theta)$. Optimisers in ANNs are required for updating the set of weights θ used for mapping the input to the output. Assume a training data set for a forecasting algorithm containing N samples, each with P dimensions. At the i -th iteration, the following holds true for the parameter set θ :

$$\theta_{i+1} = \theta_i + \Delta\theta_i \quad (7.17)$$

The convergence of the weights θ , with the aim of minimising $J(\theta)$, is achieved through the gradient descent method. In this method the updated parameter set θ_{i+1} is achieved by applying small changes $\Delta\theta_i$ which are proportional to the negative of the gradient of the function at the current point (θ_i):

$$\Delta\theta_i = -\alpha g_i \quad (7.18)$$

α : learning rate

g_i : gradient of the parameters at the i -th iteration

Several optimisers exist and the optimisers that will be investigated in this research are the Stochastic Gradient Descent, RMSprop, Adagrad, Adadelta, Adam, Adamax, and Nadam. A description of these optimisers are given in Appendix C.

7.6.3. LOSS FUNCTIONS

A loss function is a mathematical formula that calculates the difference between an observed output and its forecasted value. A very simple loss function is given in (7.19).

$$J(\boldsymbol{\theta}) = y - \hat{y}_{\boldsymbol{\theta}} \quad (7.19)$$

y : observed output

$\hat{y}_{\boldsymbol{\theta}}$: forecasted output for weights $\boldsymbol{\theta}$

Several loss functions exist and different loss functions will give different errors for the same set of input data. As will be proven in this work, the choice of the loss function has a significant effect on the performance of the forecast model. The following loss functions will be evaluated: mean square error, mean absolute error, mean absolute percentage error, mean squared logarithmic error, squared hinge, hinge, logcosh, binary crossentropy, kullback leibler divergence, poisson, and cosine proximity. The mathematical formulas of these loss functions are given in Appendix C.

7.6.4. SIMULATION RESULTS

The second goal of this Chapter was to identify the optimiser, loss function and optimiser-loss function combination that resulted in the most accurate forecasting algorithm. A brute force search across all possible combinations of optimiser and loss function was conducted for the different forecast horizons. To assess which optimiser and loss function led to the highest forecast accuracy, the forecast errors across the twelve selected sites and four forecast horizons were calculated. This provided a ranked list of combinations for each site and FH. Following this, the number of times an optimiser or loss function appeared in the top 5 of the ranked list was determined. The ranking was done for the performance evaluation metrics MAE, MAPE, and RMSE.

From the results as shown in Figure 7.6, it is observed that Adadelata is the most accurate optimiser (32.3 % of the top 5 cases), followed by Adamax (18.6 %) and Adam (18.2 %). Adadelata has the biggest share in the top 5 MAEs for each forecast horizon: 26.7 %, 20 %, 31.7 %, and 40 % for respectively FH 5, FH 15, FH 30 and FH 60.

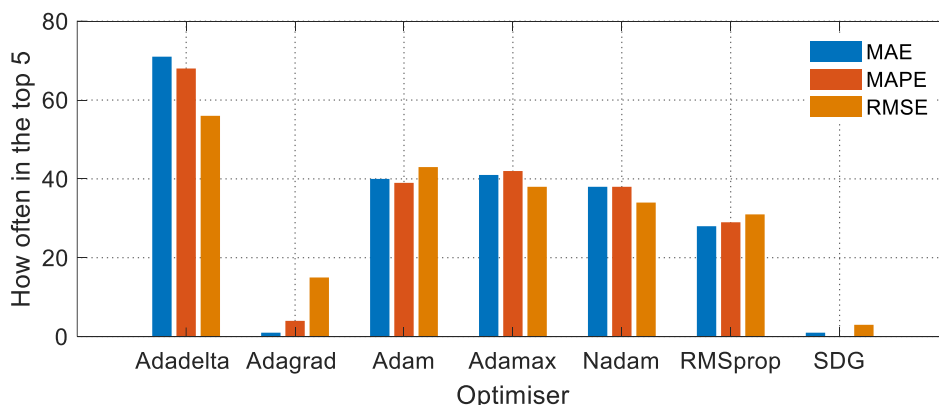


Figure 7.6 Ranking of optimisers.

The best performance of Adadelata can be explained by the fact that it does not require manual selection of the global learning rate α (see (7.18)), unlike e.g. RMSprop and Adagrad.

The influence of the learning rate on the forecast accuracy and required simulation iterations has been thoroughly investigated for different applications in [30]–[37]. These studies successfully show the effect of incorrect selection of the manual learning rate on the forecast performance. The current work complements these conclusions by providing a quantitative comparison among different optimisers. This work furthermore provides empirical evidence for the superiority of the Adadelta optimiser for short-term wind speed forecasting.

Figure 7.7 plots for each optimiser the median versus the inter quartile range (IQR) of the MAE. The left graph gives an overview of the performance of all optimisers, whereas the right graph focuses on the optimisers with the lowest median and IQR. It indeed shows Adadelta as the optimiser with the lowest median. Depending on the trade-off between variability (i.e. IQR) and accuracy (i.e. median), users can choose different optimisers as the preferred algorithm.

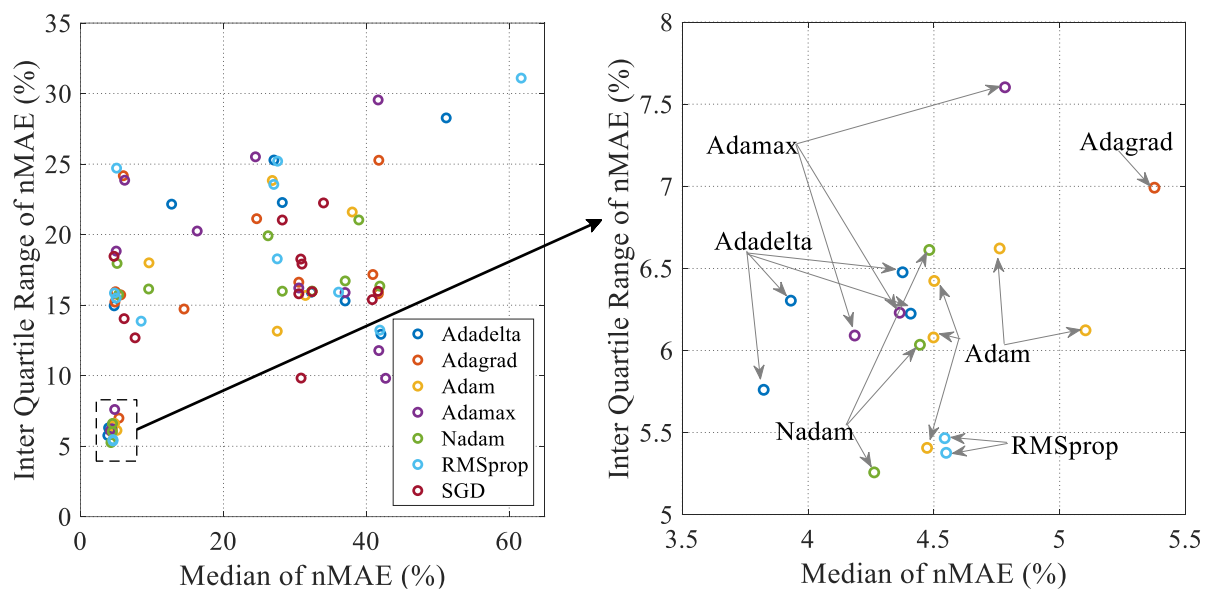


Figure 7.7 Median versus Inter Quartile Range for optimisers.

Similar analyses were performed for the loss function. Based on the ranking of the loss functions (Figure 7.8), the mean absolute error results in the most accurate forecasting algorithm (72.7 % of the top 5 cases). This holds true across all the investigated forecast horizons: its share in the top 5 MAEs for each forecast horizon is 30 %, 51.7 %, 100 %, and 85 % for respectively FH 5, FH 15, FH 30 and FH 60.

This is an interesting result, considering that most of the investigated wind speed forecast models in literature have implemented the MSE as loss function (e.g. [19], [21], [26]–[28], [38], [39]). This can be explained by the fact that historically the (R)MSE has been popular, largely because of its theoretical relevance in statistical modelling [40]. However, as (R)MSE is more sensitive to outliers than the MAE, using (R)MSE results in a slower convergence of the forecasting algorithm, leading to less accurate results for the same number of optimisation iterations. This study gives empirical evidence for the consistent superiority of the MAE as a loss function for short-term wind speed forecasting applications.

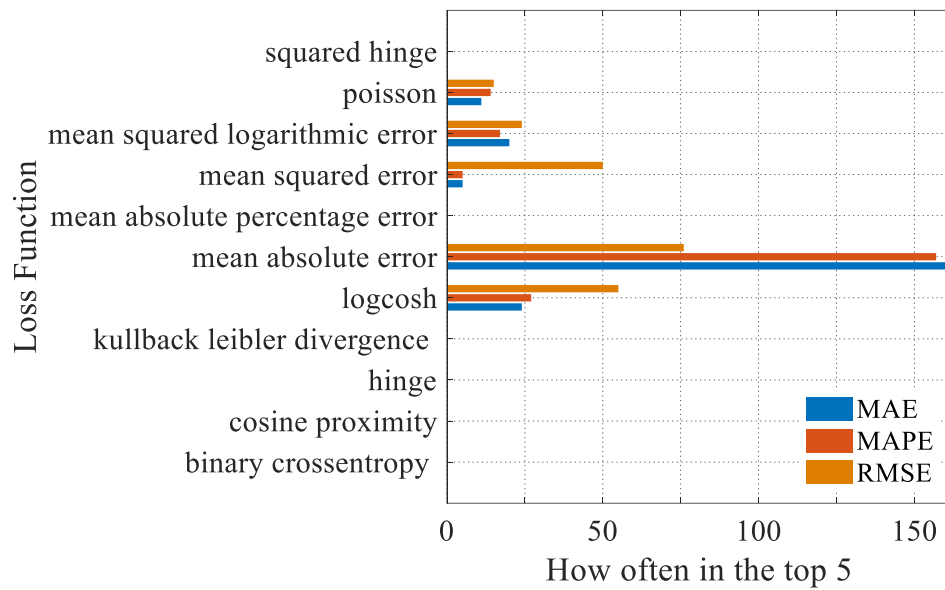


Figure 7.8 Raking of loss functions.

As was done for the optimisers, Figure 7.9 illustrates the median and the IQR for each loss function. The figure on the left gives a global overview of all the loss functions, whereas the figure on the right zooms in on the region of interest. One ANN configuration using the logcosh loss function has the lowest median, whereas the mean absolute error performs better on the IQR. As was the case with the optimisers, users might choose different loss functions depending on the trade-off between the variability and accuracy.

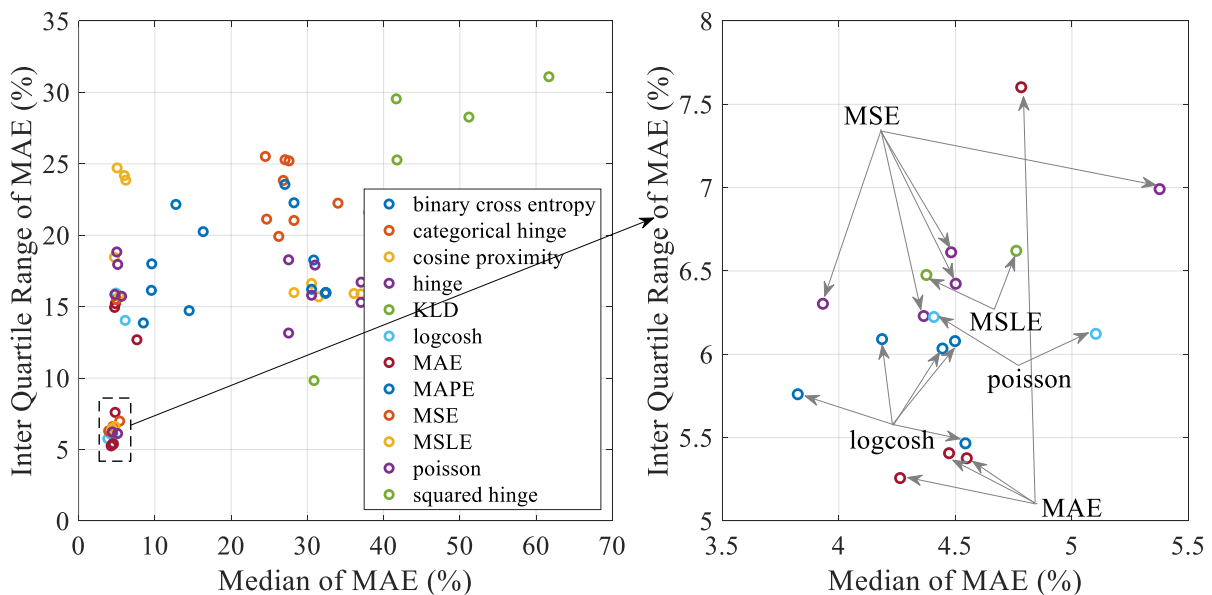


Figure 7.9 Median versus Inter Quartile Range for loss functions.

The third goal of this research was to identify whether there exists a relation between the forecast performance metrics MAE, MAPE and RMSE and the most accurate optimiser, loss function, and optimiser-loss function combination. Table 7.3 shows for the investigated

optimisers their share in the top 5 MAE, MAPE and RMSE. The order of the best optimiser is the same across all performance metrics, with the only difference for the RMSE: Adam comes second and Adamax comes third (it's the other way around for MAE and MAPE). Therefore it is concluded that the forecast performance metric has a negligible influence on the optimiser's ranking. Looking at the share of the optimisers in the top 5, it is clear that the adaptive optimisers that do not require manual selection of the learning rate (i.e. Adadelata, Adam, Adamax and Nadam) clearly outperforms other optimisers.

Table 7.3 Raking of optimisers when using MAE, MAPE, and RMSE.

Optimiser	MAE (%)	MAPE (%)	RMSE (%)
Adadelata	32.3	30.9	25.5
Adagrad	0.5	1.8	6.8
Adam	18.2	17.7	19.5
Adamax	18.6	19.1	17.3
Nadam	17.3	17.3	15.5
RMSprop	12.7	13.2	14.1
SGD	0.5	0	1.4

For the loss functions, a strong relation is observed between the RMSE metric and the MSE, as is shown in Figure 7.8 and Table 7.4. However, it is still more appropriate to use mean absolute error as the loss function and these results suggest this is the best all-purpose loss function – particularly if one is concerned with MAE or MAPE forecast errors.

Table 7.4 Raking of loss functions when using MAE, MAPE, and RMSE.

Loss Functions	MAE (%)	MAPE (%)	RMSE (%)
logcosh	10.9	12.3	25.0
MAE	72.7	71.4	34.5
MAPE	0	0	0
MSE	2.3	2.3	22.7
MSLE	9.1	7.7	10.9
poisson	5.0	6.4	6.8

The shares of the different optimiser-loss function combinations in the top 5 when using the MAE forecast performance metric, is given in Table 7.5. From this table it is observed that the Adadelata-MAE pair results in the most accurate forecast model, with a share of 22.7 % in the top 5 MAEs. The second best combination is the Adamax-MAE pair (14.5 %), followed by the Adam-MAE pair (14.1 %).

Table 7.6 and Table 7.7 give the shares in the top 5 when using MAPE, respectively RMSE. From these tables it is observed that the Adadelata-MAE pair results in the most accurate forecast model, independent of the metric used for evaluating the model's performance. Adam-MAE and Adamax-MAE are the next best pairs. The results suggest that Adadelata is the most appropriate optimiser regardless of the error that is being minimised. However, the shares differ significantly when RMSE is used. In this case, optimiser-loss function pairs with MSE as the loss function have a major increase in their top 5 shares.

Table 7.5 Raking of optimiser-loss function pairs based on MAE (%).

Optimiser → Loss function ↓	Adadelata	Adagrad	Adam	Adamax	Nadam	RMS prop	SGD
logcosh	4.5	0	1.4	1.8	2.3	0.9	0
MAE	22.7	0.5	14.1	14.5	12.7	8.2	0
MAPE	0	0	0	0	0	0	0
MSE	0.5	0	0.5	0.5	0.5	0.5	0
MSLE	1.8	0	1.8	0.5	1.8	2.7	0.5
poisson	2.7	0	0.5	1.4	0	0.5	0

Table 7.6 Raking of optimiser-loss function pairs based on MAPE (%).

Optimiser → Loss function ↓	Adadelata	Adagrad	Adam	Adamax	Nadam	RMS prop	SGD
logcosh	4.5	0	0.9	2.7	2.3	1.8	0
MAE	21.4	1.8	14.1	13.2	13.2	7.7	0
MAPE	0	0	0	0	0	0	0
MSE	0.5	0	0.5	0.5	0.5	0.5	0
MSLE	1.4	0	1.8	0.5	1.4	2.7	0
poisson	3.2	0	0.5	2.3	0	0.5	0

Table 7.7 Raking of optimiser-loss function pairs based on RMSE (%).

Optimiser → Loss function ↓	Adadelata	Adagrad	Adam	Adamax	Nadam	RMS prop	SGD
logcosh	5.9	2.7	4.1	2.7	5.5	4.1	0
MAE	10	1.4	7.7	7.7	4.5	3.2	0
MAPE	0	0	0	0	0	0	0
MSE	5.5	2.3	4.5	4.1	3.2	3.2	0
MSLE	1.8	0.5	1.4	1.8	1.4	2.7	1.4
poisson	2.3	0	1.8	0.9	0.9	0.9	0

7.7. OPTIMISED FORECASTING ALGORITHM

The following key findings result from the research on the tuning of the ANN structure and algorithm. First, increasing look ahead times require more frequent updates of the ANN's weights, reducing the most efficient batch size to 5. Second, it is observed that HDS 5 and HDS 10 lead to the most accurate forecasts. Third, it was found that the influence of the considered amount of training data, i.e. 6 months (50 %) or 9.6 months (80 %), is rather limited. Fourth, Adadelata was found to be the most accurate optimiser, as it does not require manual selection of a global learning rate. The superiority of adaptive optimisers that do not require manual selection of the learning rate over other optimisers was proven. Fifth, the MAE loss function by far leads to the most accurate forecasts, in contrast to the MSE which is commonly used in literature. Finally, a strong relation was observed between the RMSE evaluation metric

and the MSE loss function, essentially showing that it may be worth considering using the MSE loss function if (and only if) the goal is to minimise the RMSE of the forecasts.

The analysis in this work focused on two categories of parameters. The results obtained for the ANN-structure related parameters are also applicable for hybrid models, as they reveal which parameters have a large influence on the forecast accuracy and which do not (e.g. training data). For this category of parameters, any considered forecasting method would need retuning of the suggested parameters. The conclusions regarding the ANN-algorithm related parameters (i.e. optimiser and loss function) would remain valid for hybrid and complex ANN models. Hybrid and complex ANN models change the ANN's structure and it was found that the most superior optimiser and loss function are not dependent on the ANN-structure related parameters (more so for the loss function than for the optimiser). Therefore, these results are valuable and transferable to other forecasting methods utilising ANNs.

Based on the results of this work, a forecasting algorithm was developed with parameters tuned to lead to the most accurate forecast results. An overview of the observed and forecasted values including the 95 % confidence interval for one instance are shown in Figure 7.10.

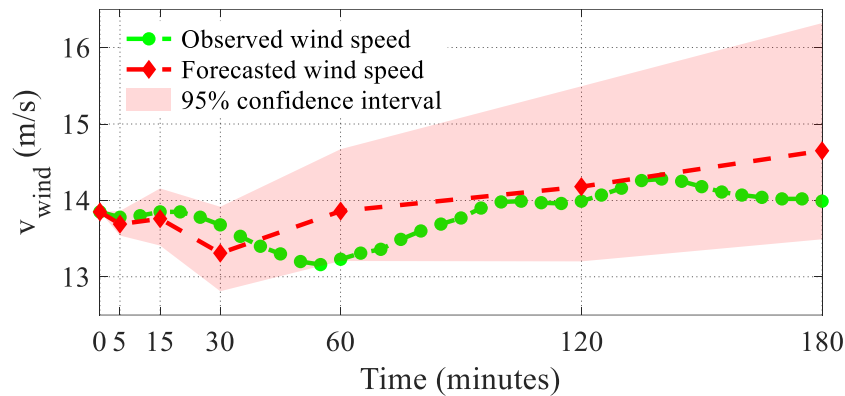


Figure 7.10 Observed versus forecasted values of most accurate implemented algorithm.

It is practically impossible to evaluate the performance of forecast models by simply comparing their accuracies. This way of evaluation only makes sense when the models have the same input data, i.e. they are forecasting the wind speed of the same wind power plant. There are two main factors that pose limitations in comparing the accuracies of forecast models. First is the accuracy metric that is used for comparison. Different metrics exist in literature for quantifying the performance of a forecast model. Some use the MAPE, other the RMSE or MAE (or their normalised versions). An important consideration is the number of forecasts that is used for calculating the 'mean' value in these accuracy metrics. Second is the geographical complexity: the same forecast model will have different accuracies depending on the complexity of the terrain where the wind power plant is located. This geographical complexity, quantified using the RIX index, has a negative impact on the forecast accuracy: the higher the RIX value, the higher the forecast error will be.

Table 7.8 illustrates the achieved improvements in forecast accuracies when the ANN structure and algorithm parameters are tuned. For FH 5 and FH 60, improvements of respectively

9.4 %-points and 4.3 %-points were gained, thus highlighting the importance of correct ANN design.

Table 7.8 Accuracy improvement due to ANN tuning.

FH	Accuracy improvement
5	9.4 %-points
15	0.8 %-points
30	0.6 %-points
60	4.3 %-points

Placing this in perspective: for a 100 MW wind power plant in the UK, a 1.2 %-points improvement in the MAE resulted in an increased estimated yearly revenue of 177,000 EUR [41]. Similar analysis were carried out for Ireland [42], Spain [43] and the IEEE 118-bus test system [44], where the decrease in system operational costs and increase in the revenue of wind power plant owners as the result of improvements in the forecast accuracy were presented. The benefits of improved forecast accuracies are not only limited to wind generation. In [45] the decrease in costs for ramping, curtailment and system operation due to improved solar power forecasting are presented.

Finally, due to smoothing effects, the forecast accuracy will decrease further with increasing geographical area. When compared to the forecast of a single wind power plant (as is the case in this research), forecast errors on control area level are up to 63 % lower [46].

7.8. CONCLUSIONS

The main contribution of this Chapter was the development of a forecasting algorithm for short-term wind speed prediction with forecast horizons of 5, 15, 30 and 60 minutes. The algorithm was developed using artificial neural networks, where the obtained performance was achieved through detailed tuning of several parameters. Three new key insights were obtained, while others were confirmed. First, it was found that increasing look ahead times require more complex ANNs. For up to 30 minutes ahead, the highest accuracy was achieved when the ANN consisted of one hidden layer with five neurons. For 60 minutes ahead, two hidden layers with ten neurons per hidden layer were required. The increasing complexity is also reflected by the more frequent updates of the weights, reducing the most efficient batch size to five. This influence of the batch size on the forecast accuracy was not reported before. For the historical data size, it is observed that HDS 5 and HDS 10 lead to the most accurate forecasts. Furthermore, it was shown that the influence of the considered amount of training data on the performance of the developed model is rather limited. The models were capable of achieving the same accuracies with six months of data, which could result in earlier deployment of such forecast models.

Second, the optimiser, the loss function, and the optimiser-loss function pair that led to the most accurate forecasts were identified. Adadelta was found to be the most accurate optimiser, as it does not require manual selection of a global learning rate. In general, the analysis gave empirical evidence for the superiority of adaptive optimisers that do not require manual

selection of the learning rate (i.e. Adadelta, Adam, Adamax and Nadam) over other optimisers. Whereas the RMSE was found to be the preferred loss function in literature, the results obtained in this study do reveal that the MAE by far leads to the most accurate short-term wind speed forecasts. The Adadelta-MAE pair was also identified as the most accurate optimiser-loss function combination.

Finally, the relation between the identified optimiser-loss function pair in the previous step and the evaluation metrics MAE, MAPE and RMSE was investigated. Whereas the Adadelta-MAE pair remains the most accurate combination independent of the evaluation metric, a strong relation was observed between the RMSE evaluation metric and the MSE loss function.

The forecasting module developed in this Chapter is one of the three modules of the proposed system level coordination based mitigation solution for DFIG-SSR. Based on the forecasted wind speed, optimum parameters for the converter control will be calculated using the control rule defined by (6.2) in Chapter 6. These optimum parameters ensure sufficient damping at the forecasted wind speed. As such, the performance of the gain scheduling approach directly rely on the performance of the forecast algorithm. In the next Chapter, the gain scheduling solution will be implemented and its performance will be evaluated.

REFERENCES

- [1] G. Giebel, R. Brownsword, and G. Kariniotakis, "The State of the Art in Short-Term Prediction of Wind Power," *ANEMOS.plus*, pp. 1–110, 2011.
- [2] A. Ahmed and M. Khalid, "A review on the selected applications of forecasting models in renewable power systems," *Renew. Sustain. Energy Rev.*, vol. 100, 2019.
- [3] H. S. Dhiman, D. Deb, and J. M. Guerrero, "Hybrid machine intelligent SVR variants for wind forecasting and ramp events," *Renew. Sustain. Energy Rev.*, vol. 108, 2019.
- [4] Q. Chen and K. A. Folly, "Wind Power Forecasting," *IFAC-PapersOnLine*, 2018.
- [5] M. Sharifzadeh, A. Sikinioti-Lock, and N. Shah, "Machine-learning methods for integrated renewable power generation: A comparative study of artificial neural networks, support vector regression, and Gaussian Process Regression," *Renew. Sustain. Energy Rev.*, vol. 108, 2019.
- [6] S. Agatonovic-Kustrin and R. Beresford, "Basic concepts of artificial neural network (ANN) modeling and its application in pharmaceutical research," *J. Pharm. Biomed. Anal.*, vol. 22, no. 5, pp. 717–727, 2000.
- [7] X. Glorot, A. Bordes, and Y. Bengio, "Deep sparse rectifier neural networks," *AISTATS '11 Proc. 14th Int. Conf. Artif. Intell. Stat.*, vol. 15, pp. 315–323, 2011.
- [8] V. Nair, G. E. Hinton, "Rectified Linear Units Improve Restricted Boltzmann Machines," 2010.
- [9] W. Shang, K. Sohn, D. Almeida, and H. Lee, "Understanding and Improving Convolutional Neural Networks via Concatenated Rectified Linear Units," 2016.
- [10] M. A. Nielsen, *Neural Networks and Deep Learning*. Determination Press, 2015.
- [11] X. Glorot and Y. Bengio, "Understanding the difficulty of training deep feedforward neural networks," in *Proceedings of the Thirteenth International Conference on Artificial Intelligence and Statistics (AISTATS-10)*, 2010, vol. 9, pp. 249–256.
- [12] K. He, X. Zhang, S. Ren, and J. Sun, "Delving deep into rectifiers: Surpassing human-level performance on imagenet classification," in *Proceedings of the IEEE International Conference on Computer Vision*, 2015, vol. 2015 Inter, pp. 1026–1034.
- [13] G. Giebel, R. Brownsword, G. Kariniotakis, M. Denhard, and C. Draxi, "Report: The state of the art in short-term prediction of wind power," p. 110, 2011.
- [14] C. Draxl and A. Clifton, "A Guide to Using the WIND Toolkit Validation Code," 2014.
- [15] C. Draxl, A. Clifton, B. M. Hodge, and J. McCAA, "The Wind Integration National Dataset (WIND) Toolkit," *Appl. Energy*, vol. 151, pp. 355–366, 2015.
- [16] C. Draxl, B. Hodge, and A. Clifton, "Overview and Meteorological Validation of the Wind Integration National Dataset Toolkit," 2015.
- [17] J. King, A. Clifton, B.-M. Hodge, "Validation of Power Output for the WIND Toolkit," 2014.

-
- [18] E. Ela and B. Kirby, “ERCOT Event on February 26 , 2008 : Lessons Learned,” 2008.
- [19] G. Li and J. Shi, “On comparing three artificial neural networks for wind speed forecasting,” *Appl. Energy*, vol. 87, no. 7, pp. 2313–2320, 2010.
- [20] M. Monfared, H. Rastegar, and H. M. Kojabadi, “A new strategy for wind speed forecasting using artificial intelligent methods,” *Renew. Energy*, vol. 34, no. 3, pp. 845–848, 2009.
- [21] E. Cadenas and W. Rivera, “Short term wind speed forecasting in La Venta, Oaxaca, México, using artificial neural networks,” *Renew. Energy*, vol. 34, no. 1, pp. 274–278, 2009.
- [22] H. Madsen, P. Pinson, G. Kariniotakis, H. A. Nielsen, and T. S. Nielsen, “Standardizing the Performance Evaluation of Short- Term Wind Power Prediction Models,” *Wind Eng.*, vol. 29, no. 6, pp. 475–489, 2005.
- [23] H. Holttinen, J. Miettinen, and S. Sillanpää, “Wind power forecasting accuracy and uncertainty in Finland,” Finland, 2013.
- [24] Global Wind Atlas, “Global Wind Atlas.” [Online]. Available: <https://globalwindatlas.info/about/purpose>. [Accessed: 07-Jul-2018].
- [25] A. Mouez Khatab, H. Olivares Espinosa Examiner, and J. Nørkaer Sørensen, “Performance Analysis of Operating Wind Farms,” no. September, 2017.
- [26] H. Masrur, M. Nimol, M. Faisal, and G. Mostafa, “Short Term Wind Speed Forecasting Using Artificial Neural Network : A Case Study,” in *2016 International Conference on Innovations in Science, Engineering and Technology (ICISSET)*, 2016, pp. 1–5.
- [27] J. P. S. Catalão, H. M. I. Pousinho, and V. M. F. Mendes, “Short-term wind power forecasting in Portugal by neural networks and wavelet transform,” *Renew. Energy*, vol. 36, no. 4, 2011.
- [28] P. Kumar, N. Singh, and M. Ansari, “Solar Radiation Forecasting Using Artificial Neural Network with different Meteorological Variables,” in *2017 Innovations in Power and Advanced Computing Technologies (I-Pact)*, 2017, pp. 487–491.
- [29] J. Mahmoudi, M. Jamil, and H. Balaghi, “Short and Mid-Term Wind Power Plants Forecasting with ANN,” in *2012 Second Iranian Conference on Renewable Energy and Distributed Generation*, 2012, pp. 167–171.
- [30] Y. Xu and S. Zhao, “Mitigation of subsynchronous resonance in series-compensated dfig wind farm using active disturbance rejection control,” *IEEE Access*, vol. 7, pp. 68812–68822, 2019.
- [31] H. Zhao, F. Liu, H. Zhang, and Z. Liang, “Research on a learning rate with energy index in deep learning,” *Neural Networks*, vol. 110, pp. 225–231, 2019.
- [32] D. She and M. Jia, “Wear indicator construction of rolling bearings based on multi-channel deep convolutional neural network with exponentially decaying learning rate,” *Meas. J. Int. Meas. Confed.*, vol. 135, pp. 368–375, 2019.
- [33] Y. Bengio, “Practical recommendations for gradient-based training of deep architectures,” *Lect.*

- Notes Comput. Sci. (including Subser. Lect. Notes Artif. Intell. Lect. Notes Bioinformatics)*, vol. 7700 LECTU, pp. 437–478, 2012.
- [34] A. Senior, G. Heigold, M. Ranzato, and K. Yang, “An empirical study of learning rates in deep neural networks for speech recognition,” *ICASSP, IEEE Int. Conf. Acoust. Speech Signal Process. - Proc.*, pp. 6724–6728, 2013.
- [35] H. L. Hsieh and M. M. Shanechi, *Optimizing the learning rate for adaptive estimation of neural encoding models*, vol. 14, no. 5. 2018.
- [36] J. Shi, J. Song, B. Song, and W. F. Lu, “Multi-Objective Optimization Design through Machine Learning for Drop-on-Demand Bioprinting,” *Engineering*, no. xxxx, pp. 0–7, 2019.
- [37] Y. Xu, H. Wang, X. Liu, and W. Sun’s, “An improved multi-branch residual network based on random multiplier and adaptive cosine learning rate method,” *J. Vis. Commun. Image Represent.*, vol. 59, pp. 363–370, 2019.
- [38] F. Fazelpour, N. Tarashkar, and M. A. Rosen, “Short-term wind speed forecasting using artificial neural networks for Tehran, Iran,” *Int. J. Energy Environ. Eng.*, vol. 7, no. 4, pp. 377–390, 2016.
- [39] A. Tesfaye, J. H. Zhang, D. H. Zheng, and D. Shiferaw, “Short-term wind power forecasting using artificial neural networks for Resource Scheduling in Microgrids,” *Int. J. Sci. Eng. Appl.*, vol. 5, no. 3, pp. 144–151, 2016.
- [40] R. J. Hyndman and A. B. Koehler, “Another look at measures of forecast accuracy,” *Int. J. Forecast.*, vol. 22, no. 4, pp. 679–688, 2006.
- [41] J. Collins, J. Parkes, and A. Tindal, “Short Term Forecasting for Utility-Scale Wind Farms - The Power Model Challenge,” *Wind Eng.*, vol. 33, no. 3, pp. 247–257, 2009.
- [42] E. V. Mc Garrigle and P. G. Leahy, “Quantifying the value of improved wind energy forecasts in a pool-based electricity market,” *Renew. Energy*, vol. 80, pp. 517–524, 2015.
- [43] I. González-Aparicio and A. Zucker, “Impact of wind power uncertainty forecasting on the market integration of wind energy in Spain,” *Appl. Energy*, vol. 159, pp. 334–349, 2015.
- [44] Q. Wang, H. Wu, A. R. Florita, C. Brancucci Martinez-Anido, and B. M. Hodge, “The value of improved wind power forecasting: Grid flexibility quantification, ramp capability analysis, and impacts of electricity market operation timescales,” *Appl. Energy*, vol. 184, pp. 696–713, 2016.
- [45] C. Brancucci Martinez-Anido *et al.*, “The value of day-ahead solar power forecasting improvement,” *Sol. Energy*, vol. 129, pp. 192–203, 2016.
- [46] U. Focken, M. Lange, K. Mönnich, H. P. Waldl, H. G. Beyer, and A. Luig, “Short-term prediction of the aggregated power output of wind farms - A statistical analysis of the reduction of the prediction error by spatial smoothing effects,” *J. Wind Eng. Ind. Aerodyn.*, vol. 90, no. 3, pp. 231–246, 2002.

8. REAL-TIME OPERATIONS

8.1. INTRODUCTION

This Chapter discusses the real-time operations module and evaluates the performance of the gain scheduling solution. In this solution, the ANN based forecasting module of Chapter 7 predicts the wind speed with an interval of five minutes. The parameters $T_{iP,PCC}$ and $T_{iQ,PCC}$, identified through monothetic sensitivity analysis, are then scheduled using the forecasted wind speed according to control rule (6.2) defined in Chapter 6.4.2.

The real-time operations simulation module is first introduced in Section 8.2. It describes the different simulation actions such as switching and gain scheduling. Section 8.3 presents the performance of the overall prediction gain scheduling control. Section 8.4 presents a statistical analysis of DFIG-SSR. In Section 8.5 the developed control is implemented in the IEEE 39-bus system as well as in a system with multi-DFIG representation. The final conclusions of this Chapter are presented in Section 8.6.

8.2. REAL-TIME OPERATIONS MODULE

The goal of the real-time operations module is twofold. First, it is responsible for scheduling the optimised values of $T_{iP,PCC}$ and $T_{iQ,PCC}$ as a function of the forecasted wind speed, where the scheduling should occur prior to the wind speed change. Second, for every time stamp the module should simulate a switching action, which leads to the radial connection of the DFIG to the series capacitor. This switching action creates the topological condition for DFIG-SSR. In practical applications, only the scheduling action is part of the gain scheduling solution.

The process of the real-time operations module is depicted in Figure 8.1 and automated using Python. The process of each simulation run starts with the initialisation of the PSCAD DFIG model and ends after termination of the simulation. A simulation run consists of twelve time stamps of five minutes each. Recall that the forecast module predicts the wind speed with a five minutes forecast horizon. Twelve time stamps per simulation run are chosen to facilitate accurate wind speed data handling, however, this number can be any value.

After initialisation, the forecasting algorithm (Module 2, developed in Chapter 7) provides the predicted wind speed for the next time stamp and using this wind speed, the optimised values of $T_{iP,PCC}$ and $T_{iQ,PCC}$ are calculated based on (6.2). The wind speed is changed with a delay of one minute following the scheduling of the rectifier parameters. Next, a switching action is performed resulting in the radial connection of the DFIG to the series capacitor. The simulation is ran for 3.5 seconds, enough to capture any DFIG-SSR dynamics, if any. For each time stamp, the observed and forecasted wind speed as well as the minimum and maximum active power are recorded. This is relevant to evaluate the performance of the PGSC. Next, the line is switched again in-service and the simulation is ran for another four seconds to make the switching transients settle. This process is repeated until all twelve time stamps are simulated, after which the simulation run is terminated.

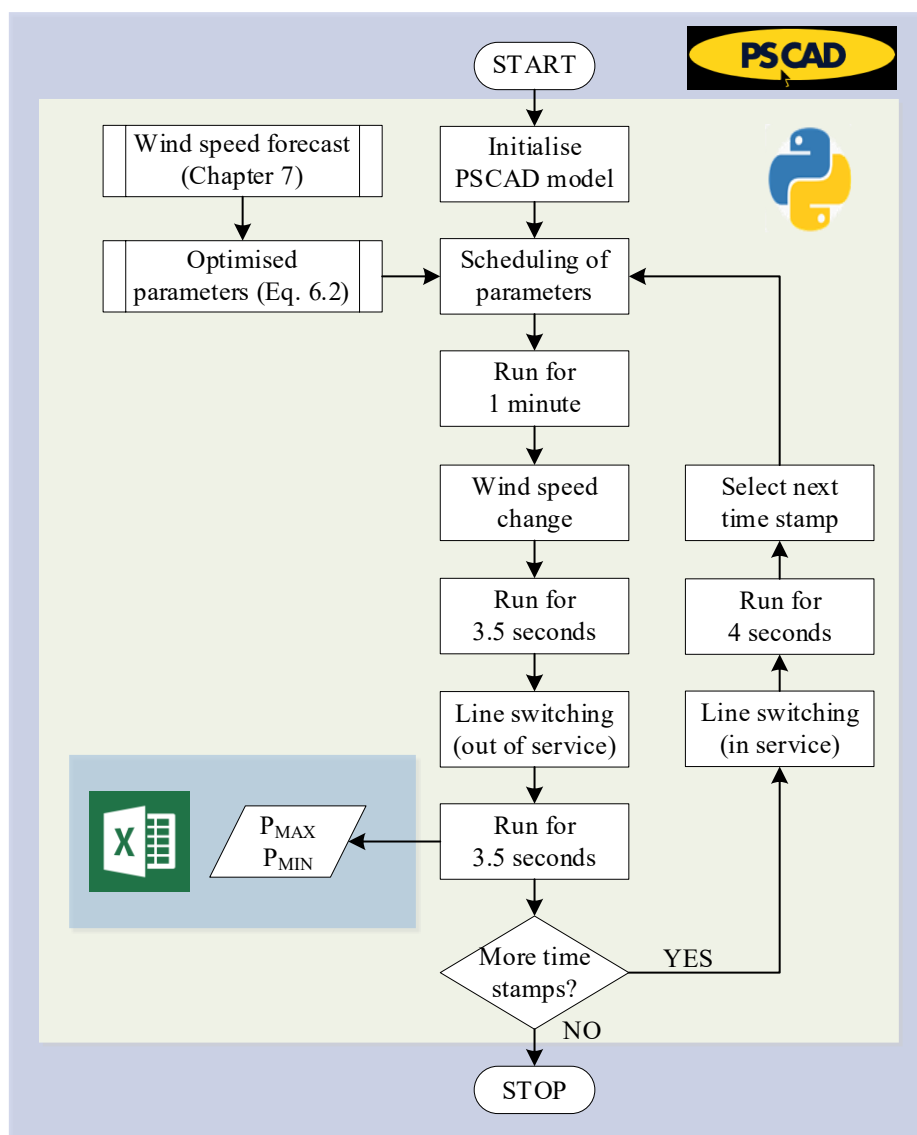


Figure 8.1 Process of real-time operations module.

8.3. PERFORMANCE OF PREDICTIVE GAIN SCHEDULING CONTROL

This Section discusses the performance aspects of the developed predictive gain scheduling control. The performance of the PGSC depends on the individual performances of the gain identification and wind speed forecasting modules. The gain identification was thoroughly discussed in Chapter 6 and the parameter optimisation and reduction steps were evaluated in Chapter 6.4. It was concluded that the obtained optimisation results (i) were effective in mitigating DFIG-SSR, (ii) respected fault ride through requirements stipulated in [1] and (iii) did not lead to small-signal instability as a result of changes in the rectifier parameters and wind speeds. As such, the set of identified parameters for each wind speed is able to effectively address DFIG-SSR. This was illustrated for a random case in Chapter 6.4.3.

The wind speed forecasting module was developed in Chapter 7. To maximise the performance of the PGSC, the parameters of the developed ANN based short-term wind speed forecasting algorithm were tuned, reducing the forecast error with up to 9.4%-points.

The performance of the predictive gain scheduling control was evaluated for five years of observed wind speeds at Site ID 8501 (see Figure 7.3 on page 143). From all the time stamps that led to DFIG-SSR using the base case DFIG (i.e. without the PGSC), Table 8.1 shows the share of those time stamps where the developed PGSC was able to mitigate DFIG-SSR. As indicated in Figure 8.1, the switching action leading to the radial connection of the DFIG occurs for every time stamp. Comparing the DFIG-SSR behaviour of the base case with the PGSC-equipped DFIG, it was found that the latter had a superior performance and was able to mitigate on average 90.6% of the DFIG-SSR cases.

Table 8.1 Performance of proposed gain scheduling solution.

Year	Accuracy (%)
2008	90
2009	87.8
2010	94.1
2011	91.8
2012	89.3
Average	90.6

The next step in the performance analysis was to investigate under which circumstances the PGSC was not able to mitigate DFIG-SSR. To a large extent, the DFIG-SSR mode became unstable when the observed wind speed was between 6 and 9 m/s while the forecasted wind speed was larger than 9 m/s. In multiple instances, the difference between the observed and forecasted wind speeds reached up to 9 m/s. In some other cases, DFIG-SSR was also observed when in the range of 6 to 9 m/s there was a difference between the observed and forecasted wind speed.

8.4. STATISTICAL ANALYSIS OF DFIG-SSR

In the next study, the probability for DFIG-SSR in the Dutch power system is investigated using statistical analysis. For this analysis, the transmission line failure rate and probability of

wind speeds are required. The probability of DFIG-SSR depends on the probability of line switching and the probability that the wind speed is below a critical value. Consider the grid topology shown in Figure 4.12. The probability that the uncompensated line is switched off is calculated according to (8.1). The unavailability and availability of a line are calculated as given in respectively (8.2) and (8.3).

$$P(l_1 \text{ out}) = U_1 \cdot A_2$$

U_1 : unavailability of line 1
 A_2 : availability of line 2

(8.1)

$$U_1 = l_1 \cdot f_1 \cdot \frac{r_1}{8760}$$

l_1 : length of line 1 (km)
 f_1 : failure rate of line 1 (failures/kmyear)
 r_1 : repair time of line 1 (hours)

(8.2)

$$A_1 = 1 - U_1$$
(8.3)

Actual failure data of the transmission line is retrieved from the Nestor Database [2]. It contains transmission asset failure data for planned and unplanned outages and other system failures in the Netherlands. The data is provided by all electricity transmission and distribution system operators in the Netherlands since 1976. Based on this database, f_1 is 0.0021/kmyear and r_1 is 8 hours. With this data, $P(l_1 \text{ out})$ can be calculated as a function of the line length.

The other missing variable for performing the statistical analysis is the wind speed probability. The wind speed probabilities are calculated using the observed wind speed at Site ID 8501 for the years 2008-2012. The observed wind speeds are retrieved from the WIND Prospector Toolkit [3]–[6] and the wind speed probabilities are shown in Figure 8.2. Only the probabilities of wind speeds between the DFIG's cut-in and cut-off wind speeds are needed for the statistical analysis, as for wind speeds outside this interval the DFIG is not in operation.

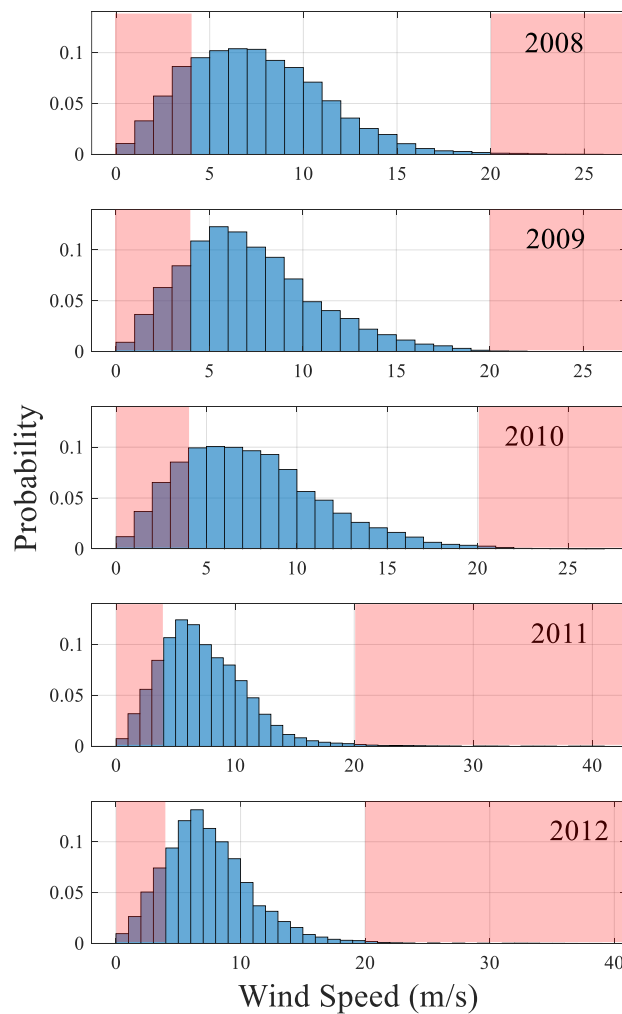


Figure 8.2 Observed wind speed and its probability for the years 2008-2012. The red shaded areas represent the DFIG's cut-in and cut-off regions.

DFIG-SSR occurs when the uncompensated line is switched off and when the wind speed is between the cut-in wind speed v_{cut-in} and a critical wind speed $v_{critical}$. At wind speeds larger than $v_{critical}$ the DFIG damping at the resonance frequency is positive and DFIG-SSR will not be observed. The probability of DFIG-SSR is then calculated using (8.4).

$$P(DFIG - SSR) = P(TL1 out) \cdot \sum_{v_{wind}=v_{cut-in}}^{v_{critical}} P(v_{wind}) \quad (8.4)$$

For the year 2010, the DFIG-SSR probability as a function of the transmission line length is calculated for the DFIG deploying the developed PGSC. The results are shown in Figure 8.3. As a comparison, the DFIG-SSR probability for the DFIG without PGSC is also shown. Finally, the probabilities are calculated for $v_{critical}$ of 9, 13 and 17 m/s. The superior performance of the PGSC is clearly visible: with the PGSC implemented in the DFIG, the risk for DFIG-SSR is reduced by a factor up to 16.95.

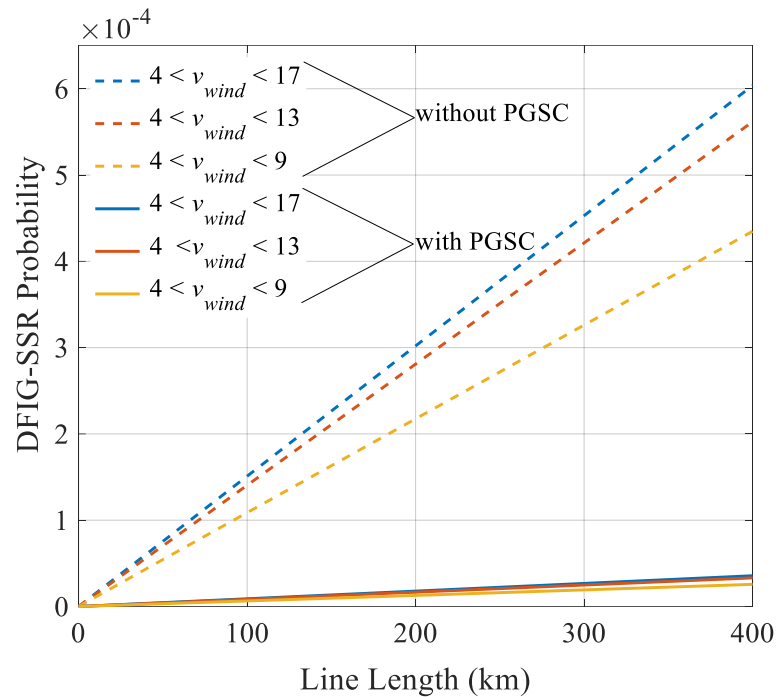


Figure 8.3 Probability of DFIG-SSR using the developed PGSC. Probabilities are given for wind speed Site ID 8501 for the year 2010.

8.5. MULTI-DFIG SYSTEM

In the analysis so far the wind power plant was modelled using a single aggregated WTG model. This single model representation is commonly used for investigating DFIG-SSR and SSCI interactions between a wind power plant and the grid. This representation, however, is only valid when all wind turbine generators of the considered power plant have the same machine and controller parameters as well as the same operating conditions [7]. The impacts of non-identical parameters and non-identical operating conditions are rarely documented. This Section aims to bridge this research gap. It will also illustrate that the developed PGSC remains effective in a wind power plant with a multi-DFIG representation. Finally, the question of deploying the developed PGSC in the centralised wind park control or decentralised DFIG control will be discussed.

8.5.1. IMPACT OF NON IDENTICAL CONTROLLER PARAMETERS

Consider the multi-DFIG wind power plant connected to the study model as shown in Figure 8.4. The WTGs are arranged in five rows across multiple columns. To investigate the impact of non-identical controller parameters on DFIG-SSR, one column with five parallel DFIGs is considered (shaded in green). Six cases will be investigated, where in the first case all DFIGs are modelled with parameters tuned according to the methodology described in Chapter 6. In the second case, 80% of the DFIGs will have tuned converter parameters and the remaining 20% will have the parameters of the initial, non-tuned DFIG model described in Chapter 4.2. This is continued until for the sixth case all DFIGs deploy non-tuned parameters

of the initial case. For sake of clarity, in all the considered six cases the total number of DFIGs remains constant. For the six cases all DFIGs are exposed to an identical wind speed of 10 m/s. Other operational conditions remain identical as well. Variations in operational conditions are explored in Section 8.5.2.

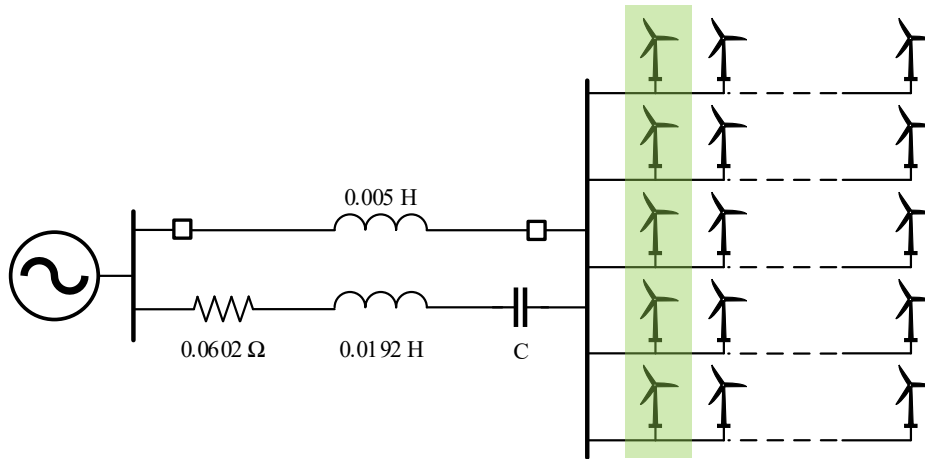


Figure 8.4 Representation of a multi-DFIG wind power plant connected to the study model. The wind power plant has three depicted columns and five rows. The green shaded wind turbines are used for the multi-DFIG analysis.

The impedance based stability method is used to investigate the stability of the combined system using non-identical controller parameters. The results for case 1 (100% of DFIGs with tuned parameters) and case 6 (0% of DFIGs with tuned parameters) are shown in Figure 8.5.

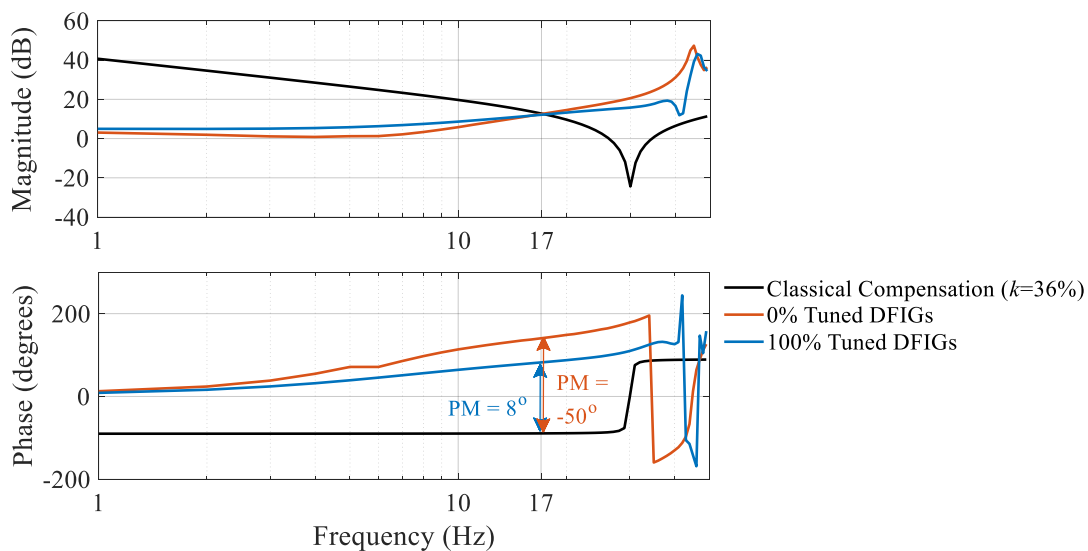


Figure 8.5 Impedance responses of the series compensated grid and different shares of tuned DFIGs.

Two main observations are made. First, the resonance frequency remains at 17 Hz and is hardly affected by the share of tuned DFIGs. Second, when all DFIGs are deployed with tuned parameters, the phase margin is positive, indicating a stable system. As such, the DFIG converter parameters have a larger influence on the phase margin than on the resonance frequency. This is in line with the findings of the sensitivity analysis in Chapter 6.3 and the

validation process in Chapter 6.4. Detailed time domain EMT simulations are performed to validate the obtained results and are shown in Figure 8.6.

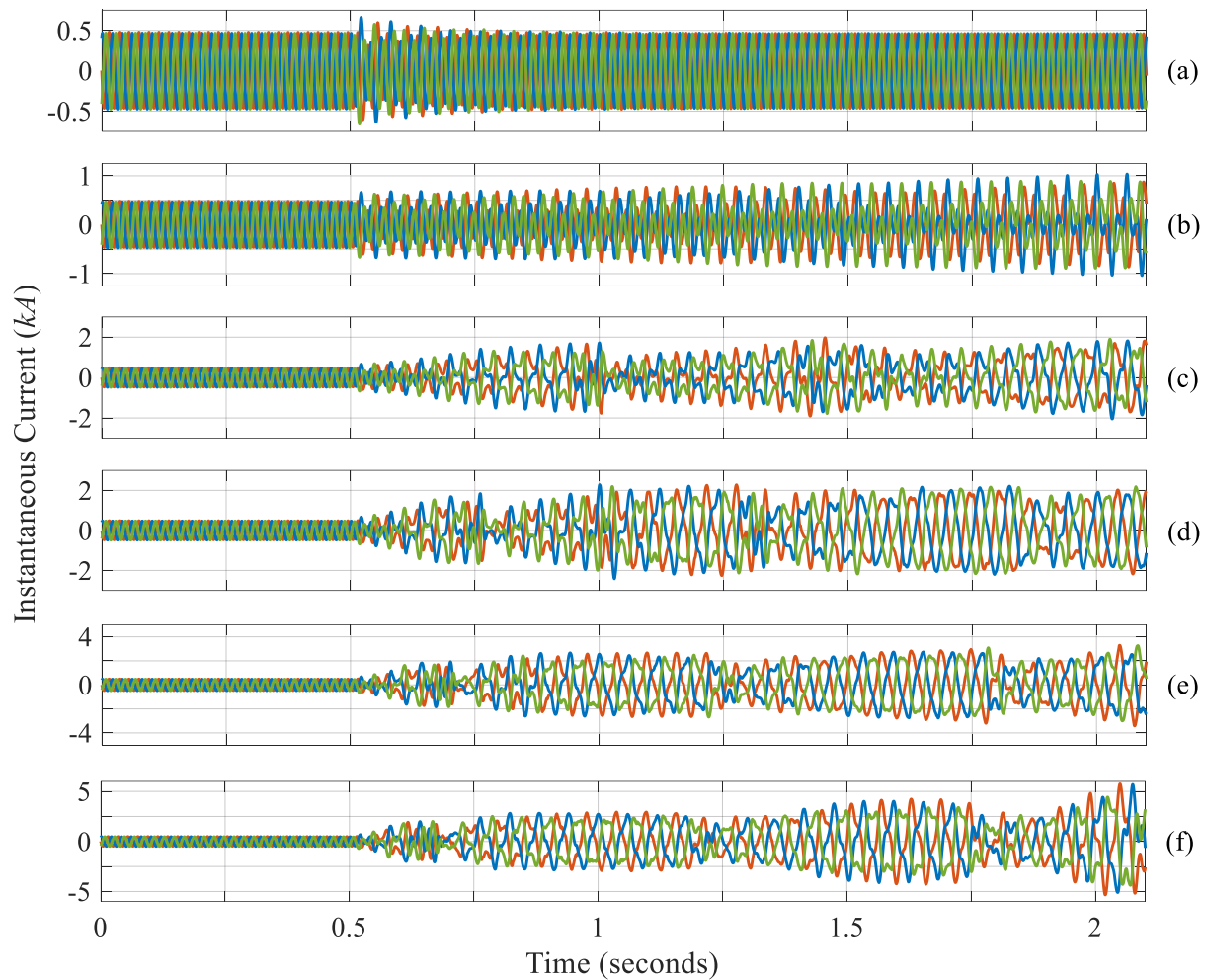


Figure 8.6 Instantaneous current response in a multi-DFIG system with different ratios of tuned DFIGs (non-identical y-axis scales). (a) 100% tuned DFIGs; (b) 80% tuned DFIGs; (c) 60% tuned DFIGs; (d) 40% tuned DFIGs; (e) 20% tuned DFIGs; (f) 0% tuned DFIGs. All DFIGs have the same wind speed of 10 m/s.

In line with the results obtained from the impedance based stability analysis, when the converter parameters of all DFIGs are tuned, the DFIG-SSR mode is well damped. With decreasing numbers of tuned DFIGs, the DFIG-SSR behaviour becomes more pronounced and is noticeable by the increasing magnitude of the sub synchronous current in the different cases. Figure 8.7 shows the harmonic content of the instantaneous currents of Figure 8.6 and the dominance of the 17 Hz mode can be observed.

Closer examination of the time domain simulations and the harmonic spectrum of the currents reveal that a low frequency oscillation (LFO) between 5 and 10 Hz emerges for the cases with 20% and 0% tuned DFIGs. Recall that this resonance frequency is not observed using the impedance based stability analysis. This is further investigated in Section 8.5.2.

In summary, this Section investigated the impact of non-identical converter parameters on DFIG-SSR. It was found that when the DFIGs have non-identical converter parameters, DFIG-SSR occurs, where the severity of the interaction depends on the share of tuned DFIGs.

On the other hand, under the circumstances that the parameters are identical, the tuning methodology proposed as part of the developed PGSC is able to effectively mitigate DFIG-SSR. In the theoretical case where also the operating conditions are identical across all DFIGs, the developed PGSC can be deployed centrally in the wind park control. However, as will be shown next, the operating conditions cannot be assumed to be identical due to wake effects.

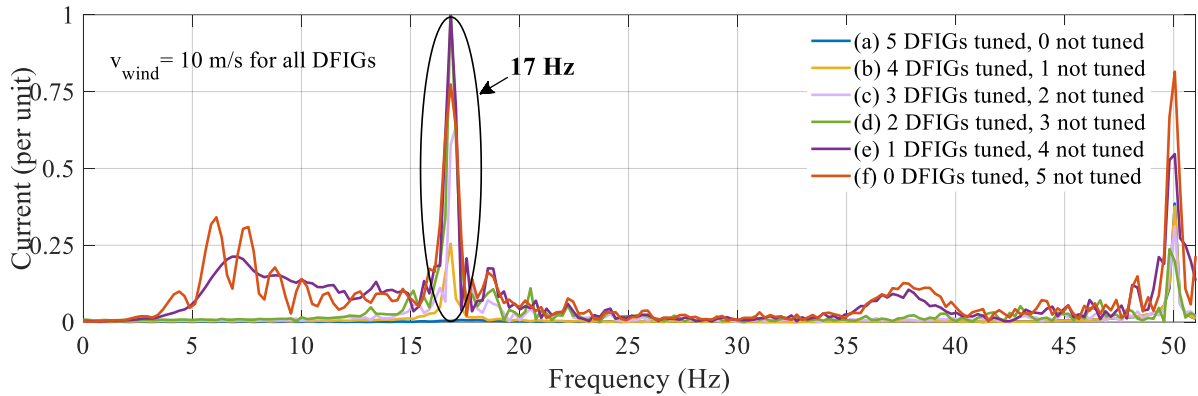


Figure 8.7 Harmonic content of the instantaneous current for different ratios of tuned DFIGs.

8.5.2. IMPACT OF WAKE EFFECT

The analysis with the multi-DFIG system in the previous Section assumed that all DFIGs are exposed to the same wind speed. This is not a valid assumption due to the presence of the wake effect. Since a wind turbine converts the aerodynamic energy in wind to electrical energy, the wind leaving the turbine must have a lower energy content than the wind arriving in front of the turbine. In the downwind direction behind the wind turbine, a turbulent and slowed down trail of wind is formed, known as a wake. The wake from one turbine will be detrimental on the wind speed and turbulence at down wind turbines. The effects of the wake spread out downwind and decay with distance. As the flow proceeds downstream, the wake recovers towards free stream conditions. The wake effect is the aggregated influence on the energy production of the wind power plant, which results from the changes in wind speed caused by the impact of the turbines on each other. The cost optimisation considering the geographical area (e.g. cost of land and cables) and the energy production of the wind power plant results in reduced but not completely absent wake effects. This Section investigates the impact of the variations in operating condition due to the wake effect on the performance of the developed PGSC.

Consider the wind power plant shown in Figure 8.8. It contains 30 DFIGs, located across five rows and six columns. The wake effect is most severe when rows or columns in a wind power plant are closely aligned with the angle of the incoming wind. The analysis will only focus on the DFIGs in column 3. After the incident wind speed v_{wind} leaves the first turbine (indicated in red), a wake is created. The resulting wake width and wind speed deficit are determined among others by the turbine characteristics such as hub height and rotor diameter [8]. The wind direction direct down the column with minimum distance between the subsequent WTGs is denoted ‘exact rotor’ (ER). Due to this minimum distance, the wake effect is maximum for flows down an ER. WTGs in wind directions with an offset from ER (i.e. $ER \pm 5^\circ$,

ER $\pm 10^\circ$ and ER $\pm 15^\circ$) observe a reduced wake created by v_{wind} , where the larger the offset, the smaller the wake effect.

The wake effect was quantified in [8] as a reduction of the power generated by wind turbines in the direction of ER and the offsets $\pm 5^\circ$, $\pm 10^\circ$ and $\pm 15^\circ$. The measured generated power of wind turbines of the Horns Rev wind power plant is given in [8]. In the linear range of the wind power curve, the generated power is proportional to the wind speed. In Figure 8.9 the wind speed reduction (based on the measured reduction in generated power) due to the wake effect is given for Horns Rev. It indeed confirms that the wake effect is most pronounced for ER. In the subsequent analysis, the wind speeds of the five DFIGs will be selected based the data for ER in Figure 8.9.

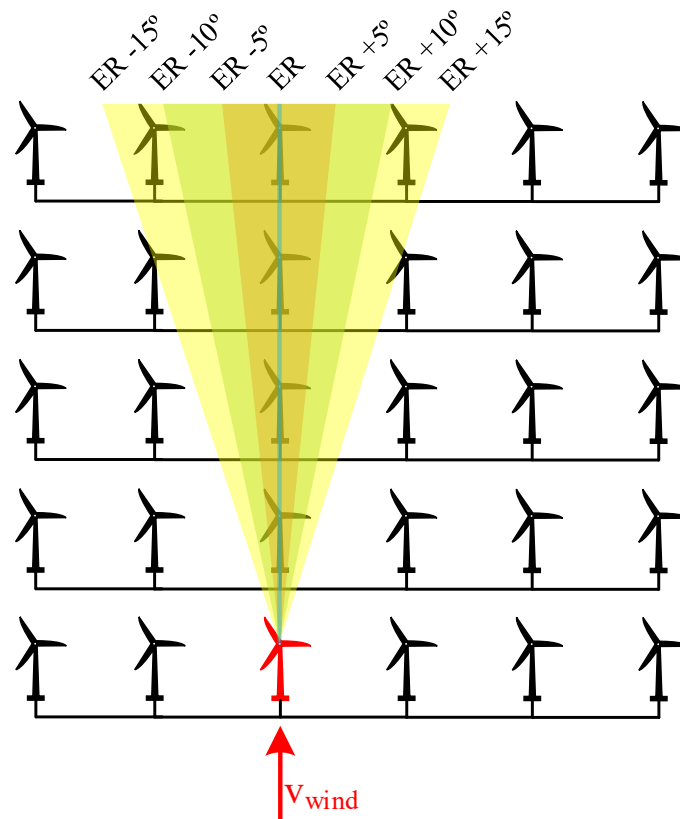


Figure 8.8 Wind power plant layout with 30 DFIGs spread over five rows and six columns. For the incident wind speed the exact rotor (ER) direction as well as the directions with an offset of $\pm 5^\circ$ (red), $\pm 10^\circ$ (green) and $\pm 15^\circ$ (yellow) are shown.

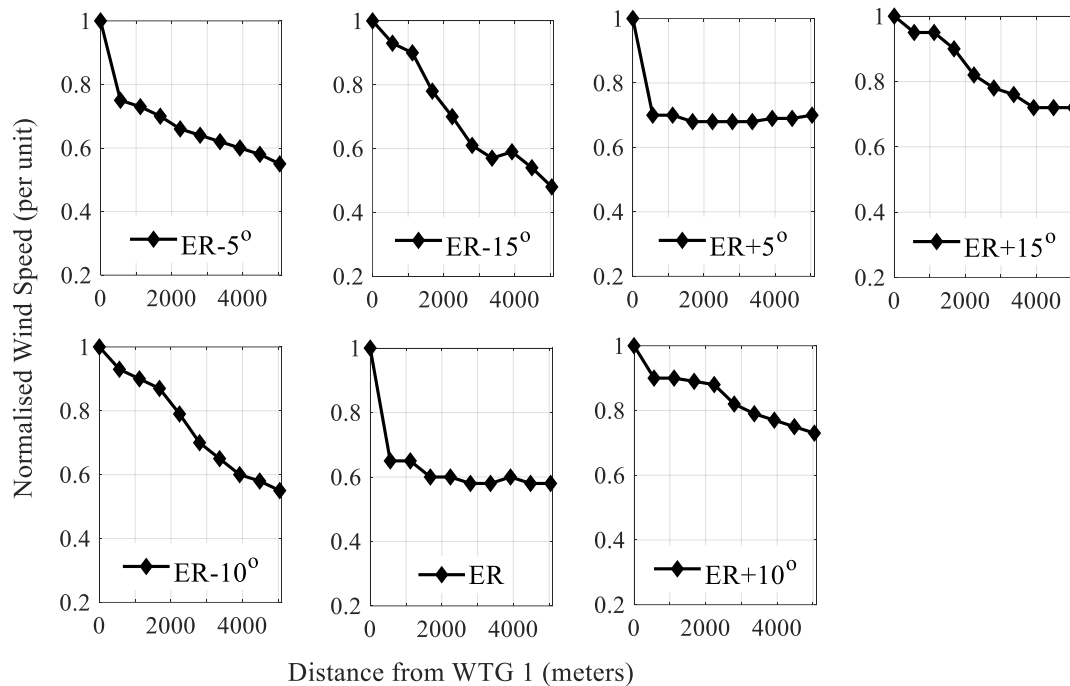


Figure 8.9 Normalised wind speed as a function of distance into the Horns Rev wind power plant [8]. In the linear range of the wind power curve, the wind speed is proportional to the power output.

To assess the impact of the variations in operating conditions due to the wake effect on DFIG-SSR, five DFIGs are modelled according to ER shown in Figure 8.8. Assume that the first DFIG is exposed to a wind speed of 10 m/s. Then, in line with Figure 8.9, the remaining four DFIGs in the column will have a wind speed of 6 m/s.

In the first analysis it is assumed that the PGSC does not schedule the gains according to the actual wind speed of each individual DFIG (i.e. 10 m/s and 6 m/s), but according to the wind speed of the first DFIG (i.e. 10 m/s). In this case, all five DFIGs have their converter parameters scheduled based on the tuning for wind speed 10 m/s. However, only the first DFIG will actually observe the 10 m/s; the wind speed will reduce to 6 m/s for the remaining four DFIGs. After 0.5 seconds, the non-compensated line is switched off, resulting in the radial connection of the five DFIGs to the series capacitor. The results from detailed time domain simulations and the impedance based analysis are shown in Figure 8.10.

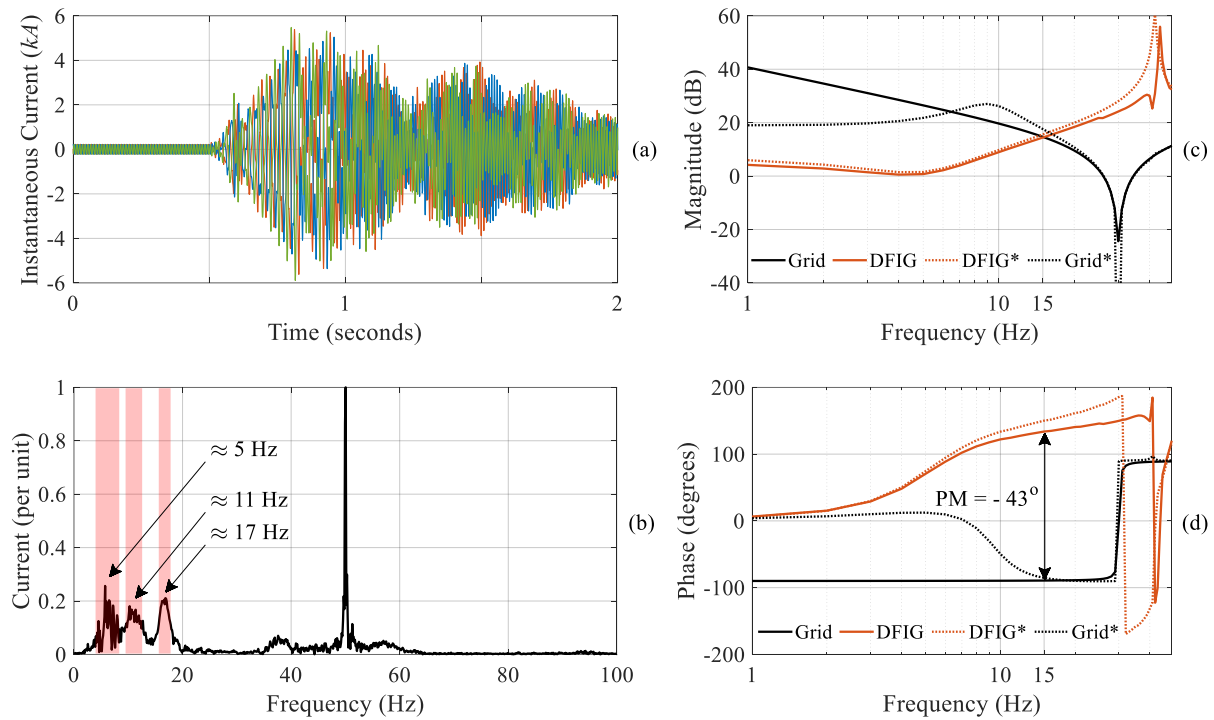


Figure 8.10 Detailed EMT time domain simulations and impedance based stability analysis results for the five-DFIG wind power plant considering wake effects. PGSC does not take wake effects into account. (a) instantaneous currents; (b) frequency spectrum of instantaneous current; (c) and (d) impedance response of the combined system. Solid lines represent impedance response following partitioning along source-load combination 1; dotted lines represent impedance response following partitioning along source-load combination 2.

The first observation is that when the wake effects are not considered by the PGSC, DFIG-SSR occurs (Figure 8.10a). When the harmonic spectrum of the instantaneous current is analysed, three sub synchronous frequencies are observed: 5 Hz, 11 Hz and 17 Hz (shaded red in Figure 8.10b). To prove that these frequencies are not introduced by their coupled frequencies (as explained in Chapter 4.4.4), the frequency components up to the second harmonic are shown in Figure 8.10b. Of these frequencies, only the 17 Hz component was identified using the impedance based stability analysis (Figure 8.10c and Figure 8.10d). The stability analysis was performed for partitioning along the two source-load impedance combinations as shown in Figure 8.11. In the first combination, the source impedance was comprised of the study model network, while the load impedance consisted of all five DFIGs. The identified corresponding resonance frequency was 15 Hz, as indicated by the solid response in Figure 8.10c. In the second combination, the source impedance consisted of the study model network and the first DFIG ($v_{wind} = 10$ m/s), while the remaining four DFIGs ($v_{wind} = 6$ m/s) determined the load impedance. The corresponding resonance frequency was 17 Hz, as indicated by the dotted responses in Figure 8.10c. The latter is in line with the observed current response, indicating that the interaction was among the two subsystems partitioned along the second source-load combination.

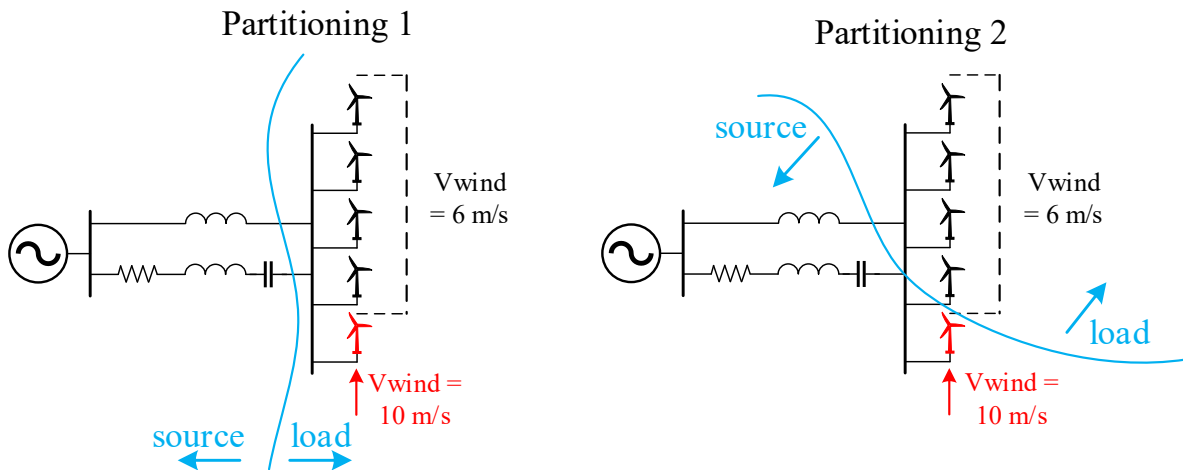


Figure 8.11 Partitioning of source-load subsystems.

The next analysis focused on identifying the source of the 5 Hz and 11 Hz oscillations. The impedance based stability analysis did not identify these resonance frequencies along the two considered partitioning possibilities. This means that these modes are not network modes, in contrast to the 17 Hz resonance. To investigate the LFOs, detailed EMT simulations are performed for cases with a varying number of DFIGs according to Table 8.2. Case 1a is identical to case 2a.

Table 8.2 Description of simulation cases for investigation of low frequency oscillations.

Case	# DFIGs _{6 m/s}	# DFIGs _{10 m/s}	Σ DFIG
case 1a	4	1	5
case 1b	4	0	4
case 1c	3	0	3
case 1d	2	0	2
case 2a	4	1	5
case 2b	3	1	4
case 2c	2	1	3
case 2d	1	1	2

Figure 8.12 and Figure 8.13 show the simulation results for respectively case 1 and case 2. The changes in the network resonance frequency with varying numbers of DFIGs can be observed. Furthermore, it is evident that in some cases the LFOs are observed, while in others they are not present. This is summarised in Table 8.3.

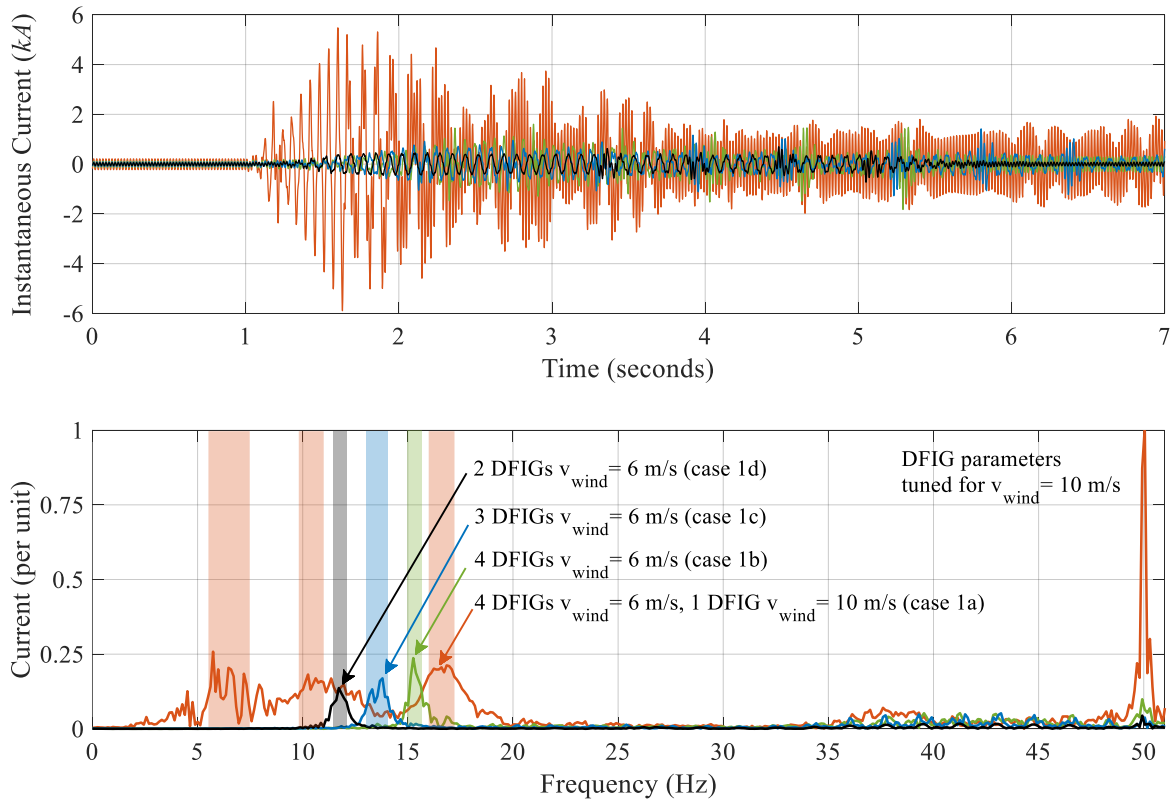


Figure 8.12 Detailed EMT time domain simulation results for case 1. PGSC does not take wake effects into account. All DFIGs have parameters tuned for wind speed 10 m/s. (a) instantaneous currents; (b) frequency spectrum of instantaneous current.

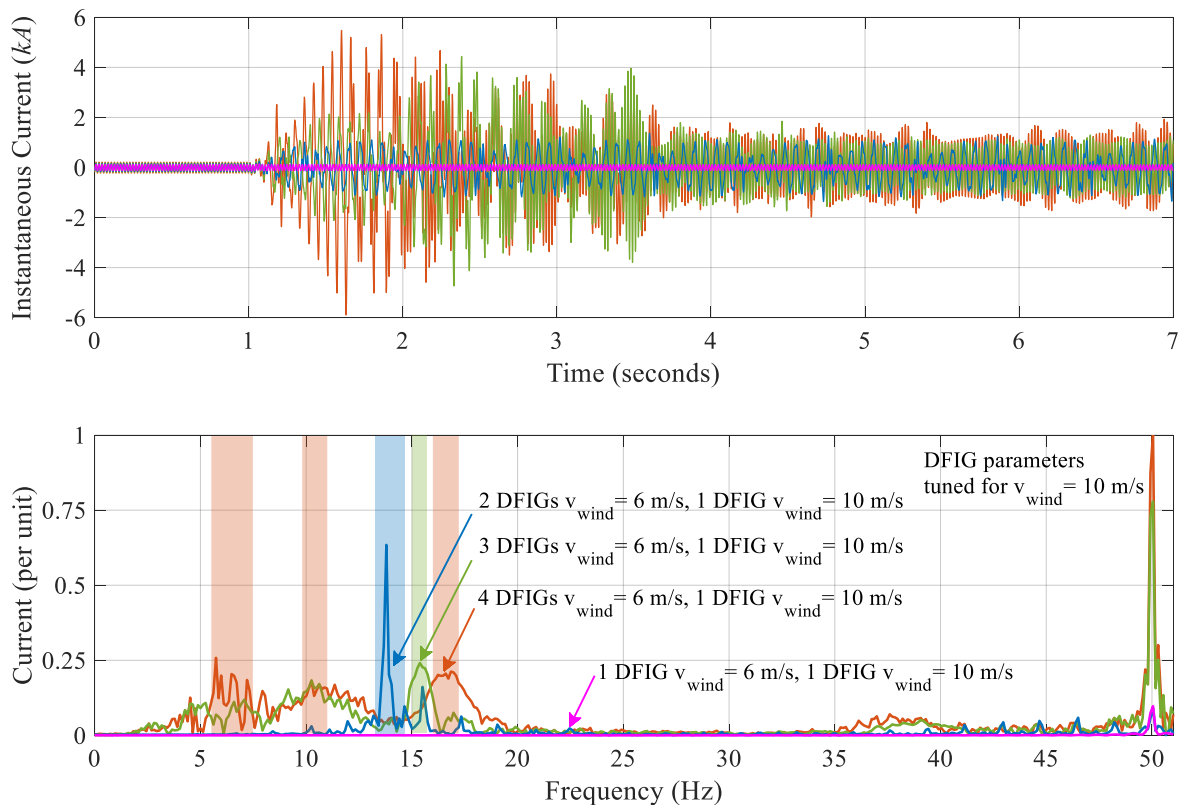


Figure 8.13 Detailed EMT time domain simulation results for case 2. PGSC does not take wake effects into account. All DFIGs have parameters tuned for wind speed 10 m/s. (a) instantaneous currents; (b) frequency spectrum of instantaneous current.

Table 8.3 Summary of simulations with low frequency oscillations.
 The shaded cases represent the simulations of Section 8.5.1 and for these cases
 subscripts '6 m/s' and '10 m/s' represent respectively not tuned DFIGs and tuned DFIGs.

Case	# DFIGs _{6 m/s}	# DFIGs _{10 m/s}	Σ DFIG	LFO	Figure
	0	5	5	X	Figure 8.7
	1	4	5	X	
	2	3	5	X	
	3	2	5	X	
	4	1	5	✓	
	5	0	5	✓	
case 1a	4	1	5	✓	Figure 8.12
case 1b	4	0	4	X	
case 1c	3	0	3	X	
case 1d	2	0	2	X	
case 2a	4	1	5	✓	Figure 8.13
case 2b	3	1	4	✓	
case 2c	2	1	3	X	
case 2d	1	1	2	X	

In Table 8.3, non-tuned DFIGs (Section 8.5.1) and DFIGs deployed with parameters for the wrong wind speed (wake effect) are in both circumstances categorised as to be DFIGs with non-tuned parameters. When analysing Table 8.3 in more detail, it is concluded that the LFO emerges under two possible scenarios. First, when the DFIG wind power plant has DFIGs with both tuned and non-tuned parameters, LFO occurs when the share of the tuned DFIGs is below 25% (Figure 8.7 and cases 1a and 2b). Second, when the power plant consists of only non-tuned DFIGs, LFO occurs when there are at least five DFIGs in operation (Figure 8.7). These findings were successfully validated by extending the number of DFIGs in the wind power plant to eight and performing the simulations again.

In Chapter 2.4 it was stated that low frequency oscillations could also emerge in DFIGs when the bandwidths of the DC-link voltage control and the inverter PLL are close to each other. To investigate whether the observed LFO in Figure 8.10, Figure 8.12 and Figure 8.13 are caused by the bandwidths of the DC-link voltage control and the inverter PLL, the PLL gains were varied and the corresponding oscillations were observed. It was found that variations in the PLL parameters of the inverter did not affect the LFO mode, indicating that this oscillation is not a SSCI-CGI.

It is worth mentioning that in none of the cases where the low frequency oscillations were observed, the impedance based stability analysis was able to identify those. This means that although the impedance based method is able to correctly and accurately identify the network mode, it does not provide any visibility of the low frequency modes. Even when the partitioning is adjusted, this visibility is not obtained. The detailed investigation of the low frequency modes as well as the required modifications to the impedance based method to identify these modes are left for further research.

Finally, when the PGSC does take the wake effect into account, the gains of each DFIG are scheduled according to the observed wind speed considering wake effects at each DFIG. In this case, the first DFIG observes a wind speed of 10 m/s and the gains are scheduled according to the observed wind speed. The remaining four DFIGs observe a wind speed of 6 m/s due to wake effects. Their gains are scheduled accordingly. Figure 8.14 shows that when the wake effects are accounted for by the PGSC, DFIG-SSR is effectively mitigated (Figure 8.14a). The well damped 18 Hz oscillation (Figure 8.14b) is in line with the results of the impedance based stability analysis (Figure 8.14c and Figure 8.14d).

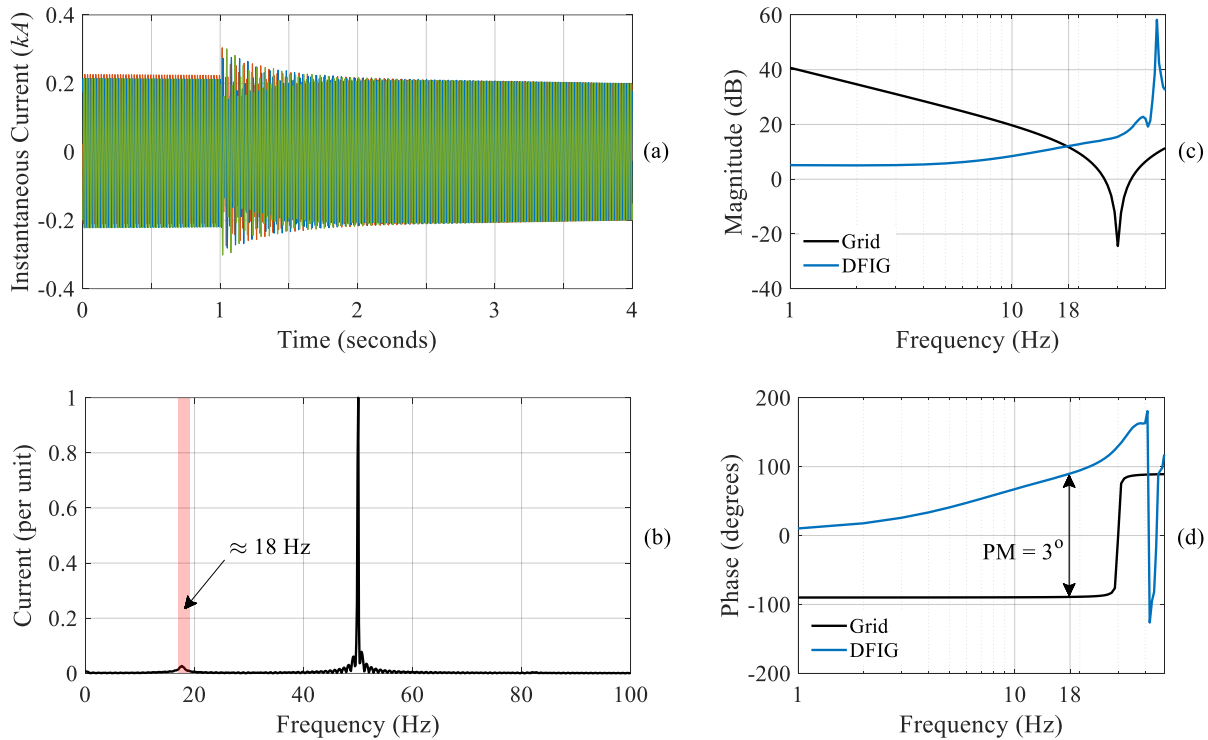


Figure 8.14 Detailed EMT time domain simulations and impedance based stability analysis results for the five-DFIG wind power plant considering wake effects. PGSC does take wake effects into account. (a) instantaneous currents; (b) frequency spectrum of instantaneous current; (c) and (d) impedance response of the combined system.

The impact of wake effects on the performance of DFIG-SSR mitigation solutions was not yet reported in literature. However, as the simulations above show, it is necessary to also assess mitigation capabilities in the presence of wake effects. For the PGSC it is concluded that a decentralised control deployed in each DFIG and that takes wake effects into account, has better DFIG-SSR mitigation capabilities than when the PGSC is deployed on wind park level and does not account for wake effects.

8.5.3. IEEE 39-BUS SYSTEM

The IEEE 39-bus system described in Chapter 4 is used next to validate the performance of the developed PGSC. The DFIG parameters were re-tuned to account for the IEEE 39-bus system's worst $N-5$ grid condition. This worst case is defined as the $N-5$ grid topology with the lowest phase margin at the resonance frequency. The tuning of the DFIG and validation of the parameters was performed using the methodologies proposed in Chapter 6.

Using the impedance based stability analysis on the IEEE 39-bus system and the DFIG (base case) an oscillation of approx. 20 Hz is observed when the DFIG is not tuned (Figure 8.15). The corresponding phase margin is -65° . With tuned parameters of the DFIG, the phase margin increases to 3.5° , indicating stability. The stability is confirmed by the results of the detailed EMT simulations shown in Figure 8.15.

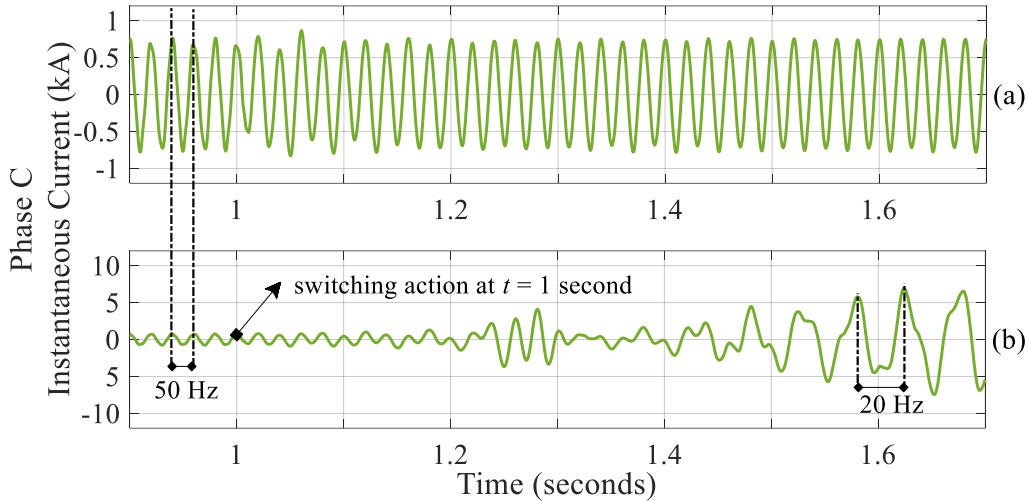


Figure 8.15 Detailed EMT time domain simulations for IEEE 39 bus system. (a) Tuned DFIG parameters. (b) DFIG parameters according to base case.

Section 8.5.1 shows that when the phase margin is 8° , there are some cycles of 17 Hz oscillations observed in the instantaneous current. Although the phase margin when using the IEEE 39-bus system is only 3.5° for the stable case, the 20 Hz oscillations are hardly observed. It would be expected that with lower phase margins, oscillations would take more time to damp out. This can be explained as follows. It is correct that when the phase margin is lower, the oscillation is less damped. However, this is true when the phase margins are compared for the same system. When phase margins of different systems are compared, it is necessary to also look at the grid damping. When looking at the SMIB system, the phase margin at the resonance frequency (17 Hz) is 8° . For the SMIB this corresponds to a grid damping of 0.060Ω at 17 Hz. When looking at the IEEE 39 bus system, the phase margin at the resonance frequency (20 Hz) is lower, i.e. 3.5° . However, the corresponding grid damping at 20 Hz is 1.485Ω , which is almost 25 times higher than the grid damping at the resonance frequency in the SMIB. This major increased grid damping is the reason that the oscillation in the IEEE 39-bus system is hardly observed.

8.6. CONCLUSIONS

This Chapter described the goal and performance of the real-time operations module. The real-time operations module uses the input from the gain identification (Module 1) and wind speed forecasting modules (Module 2) to schedule the $T_{iP,PCC}$ and $T_{iQ,PCC}$ parameters of the DFIG for every five minute time stamp. With the goal to assess the overall performance of the prediction gain scheduling control, a switching action creating the condition for DFIG-SSR was

simulated for each time stamp. Five years of observed wind speed data at Site ID 8501 were used for this purpose. Over this five years period, the developed PGSC was able to mitigate DFIG-SSR on average in 90.6% of the time. Further analysis revealed that when the PGSC was not able to mitigate DFIG-SSR, it was mainly under the circumstances when the observed wind speed was between 6 and 9 m/s and the forecasted wind speed was larger than 9 m/s. At multiple instances, the forecast error reached up to 9 m/s. To a lesser extent, DFIG-SSR occurred when the actual and forecasted wind speeds were different in the range 6-9 m/s.

The DFIG-SSR probability was calculated next. This calculation required on the one hand the probability of a radial connection of the DFIG to a series capacitor, and on the other hand the probabilities of different wind speeds. The probability of the radial connection was calculated using actual outage and failure data of power system equipment in the Netherlands. The probabilities of the wind speeds were determined using five years of measured wind speed data at Site ID 8501. The results showed that compared to the base case, the developed PGSC reduced the DFIG-SSR risk by a factor up to 16.95.

The impact of non-identical operating conditions and converter parameters in a multi-DFIG wind power plant was investigated. It was concluded that when the DFIGs had non-identical converter parameters, DFIG-SSR occurred and the severity of the interaction depended on the share of tuned DFIGs. On the other hand, under the circumstances that the parameters were identical, tuning using the proposed tuning methodology effectively mitigated DFIG-SSR.

The impact of the variations in operating condition due to the wake effect on the performance of the developed PGSC was also investigated. The wake was modelled using measured wind speeds at the Horns Rev wind power plant. It was concluded that when wake effects were modelled in the wind power plant, but not included in the PGSC, DFIG-SSR was not mitigated. On the contrary, an additional low frequency oscillation was introduced. This oscillation emerged under two possible scenarios. First, when the DFIG wind power plant had a mixture of tuned and not tuned DFIGs, the low frequency oscillations occurred when the share of the tuned DFIGs was below 25%. Second, when the power plant consisted of only not tuned DFIGs, the low frequency oscillations emerged when there were at least five DFIGs in operation. Although the impedance based method was able to correctly and accurately identify the network mode, it did not provide any visibility of the low frequency modes. Even when the partitioning was adjusted, this visibility was not obtained. Detailed investigation of the low frequency modes as well as the identification of required modifications to the impedance based method to identify these modes were proposed as topics for further research.

When the wake effects are accounted for in the developed PGSC, it was able to successfully mitigate DFIG-SSR. When considering the location of the PGSC, it was shown that a decentralised PGSC deployed in each DFIG results in the best DFIG-SSR mitigation. This is due to the fact that the PGSC in the individual DFIGs can better estimate the actual wind speed.

Finally, the results were successfully validated using the IEEE 39-bus system.

REFERENCES

- [1] European Commission, “COMMISSION REGULATION (EU) 2016/631 of 14 April 2016 establishing a network code on requirements for grid connection of generators,” *Off. J. Eur. Union*, no. L 112, pp. 1–68, 2016.
- [2] Netbeheer Nederland, “Nestor Data.” [Online]. Available: www.nestordata.nl/.
- [3] C. Draxl and A. Clifton, “A Guide to Using the WIND Toolkit Validation Code,” 2014.
- [4] C. Draxl, A. Clifton, B. M. Hodge, and J. McCaa, “The Wind Integration National Dataset (WIND) Toolkit,” *Appl. Energy*, vol. 151, pp. 355–366, 2015.
- [5] C. Draxl, B. Hodge, and A. Clifton, “Overview and Meteorological Validation of the Wind Integration National Dataset Toolkit,” 2015.
- [6] J. King, A. Clifton, and B.-M. Hodge, “Validation of Power Output for the WIND Toolkit,” 2014.
- [7] W. Du, W. Dong, H. Wang, and J. Cao, “Dynamic Aggregation of Same Wind Turbine Generators in Parallel Connection for Studying Oscillation Stability of a Wind Farm,” *IEEE Trans. Power Syst.*, vol. 34, no. 6, pp. 4694–4705, 2019.
- [8] R. J. Barthelmie *et al.*, “Quantifying the impact of wind turbine wakes on power output at offshore wind farms,” *J. Atmos. Ocean. Technol.*, vol. 27, no. 8, pp. 1302–1317, Aug. 2010.

9. CONCLUSIONS

9.1. RESEARCH SYNTHESIS

The energy transition is posing several technical challenges for transmission system operators worldwide. As part of the research activities, an overview of such challenges was created and validated by the industry. These challenges were categorised in three classes. The first class (Reduced Voltage and Frequency Support) consisted of technical challenges resulting from insufficient availability or inability to meet the ancillary services demand, both in terms of type and volume. A practical example of a technical challenge in this category is the increasing rate of change of frequency. The second class (New Operation of the Power System) grouped together those challenges that require new ways of operating the power system. Power system restoration in the presence of high shares of power electronics interfaced generation is a related example. Finally, the third class (New Behaviour of the Power System) described technical challenges that result in a new behaviour of the power system. An example of such a challenge is the risk for DFIG-SSR, i.e. adverse interactions between a DFIG and a series compensated transmission line.

The objective of this work was to investigate and validate the degree of effectiveness of existing methods and the design and validation of new principles to mitigate DFIG-SSR. To this extent the existing phase imbalance compensation concept and the newly developed predictive gain scheduling control were evaluated. The phase imbalance compensation concept, which is an alternative way of fixed series compensation, was initially designed to address SSR. Its capability to mitigate DFIG-SSR was thoroughly investigated in this thesis and it was concluded that the phase imbalance concept is an effective measure when the required compensation degree of a transmission line is below a critical, system dependent compensation degree.

The newly developed predictive gain scheduling control utilises the forecasted wind speed to schedule two parameters in the rectifier's double loop control. Using actual wind speed and transmission line failure data, it was found that compared to classical compensation, the developed predictive gain scheduling control reduced the DFIG-SSR risk with a factor up to 16.95.

Detailed analysis also showed that the developed control was able to successfully mitigate DFIG-SSR in a multi-DFIG representation of a wind power plant, while accounting for non-identical operating conditions of individual DFIGs. Finally, all the findings were validated using the larger IEEE 39-bus system.

To methodically address the main research objective, this thesis was structured around the following four research questions:

- RQ 1. How can emerging SSO phenomena be positioned in the existing classification of sub synchronous oscillations?
- RQ 2. What are the limitations and recognised application boundaries of existing approaches for mitigating DFIG-SSR?
- RQ 3. To what extent is the phase imbalance compensation concept as a potential hardware solution able to mitigate DFIG-SSR?
- RQ 4. How can gain scheduling control based on system level coordination be used to mitigate DFIG-SSR?

In the following sections the answers to these questions as well as a more complete overview of the obtained results are given.

9.1.1. RECLASSIFICATION OF SSO

The first research question addressed the positioning of DFIG-SSR and other emerging SSO phenomena within the wider scope of SSO and the reclassification of the latter. Since recent years, the power industry has been experiencing three new types of electromagnetic sub synchronous oscillations, which cannot be categorised under the existing SSO framework. These oscillations are fundamentally different and occur under different circumstances as is summarised in the next paragraph. Also, the existing SSO definition explicitly only considers electromechanical oscillations. Finally, there is a lack of consensus in academia and industry regarding the terminology of the emerging oscillations, leading to addressing fundamentally different phenomena with the same terminology. These reasons underlined the need for, on the one hand, a new definition of SSO, and on the other hand, a reclassification of SSO to include the emerging oscillations. This research gap was addressed in this work resulting in a proposal for a new definition and classification of SSO.

The first phenomenon was defined in this work as DFIG-SSR and occurs when a DFIG gets radially connected to a series compensated transmission line. This phenomenon is sometimes also referred to as ‘sub synchronous controller interaction’ or ‘sub synchronous controller instability’. However, as the DFIG’s controllers do not participate in this SSO mode, ‘controller interaction’ is not the correct terminology for this oscillation. The second phenomenon was defined as SSCI-CGI, which is the interaction between a converter and a weak grid. It was shown that when the inverter is deployed with active power control, SSCI-CGI was manifested as a low frequency oscillation. When DC-link voltage control was used, a PLL with low bandwidth made the low frequency mode unstable, whereas a high PLL bandwidth mainly deteriorated the stability of the sub synchronous mode. Finally, the last phenomenon was defined as SSCI-CCI and occurs when two electrically close converters adversely interact.

9.1.2. MITIGATION OF DFIG-SSR

The second research question focused on the identification of the limitations and recognised application boundaries of existing measures to mitigate DFIG-SSR. The existing solutions were grouped based on their geographical location of implementation into hardware solutions, solutions based on system level coordination and control solutions. Control solutions were defined in this thesis as control modifications or new control concepts that are deployed in the rectifier or inverter control of the converter. It was found that so far mainly the tuning of existing double loop control parameters has been used for practical implementation, as new control concepts have too many performance related uncertainties.

Hardware solutions were defined as those solutions that require additional hardware to be installed in either the high or low voltage side of the coupling transformer. These solutions can be broadly divided into FACTS controllers and other VSC based methods. A major drawback of any FACTS based solution is that it requires capital intensive investments. It is only considered a cost-effective solution when on top of DFIG-SSR mitigation, additional system services such as voltage support are required. When a risk for DFIG-SSR is identified in the design stage, the TCSC is one of the preferred mitigation solutions. Replacing a fixed series capacitor before the end of its lifetime is not a cost-effective measure. Therefore, when a risk for DFIG-SSR is identified after commissioning, other measures including operational measures (e.g. topological restrictions) are preferred. With regards to the other emerging SSO phenomena, it was found that FACTS controllers installed for mitigating SSCI-CGI could potentially create SSCI-CCI.

Finally, solutions based on system level coordination were defined as control actions that require coordination between the converter's behaviour and the changing grid response. The only practical implementation in the context of DFIG-SSR is the sub synchronous frequency relay. However, from system operation perspective, protection solutions are the most intrusive, as they abruptly disconnect generation and/or change the system topology and transform a small-signal stability problem into a more difficult to manage large disturbance. Therefore, protection solutions should be used as the last resort to mitigate SSO.

9.1.3. HARDWARE SOLUTION: PHASE IMBALANCE COMPENSATION

The third research question investigated the capability of the phase imbalance compensation concept, as a hardware solution, to mitigate DFIG-SSR. It is an alternative way of fixed series compensation, where the imbalance can be implemented as a series or parallel resonance scheme, in one or two phases of the compensated transmission line. An analytical model was developed for the series scheme, which made it possible to understand how the resonance frequency of the compensated line shifted for different degrees of compensation asymmetry. It was found that the shift in resonance frequency is always positive in the series scheme, where the change in resonance frequency is inversely proportional to the degree of asymmetry. As the negative resistance of the DFIG becomes even more negative with an increase in the resonance frequency, it was shown that as long as the resonance frequency resulting from the series scheme remained within the negative resistance region of the DFIG, the stability of the system decreased even further compared to when classical compensation

was used. The deterioration of the stability was even more pronounced when the series scheme was deployed in two phases, as the resulting increase in resonance frequency is larger.

The parallel scheme on the other hand was able to decrease the frequency of the series resonance, and consequently increase the phase margin, albeit that with an initial compensation degree of 36% this resonance remained unstable. The parallel phase imbalance compensation introduced an additional parallel resonance in the frequency range between 20 and 30 Hz. It was shown that depending on the ratios of C_1/C_2 and C_A/C_1 the parallel resonance could be stable. The findings from the assessment of the series and parallel schemes were used to develop a methodology for the systematic assessment of the phase imbalance compensation concept in the context of DFIG-SSR mitigation. This methodology was used on the IEEE 39 bus system to successfully design a phase imbalance scheme capable of mitigating DFIG-SSR.

To assess the stability of the classical compensation concept and of the one and two phase series and parallel imbalance compensation concepts under varying operating conditions, their marginal stabilities under different short circuit levels were examined. The compensation degree leading to marginal stability was found to be proportional to the short circuit level. The highest compensation degree for marginal stability was achieved using the two phase parallel scheme, whereas the two phase series scheme resulted in the lowest compensation degree. This finding was true for all the considered short circuit levels, albeit that the difference in compensation degree among the various concepts reduced with decreasing short circuit levels.

9.1.4. SYSTEM LEVEL COORDINATION: PREDICTIVE GAIN SCHEDULING CONTROL

The final research question aimed at developing a novel system level coordination based solution to mitigate DFIG-SSR. To this extent, a prediction based gain scheduling control consisting of three modules was developed. The first module focused on the gain identification and scheduling. Monothetic sensitivity analysis was used to identify those DLC parameters of the DFIG's converters that influenced the electrical damping. Then, for wind speed dependent operating conditions, adequate DLC parameter values capable of mitigating DFIG-SSR were determined using single objective bound constrained optimisations. For each wind speed, a six dimension solution space was obtained, which was successfully reduced to two dimensions. Based on the optimisation results, a non-linear control rule was developed for the gain scheduling control. The optimised results were validated in three steps. The first step confirmed that the optimised parameters were indeed capable of mitigating DFIG-SSR. The second validation step investigated how the fault ride through behaviour of the optimised DFIG changed and ensured that the DFIG remained compliant to requirements as stipulated in grid codes. The last validation step proofed that changes in the wind speed and the scheduling of the gains did not lead to small-signal instability.

The goal of the second module was to forecast the wind speed, which is used in the control rule to determine the value of the gains. To this end, a short-term wind speed forecast model based on feedforward artificial neural networks was developed for forecast horizons of 5, 15, 30 and 60 minutes. As part of this development, parameters of the ANN structure and algorithm were tuned to obtain the highest forecast accuracy. It was found that increasing look ahead times required more complex ANNs, which was reflected by the increase in the historical data size, the number of hidden layers and the number of neurons in each hidden layer. Furthermore,

the optimiser and loss function leading to the most accurate forecasts were identified. In general, the analysis gave empirical evidence for the superiority of adaptive optimisers (i.e. Adadelta, Adam, Adamax and Nadam) that do not require manual selection of the learning rate over other optimisers. From all the considered optimisers, an ANN with the adaptive optimiser Adadelta led to the most accurate forecasts. Finally, although ‘root mean square error’ was found in literature to be the preferred loss function, the results obtained in this study do reveal that the ‘mean absolute error’ by far leads to the most accurate forecasts.

The real-time operations module is the last part and was developed with two goals. First, it was responsible for scheduling the correct values of the rectifier control parameters $T_{iP,PCC}$ and $T_{iQ,PCC}$ as a function of the forecasted wind speed, where the scheduling should occur prior to the wind speed change. Second, for every time stamp the module performed a switching action, which resulted in the radial connection of the DFIG to the series capacitor and created the topological condition for DFIG-SSR. The performance of the developed control was assessed using five years of observed wind speed data. Compared to the case without gain scheduling control, the proposed solution was able to mitigate DFIG-SSR on average in 90.6% of the time. Using real failure data, the probability of DFIG-SSR was assessed, showing that the developed control reduced the DFIG-SSR risk by a factor up to 16.95 compared to the base case. The developed solution was also validated on the IEEE 39-bus system.

The impact of non-identical converter parameters and operating conditions in a multi-DFIG wind power plant was investigated as well. It was concluded that when the DFIGs had non-identical converter parameters, DFIG-SSR occurred and the severity of the interaction depended on the share of tuned DFIGs. On the other hand, under the circumstances that the converter parameters were identical, the tuning proposed as part of the developed control effectively mitigated DFIG-SSR.

The impact of non-identical operating conditions on the performance of the developed control was investigated by considering the wake effect. It was concluded that when wake effects were modelled in the wind power plant, but excluded in the proposed control, DFIG-SSR was not mitigated. On the contrary, an additional low frequency oscillation was introduced. This oscillation emerged under two possible scenarios. First, when the DFIG wind power plant consisted of tuned and not tuned DFIGs, low frequency oscillations occurred when the share of the tuned DFIGs was below 25%. Second, when the power plant only consisted of not tuned DFIGs, the low frequency oscillations emerged when there were at least five DFIGs in operation. Finally, when the developed control did account for the investigated wake effects, it was able to successfully mitigate DFIG-SSR. When considering the location of the control, it was shown that a decentralised control deployed in each DFIG resulted in the best DFIG-SSR mitigation.

9.2. SCIENTIFIC CONTRIBUTIONS

The research questions developed in the beginning of this work resulted in novel scientific contributions. These contributions are directly relevant for both, the academia and the industry and are summarised as follows:

1. An industry validated overview of operational challenges due to the energy transition was created (Chapter 1). The clear benefit of this overview is that it presents the research needs of industry based on the actual input from and views of system operators throughout the world. It is already being used by the Dutch-German transmission system operator TenneT in the Netherlands and Germany to develop its research and development road map for future system operations. Other institutions such as CIGRE are using it as a basis for their future activities.
2. The proposed reclassification of SSO (Chapter 2) takes away the ambiguity related to the terminology of distinct SSO phenomena and will help academia and industry to correctly address these. Furthermore, this reclassification also enables the better understanding of the fundamental differences between the distinct phenomena.
3. An assessment with the goal of identifying the advantages as well as limitations and recognised application boundaries of existing DFIG-SSR mitigation solutions was performed (Chapter 3). This assessment can help network owners and vendors of power electronics interfaced devices in selecting adequate solutions for DFIG-SSR.
4. Recommendations were developed to obtain the frequency dependent impedance of black box, non-linear power electronics interfaced devices through numerical EMT simulations (Chapter 4). These recommendations are valid for offline (e.g. PSCAD) as well as online (hardware in the loop) EMT environments and will be beneficial to vendors, network owners and third parties in the context of interaction and harmonic studies. The influence of the impedance calculation time, granularity of the model and composition of the perturbation signal on the obtained impedance was presented and guidelines were given on how to select correct settings. The decrease in phase margin as a result of using the average model instead of the detail model was quantified and its impact was illustrated.
5. A methodology was developed to design the phase imbalance compensation concept for mitigating DFIG-SSR (Chapter 5). The influence of the series and parallel schemes and their different degrees of asymmetry on the stability of the system was thoroughly investigated, showing that the effectiveness of the concept in mitigating DFIG-SSR is determined by the required compensation degree.
6. A predictive gain scheduling control for DFIG-SSR was developed, which was able to reduce the risk for DFIG-SSR by a factor up to 16.95 (Chapters 6-8). A validation methodology was proposed, which ensured that solutions not only mitigate DFIG-SSR, but also respect any imposed fault ride through requirements and do not create small-signal instability. The latter two validation steps are often not considered in existing scientific publications.
7. The influence of several ANN structure and algorithm related parameters on the accuracy of a short-term wind speed forecasting model was identified (Chapter 7). With these insights it becomes possible to further increase forecast accuracies and consequently decrease the system operational costs.

9.3. RECOMMENDATIONS FOR FUTURE WORK

9.3.1. IMPEDANCE BASED STABILITY ANALYSIS

In this thesis, the impedance based stability method was used to screen for the potential risk of DFIG-SSR. In this method the power system is partitioned in two subsystems and the stability is assessed along this partitioning. The point of common coupling is a logical partitioning point when performing interaction assessments.

When the wind power plant was aggregated and represented as a single machine in the interaction analysis, the impedance method accurately identified the resonance frequency of the system. However, when the wind power plant had a multi-DFIG representation in the interaction analysis, the impedance method failed to identify low frequency oscillations that were otherwise visible using detailed time domain EMT simulations. This leads to false dismissals of SSO in the screening process. Further research is needed to assess the nature of this interaction within a wind power plant and methods need to be identified on how to increase the observability of the impedance based stability method to prevent such false dismissals.

9.3.2. GRID FORMING CONTROL

Grid forming control is gaining increasing attention in the industry as a potential solution for addressing operational challenges such as the increasing rate of change of frequency and the instability related to the phase lock loop. A battery energy storage system equipped with grid forming control is even already operational in Australia and is one of the first commercially commissioned grid forming applications. In Europe, grid forming control is seen as one of the measures to maintain operational reliability in the context of proliferation of renewable energy sources. As such, several grid forming control concepts are already designed and existing and ongoing research on grid forming control mainly focus on its ability to provide synthetic inertia, to provide blackstart capabilities and to operate in power systems with low short circuit levels. In the context of mitigation solutions, it will be interesting and relevant to investigate the capability of grid forming control to mitigate DFIG-SSR.

9.3.3. FORECASTING

It is acknowledged that practical forecast models will often implement more complex ANNs such as recurrent networks or hybrid models, than the one that is implemented within this thesis. Some of these forecast models have a higher forecast accuracy than the model developed in this research. It is recommended to investigate whether this increased forecast accuracy is also reflected in a further reduction of DFIG-SSR risks, when such an advanced and more complex forecast model is used in the developed predictive gain scheduling control.

APPENDIX A. DFIG EMT PARAMETERS

The tables below contain the data of the EMT DFIG model that was developed in the framework of the MIGRATE project. It is based on the following reference:

MIGRATE, “MIGRATE Project Type 3 and Type 4 EMT Model Documentation,” 2017.

Table A1 DFIG Converter Parameters

Parameter	Value/Range	Description
Capacitance	18000 [μ F]	DC bus capacitance
AC system frequency	50 [Hz]	Nominal AC system frequency
Voltage on high side of TRF	161 [kV]	Voltage of the collector system
System MW at PCC	3.6 [MW]	The expected full active power at the point of common coupling.
Machine rating	4.0[MVA]	The MVA rating of the machine.
Machine terminal voltage	0.9 [kV]	Nominal voltage of the stator terminals
Stator resistance	0.005 [pu]	Resistance of the stator windings
Slip_max	0.3	Maximum operating slip of the machine
Stator/Rotor turns ratio	0.3	Turns ratio between stator and rotor windings
Cutoff frequency	300 [Hz]	Cut-off frequency for the low pass filter
Cfilter	300 [μ F]	Main filter capacitance
Cdamp	350 [μ F]	Damping branch capacitance
Ldamp	621 [μ H]	Damping branch inductance
Rdamp	1.332 [ohm]	Filter’s damping resistance
Activation voltage	1.65 [kV]	Chopper hysteresis control activation voltage
Off voltage	1.6 [kV]	Chopper hysteresis control turn off voltage
Shunt resistor	1.0 [ohm]	Chopper resistance
DC crow bar on voltage	1.75 [kV]	Crow bar activation by DC link overvoltage: Activation voltage
Maximum Irotor	3 [kA]	Crow bar activation by overcurrent in rotor circuit: Activation current
Crow bar resistance	0.2 [ohm]	Crow bar resistance
Crow bar inductance	20 [μ H]	Value of inductance series to crow bar system

Table A2 DFIG Inverter Parameters

Parameter	Value/Range	Description
Rated MVA	1.5 [MVA]	Rating of the grid side converter in MVA. Typically between 20 and 40% of the Wind Turbine Generator rating
Rated AC voltage	0.69 [kV]	Voltage on the AC side of the grid side converter
Vdc base	1.45 [kV]	Base DC voltage of DC bus
Current controller upper limit order	1.2 [pu]	Maximum current allowed in converter compared to nominal current at nominal voltage
Converter VSC reactor	200 [μ H]	VSC reactor for Grid Side Converter
Carrier frequency multiple	60	Carrier frequency expressed as a multiple of the fundamental frequency
d regulator gain	0.01-5	d-axis PI controller proportional gain
d regulator time constant	0.01-0.5	d-axis PI controller time constant
q regulator gain	0.01-5	d-axis PI controller proportional gain
q regulator time constant	0.01-0.5	d-axis PI controller time constant
E _{dc} regulator gain	0.01-10	DC voltage PI controller proportional gain
E _{dc} regulator time constant	0.01-0.5	DC voltage PI controller time constant
Q regulator gain	0.01-5	Reactive power PI controller proportional gain
Q regulator time constant	0.01-0.5	Reactive power PI controller time constant
K _i _PLL_Gr	1-2000	Grid side converter PLL integral gain
K _p _PLL_Gr	1-5000	Grid side converter PLL proportional gain

Table A3 DFIG Rectifier Parameters

Parameter	Value/Range	Description
Rated MVA	1.5 [MVA]	Rating of the grid side converter in MVA. Typically between 20 and 40% of the Wind Turbine Generator rating
Rated AC voltage	0.69 [kV]	Voltage on the AC side of the grid side converter
Current controller upper limit order	1.2 [pu]	Maximum current allowed in converter compared to nominal current at nominal voltage
Carrier frequency multiple	37	Carrier frequency expressed as a multiple of the fundamental frequency
Kpd_R	0.01-5	d-axis PI controller proportional gain to be used in the inner PI controller
Tid_R	0.01-0.5	d-axis PI controller time constant to be used in the inner PI controller
KpP_PCC	0.01-5	d-axis PI controller proportional gain to be used in the PCC active power PI controller.
TiP_PCC	0.01-0.5	d-axis PI controller time constant to be used in the PCC active power PI controller.
Kpq_R	0.01-5	q-axis PI controller proportional gain to be used in the inner PI controller
Tiq_R	0.01-0.5	q-axis PI controller time constant to be used in the inner PI controller
KpQ_PCC	0.01-5	q-axis PI controller proportional gain to be used in the PCC reactive power PI controller.
TiQ_PCC	0.01-0.5	q-axis PI controller time constant to be used in the PCC reactive power PI controller.
Ki_PLL_DFIG	1-5000	Rotor side converter PLL integral gain
Kp_PLL_DFIG	1-5000	Rotor side converter PLL proportional gain

APPENDIX B. BEST PERFORMING ANN

The lowest forecast errors and associated ANN parameters for each investigated site and forecast horizon are given in the tables below.

Table B1 Best ANN parameters for FH 5

Site	HL	N_{HL}	BS	HDS	TD	MAE(%)
136	2	5	10	10	0.8	2.405
1508	1	5	5	10	0.8	1.252
7115	3	5	5	10	0.5	1.534
8501	1	10	5	10	0.5	2.363
13604	1	10	5	10	0.5	1.526
15184	1	5	10	5	0.5	1.613
48312	2	5	10	5	0.5	1.340
64408	3	5	5	5	0.5	1.874
79930	1	10	5	10	0.5	0.871
92687	2	5	5	5	0.5	0.468
94690	1	3	5	5	0.5	0.828
112142	3	3	5	5	0.5	1.160

Table B2 Best ANN parameters for FH 15

Site	HL	N_{HL}	BS	HDS	TD	MAE(%)
136	2	3	5	5	0.8	3.606
1508	3	3	20	5	0.5	2.537
7115	1	10	10	10	0.8	4.582
8501	1	10	20	10	0.5	4.116
13604	3	10	5	10	0.8	3.921
15184	1	3	10	5	0.5	4.108
48312	1	5	5	5	0.8	2.910
64408	2	5	10	10	0.8	3.819
79930	3	5	5	10	0.8	2.151
92687	2	3	5	5	0.5	1.906
94690	3	10	5	10	0.8	2.926
112142	2	5	5	5	0.5	3.718

Table B3 Best ANN parameters for FH 30

Site	HL	N_{HL}	BS	HDS	TD	MAE(%)
136	1	10	10	10	0.5	4.442
1508	3	5	10	5	0.5	3.409
7115	2	3	5	5	0.5	6.911
8501	3	5	5	5	0.5	4.893
13604	1	5	10	5	0.8	6.547
15184	2	5	5	5	0.8	6.049
48312	3	5	5	5	0.5	4.447
64408	1	10	10	10	0.8	4.930
79930	3	20	5	20	0.2	4.035
92687	3	5	5	5	0.8	3.503
94690	1	5	5	5	0.5	5.272
112142	1	5	10	5	0.5	6.215

Table B4 Best ANN parameters for FH 60

Site	HL	N_{HL}	BS	HDS	TD	MAE(%)
136	2	5	5	10	0.8	5.840
1508	2	10	5	10	0.8	5.288
7115	3	10	5	10	0.5	11.542
8501	3	5	5	5	0.5	6.347
13604	3	5	5	5	0.5	9.331
15184	1	3	5	5	0.5	10.737
48312	2	10	5	10	0.8	6.389
64408	3	10	5	10	0.8	7.257
79930	2	5	5	5	0.5	6.053
92687	2	10	5	10	0.8	6.053
94690	3	10	5	10	0.5	7.985
112142	3	5	5	10	0.8	9.554

APPENDIX C. OPTIMISERS AND LOSS FUNCTIONS

For each considered optimiser, a description is given below.

For each considered loss function, the mathematical formula is given below.

OPTIMISERS

Stochastic Gradient Descent

The Stochastic Gradient Descent (SGD) method [1] calculates the gradient of a loss function $J(\theta)$ with regards to the weights θ after each sample pair (x^i, y^i) . A learning rate α needs to be determined manually and remains unchanged throughout the full set of simulations. For the SGD method, α is identical for all input neurons and is therefore defined as a global learning rate. The set of weights θ are updated N times per epoch:

$$\theta_{i+1} = \theta_i - \alpha \nabla_{\theta} J(\theta; x^i, y^i) \quad (C1)$$

On the contrary, when using the batch gradient descent method, the weights are updated only once per epoch.

Adagrad

The adaptive gradient descent (Adagrad) algorithm [2] contains a global learning rate α . This α , however, is not constant and is updated after each iteration i . To implement this adaptive characteristic, Adagrad introduces an exponentially decaying correction factor for each dimension P and is based on all previous gradients of dimension P :

$$\Delta\theta_i = -\frac{\alpha}{\sqrt{\sum_{n=1}^i g_n^2}} g_i \quad (C2)$$

α : global learning rate

In this way, each dimension P has its own dynamic $\Delta\theta_i$ which is inversely proportional to the past gradient magnitudes. Because of this characteristic, the algorithm is suitable for data sets with high levels of sparsity [3]. One of the drawbacks of this method is the manual selection of an initial global α .

Adadelta

The Adadelta method [4] dynamically adapts the learning rate over time using, among others, an exponentially decaying average of the previous squared gradients. Furthermore, it eliminates the need for the manual selection of a global α as shown in (C3).

$$\Delta\theta_i = -\frac{RMS[\Delta\theta]_{i-1}}{RMS[g]_i} g_i \quad (C3)$$

One of the advantages of the Adadelta algorithm is its robustness against different initial values of α , which is not the case with the SGD or Adagrad algorithm. The RMSprop and Adadelta methods are somewhat similar. The main difference is that RMSprop still requires the manual selection of the learning rate.

Adam

The adaptive moment estimation (Adam) method [5], like Adagrad, determines a unique learning rate α_i for each weight θ_i , which is updated for every sample pair (x^i, y^i) . It uses two correction factors for the update rule: an exponentially decaying average of the previous squared gradients (like Adagrad and Adadelta) and an exponentially decaying average of the previous updates $\Delta\theta_i$. In [5] it was shown that Adam has a better performance than other adaptive optimiser algorithms. It is among the most popular optimisers used in ANNs [6]. When Adam is generalized, the Adamax algorithm is achieved.

Nadam

The Nesterov-accelerated adaptive moment estimation (Nadam) method [6] is developed based on the Adam algorithm. The main difference is that whereas Adam uses a classical momentum for determining the exponentially decaying factor, Nadam uses the Nesterov accelerated gradient.

LOSS FUNCTIONS

$$\text{Mean Squared Error} \quad \text{loss}(y, \hat{y}) = \frac{1}{N} \sum_{i=1}^N (y_i - \hat{y}_i)^2 \quad (C4)$$

$$\text{Mean Absolute Error} \quad \text{loss}(y, \hat{y}) = \frac{1}{N} \sum_{i=1}^N |y_i - \hat{y}_i| \quad (C5)$$

$$\text{Mean Absolute Percentage Error} \quad \text{loss}(y, \hat{y}) = \frac{100}{N} \sum_{i=1}^N \left| \frac{y_i - \hat{y}_i}{y_i} \right| \quad (C6)$$

$$\text{Mean Squared Logarithmic Error} \quad \text{loss}(y, \hat{y}) = \frac{1}{N} \sum_{i=1}^N (\log(y_i + 1) - \log(\hat{y}_i + 1))^2 \quad (C7)$$

$$\text{Hinge} \quad \text{loss}(y, \hat{y}) = \sum_{i=1}^N \max\left(0, \frac{1}{2} - y_i \hat{y}_i\right) \quad (C8)$$

$$\text{Squared Hinge} \quad \text{loss}(y, \hat{y}) = \sum_{i=1}^N \max\left(0, \frac{1}{2} - y_i \hat{y}_i\right)^2 \quad (\text{C9})$$

$$\text{Log-Cosh} \quad \text{loss}(y, \hat{y}) = \sum_{i=1}^N \log(\cosh(\hat{y}_i - y)) \quad (\text{C10})$$

$$\text{Binary Cross-Entropy} \quad \text{loss}(y, \hat{y}) = \frac{1}{N} \sum_{i=1}^N [y_i \cdot \log(\hat{y}_i) + (1 - y_i) \log(1 - \hat{y}_i)] \quad (\text{C11})$$

$$\text{Kullback Leibler Divergence} \quad \text{loss}(y, \hat{y}) = \frac{1}{N} \sum_{i=1}^N (y_i \cdot \log(y_i)) - \frac{1}{N} \sum_{i=1}^N (y_i \cdot \log(\hat{y}_i)) \quad (\text{C12})$$

$$\text{Poisson} \quad \text{loss}(y, \hat{y}) = \frac{1}{N} \sum_{i=1}^N (\hat{y}_i - y_i \cdot \log(\hat{y}_i)) \quad (\text{C13})$$

$$\text{Cosine Proximity} \quad \text{loss}(y, \hat{y}) = \frac{\sum_{i=1}^N y_i \cdot \hat{y}_i}{\sqrt{\sum_{i=1}^N (y_i)^2} \cdot \sqrt{\sum_{i=1}^N (\hat{y}_i)^2}} \quad (\text{C14})$$

REFERENCES

- [1] H. Robbins and S. Monro, “A Stochastic Approximation Method,” *Ann. Math. Stat.*, vol. 22, no. 3, pp. 400–407, 1951.
- [2] J. Duchi, E. Hazan, and Y. Singer, “Adaptive Subgradient Methods for Online Learning and Stochastic Optimization,” *J. Mach. Learn. Res.*, vol. 12, pp. 2121–2159, 2011.
- [3] S. Ruder, “An overview of gradient descent optimization algorithms,” 2016.
- [4] M. D. Zeiler, “ADADELTA: An Adaptive Learning Rate Method,” 2012.
- [5] D. P. Kingma and J. Ba, “Adam: A Method for Stochastic Optimization,” in *International Conference on Learning Representations*, 2014, pp. 1–15.
- [6] T. Dozat, “Incorporating Nesterov Momentum into Adam,” *ICLR Work.*, no. 1, pp. 2013–2016, 2016.

GLOSSARY

LIST OF ABBREVIATIONS

ADRC	Active disturbance rejection control
ANN	Artificial neural network
ASPAS	Automated stability phasor-based algorithm system
AUD	Australian Dollar
BESS	Battery energy storage system
BS	Batch size
CCI	Converter-converter interaction
CGI	Converter-grid interaction
DDSSO	Device dependent sub synchronous oscillation
DFIG	Doubly fed induction generator
DLC	Double loop control
D-PMSG	Direct drive permanent magnet synchronous generator
EMT	Electromagnetic transient
ER	Exact rotor
ERCOT	Electricity reliability council of Texas
FACTS	Flexible alternating current transmission system
FFBP	Feed forward back propagation
FH	Forecast horizon
FLC	Feedback linearisation control
FRT	Fault ride through
FSC	Fixed series compensation/capacitor
GF	Grid forming
GSC	Grid side converter
GW	Giga watt
HDS	Historical data size
HL	Number of hidden layers
HVDC	High voltage direct current
ICS	Input control signal
IEC	International Electrotechnical Commission
IEEE	Institute of Electrical and Electronics Engineers
IGBT	Insulated gate bipolar transistor
IGE	Induction generator effect
IQR	Inter quartile range
LCC	Line commutated converter
LFO	Low frequency oscillation
MAE	Mean absolute error

MAPE	Mean absolute percentage error
MIGRATE	Massive integration of power electronics devices
MMAC	Multiple-model adaptive control
MMF	Magnetomotive force
MSE	Mean squared error
MSLE	Mean squared logarithmic error
NCH	Non-characteristic harmonic
NREL	National Renewable Energy Laboratory
NWP	Numerical weather predictions
OFAT-SA	One factor at a time sensitivity analysis
PCC	Point of common coupling
PE	Power electronics
PEID	Power electronics interfaced devices
PGSC	Prediction based gain scheduling control
PIC	Phase imbalance compensation
PLL	Phase locked loop
PM	Phase margin
PMU	Phasor measurement unit
PSCAD	Power system computer aided design
PV	Photovoltaic
PWM	Pulse width modulation
RES	Renewable energy sources
RIX	Ruggedness index
RMS	Root mean square
RMSE	Root mean square error
ROCOF	Rate of change of frequency
RSC	Rotor side converter
SCR	Short circuit ratio
SDC	Supplementary damping controller
SDG	Stochastic gradient descent
SMC	Sliding mode control
SSC	Short circuit capacity
SSCI	Sub synchronous controller interaction/instability
SSO	Sub synchronous oscillation
SSR	Sub synchronous resonance
SSSC	Static synchronous series compensator
SSTI	Sub synchronous torsional interaction
STATCOM	Static compensator
SVC	Static var compensator
TCSC	Thyristor controlled series capacitor
TD	Training data
TSO	Transmission system operator
UIF	Unit interaction factor

UK	United Kingdom
UPFC	Universal power flow controller
VC	Vector control
VSC	Voltage source converter
VSM	Virtual synchronous machine
WTG	Wind turbine generator

LIST OF SYMBOLS

CHAPTER 2

f_r	Resonance frequency (Hz)
f_0	Fundamental frequency
X_C	Series capacitor impedance
X_G	Equivalent grid impedance
X_L	Transmission line impedance
X_T	Transformer impedance
f_m	Mechanical natural frequency of turbine-generator system
L	Inductance of transmission line
C	Capacitance of series capacitor
ω_r	Resonance frequency (rad/s)
k	Compensation degree
ΔP	Change in active power transfer resulting from series compensation
Z_{DFIG}	Impedance of the DFIG
Z_{GS}	Grid side impedance
Z_{GSC}	Grid side converter impedance
Z_{RS}	Rotor side impedance
Z_{RSC}	Rotor side converter impedance
Z'_{RSC}	Rotor side converter impedance referred to the stator side
Z_{L1}, Z_{L2}	Impedance of filter inductor
Z_{C1}	Impedance of filter capacitor
χ	Slip
ω_e	Electrical speed
R_s	Resistance of stator winding (induction machine)
Z_{Ls}	Impedance of stator leakage reactance (induction machine)
Z_{Lm}	Impedance of magnetising reactance (induction machine)
Z_{Lr}	Impedance of rotor leakage reactance (induction machine)
R_r	Resistance of rotor winding (induction machine)
R'_r	Resistance of rotor winding referred to the stator side
V_{DC}	DC-link voltage
$P_{rectifier}$	Active power flowing into the DC-link
$P_{inverter}$	Active power flowing out of the DC-link

$K_{P,PLL}$ Proportional gain of inverter PLL

CHAPTER 3

Δy Input to supplementary damping controller
 $\Delta\omega_m$ DFIG's rotor speed deviation
 I_{line} Line current
 V_C Voltage across series capacitor
 T_w, T_n Time constants of supplementary damping controller
 $E_{dc,ref}$ DC-link reference voltage
 E_{dc} DC-link voltage
 $E_{d,ref}, E_{q,ref}$ d-axis and q-axis reference voltages of inverter control
 $V_{d,ref}, V_{q,ref}$ d-axis and q-axis reference voltage of rectifier control
 $I_{d,ref}, I_{q,ref}$ Outer loop reference currents
 $K_{p,dc}$ DC voltage PI controller proportional gain
 $K_{p,dS}$ d-axis PI controller proportional gain
 $K_{p,Q}$ Reactive power PI controller proportional gain
 $K_{p,qS}$ d-axis PI controller proportional gain
 $K_{pP,PCC}$ d-axis PI controller proportional gain for PCC active power control
 $K_{p,dR}$ d-axis PI controller proportional gain for the inner PI controller
 $K_{pQ,PCC}$ q-axis PI controller proportional gain for PCC reactive power control
 $K_{p,qR}$ q-axis PI controller proportional gain for the inner PI controller
 $T_{i,dc}$ DC voltage PI controller time constant
 $T_{i,dS}$ d-axis PI controller time constant
 $T_{i,Q}$ Reactive power PI controller time constant
 $T_{i,qS}$ d-axis PI controller time constant
 $T_{iP,PCC}$ d-axis PI controller time constant for PCC active power control
 $T_{i,dR}$ d-axis PI controller time constant for the inner PI controller
 $T_{iQ,PCC}$ q-axis PI controller time constant for PCC reactive power PI control
 $T_{i,qR}$ q-axis PI controller time constant for the inner PI controller
 L_{conv} VSC reactor for GSC

CHAPTER 4

E_s Source voltage
 Z_{load} Impedance of load subsystem
 Z_{source} Impedance of source subsystem
 $Z_{grid}(f_r)$ Grid impedance at f_r
 $Z_{DFIG}(f_r)$ DFIG impedance at f_r
 \angle Angle (degrees)
 $V_{abc,p}$ White noise signal
 V_p Magnitude of perturbation voltage

$\omega_{p,\psi}$	Perturbation frequency
ϕ_ψ	Phase angle associated with perturbation frequency
ψ	Vector with perturbation frequencies
f_p	Perturbation frequency
f_{nc}	Non-characteristic frequency
$V(f_p)$	Voltage at frequency f_p
$I(f_p)$	Current at frequency f_p
$\overline{Z}_{DFIG}(f_p)$	DFIG impedance accounting for frequency cross coupling
Z_{SYSTEM}	System impedance
Σ	Machine multiplier component

CHAPTER 5

L_A	Phase imbalance inductance in phase A
C_A	Phase imbalance capacitance in phase A
Z'	Line impedance in classical compensation scheme
Z''	Line impedance in phase imbalance compensation scheme
$\omega''_{r,B}$	Resonance frequency of phase B using phase imbalance compensation
$\omega'_{r,B}$	Resonance frequency of phase B using classical compensation
\hat{I}_{ABC}	Maximum phase current
$\Delta\omega_r, \Delta f_r$	Resonance frequency deviation
Q	Degree of asymmetry
$f_{r,classical}$	Resonance frequency using classical compensation
$f_{r,series PIC}$	Resonance frequency using series PIC
C_1, C_2	Capacitances of the parallel PIC scheme
$f_{r,parallel PIC}$	Resonance frequency using parallel PIC

CHAPTER 6

x	Vector of optimisation variables
x_{min}	Minimum values of optimisation variables
x_{max}	Maximum values of optimisation variables
η	Oscillation energy
c	Real constant
v_{wind}	Wind speed
$T_{i,low}, T_{i,high}$	Parameters of control rule for gain scheduling
T_i	Calculated value of control parameter using developed control rule

CHAPTER 7

\hat{y}_M	Output neuron
$w_{n,k}$	Weight between neurons n and k

u_j	Neuron in first hidden layer
$\phi(\tau)$	Rectifier function
x_n	Neuron n in the input later
$J(\theta)$	Forecast error due to vector of weighting factors
y_i	Observed output
\hat{y}_i	Forecasted output
ε	Average forecast error
N_{HL}	Number of neurons in a hidden layer
$\Delta\theta_i$	Change in weight
g_i	Gradient of the parameters at the i -th iteration
α	Global learning rate
\hat{y}_θ	Forecasted output due to vector of weighting factors

CHAPTER 8

$P(L_x \text{ out})$	Probability that line x is switched off
U_x	Unavailability of line x
A_x	Availability of line x
l_x	Length of line x
f_x	Failure rate of line x
r_x	Repair time of line x
$v_{critical}$	Critical wind speed
v_{cut-in}	Cut in wind speed

LIST OF FIGURES

Figure 1.1 Annual electrical energy production from coal, wind and solar PV.....	2
Figure 1.2 Curtailment against wind generation penetration in Britain and Germany	3
Figure 1.3 Overview of system operational challenges due to the energy transition.....	4
Figure 1.4 Thesis Outline	9
Figure 2.1 Existing classification of sub synchronous oscillations.....	16
Figure 2.2 Turbine-Generator and series compensation single line diagram.....	16
Figure 2.3 Overview of installed wind generation and published SSO events	18
Figure 2.4 Overview of the classical compensation scheme.....	19
Figure 2.5 Vector diagram of the phase impedances at fundamental frequency	19
Figure 2.6 Influence of the compensation degree on the resonance frequency	21
Figure 2.7 Single line diagram of compensated power system in Hydro-Quebec.....	22
Figure 2.8 765 kV series compensated transmission corridor in South Africa.....	23
Figure 2.9 Schematic diagram of a DFIG WTG	24
Figure 2.10 Electrical connection of the DFIG	24
Figure 2.11 South Texas transmission system with coastal wind power plants	27
Figure 2.12 Oscilloscope record of 2009 sub synchronous event.....	27
Figure 2.13 d-axis control philosophies for inverter control	28
Figure 2.14 Voltage and active power at Hornsea One.....	31
Figure 2.15 Single line diagram for the Australian SSCI-CCI example.....	32
Figure 2.16 Voltage oscillations of 7.3 Hz following SSCI-CCI.....	33
Figure 2.17 Proposed reclassification of SSO phenomena	34
Figure 3.1 Proposed framework for mitigation solutions	42
Figure 3.2 Overview of mitigation solutions for DFIG-SSR, SSCI-CGI and SSCI-CCI.....	42
Figure 3.3 Overview of reviewed potential control solutions.....	43
Figure 3.4 Generic inverter control of a DFIG.....	44
Figure 3.5 Generic rectifier control of a DFIG	44
Figure 3.6 Control structure of a generic supplementary damping controller	47
Figure 3.7 Overview of reviewed hardware solutions	49
Figure 3.8 Overview of reviewed system level coordination-based solutions.....	52
Figure 4.1 Schematic diagram of a DFIG WTG	62
Figure 4.2 Equivalent representation of source and load system.....	64
Figure 4.3 Evaluation of DFIG-SSR using impedance based stability analysis	66
Figure 4.4 Example of DFIG-SSR evaluation using impedance based stability analysis.....	67
Figure 4.5 Numerical simulation set up for impedance calculation.....	67
Figure 4.6 Identification of perturbation signal and impedance calculation time.....	69
Figure 4.7 Current measurements following white noise perturbation.....	70
Figure 4.8 Evolution of the generator speed state variable over time.....	70

Figure 4.9 DFIG impedance response captured in stage II and stage III	71
Figure 4.10 Impact of the number of frequencies on the measured DFIG impedance.	72
Figure 4.11 DFIG impedance response using the average and detail EMT model.....	73
Figure 4.12 Study model for DFIG-SSR mitigation	76
Figure 4.13 Impedance responses of the study model	76
Figure 4.14 Modified IEEE 39-bus system.....	77
Figure 5.1 Study model for DFIG-SSR mitigation	82
Figure 5.2 Overview of classical and series phase imbalance compensation schemes.....	83
Figure 5.3 Vector diagram of the phase impedances at sub synchronous frequency.....	84
Figure 5.4 Influence of k and Δf_r on the required degree of asymmetry Q	87
Figure 5.5 Influence of the degree of asymmetry Q on the resonance frequency.....	87
Figure 5.6 Positive sequence impedance and resonance frequency of the overall system	88
Figure 5.7 Successful rectifier controller tuning ($\eta = 0.01$)	89
Figure 5.8 Optimisation of Q with the goal to mitigate DFIG-SSR.....	90
Figure 5.9 Positive sequence impedance of DFIG and compensated transmission line	90
Figure 5.10 Detailed time domain EMT simulations for series PIC	91
Figure 5.11 DFIG damping under different windspeed conditions	92
Figure 5.12 Series and parallel phase imbalance compensation schemes.....	93
Figure 5.13 Impedance of compensated phase A	95
Figure 5.14 Positive sequence impedance of DFIG and compensated grid.....	96
Figure 5.15 Measured instantaneous current and its harmonic spectrum	97
Figure 5.16 DFIG-SSR screening results for different parallel PIC cases.....	98
Figure 5.17 DFIG-SSR screening results for series resonance	100
Figure 5.18 DFIG-SSR screening results for C_A/C_1 -ratio 2 under varying C_1/C_2 -ratios.....	101
Figure 5.19 DFIG-SSR screening results for parallel resonances.....	102
Figure 5.20 EMT simulations for one phase parallel PIC with C_1/C_2 -ratio of 2.....	103
Figure 5.21 EMT simulations for parallel PIC with C_1/C_2 -ratio of 1.....	103
Figure 5.22 EMT simulations for parallel PIC with C_1/C_2 -ratio of 0.5.....	104
Figure 5.23 Compensation degrees leading to marginal stability	105
Figure 5.24 Phase C instantaneous currents for marginal stability case.....	106
Figure 5.25 Phase C instantaneous currents for 19 % compensation	106
Figure 5.26 DFIG-SSR screening under different system strength conditions.....	107
Figure 5.27 DFIG-SSR screening for marginal stability.....	108
Figure 5.28 Compensation degrees for different series compensation concepts	108
Figure 5.29 DFIG-SSR assessment for classical series compensation	109
Figure 5.30 Phase C instantaneous currents for classical compensation.....	109
Figure 5.31 Process for DFIG-SSR mitigation using phase imbalance compensation	110
Figure 5.32 Identification of a N-5 grid topology resulting in DFIG-SSR	111
Figure 5.33 Impedance responses of DFIG (red) and the IEEE 39 bus system.....	112
Figure 5.34 Phase A instantaneous currents for N-5 topology in the IEEE 39-bus system ...	112
Figure 5.35 Electrical damping coefficients under different wind generation levels	113
Figure 6.1 TenneT's control room of the future program.	118
Figure 6.2 Adaptive control proposed in [2]	118

Figure 6.3 Overview of prediction based gain scheduling control	120
Figure 6.4 Observed and forecasted wind speeds for twelve hours.	122
Figure 6.5 General architecture of an artificial neural network	123
Figure 6.6 Study model for development of DFIG-SSR mitigation solutions.....	124
Figure 6.7 Generic rectifier control of a DFIG	124
Figure 6.8 Generic inverter control of a DFIG.....	125
Figure 6.9 Impedance response of grid and DFIG under inverter parameter variations.....	127
Figure 6.10 Impedance response of grid and DFIG under rectifier parameter variations	127
Figure 6.11 Influence of 10% increase in rectifier parameters on the phase margin.....	128
Figure 6.12 Parameter reduction for gain scheduling	130
Figure 6.13 Graphical representation of parameters' values as a function of wind speed....	131
Figure 6.14 Impedance response of the grid and DFIG before and after parameter tuning...	131
Figure 6.15 Validation of parameter optimisation and reduction	132
Figure 6.16 Validation of FRT performance against grid code requirements	132
Figure 6.17 Validation of small-signal stability assessment using fictive wind speeds	133
Figure 7.1 Generic architecture of an artificial neural network	139
Figure 7.2 ANN for development of feedforward back propagation algorithm	140
Figure 7.3 Location and site identification numbers of considered wind power plants.....	143
Figure 7.4 First Quartile of MAE.....	145
Figure 7.5 Parametric evaluation of ANN based forecast model.....	146
Figure 7.6 Ranking of optimisers.....	149
Figure 7.7 Median versus Inter Quantile Range for optimisers	150
Figure 7.8 Raking of loss functions	151
Figure 7.9 Median versus Inter Quantile Range for loss functions.....	151
Figure 7.10 Observed versus forecasted values of most accurate implemented algorithm ...	154
Figure 8.1 Process of real-time operations module.....	162
Figure 8.2 Observed wind speed and its probability for the years 2008-2012.....	165
Figure 8.3 Probability of DFIG-SSR using the developed PGSC.....	166
Figure 8.4 Representation of multi-DFIG wind power plant connected to study model.....	167
Figure 8.5 Impedance responses of grid and different shares of tuned DFIGs.....	167
Figure 8.6 Instantaneous current response in a multi-DFIG system.....	168
Figure 8.7 Harmonic content of instantaneous current	169
Figure 8.8 Wind power plant layout with 30 DFIGs.....	170
Figure 8.9 Normalised wind speed as a function of distance.....	171
Figure 8.10 EMT simulations considering wake effects.....	172
Figure 8.11 Partitioning of source-load subsystems	173
Figure 8.12 EMT simulation results for case 1	174
Figure 8.13 EMT simulation results for case 2	175
Figure 8.14 EMT simulations considering wake effects.....	176
Figure 8.15 EMT simulations for IEEE 39 bus system.....	177

LIST OF TABLES

Table 2.1 Overview of research on various inverter d-axis control concepts.....	29
Table 3.1 Overview of FACTS controllers in 12 regions	50
Table 3.2 Overview of Mitigation Solutions.....	55
Table 5.1 Maximum current at f_r for phase A for different levels of asymmetry	91
Table 5.2 Negative resistance region of DFIG for different windspeed	92
Table 5.3 Identified parallel resonances.....	97
Table 6.1 Parameter influence on DFIG-SSR and SSCI.....	126
Table 6.2 Genetic algorithm solver settings.....	129
Table 6.3 Values for the constants of control rule (6.2).....	130
Table 7.1 Forecast time horizons in operational planning	138
Table 7.2 Geographical coordinates of considered wind power plants.....	143
Table 7.3 Raking of optimisers when using MAE, MAPE, and RMSE	152
Table 7.4 Raking of loss functions when using MAE, MAPE, and RMSE.....	152
Table 7.5 Raking of optimiser-loss function pairs based on MAE	153
Table 7.6 Raking of optimiser-loss function pairs based on MAPE	153
Table 7.7 Raking of optimiser-loss function pairs based on RMSE	153
Table 7.8 Accuracy improvement due to ANN tuning	155
Table 8.1 Performance of proposed gain scheduling solution	163
Table 8.2 Simulation cases for investigation of low frequency oscillations.....	173
Table 8.3 Summary of simulations with low frequency oscillations	175

LIST OF PUBLICATIONS

PHD PUBLICATIONS

JOURNAL PAPERS

- [1] **V. N. Sewdien**, R. Chatterjee, M. Val Escudero, and J. van Putten, “System Operational Challenges from the Energy Transition,” *CIGRE Science & Engineering Journal*, vol. 17, pp. 5–20, 2020.
- [2] **V. N. Sewdien**, X. Wang, J. L. Rueda Torres, and M. A. M. M. van der Meijden, “Critical Review of Mitigation Solutions for SSO in Modern Transmission Grids,” *Energies*, vol. 13, no. 13, p. 3449, 2020.
- [3] **V. N. Sewdien**, R. Preece, J. L. Rueda Torres, E. Rakhshani, and M. A. M. M. van der Meijden, “Assessment of Critical Parameters for Artificial Neural Networks based Short-Term Wind Generation Forecasting,” *Renewable Energy*, vol. 161, pp. 878–892, 2020.
- [4] **V. N. Sewdien**, J. L. Rueda Torres, and M. A. M. M. van der Meijden, “Evaluation of Phase Imbalance Compensation for Mitigating DFIG-Series Capacitor Interaction,” *Energies*, vol. 13, no. 17, p. 4512, 2020.
- [5] **V. N. Sewdien**, R. Preece, J. L. Rueda Torres, and M. van der Meijden, “Systematic Procedure for Mitigating DFIG-SSR using Phase Imbalance Compensation,” *under review*.
- [6] **V. N. Sewdien**, X. Xie, J. L. Rueda Torres, and M. van der Meijden, “Predictive Gain Scheduling Control for Mitigating SSR in DFIG Wind Power Plants,” *under review*.

CONFERENCE PAPERS

- [1] **V. N. Sewdien**, R. Preece, J. L. Rueda Torres, and M. A. M. M. van der Meijden, “Parametric Evaluation of Different ANN Architectures: Forecasting Wind Power Across Different Time Horizons,” in *2018 IEEE PES Transmission & Distribution Conference and Exhibition - Latin America (T&D-LA)*, 2018.
- [2] **V. N. Sewdien**, R. Preece, J. L. Rueda Torres, and M. A. M. M. van der Meijden, “Evaluation of PV and QV based Voltage Stability Analyses in Converter Dominated Power Systems,” in *2018 IEEE PES Asia Pacific Power and Energy Engineering Conference and Exhibition*, 2018.

- [3] **V. N. Sewdien** *et al.*, “Effects of Increasing Power Electronics on System Stability: Results from MIGRATE Questionnaire,” in *2018 IEEE PES International Conference on Green Energy for Sustainable Development*, 2018.
- [4] **V. N. Sewdien** and J. L. Rueda Torres, “Evaluation of Phase Imbalance Compensation for Mitigating DFIG-Series Capacitor Interaction,” in *29th IEEE International Symposium on Industrial Electronics*, 2020.

BOOK CHAPTERS

- [1] **V. N. Sewdien**, “Operation of FACTS Controllers,” in *Flexible AC Transmission Systems*, S. Nilsson and B. Andersen, Eds. Cham: Springer Nature, 2020, pp. 1063–1070.
- [2] S. Almeida de Graaff and **V. N. Sewdien**, “Power System Operation and Control,” in *Electricity Supply Systems of the Future*, N. Hatziargyriou and I. P. de Siqueira, Eds. Cham: Springer Nature, 2020, pp. 377–419.

MIGRATE TECHNICAL REPORTS

- [1] MIGRATE WP 1, “Deliverable D1.1 Report on Systemic Issues,” 2016.
- [2] MIGRATE WP 1, “Deliverable D1.2 Power System Analysis and KPIs,” 2018.
- [3] MIGRATE WP 1, “Deliverable D1.4 Tools for Monitoring and Forecasting PE Penetration,” 2018.
- [4] MIGRATE WP 1, “Deliverable D1.5 Power System Risk Analysis and Mitigation Measures,” 2019.
- [5] MIGRATE WP 1, “Deliverable D1.6 Demonstration of Mitigation Measures and Clarification of Unclear Grid Code Requirements,” 2019.

OTHER PUBLICATIONS

JOURNAL PAPERS

- [1] P. Maibach, A. Hernandez, J. Peiro, C. Smith, **V. N. Sewdien**, and J. van Putten, “Capabilities of Power Electronic Devices in Enabling the Energy Transition and Mitigating System Operational Challenges,” *CIGRE Science & Engineering. Journal.*, vol. 20, 2021.
- [2] E. Rakhshani, D. Gusain, **V. N. Sewdien**, J. R. Torres, and M. van der Meijden, “A Key Performance Indicator to Assess the Frequency Stability of Wind Generation Dominated Power System,” *IEEE Access*, vol. 7, pp. 130957–130969, 2019.

CONFERENCE PAPERS

- [1] V. N. Sewdien, R. Preece, and J. L. Rueda Torres, "Normalised Voltage Instability Sensitivity Index: A New Concept for Monitoring Voltage Stability in the Control Centre," in *Proceedings of the 2019 CIGRE Canada Conference*, 2019.

CIGRE TECHNICAL BROCHURES

- [1] CIGRE JWG C2/C4.37, "Technical Brochure 742: A Proposed Framework for Coordinated Power System Stability Control," Paris, 2018.
- [2] CIGRE JWG C2/B4.38, "Capabilities and requirements definition for power electronics based technology for secure and efficient system operation and control," Paris, 2020.

ACKNOWLEDGEMENT

I wish to express my gratitude to all who had a pivotal role in the completion of this thesis. This research would not even have started were it not for my colleagues Maartje van Gelder and Danny Klaar. Thank you for guiding me since the very beginning and especially in drafting the project proposal and obtaining the board approval for funding. I am grateful to my employer TenneT TSO B.V. for granting me the opportunity to pursue this PhD by combining my work and research interests.

At the TU Delft, I would like to thank my promotor prof. Mart van der Meijden and José Rueda Torres. Mart, thank you for listening to my struggles, for reassuring me that these are inherent to the PhD journey and for providing refreshing ways to tackle issues. José, thank you for having 48 hours in a day, as there is no other way I can explain your very fast reviews on my manuscripts. Ellen Schwencke-Karlas, Sharmila Rattansingh and Carla Jager, thank you for all the administrative support at the university since the very beginning.

This journey would have been less enjoyable without my great roommates at the university. Thank you Hossein Khalilnezhad and Lian Liu for sharing your experiences along your own PhD journeys. They made it easier for me to set expectations. *Mamnoon*, Nakisa Farrokhseresht for being the living embodiment of kindness. I always enjoyed our discussions on the human behaviour and societal issues, which always resulted in either lots of laughter or joint frustration towards human nature. Rishabh Bhandia, thank you for the fun discussions on history, geopolitics and the Indian culture.

I would like to thank prof. Udaya Annakkage of the University of Manitoba for hosting me at his institution in Canada in 2018 and for the discussions we had on this thesis. A special thanks goes to Dharshana Muthumuni, managing director of Manitoba HVDC Research Centre, for the collaboration with regards to PSCAD and for being a genuine friend and mentor.

Robin Preece, thank you very much for the great collaboration we had during the MIGRATE project and during this PhD journey. Your academic rigor, focus, and selflessness make you the great academic and even greater human being that you are. I enjoyed our fruitful collaboration and my visits to Manchester.

A word of appreciation also goes into the direction of the members of the doctoral examination committee for the time and effort spent in reviewing this work. Our discussions and your feedback improved the quality of this work, for which I am grateful.

Combining work with research was not always easy and I would like to express my gratitude to my TenneT colleagues for their support. *Muito obrigado* Susana de Graaff, for being the friend you are, for understanding the ups and downs inherent to this journey and for being though when needed. It has been a privilege to work together with you and support your chairmanship in my role as technical secretary of CIGRE study committee C2. It was an enriching experience, where I made great connections and built some long-lasting relationships.

Kees Jansen, thank you for your patience and time for our regular meetings, where we spent hours on discussing technical content as well as life. A special word of appreciation goes to Frank Nobel and Assia Sand for proofreading the manuscript. Hannes Munzel, *Vielen Dank* for your support during, and especially after, the MIGRATE project. I am still waiting to buy you that beer in Arnhem!

Friends are indeed the family we choose. Pravakar Pradhan, dear friend from Bhutan, *kadrin chhe la* for all the fun times and making me realise that life is much more than an efficiency constraint optimisation problem. I carry this lesson for the rest of my life. Aarif, Amrish, Bart, Gita, Kim, Madhawi, Madhvi, Renu, Twan, Zahierra thank you for the fun times, patience and for forgiving that I could not always be present at our gatherings in the past years.

Without the support from my family members, this journey would have been completely different, as they have been the source of energy and inspiration I continuously tapped into throughout this journey. For that and for the patience and the unconditional support, I want to thank from the bottom of my heart my Mom, Ajay and Vanya, Jayant, Varsha and *Barki Mai* and family.

Finally, I want to thank all my friends and colleagues whom I didn't have the chance to mention here.

Vinay Sewdien
Arnhem, June 2021

CURRICULUM VITAE



Vinay Sewdien was born on 18 November 1990 in Paramaribo, Suriname. He obtained his Bachelor of Science degree in Electrical Engineering in 2011 from the Anton de Kom Universiteit van Suriname and his Master of Science degree in Electrical Engineering (*cum laude*) from the KU Leuven in 2013. Since his graduation, Vinay is with the Dutch-German transmission system operator TenneT TSO B.V. He is currently a senior policy advisor in the System Operations Development team, working on the impact assessment of the energy transition on system operation and on the development of new concepts and methodologies for maintaining operational reliability. In January 2016 Vinay joined the Intelligent Electrical Power Grids group at the Electrical Engineering, Mathematics and Computer Science Faculty of the TU Delft as a part-time PhD researcher. From August 2016 to August 2020 he was also the Technical Secretary of CIGRE's international study committee on Power System Operation and Control and currently serves as a member of CIGRE Electra's Editorial Board. Vinay is the founder and chair of the Education for Development Foundation and is a member of CIGRE and IEEE, actively contributing to several working groups.

